

THE COLOUR OF AuAgCu ALLOYS

A thesis submitted in partial
fulfilment of the regulations
of the Council of National
Academic Awards for the degree
of Doctor of Philosophy.

by

R.HUNT BSc

Sponsoring Establishment

Department of Metallurgy
Sir John Cass School of Science and Technology
City of London Polytechnic
Whitechapel High Street
London E1

December 1983

Collaborating Establishment

Worshipful Company of Goldsmiths
Foster Lane
London EC1

DECLARATION

I, the undersigned ROBERT HUNT hereby declare that the work contained in this thesis has not been submitted before or elsewhere for an academic qualification and that I have not been, during my registration with the CNAА for the PhD candidature, registered with any other academic or professional institution as a candidate. This work has been sponsored by the Right Worshipful Company of Goldsmiths. I attended the lectures of the MSc in Solid State Physics (CLP) and passed the qualifying examination, paper II.

Signed *R. Hunt*

ACKNOWLEDGEMENTS

I would like to express my gratitude to Dr. E.F.I. Roberts for his constant support and encouragement, Dr. K.M. Clarke for many stimulating discussions, Mr. R. Cohen for assistance in the fabrication of alloys, and finally to the Goldsmiths Research Foundation for sponsoring the work.

THE COLOUR OF AuAgCu ALLOYS

R Hunt BSc

Abstract

The colorimetric properties of the AuAgCu ternary system have been examined with a nulling spectro-ellipsometer. The use of an ellipsometer to derive the colour co-ordinates of a sample is a novel technique. The ellipsometer has the advantages for use as a physical colorimeter in that its calibration is goniometric and it does not require a particularly stable light source or secondary reflectance standard.

The spectro-ellipsometer was operated in the PCSA configuration at 75 Deg. angle of incidence. The compensator fast axis was fixed at $-\pi/4$ azimuth and nulling was achieved by adjustment of the polariser/analyser azimuths. Data was taken over the wavelength range of 250nm to 850nm at intervals of 10nm and an optical bandwidth of 10nm. The AuAgCu alloys were fabricated with an equilibrium temperature of 600 C as 10 x 20 x 1 mm plaquettes mounted in thermo-setting resin. The compositional range of the alloys covered the entire AuAgCu system in 10 weight percentage increments (36 alloys in all). The plaquettes were hand polished and finished with a $\frac{1}{4}\mu$ lapp.

The colour co-ordinates of each alloy were derived by recording the analyser/polariser nulling azimuths at a range of wavelengths. This data was reduced to Ψ , Δ & λ sets from which the complex refractive index spectra were calculated and finally the colour co-ordinates calculated in the CIE 1931 convention for illuminant 'C'.

The colour co-ordinates derived by this method were found to violate Grassmanns' third law of colour mixing (addition). The majority of the alloys examined were duplex-phase and linear colour loci for a constant weight percentage of Au were expected. The linear loci were not observed. This deviation is shown to be an instrumental artifact present when examining poly-phase substrates. An optical model is proposed to explain this effect. The model was tested on the AgCu-CuAg binary system. The model is used to re-assess the colorimetry of the AuAgCu ternary system.

CONTENTS

Declaration

Acknowledgements

Abstract

Contents

Glossary

| | | |
|-----|---|----|
| 1. | Introduction | 1 |
| 2. | Literature Survey | |
| 2.1 | Introduction | 4 |
| 2.2 | Representation of light | 4 |
| 2.3 | Sign convention and definition | 5 |
| 2.4 | Stokes vector and Poincaré sphere | 7 |
| 2.5 | Jones matrix | 10 |
| 2.6 | Mueller matrix | 14 |
| 2.7 | Ellipsometric nulling | 15 |
| 2.8 | Component imperfections (Jones matrices) | 16 |
| 2.9 | Zone averaging | 17 |
| 3. | Ellipsometer Construction | |
| 3.1 | Design principles of an automatic nulling ellipsometer | 30 |
| 3.2 | Ellipsometer construction | 32 |
| 3.3 | Photomultiplier head amplifier | 33 |
| 3.4 | Bandpass amplifier | 34 |
| 3.5 | Phase-sensitive rectifier and low- pass filter | 34 |

| | | |
|-------|--|-----|
| 3.6 | Linear amplifier | 36 |
| 3.7 | Goniometer position control and display | 37 |
| 3.8 | Faraday modulator | 39 |
| 3.9 | System performance | 42 |
| | | |
| 4. | Experimental Procedures | |
| 4.1 | Ellipsometer optical alignment | 58 |
| 4.1.1 | Reference axes (p-s) | 59 |
| 4.1.2 | Analyser/Polariser azimuths | 60 |
| 4.1.3 | Compensator axes at $\pm\pi/4$ | 64 |
| 4.1.4 | Summary of azimuth alignments for the polariser, analyser and compensator | 66 |
| 4.1.5 | Compensator calibration | 67 |
| 4.1.6 | Monochromator calibration | 69 |
| 4.2 | Alloy fabrication | 70 |
| 4.3.1 | Ellipsometer data reduction | 72 |
| 4.3.2 | Calculation of colour co-ordinates | 74 |
| | | |
| 5. | Results | |
| 5.1 | Absorption edges | 88 |
| 5.2 | Colorimetry | 90 |
| | | |
| 6. | Discussion | |
| 6.1 | Introduction | 123 |
| 6.2 | Comparison with published data | 127 |
| 6.3 | Optical model | 131 |
| 6.4 | Conclusion | 143 |

Ellipsometry

7. Further Work

181

- References**
- Appendices**
- A_i - analyser nulling azimuth in i^{th} zone
- ΔA_i - small offset in analyser nulling azimuth
- Res A** - residue formed by adding/subtracting analyser nulling azimuths
- B - magnetic field density
- c - speed of light
- C_i - compensator azimuth in i^{th} zone
- ΔC_i - small offset in compensator azimuth
- D - electric field density
- E - electric field strength
- E_{ijR} - element of Jones matrix
- H - magnetic field strength
- I - light intensity transmitted by the complete ellipsometer
- J - current density
- k - complex component of refractive index
- \hat{k} - unit vector in the direction of propagation of an electromagnetic wave
- Δ - propagation vector
- n_c - complex refractive index
- n - real component of refractive index
- P_i - polariser nulling azimuth in i^{th} zone
- ΔP_i - small offset in polariser azimuth
- Res P** - residue formed by adding/subtracting polariser nulling azimuths

GLOSSARY

- P - plane Ellipsometry the plane of incidence
- $R(\theta)$ - matrix for the rotation of an optical
- A_i - analyser nulling azimuth in i^{th} zone
- δA - small offset in analyser nulling azimuth
- Res A - residue formed by adding/subtracting
analyser nulling azimuths
- \underline{B} - magnetic field density
- c - speed of light
- C_i - compensator azimuth in i^{th} zone
- δC - small offset in compensator azimuth
- \underline{D} - electric field density
- \underline{E} - electric field strength
- f_{ijR} - element of Jones matrix
- \underline{H} - magnetic field strength
- I - light intensity transmitted by the
complete ellipsometer
- \underline{J} - current density
- k - complex component of refractive index
- \underline{k} - unit vector in the direction of propagation
of an electromagnetic wave
- \underline{r} - propagation vector
- n_c - complex refractive index
- n - real component of refractive index
- P_i - polariser nulling azimuth in i^{th} zone
- δP - small offset in polariser azimuth
- Res P - residue formed by adding/subtracting
polariser nulling azimuths

- p - plane parallel to the plane of incidence
 $R(\theta)$ - matrix for the rotation of an optical
 components azimuth by θ
 \underline{r} - propagation vector
 r_p - complex reflection coefficient in p-direction
 r_s - complex reflection coefficient in s-direction
 S_i - elements of Stokes vector
 s - plane perpendicular to the plane of incidence
 T_i - elements of Jones matrix
 ∂T - matrix of imperfections in a Jones matrix
 t - compensator transmission ratio
 t - time
 $\underline{x}, \underline{y}, \underline{z}$ - unit vectors in orthogonal coordinate space
 Z_i - nulling azimuth of general component
 ∂Z_i - nulling azimuth error in Z_i
 α - amplitude attenuation coefficient
 β - Jones matrix element
 γ'_k - coupling coefficient between component
 imperfections, nulling azimuths and ρ
 Δ - relative phase shift between p-s components
 δ' - difference from $\pi/2$ of compensator retardation
 δ_i - absolute phase
 θ - angle of rotation relative to the principal
 frame of an optical component
 θ - compensator retardation

- λ - wavelength
- ρ - electron charge density
- ρ - complex relative amplitude reflection coefficient
- ρ_c - compensator complex amplitude transmission coefficient
- ϕ - angle of incidence
- χ - polarisation vector
- ψ - $\tan\psi$, relative amplitude reflection ratio
- ω - radial frequency
- $\partial\omega$ - incremental radial frequency

Colorimetry

- $E_x(\lambda), E_y(\lambda), E_z(\lambda)$ - spectral eye response
- ΔE - colour difference parameter
- $I(\lambda)$ - illuminance at an object
- Lab - CIE 1974 uniform colour space co-ordinates
- $\Delta L, \Delta a, \Delta b$ - colour difference in Lab co-ordinates
- $R(\lambda)$ - spectral reflectance
- R - normal reflectance
- X, Y, Z - CIE 1931 tri-stimulus colour co-ordinates
- x, y, z - CIE 1931 colour co-ordinates

CHAPTER ONE

INTRODUCTION

The colour of an object is of prime importance when that object is made for decoration. The jewellery and silversmithing industry is concerned with the manufacture of such objects and it is one of the most ancient of all crafts. Despite this long history the measurement of colour, until very recently, has been made by subjective comparison. That is, a sample with an unknown colour is compared subjectively to a range of reference samples. The basis of many commercial gold and silver alloys is the AuAgCu ternary system. The earliest extensive mapping of the colorimetry of this system was made by Leuser (1949) who examined subjectively a large number of alloys. This colour map was later published by Wise (1964), although in translation some of the colour descriptions were modified. The translation of the colour names by Wise highlights an additional problem, which is that not only will an individual alloy be given different colour descriptions by different individuals, but, that in communication between different countries, jewellery and silversmithing is an international trade, colour descriptions will change by translation. An attempt to provide a set of reference samples which were both few in number and encompassed

many commercial alloys was made by the German standard DIN 8328. This is a set of 14 and 18 carat alloys based on an earlier Swiss watch industry standard.

The limitations of a subjective test have been highlighted by Groenwald et al (1977) who showed the variation in colour descriptions given by bullion dealers and manufacturers to particular alloys. These variations in the colorimetric descriptions also contain, implicitly, variations in the ability of individuals to distinguish between or match two coloured samples. And then to subjectively describe any apparent colour difference, but the observers ability to detect colour differences itself depends on the colour, M^CAdam (1942) and Wright (1941).

The limitations of this subjective comparison between reference samples and unknown alloys were such that in 1974 the Worshipful Company of Goldsmiths sponsored a research programme at the City of London Polytechnic with the objective " To examine the optical and other characteristics of carat gold alloys with a view to linking the metal colour to positive parameters and, if successful, to suggest an instrumental method for readily determining the relevant parameters and, hence, colour of the metal" Roberts (1978).

A spectro-ellipsometer was to be used in determining

the normal reflectance spectra of a set of alloys which covered the entire AuAgCu system in weight increments of 10%. A spectro-ellipsometer has two particular advantages compared to a reflectometer in that a) it does not require a reference or comparison surface e.g. mirror or barium sulphate screen, and b) it does not require that the detector is linear. The calibration of an ellipsometer is goniometric and once established it is very stable.

The colorimetric examination of the AuAgCu system comprised two sections. Firstly, the examination of the binary systems AuAg, AgCu and CuAu, Clarke (1980), and secondly this work which examined the AuAgCu ternary system.

CHAPTER TWO

LITERATURE SURVEY

2.1 Introduction

Ellipsometry is the study of elliptically polarised light, its production and analysis. The change in the state of polarisation due to a beam passing through an optical system is the basis of ellipsometric analysis. The beam polarisation parameters are:-

a) the amplitude ratio along orthogonal axes, $\tan \Psi$

b) the relative phase-shift along the two axes, Δ

The analysis of an optical system is thus based on determining Ψ and Δ in the presence of component imperfections and azimuth mis-alignments.

2.2 Representation of Light

Polarisation is a property which is common to all transverse wave vectors. Light is an electromagnetic wave which is described by the four field-vectors

E - electric field strength

D - electric field density

B - magnetic field strength

H - magnetic field density

The four vector-fields are related by Maxwell's equations,

$$\nabla \wedge \underline{E} = -\frac{\delta \underline{B}}{\delta t}$$

$$\nabla \cdot \underline{B} = 0$$

$$\nabla \cdot \underline{D} = \sigma$$

$$\nabla \wedge \underline{H} = \underline{J} + \frac{\delta \underline{D}}{\delta t}$$

J - current density

In general when \underline{E} is known the remaining three quantities can be deduced from Maxwell's equations. In examining polarisation only the \underline{E} field will be considered.

Consider an electric vector \underline{E} at some random orientation in space, the vector property of the wave can be used to resolve it along three mutually orthogonal axes, figure 2.1, with the resultant components:-

$$E_x, E_y, E_z$$

$$\underline{E} = E_x \underline{x} + E_y \underline{y} + E_z \underline{z}$$

$\underline{x}, \underline{y}, \underline{z}$ - unit vectors along each axis

Assuming that the wave is monochromatic i.e. $\omega \gg \partial\omega$ then each component will have the form $E_i \cos(\omega t + \theta_i)$

where E_i is the amplitude, ω the angular frequency, t the time (relative to an arbitrary time of zero) and θ_i the absolute phase (relative to an arbitrary zero).

Azzam & Bashara (1977) have shown that a vector drawn from the origin of the axes x, y, z will trace out an ellipse. It is the description of this ellipse which forms the basis of ellipsometry.

2.3 Sign Convention and Definition

The mathematical formulation of ellipsometry presents ample opportunity for confusion. Muller (1969) discusses nine two-fold sign conventions in detail, showing the different, but equally valid, basis from which ellipsometric theory can be derived.

The multiplicity of possible conventions is due to the choice of:-

a) the positive directions of the p and s components of the incident and reflected \underline{E} vectors

b) the absolute phase-shift of an electromagnetic wave upon reflection

c) the formulation of the electromagnetic wave to be consistent with theories developed in other fields e.g. nuclear physics and microwave electronics

d) the description of a surface by a refractive index which is independent of the angle of incidence

The available choices lead to eight numerically different combinations. The convention which Muller proposed is formulated

$$\underline{E} = E_0 \exp \{ i(\omega t + \vartheta) \} \exp (-i\mathbf{k} \cdot \underline{\mathbf{r}}) \exp (-\alpha z)$$

complex relative amplitude attenuation $\underline{\rho}$

$$\underline{\rho} = r_p / r_s$$

$$= \frac{|E''_p| / |E''_s|}{|E_p| / |E_s|} \exp \{ i(\vartheta_p - \vartheta_s) \}$$

$$= \tan \psi \exp (i\Delta)$$

$$\tan \psi = |r_p| / |r_s| \quad : \quad \Delta = \vartheta_p - \vartheta_s$$

complex refractive index n_c

$$n_c = n - ik$$

and a co-ordinate system, figure 2.2

where E_p & E_s - p-s components of \underline{E} before reflection

E''_p & E''_s - p-s components of \underline{E} after reflection

r_p & r_s - complex reflection amplitude coefficients

Physically this convention gives a complex refractive index which is independent of the angle of incidence, and is a material constant at a given wavelength. This complex refractive index is simply related to other properties such as magnetic permeability, dielectric constant and conductivity; but results in the physically less meaningful complex angle of refraction, θ

The choice of positive time dependency for the electric field vector is consistent with microwave and electronic engineering notation but it is at variance with nuclear physics notation.

The convention does have one important inconsistency which is that in order to maintain a right-handed co-ordinate system for both incident and reflected waves, the positive directions of the incident and reflected waves in the p- and s- directions are anti-parallel. This gives different reflection co-efficients for p- and s- components at normal incidence.

2.4 Stokes Vector and Poincaré Sphere

The representation of polarised light by a pair of equations of the form

$$E_x = A_1 \cos (\omega t + \partial_x)$$

$$E_y = A_2 \cos (\omega t + \partial_y)$$

has been shown, Azzam & Bashara (1977), to represent all possible states of total polarisation by suitable choices of A_1 , A_2 , ∂_x and ∂_y for a given value of ωt .

These quantities are, in general, complex in amplitude and a very convenient way of describing the state of polarisation is in terms of intensities, which are related to measurable quantities. To this end Stokes (1852) parameters S_0 , S_1 , S_2 and S_3 are derived as :-

$$S_0 = \langle E_x^2 \rangle + \langle E_y^2 \rangle$$

$$S_1 = \langle E_x^2 \rangle - \langle E_y^2 \rangle$$

$$S_2 = 2\langle E_x E_y \cos(\delta_y - \delta_x) \rangle$$

$$S_3 = 2\langle E_x E_y \sin(\delta_y - \delta_x) \rangle$$

The angle brackets $\langle \rangle$ denote a time average over many cycles of ωt . These parameters represent the intensity of the polarised light. Given any three parameters the fourth is obtained from the relation

$$S_0^2 = S_1^2 + S_2^2 + S_3^2$$

For partially polarised light the parameters are related by the inequality

$$S_0^2 > S_1^2 + S_2^2 + S_3^2$$

from which the degree of polarisation is defined as

$$P = (S_1^2 + S_2^2 + S_3^2) / S_0^2$$

P varies from 0 for unpolarised light to 1 for totally polarised light

S_0 - intensity of beam

S_1 - difference in intensity between the x & y directions

S_2 - preference of the wave in the $\pm\pi/4$ directions

S_3 - preference of the wave to circular polarisation

The Stokes parameters are collected into a 4 x 1 matrix to form the Stokes Vector S

$$S = \begin{pmatrix} S_0 \\ S_1 \\ S_2 \\ S_3 \end{pmatrix}$$

Several examples of normalised intensity states of polarisation with their Stokes Vectors are shown in table 2.1

A very important feature of the Stokes Vector is that the result of adding several incoherent polarised beams is described by the addition of their Stokes Vectors. Thus the overall state of polarisation S due to the addition of N incoherent waves is

$$S = \sum_{i=1}^N S_i$$

where S_i is the Stokes Vector of the i^{th} wavefront.

Poincaré Sphere

The Poincaré Sphere (1892) is derived by plotting the Stokes parameters, normalised to S_0 , along three mutually orthogonal directions S_1 , S_2 & S_3 . Thus any state of total polarisation is on the surface of a unit sphere, partially polarised light is represented by points within the sphere.

The sphere has several interesting symmetries which are:-

- a) the poles of the sphere represent left and right circularly polarised light
- b) the equator of the sphere is the locus of all linear polarisations
- c) the lines of longitude from the north to south pole are loci of elliptically polarised light of constant azimuth

- d) the lines of latitude around the sphere are the loci of elliptically polarised light of constant ellipticity
- e) all points on the northern hemisphere are right-handed, on the southern hemisphere they are left-handed

The Poincaré Sphere representation of several states of polarisation are shown in figure 2.3

2.5 Jones Matrix

The representation of an arbitrary state of polarisation by components along two orthogonal directions provides a convenient method by which states of polarisation are described in a form suitable for matrix manipulation. The matrix formulation was first derived by Jones (1941 a, b, 1942). This technique described totally polarised light as a 2 x 1 column matrix. The change of polarisation of the light upon passing through a polarising element is described by multiplying the 2 x 1 matrix by a 2 x 2 Jones Matrix which contains the properties of the polarising element.

$$\begin{pmatrix} E'_x \\ E'_y \end{pmatrix} = T \begin{pmatrix} E_x \\ E_y \end{pmatrix}$$

where E_x, E_y - incident electric field components

E'_x, E'_y - exiting electric field components

T - Jones Matrix of the polarising element

and for a series of polarising elements

$$\begin{pmatrix} E'_x \\ E'_y \end{pmatrix} = \prod_{i=1}^N T_i \begin{pmatrix} E_x \\ E_y \end{pmatrix}$$

The elements of any particular matrix e.g. polariser matrix are derived from a cartesian transformation of the form

$$E'_x = E_x f_{11} + E_y f_{12}$$

$$E'_y = E_x f_{21} + E_y f_{22}$$

where f_{11} , f_{12} , f_{21} & f_{22} are the elements of the Jones Matrix T,

$$T = \begin{pmatrix} f_{11} & f_{12} \\ f_{21} & f_{22} \end{pmatrix}$$

The particular elements f_{ij} of the Jones matrix are deduced by considering the transformation of the state of polarisation caused by the optical component, when both the initial and final states are known. Since the Jones matrix has four elements and the state of polarisation is described by a two-element vector, two different initial polarisation states with their corresponding final states are required.

e.g. Jones matrix of an ideal polariser

Initial State 1

Plane polarised light in the x-direction, polariser pass-plane in the x-direction, output state is linearly polarised light in the x-direction, thus

$$\begin{pmatrix} E'_x \\ 0 \end{pmatrix} = \begin{pmatrix} f_{11} & f_{12} \\ f_{21} & f_{22} \end{pmatrix} \begin{pmatrix} E_x \\ 0 \end{pmatrix}$$

$$E'_x = E_x f_{11} + 0 f_{12}$$

$$0 = E_x f_{21} + 0 f_{22}$$

Initial State 2

Plane polarised light on the y-direction and the pass-plane of the polariser in the x-direction; the light is extinguished.

$$\begin{pmatrix} 0 \\ 0 \end{pmatrix} = \begin{pmatrix} f_{11} & f_{12} \\ f_{21} & f_{22} \end{pmatrix} \begin{pmatrix} 0 \\ E_y \end{pmatrix}$$

$$0 = 0 f_{11} + E_y f_{12}$$

$$0 = 0 f_{21} + E_y f_{22}$$

The values of f_{ij} are:-

$$f_{11} = 1$$

$$f_{12} = 0$$

$$f_{21} = 0$$

$$f_{22} = 0$$

The Jones matrix for an ideal polariser with its pass-plane along the x-axis is therefore

$$\begin{pmatrix} 1 & 0 \\ 0 & 0 \end{pmatrix}$$

The same technique will yield the elements of any optical component.

The particular merit of this type of matrix representation is that it allows the derivation of the properties of an optical component in any convenient frame of reference. This frame of reference can be rotated into any other frame by pre-multiplying it by the rotation matrix $R(\theta)$

$$\text{i.e. } T(\theta) = T R(\theta)$$

$$R(\theta) = \begin{pmatrix} \cos(\theta) & \sin(\theta) \\ -\sin(\theta) & \cos(\theta) \end{pmatrix}$$

Usually, however, it is convenient to maintain a constant frame of reference, in which case the matrix T is also post-multiplied by R(-θ), thus

$$\begin{pmatrix} E'_x \\ E'_y \end{pmatrix} = R(-\theta) T R(\theta) \begin{pmatrix} E_x \\ E_y \end{pmatrix}$$

where E_x , E_y , E'_x & E'_y are in the same frame of reference.

Any sequence of polarising components is represented by a single matrix T which is formed by multiplying the matrices of components in their principal frames by the appropriate rotation matrices.

$$T = \prod_{i=1}^N R(-\theta_i) T_i R(\theta_i)$$

The Jones matrices for a polariser and λ/4 retarder are given in table 2.2 .

The elements of the Jones matrix can be associated with the general properties of the component. A diagonal matrix, in its principal frame,

$$\begin{pmatrix} f_{11} & f_{12} \\ f_{21} & f_{22} \end{pmatrix}$$

is characteristic of a linear component, such as a polariser or retarder. If, however, the cross-terms f_{12} , f_{21} are finite then there is cross-scattering between the x & y directions; this is characteristic of an optically active component e.g. a polarisation modulator based upon the Faraday effect.

2.6 Mueller Matrix

The most significant limitation of the Jones formulation is that it is unable to describe partially polarised light, there being no Maxwell column for unpolarised light.

This limitation was removed by Mueller (1948) with the introduction of a 4 x 4 matrix which operates on the Stokes vector in the same manner as the Jones matrix operates on the Maxwell column. The Mueller analysis is capable of describing all states of polarisation.

The Mueller matrix elements can be derived from the Jones matrix elements (Gerrard and Burch 1975) and by considering the effect of an optical component upon light of known polarisation in an analogous treatment to that used to derive the elements of the Jones matrices. For the Mueller matrix we have

$$\begin{pmatrix} S_0 \\ S_1 \\ S_2 \\ S_3 \end{pmatrix} = \begin{pmatrix} M_{11} & M_{12} & M_{13} & M_{14} \\ M_{21} & M_{22} & M_{23} & M_{24} \\ M_{31} & M_{32} & M_{33} & M_{34} \\ M_{41} & M_{42} & M_{43} & M_{44} \end{pmatrix} \begin{pmatrix} S_0 \\ S_1 \\ S_2 \\ S_3 \end{pmatrix}$$

To derive the sixteen elements of the Mueller matrix from Stokes vectors of four components it is necessary to examine four independent states of initial polarisation. The Mueller matrices for an ideal polariser and $\lambda/4$ retarder are shown in table 2.3 .

2.7 Ellipsometric Nulling

The optical system under ellipsometric examination can be assigned a Jones matrix which maps the input polarisation onto an output state. Azzam and Bashara (1977) have shown that the mapping of the incident polarisation χ_i to the output state χ_o is described by the transform

$$\chi_o = \frac{f_{22} \chi_i + f_{21}}{f_{12} \chi_i + f_{11}} \quad ; \quad (\chi_i = \tan \psi_i \exp i\Delta_i)$$

and that this transform is uniquely determined by the mapping of three input polarisations onto three output polarisations and they deduce that

$$f_{11} = \chi_{i2} - \chi_{i1} H$$

$$f_{12} = H - 1$$

$$f_{21} = \chi_{i2} \chi_{o1} - \chi_{i1} \chi_{o2} H$$

$$f_{22} = -\chi_{o1} + \chi_{o2} H$$

$$H = \frac{(\chi_{o3} - \chi_{o1})(\chi_{i3} - \chi_{i2})}{(\chi_{o3} - \chi_{o2})(\chi_{i3} - \chi_{i1})}$$

In the case of nulling ellipsometry the input and output polarisations will be elliptical and linear. Thus to completely describe the surface three independent nulls are required.

In practice, however, we are interested only in the normalised Jones matrix obtained by dividing each element by f_{22} ($\neq 0$) and obtaining f_{11}/f_{22} , f_{12}/f_{22} , f_{21}/f_{22} & 1. Also it is assumed that the surface is linear, $f_{12}=f_{21}=0$. The matrix reduces to

$$\begin{pmatrix} f_{11}/f_{22} & 0 \\ 0 & 1 \end{pmatrix}$$

With these simplifications it is possible to obtain all of the data from the measurement of a single null, i.e.

$$\chi_o = (f_{22}/f_{11}) \chi_i$$

2.8 Component Imperfections (Jones Matrices)

The analysis of the effects which component imperfections have upon the value of Ψ and Δ deduced from a null measurement have been treated in a piecemeal fashion by many authors, McCrackin et al (1963), Hölmes and Feucht (1967), Hunter (1970, 1973), Holmes (1964) and Winterbottom (1955).

Azzam and Bashara (1971a,b,c,d,e,1972) unified the error analysis of nulling ellipsometry and treated both component imperfections and azimuth misalignment. Their first-order treatment is based on the assumption that each component which contains an imperfection has a Jones matrix which can be subdivided into the matrix of a perfect component and a second matrix containing the imperfections, i.e.

$$T = T^0 + \partial T$$

where T - Jones matrix with imperfections

T^0 - Jones matrix of the perfect component

∂T - Jones matrix of imperfections

Similarly for azimuth errors

$$Z = Z^0 + \partial Z$$

The surface characteristic ρ_s is a function of the nulling angles Z_i and component matrices T_i

$$\rho_s = g(Z_i , T_i)$$

where the subscript i ranges over all the components.

The linear Taylor expansion around z^0 and T^0 is

$$\rho_s = g(z_i^0, T_i^0) + \sum_k \gamma'_k \partial z_k + \sum_{ijk} \gamma_{ijk} \partial T_{ijk}$$

The summation ij includes the four nulling positions and k ranges over all the optical elements. The quantities γ'_k and γ_{ijk} are the coupling coefficients by which component imperfections and azimuth error propagate into ρ_s . The coupling coefficients which were deduced are shown in table 2.4

The variables are:-

- ρ_c - compensator characteristics
- A - analyser azimuth
- P - polariser azimuth
- C - compensator fast-axis azimuth

These coupling coefficients can be used to determine the direct effects of the errors and imperfections upon Ψ and Δ .

The subscripts 1,3 and 2,4 denote the zones with the fast-axis of the compensator at $-\pi/4$ and $+\pi/4$ respectively. The first-order corrections to Ψ and Δ are given in table 2.5 for each of the four zones.

2.9 Zone Averaging

Classically Ψ and Δ are deduced from the average of readings taken in four zones, in which the errors due to imperfections and azimuth offsets are eliminated e.g. McCrackin (1963). Azzam and Bashara (1971a) define the parameter of residue for two and four zone averages to demonstrate the manner in which imperfections and errors are eliminated.

The imperfections will, in general, be complex

$$f_{12} = f_{12R} + f_{12I}$$

where the R and I subscripts denote the real and imaginary components. A further subscript is added to denote the optical component,

P - polariser

C - compensator

A - analyser

Thus, for example, the imaginary component of the f_{21} element of the Jones matrix of a compensator is f_{21IC} . Using this notation the imperfections which affect the Ψ and Δ values for each of the four zones are listed in table ~~2.6~~ **2.5**

The residues defined by Azzam & Bashara reject the Ψ and Δ information and enhance the imperfections, the residues are:-

$$\begin{aligned} \text{Res } A^+ &= A_4 + A_2 \\ &= - f_{22RC} \sin 2\Psi \sin \Delta + 2 \sin 2\Psi \cos \Delta \partial C - 2\partial A \end{aligned}$$

$$\begin{aligned} \text{Res } P^+ &= P_4 - P_2 \\ &= - f_{22IC} \sin \Delta \end{aligned}$$

$$\text{Res } A^- = f_{22RC} \sin 2\Psi \sin \Delta + 2 \sin 2\Psi \cos \Delta \partial C - 2\partial A$$

$$\text{Res } P^- = f_{22IC} \sin \Delta$$

These residues can be used to determine the compensator characteristics; the difference between the ideal characteristics and its actual values are:-

$$f_{22IC}^\pm = - \text{Res } P^\pm / \sin \Delta$$

$$f_{22RC}^\pm = \pm \text{Res } A^\pm / \sin 2\Psi \sin \Delta$$

This is in agreement with the formula derived by McCrackin et al (1963) for the error in the compensator retardation (θ).

$$\theta - \pi/2 = (a_p - a_s) / (\cos 2P \sin 2\Psi)$$

Note: in the McCrackin notation $\Delta = \pi/2 + 2P$

In addition the residuals can be formed from four-zone measurements as

$$\begin{aligned} \text{Res 1A} &= A_1 - A_2 - A_3 + A_4 \\ &= 4f_{21IP} \sin 2\Psi \end{aligned}$$

$$\text{Res 2A} = 2f_{12RC} \sin 2\Psi \sin \Delta$$

$$\begin{aligned} \text{Res 3A} &= (f_{12RC}^- - f_{12RC}^+) \sin 2\Psi \sin \Delta + 4\sin 2\Psi \cos \Delta \partial C \\ &\quad - 4\partial A \end{aligned}$$

$$\text{Res 1P} = -4f_{12RP} - 4\partial P + 4\partial C$$

$$\text{Res 2P} = 2f_{21IC} \sin \Delta$$

$$\text{Res 3P} = (f_{21IC}^- - f_{21IC}^+) \sin \Delta$$

f_{12RP} - polariser azimuth error

f_{21IP} - polariser ellipticity

The component imperfections are thus

polariser ellipticity $\text{Res 1A} / (4\sin 2\Psi)$

compensator retardation $\pi/2 + \text{Res 2A} / (2\sin 2\Psi \sin \Delta)$

compensator transmission ratio $1 + \text{Res 2P} / (2\sin \Delta)$

It is not necessary to know the imperfections described above in order to correct, with reference to table 2.5, the measured Ψ and Δ values. It can be seen that for a two-zone average in Ψ and Δ that

a) Ψ is free of error due to

- 1) all azimuth errors
- 2) compensator deviation from $\pi/2$ retardation
- 3) analyser imperfections

Ψ is still subject to polariser ellipticity

b) Δ is free of error due to

- 1) analyser azimuth error
- 2) polariser and analyser ellipticities
- 3) compensator deviation from $\pi/2$ retardation

Δ is still subject to polariser and compensator azimuth errors.

Finally, in the classical four-zone average it can be seen that both Ψ and Δ are free from all first-order imperfections of the optics and azimuth errors.

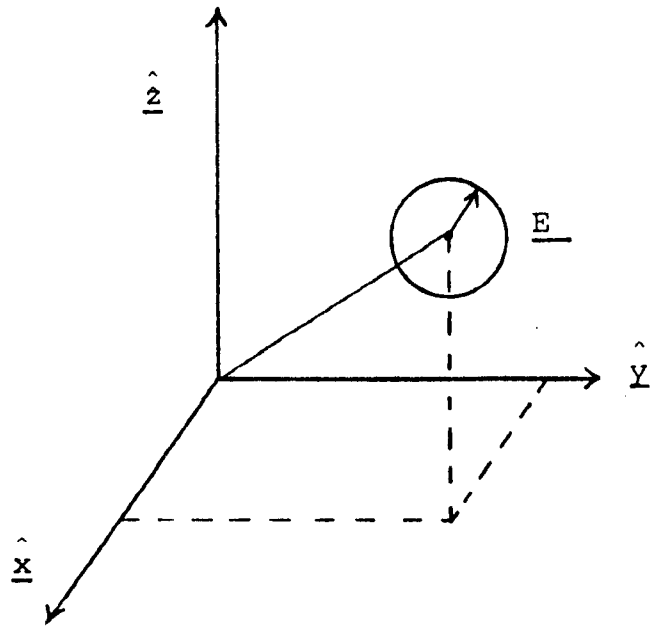
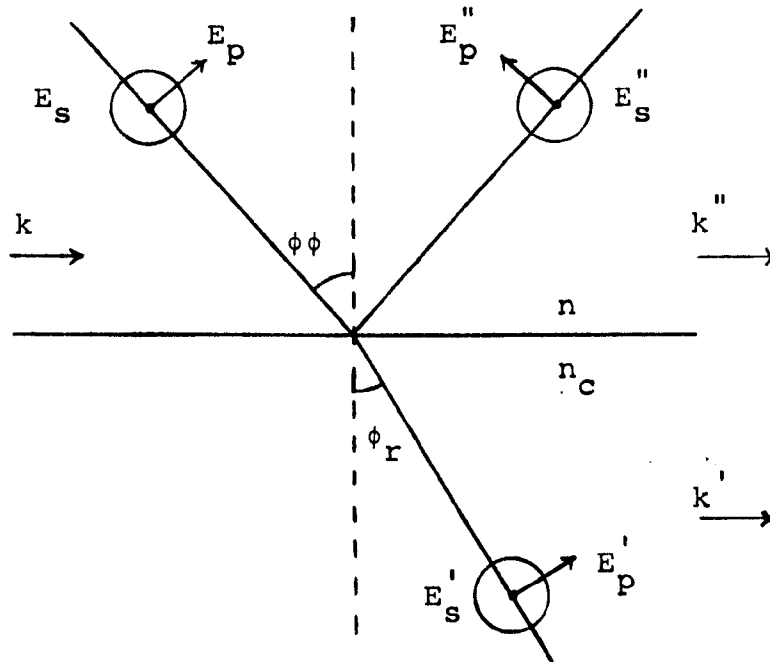
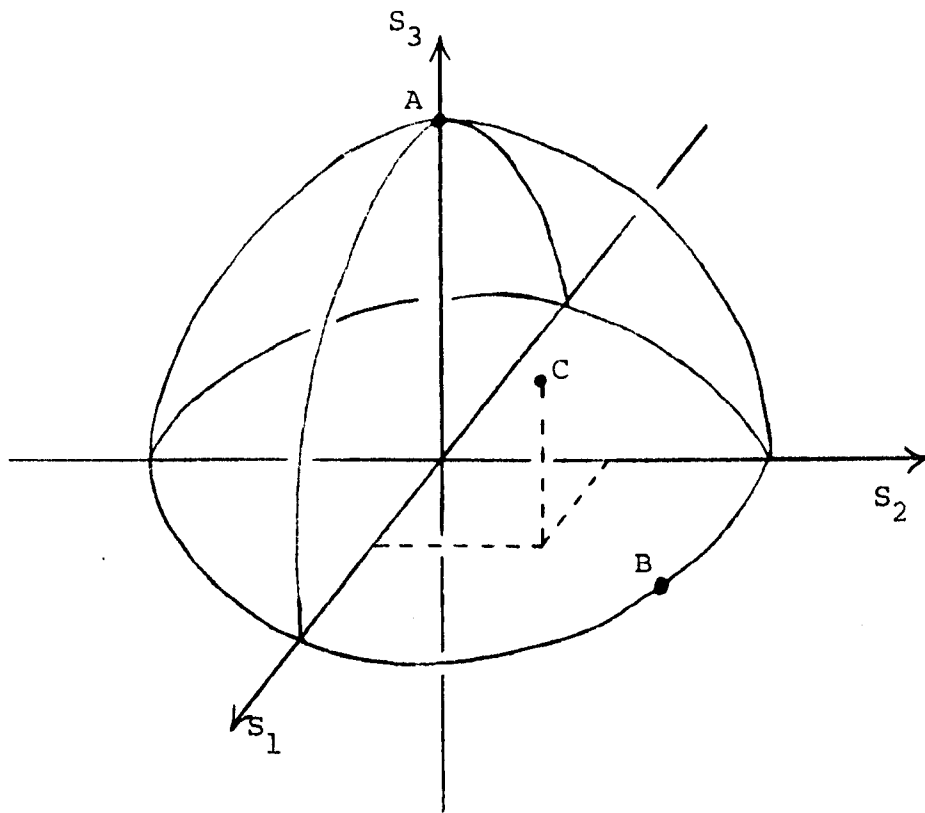


Figure 2.1



- E, E', E'' - positive directions of the incident, refracted, and reflected waves in the p-s directions
- n - refractive index of the incident medium
- n_c - refractive index of the reflecting medium
- k, k', k'' - propagation vectors

Figure 2.2 Co-ordinate system



- A - left-handed circular polarisation
- B - linear polarisation
- C - point inside the sphere, partially polarised

Figure 2.3 Points on the Poincaré Sphere

State of Polarisation

Stokes Vector

Unpolarised

$$\begin{pmatrix} 1 \\ 0 \\ 0 \\ 0 \end{pmatrix}$$

Linearly polarised along x-axis

$$\begin{pmatrix} 1 \\ 1 \\ 0 \\ 0 \end{pmatrix}$$

Circularly polarised

$$\begin{pmatrix} 1 \\ 0 \\ 0 \\ 1 \end{pmatrix}$$

Table 2.1 Stokes Vectors

Polariser with its pass-plane at θ to the x-axis

$$\begin{pmatrix} \cos^2 \theta & \cos \theta \sin \theta \\ \cos \theta \sin \theta & \sin^2 \theta \end{pmatrix}$$

$\lambda/4$ retarder with its fast-axis at θ to the x-axis

$$\begin{pmatrix} \cos^2 \theta - i \sin^2 \theta & \cos \theta \sin \theta (1 + i) \\ \cos \theta \sin \theta (1 + i) & \sin^2 \theta - i \cos^2 \theta \end{pmatrix}$$

Table 2.2 Jones matrices of a perfect polariser and compensator.

Polariser with its pass-plane at an angle θ to the x-axis

$$\frac{1}{2} \begin{pmatrix} 1 & \cos 2\theta & \sin 2\theta & 0 \\ \cos 2\theta & \cos^2 2\theta & \cos 2\theta \sin 2\theta & 0 \\ \sin 2\theta & \cos 2\theta \sin 2\theta & \sin^2 2\theta & 0 \\ 0 & 0 & 0 & 0 \end{pmatrix}$$

$\lambda/4$ retarder with its fast axis at θ to the x-axis

$$\frac{1}{2} \begin{pmatrix} 1 & 0 & 0 & 0 \\ 0 & \cos^2 2\theta & \cos 2\theta \sin 2\theta & -\sin 2\theta \\ 0 & \cos 2\theta \sin 2\theta & \sin^2 2\theta & \cos 2\theta \\ 0 & \sin 2\theta & -\cos 2\theta & 0 \end{pmatrix}$$

Table 2.3 Mueller matrices of ideal components

Polariser

$$\gamma_P = - \frac{\rho_C \tan A \sec^2 C \sec^2 P^*}{(1 - \rho_C \tan C \tan P^*)^2}$$

$$\gamma'_P = - \frac{\rho_C \tan A \sec^2 P^* \sec^2 C}{(1 - \rho_C \tan C \tan P^*)^2}$$

where $P^* = P - C$

Zones 1&3 $C = -\pi/4, \rho_C = -i$

$$\gamma_P^{13} = \gamma'_P{}^{13} = -2 \tan A \exp i2P$$

Zones 2&4 $C = \pi/4, \rho_C = -i$

$$\gamma_P^{24} = \gamma'_P{}^{24} = -2 \tan A \exp -i2P$$

Compensator

$$\gamma_C = - \frac{\tan A \sec^2 C \tan P^*}{(1 - \rho_C \tan C \tan P^*)^2}$$

$$\gamma'_C = - \frac{\tan A \sec^2 C (1 - \tan^2 P^* - \rho_C \sec^2 P^*)}{(1 - \rho_C \tan C \tan P^*)^2}$$

where $P^* = P - C$

Zones 1&3 $C = -\pi/4, \rho_C = -i$

$$\gamma_C^{13} = -i \tan A \cos 2P \exp i2P$$

$$\gamma'_C{}^{13} = -2 \tan A (-1 - i \sin 2P) \exp i2P$$

Table 2.4 Coupling constants.

Zones 2&4 $C = \pi/4, \quad \rho_C = -i$

$$\gamma_C^{24} = i \tan A \cos 2P \exp -i2P$$

$$\gamma_C'^{24} = -2 \tan A (-1 + i \sin 2P) \exp -i2P$$

Analyser

$$\gamma_a = 0$$

$$\gamma_a' = - \frac{\sec^2 A (\tan C + \rho_C \tan P^*)}{(1 - \rho_C \tan C \tan P^*)}$$

Zones 1&3 $C = -\pi/4, \quad \rho_C = -i$

$$\gamma_a'^{13} = i \sec^2 A \exp i2P$$

Zones 2&4 $C = \pi/4, \quad \rho_C = -i$

$$\gamma_a'^{24} = -i \sec^2 A \exp -i2P$$

Table 2.4 (contd.) Coupling constants.

| <u>Zone</u> | <u>Ellipsometric angles Ψ and Δ corrected to first-order</u> |
|-------------|---|
| 1 | $\Psi = A_1 - \beta_{PI} \sin 2A_1 - \frac{1}{2} \beta_{CR} \sin 2A_1 \cos 2P_1$ $+ \sin 2A_1 \sin 2P_1 \partial C + \partial A$ |
| 3 | $\Psi = -A_3 + \beta_{PI} \sin 2A_3 + \frac{1}{2} \beta_{CR} \sin 2A_3 \cos 2P_3$ $- \sin 2A_3 \sin 2P_3 \partial C - \partial A$ |
| 2 | $\Psi = A_2 + \beta_{PI} \sin 2A_2 - \frac{1}{2} \beta_{CR} \sin 2A_2 \cos 2P_2$ $+ \sin 2A_2 \sin 2P_2 \partial C + \partial A$ |
| 4 | $\Psi = -A_4 - \beta_{PI} \sin 2A_4 + \frac{1}{2} \beta_{CR} \sin 2A_4 \cos 2P_4$ $- \sin 2A_4 \sin 2P_4 \partial C - \partial A$ |
| 1 | $\Delta = 2P_1 + \pi/2 + 2\beta_{PR} + 2\partial P - \beta_{CI} \cos 2P_1 - 2\partial C$ |
| 3 | $\Delta = 2P_3 - \pi/2 + 2\beta_{PR} + 2\partial P - \beta_{CI} \cos 2P_3 - 2\partial C$ |
| 2 | $\Delta = -2P_2 - \pi/2 - 2\beta_{PR} - 2\partial P - \beta_{CI} \cos 2P_2 + 2\partial C$ |
| 4 | $\Delta = -2P_4 + \pi/2 - 2\beta_{PR} - 2\partial P - \beta_{CI} \cos 2P_4 + 2\partial C$ |

A_i & P_i are the nulling azimuths in the i^{th} zone.

Table 2.5

CHAPTER THREE

ELLIPSOMETER CONSTRUCTION

3.1 Design Principle of an Automatic Nulling Ellipsometer

The ellipsometric arrangement which has been used is the polariser - compensator - sample - analyser (PCSA) configuration (McCrackin et al 1963). The compensator axes are set at $\pm\pi/4$ to the plane of incidence and the nulling is achieved by adjusting the azimuths of the polariser and analyser. The outline diagram of the ellipsometer is shown in figure 3.1

Light from a high-pressure short-arc Xenon lamp (Clarke 1980) is collimated by the lens L and then passes sequentially through the polarising prism P, compensator C, is reflected from the sample S and is extinguished by the analyser A. The wavelength selection is performed by a grating monochromator M and the optical flux is detected by a photomultiplier. The optical axis is defined by a series of irises I_1 to I_5

The ellipsometer is required to locate and track nulls automatically; the method used to achieve automatic null balancing involves modulating the plane of polarisation at the polariser and analyser. The classical method of achieving a null (McCrackin et al 1963) is to rotate one of the polarising component azimuths away from the null until some arbitrary signal level, which is conveniently large to measure accurately is obtained, the azimuth is then changed such that the detected signal first decreases then increases

again to the same level as before. The null is then calculated as the arithmetic mean of the azimuths at which the signal levels are the same. The azimuths of the two polarising elements are adjusted in turn by this method until a stable null is located. It is possible to automate this procedure by utilising a polarisation modulator in which the rotation of the plane of polarisation is related to an electrical quantity. The Faraday effect is suitable for use in such a modulator.

The Faraday effect is magneto-optical in nature, in that when a magnetic field is established along the optical axis of a material the plane of polarisation of light travelling along the optical axis is rotated. The degree of rotation is proportional to the magnitude of the magnetic flux density. The manner in which this modulation is used to perform automatic nulling is demonstrated with reference to figure 3.2

Consider the intensity of the transmitted flux as the azimuth of one of the polarising elements is varied through a null. The intensity/azimuth relationship is symmetric in azimuth-displacement in the region of the null. If the plane of polarisation at any particular azimuth is varied a small amount by the modulator then two important features are evident. Firstly that the phase of the modulation is inverted on one side of the null relative to the other side. Secondly that at the null the modulation becomes unipolar i.e. the modulation always increases the transmitted flux whereas at an off-null position the flux will both increase and decrease. If the modulated component of the optical flux

is synchronously rectified with respect to the modulating signal and smoothed, then an output is produced which is positive on one side of the null, negative on the other and zero at the null. This output is suitable for sensing the azimuth error relative to the null and controlling a servo-loop to provide an automatic azimuth adjustment. Thus automatic nulling can be achieved on any polarising component by combining the component with a modulator to vary its azimuth by a small amount. In the PCSA configuration the modulators are placed after the polariser, to modulate the polariser azimuth and before the analyser, to modulate the analyser azimuth.

3.2 Ellipsometer Construction

The automatic nulling ellipsometer was constructed using the modulation principles described above, an outline block diagram is shown in figure 3.3. The nulling is achieved by controlling the azimuths of the polariser and analyser with the compensator in a fixed azimuth; the fast/slow axes being at $\pm\pi/4$ to the plane of incidence.

An automatic nulling ellipsometer was already in existence within the department (Meadows 1975) and the new ellipsometer was constructed using some of the optical components from this instrument. The components used were:-

- a) polariser and analyser prisms in air-bearing goniometers driven by stepping motors (Meadows 1975)
- b) achromatic compensator and mount (Clapham, Downs & King 1963)
- c) high pressure Xenon lamp and power supply (Clarke 1980)

- d) Minimate monochromator
- e) two photomultipliers type 9656 QR (EMI)
8852 (RCA)
- f) sample alignment stage
- g) optical bench and surface table

The servo-loops to control the azimuths of the analyser and polariser are identical in construction and operation, differing only in modulation frequencies. The polariser operates at 1227Hz and the analyser at 1671Hz, these frequencies are nominal and vary by ± 5 Hz. A detailed block diagram of the servo-loop is shown in figure 3.4

3.3 Photomultiplier Head Amplifier

The photomultiplier is a current source device in which the current is proportional to the number of photons incident on the photomultiplier cathode. To convert this current into a voltage it is necessary to use a high value anode load resistor. This, however, results in a decrease in the maximum operating frequency as the load resistor is effectively by-passed by the capacitance of the screened cable between the photomultiplier and the equipment rack. For example, a load resistor of 1M and 4m of co-axial cable has an upper 3db point of 1500Hz, which is in the region of the modulation frequencies.

To minimise the effect of capacitive loading, a head pre-amplifier was located adjacent to the photomultiplier. The circuit diagram is shown in figure 3.5 The circuit is a non-inverting a.c. coupled buffer with an input impedance of 1M, an output impedance of 3K3 and a voltage gain of 5.

The low output impedance enables the circuit to drive a long co-axial cable to the equipment rack without a degradation in the signal level.

3.4 Bandpass Amplifier

The buffered signal from the photomultiplier is a broadband signal which has a low signal to noise ratio. To improve the signal to noise ratio before phase sensitive rectification the signal is passed through a two-stage bandpass filter, the circuit is shown in figure 3.6. The centre frequency is 1400Hz, bandwidth 700Hz ($Q = 2$) and voltage gain of unity.

3.5 Phase Sensitive Rectifier and Low-Pass Filter

The phase-sensitive rectifier synchronously demodulates the detected signal with respect to the modulation, the circuit diagram is shown in figure 3.7. The circuit relies for its operation on the switching of the input signal between the inverting and non-inverting inputs of a differential amplifier. A reduced circuit diagram is shown in figure 3.8 a & b. Consider the circuit in figure 3.8a, the input signal passes through an attenuator formed by the F.E.T. and resistor R before reaching the inverting input of the amplifier. When the F.E.T. is biased into its 'off' state, its resistance is high $\sim 10^9$ ohms and very little of the input signal reaches the amplifier. Conversely when the F.E.T. is biased into its 'on' state its resistance is low ~ 40 ohms and the input signal passes with very little attenuation to the amplifier. The operation of the non-inverting stage, figure 3.8b, is directly analogous to that of the inverting stage.

To form a synchronous rectifier it is only necessary to ensure that the F.E.T's in the inverting and non-inverting inputs are switched alternately on and off and in phase opposition to each other. The synchronising waveform is derived from the a.c. waveform which is applied to the modulator coils, and is passed through one inverting stage before driving the F.E.T. in the inverting input stage. To ensure the phase opposition in the F.E.T. state the switching waveform of the inverting F.E.T. is inverted to drive the non-inverting F.E.T.

The low-pass filter which limits the overall bandwidth of the servo-loop is located immediately on the output of the phase sensitive rectifier and is a series resistor/capacitor with a time constant of 2.7 seconds.

The smoothed output from the phase sensitive rectifier is a measure of the offset from the null azimuth and it is important that there are no offsets present and that the gains of the inverting and non-inverting stages are equal. The alignment procedure to ensure that there are no offsets is:-

- a) with zero signal input and without a reference input, the output is set to zero using the offset control of the amplifier
- b) with a constant voltage ($\pm 1V$) applied to the test point, T.P., and a reference signal present the 10K preset gain balance resistor is adjusted for zero output.

It may be necessary to repeat the alignment procedure iteratively as the gain balance control will have a small

effect on the bias offset removed by 'a'. The phase-sensitive rectifier is now correctly adjusted for offset and gain balance.

3.6 Linear Amplifier

The output from the phase sensitive rectifier will be zero at the null and finite when off the null. In order to control the loop performance such that it is limited by noise generated in the photomultiplier a linear amplifier is required after the phase sensitive rectifier. In addition the amplifier is required to have a differential output to drive the voltage to frequency converters which follow. The gain of the amplifier is determined by the requirement that the noise from the photomultiplier which is approximately 1.5 mV p-p is equal to the dead band of the voltage to frequency convertors which is $\pm 0.6V$. The required gain is thus 800. Fine adjustment of the loop gain is achieved by adjusting the E.H.T. and hence gain of the photomultiplier.

The phase-splitting for the differential output is performed by inverting the output with a unity gain inverting buffer.

The linear amplifier is the last linear stage in the control loop before the signal is converted into a digital form and, to eliminate drifts due to time and temperature the output can be set to zero to compensate for offsets in the phase - sensitive - rectifier and linear amplifier, figure 3.9 The output from one phase is continuously monitored with a moving coil meter and a front panel offset control provided to zero the output. It is therefore possible to check the servo-loop for offsets by reducing the photomultiplier E.H.T.

and observing the meter. Any offsets evident can then be removed with the front panel control. This adjustment can be performed at any time before, during and after an experiment without any risk of corrupting the experimental data.

3.7 Goniometer Position Control and Display

The output of the linear amplifier is used to control the position of the goniometer. The control being achieved by converting the linear output to a pulse train with voltage to frequency convertors and driving a stepping motor with the pulse train. The output from the linear amplifier is differential, i.e. one output will be positive for a positive error and the other positive for a negative error. If voltage to frequency convertors are attached to each output then two separate pulse trains will be generated, one for a positive error and one for a negative error; for zero input there is no output.

The voltage to frequency convertor design is due to Meadows (1975) with the timing capacitor adjusted to give a maximum operating frequency of 3kHz. The stepping motor is an Astrosyn type 23PM-C301 driven by a Digicard (P.K.S. Design Ltd.)

The drive signals for the Digicard are a step pulse and a direction pulse. The circuit to convert the pulse trains from the voltage to frequency convertors to a form compatible with the Digicard is shown in figure 3.10 Consider an incoming pulse train along the step clockwise line. The pulses are transmitted through the RDL OR gate and successively trigger two 50 μ s period monostables to

send a step pulse to the Digicard after a $50\mu\text{s}$ delay. During this period the clockwise/anti-clockwise line set by the $150\mu\text{s}$ monostable is left unaffected in the clockwise position. A pulse on the step anti-clockwise line is also transmitted by the OR gate and produces a step pulse as before, but it also triggers the direction monostable into the anti-clockwise direction for $150\mu\text{s}$. Thus the pulse produces an anti-clockwise rotation.

The different pulse lengths, $50\mu\text{s}$ delay and output inverters are required to ensure that the direction changes only when the step pulse is 'high'.

The angular position is derived by counting the number of steps/direction through which the stepping motor is driven. The angular position is then a simple linear function of the step count. The stepping motor is driven in the half-step mode and drives the goniometer through two gearboxes of 90:1 and 100:1 reduction, each step thus corresponds to an angular movement of 0.0001 degrees.

A 7 - decade CMOS digital counter was constructed to count the number of steps through which the motor is driven. The 7 - decades provide a 0 to 999.9999 degree range with a resolution of 0.0001 degrees. The circuit of one decade is shown in figure 3.11. The complete counter is constructed by cascading seven stages and linking the carry/borrow lines between each stage. The counter control lines are count and direction, these are compatible with and are directly connected to the step and direction lines which drive the Digicard.

In the event of the counter being driven negative the display registers the 10's complement of the count. There is a reset line which zero's all digits.

3.8 Faraday Modulator

The Faraday modulator is used to modulate the plane of polarisation by a small, approximately 1-2 deg. amount about its mean orientation. The modulator uses the Faraday effect in which the plane of polarisation is rotated as the optical flux passes through a material in which a magnetic field has been established. The requirement that the magnetic flux and therefore the ampere-turns of the solenoid be as large as possible necessitates that the number of turns in the solenoid be large. However, this results in the solenoid having an appreciable inductance, which has a significant reactance at the modulating frequency and without compensation would severely limit the operating current. The inductance can be compensated with a series capacitor chosen to produce a frequency of series resonance equal to the modulation frequency. At this frequency the coil-capacitor appears purely resistive. This method was used by Meadows (1975). However, the drawback of Meadows approach is that the frequencies of modulation and resonance are not linked and any relative changes will cause a reactive mismatch between the modulator and driving circuit and reduce the modulation efficiency.

The problems inherent in linking the modulation and resonance frequencies can be eliminated by making the coil-

capacitor part of the frequency selection circuitry

figure 3.12 In this arrangement the power amplifier which drives the modulator is turned into an oscillator by the addition of positive feedback. The circuit will oscillate providing that the loop gain is greater than unity and the circuit Q exceeds 0.5

The oscillator was constructed, figure 3.13, using a commercially available power amplifier which is non-inverting and has a fixed gain of 30. The equivalent series resistance of the modulator is 8Ω at 1500Hz and a feedback resistance of 0.25 ohms is required to reduce the loop gain to unity. In order to set the gain and account for small differences between calculated and actual circuit parameters the 0.25 ohm resistor is realised as a 1k Ω preset resistor in parallel with 0.47 ohms. The necessary loop gain for oscillation is set by adjusting the preset resistor such that the output voltage from the amplifier shows significant clipping when viewed on an oscilloscope. The gain is then reduced until the clipping is only just noticeable. The loop gain under this condition is sufficient for the oscillator to start reliably and the clipping not severe enough to cause excessive dissipation in the modulator coil. The output from the amplifier is 30V p-p which gives a dissipation of 14W into the load equivalent series resistance of 8 ohms.

The differing frequencies for the polariser and analyser servo-loops are set by adjusting the value of the series capacitor, 1 μ F for 1671Hz and 2 μ F for 1227Hz; the nominal inductance of the modulator coils is 8mH.

The modulator coil was constructed from a tufnol tube with a collar at each end; the tube has a 15 mm bore in which the modulator core is located, figure 3.14

The coil winding consists of seven layers of close wound 24 s.w.g. enamelled copper wire with each layer varnished into place. The dissipation in the coil is approximately 14 watts when being driven in resonance and to minimise thermal effects the coil is contained in a cooling water jacket. To ensure that the assembly is watertight the end collars are bonded with Araldite to the central tube and the space between the collars and the water jacket sleeve is filled by 'O' rings recessed into the collars.

The modulator core, which produces the optical rotation is located in the centre of the modulator coil. The core is conventionally constructed from a solid glass cylinder which is carefully selected and annealed to minimise stress bi-refringence. However, if the core is subjected to any stress it will become significantly bi-refringent. This stress can be mechanical in origin, for example, clamping the core into position or thermal due to uneven heating by the modulator coil. The first can be eliminated by careful mechanical design such that the core is not subjected to any forces other than gravitational, but the requirement for thermal stability is more stringent when the core is in close proximity to the coil. It is possible to reduce both mechanical and thermal constraints by constructing the core from a liquid.

The liquid cell for the modulator was constructed from

a perspex tube, figure 3.15, with end caps to which are attached silica microscope cover slips. The cell is filled with de-ionised water which has been passed through a 0.5 μ m filter.

3.9 System performance

The ellipsometer performance was assessed for resolution, stability and transient response. The resolution at 500nm, 10 nm bandwidth in the 'straight through' position with the incidence and reflection arms co-linear is ± 0.0002 deg. The stability under the same conditions is ± 0.0006 deg/hr.

The transient response was examined by offsetting the polariser by 1.0 deg from the null and allowing the ellipsometer to null under servo-control. The ellipsometer achieved a null to within 0.01 deg. in 30 seconds.

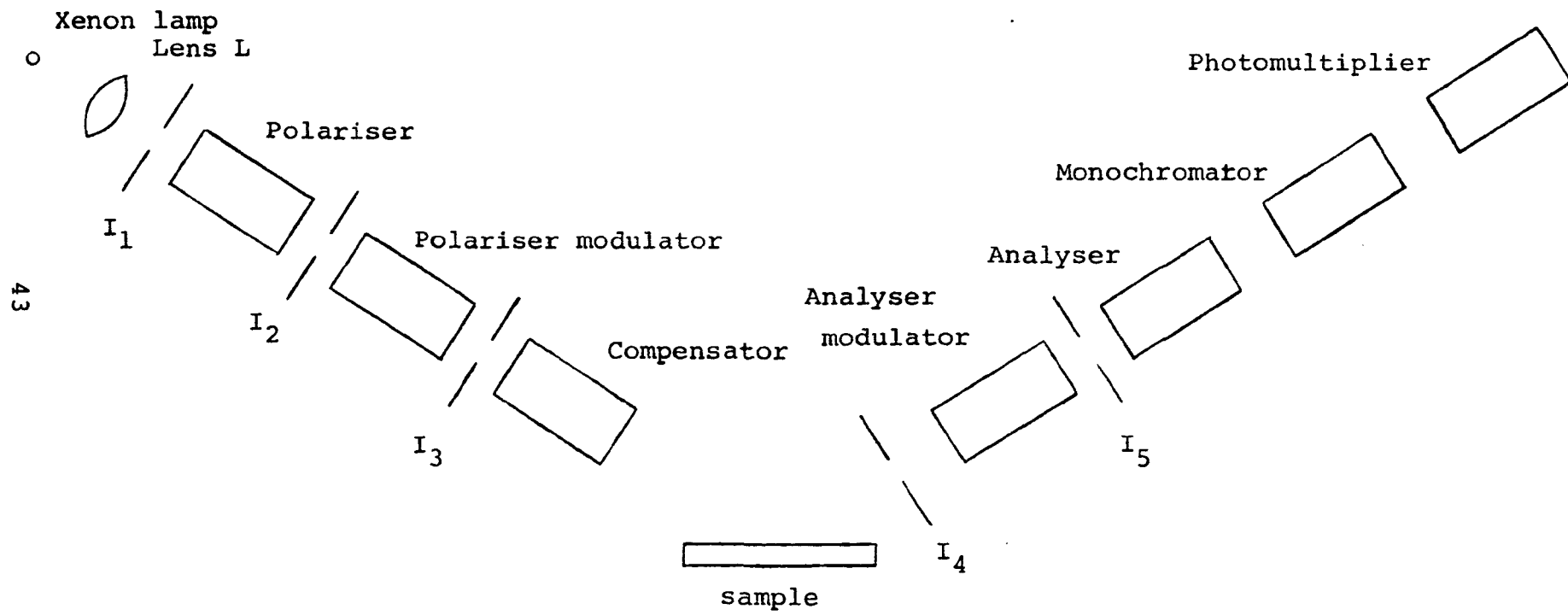


Figure 3.1 Ellipsometer configuration

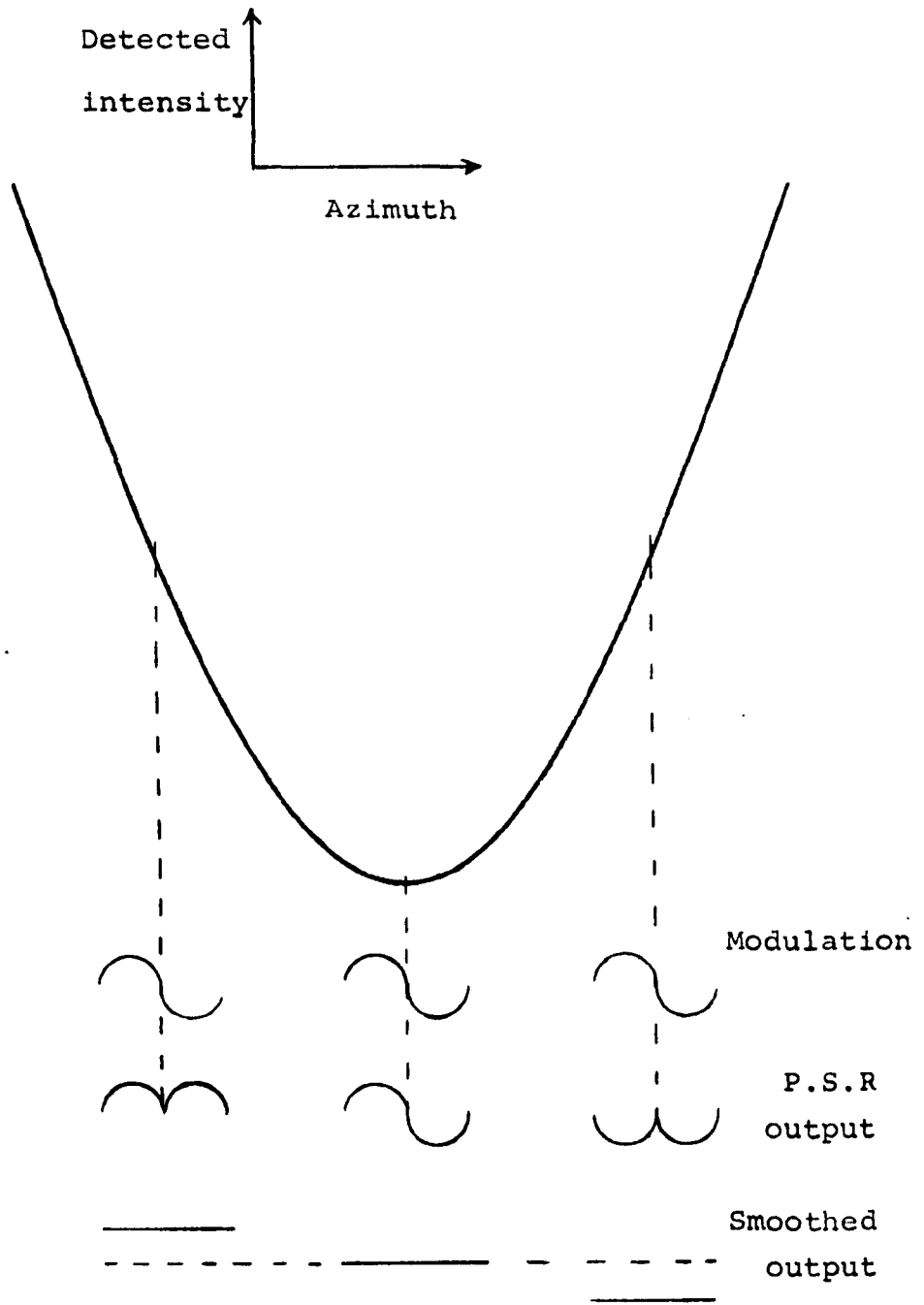


Figure 3.2 Detected signal in the region of a null

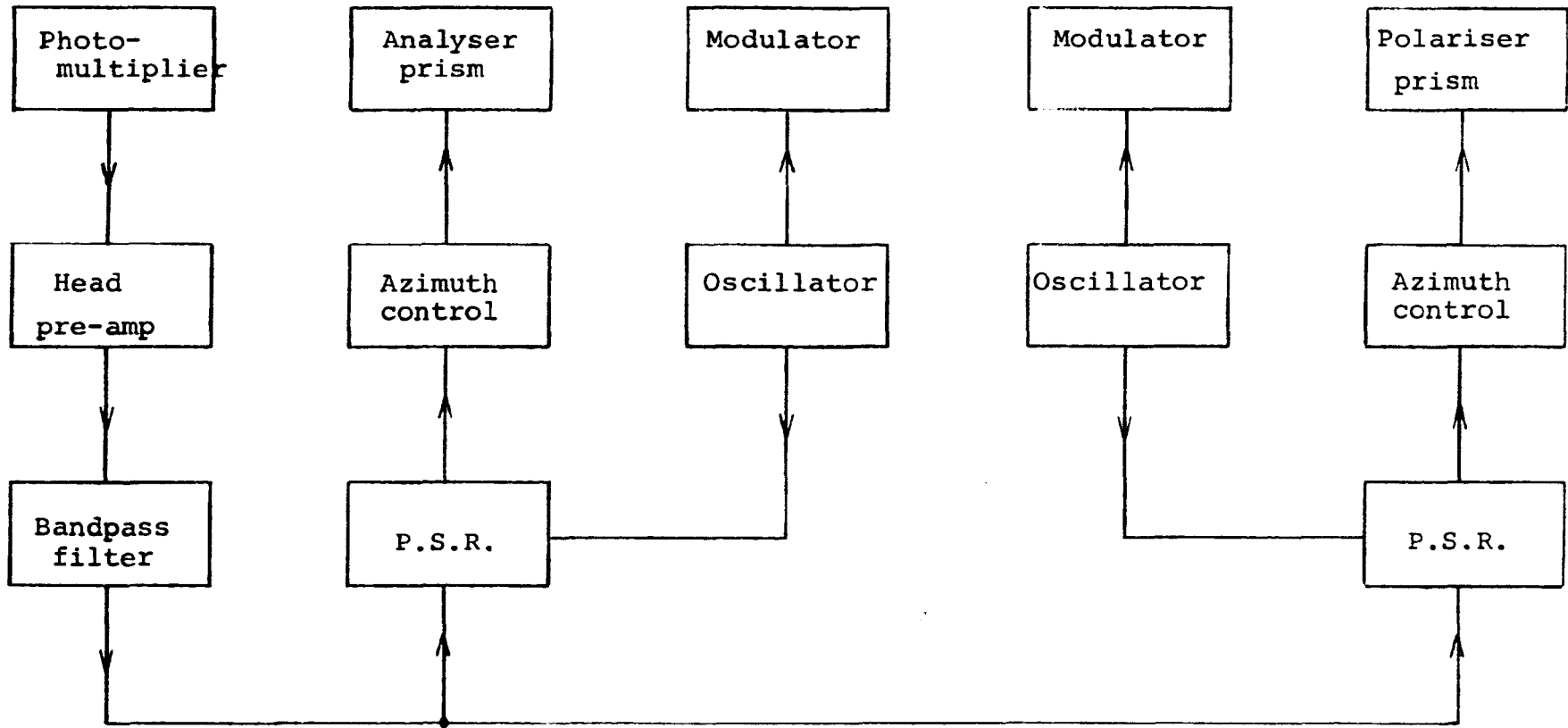


Figure 3.3 Constructional diagram of the ellipsometer electronics

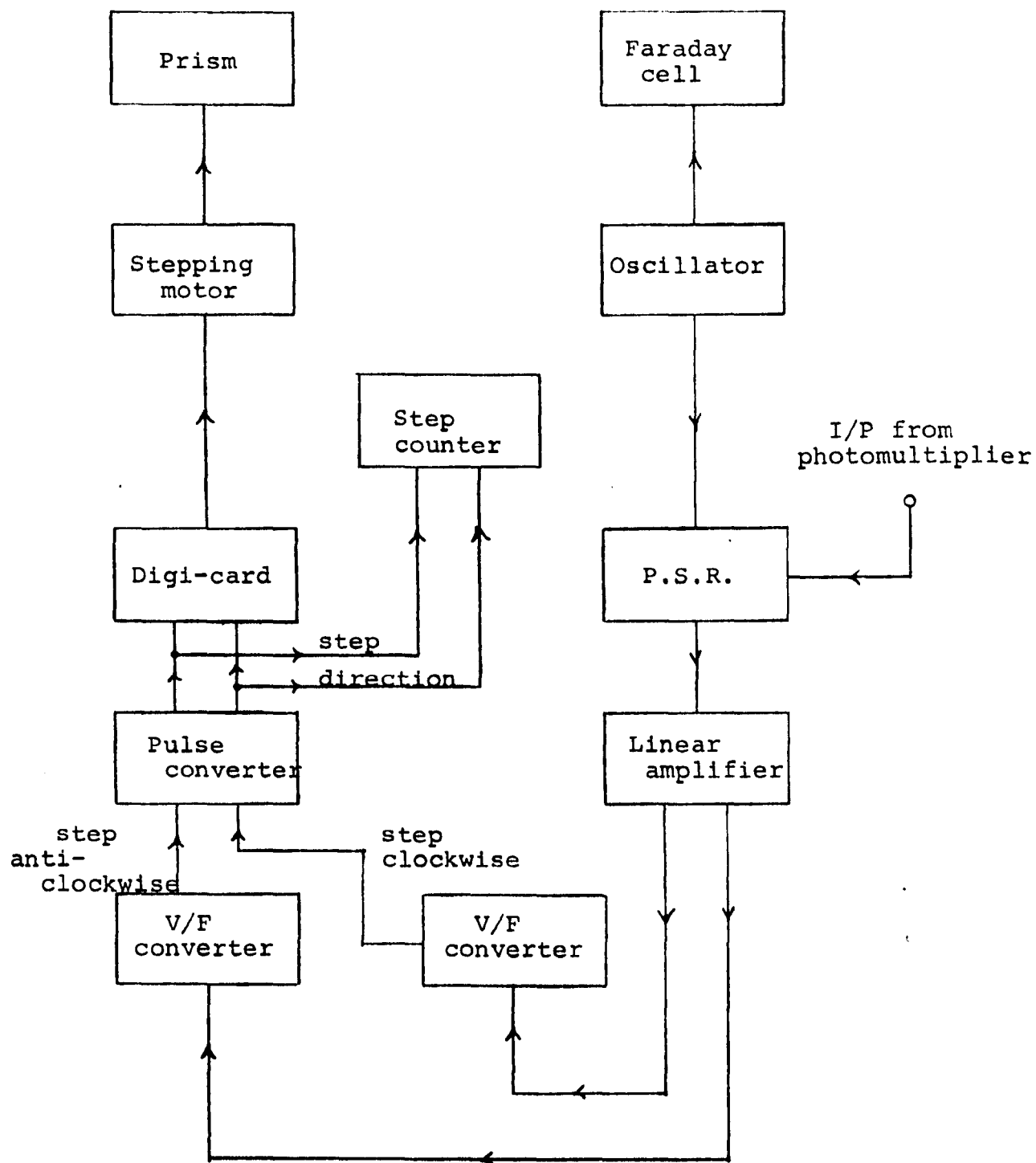


Figure 3.4 Detailed block diagram of one servo-loop

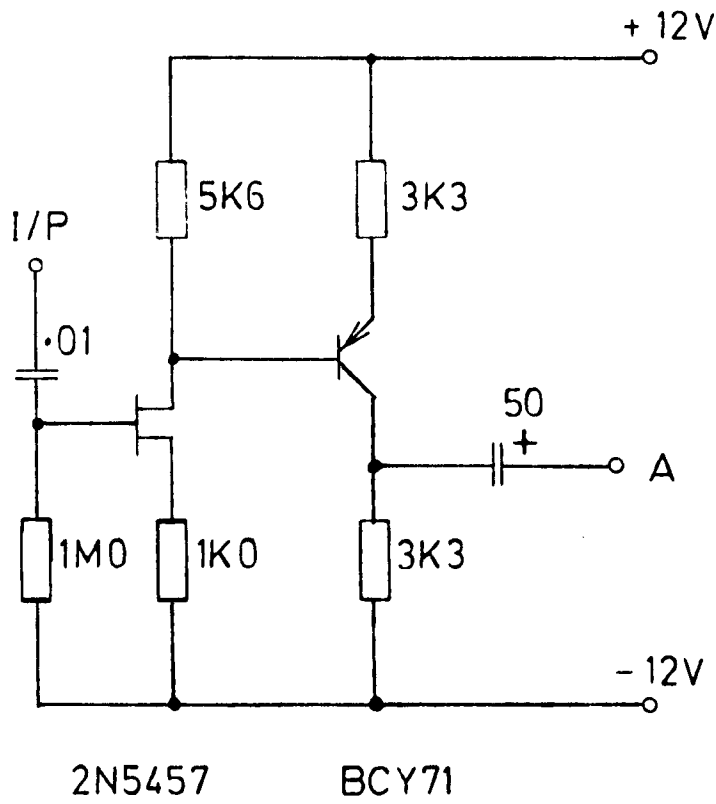


Figure 3.5 Photomultiplier head amplifier

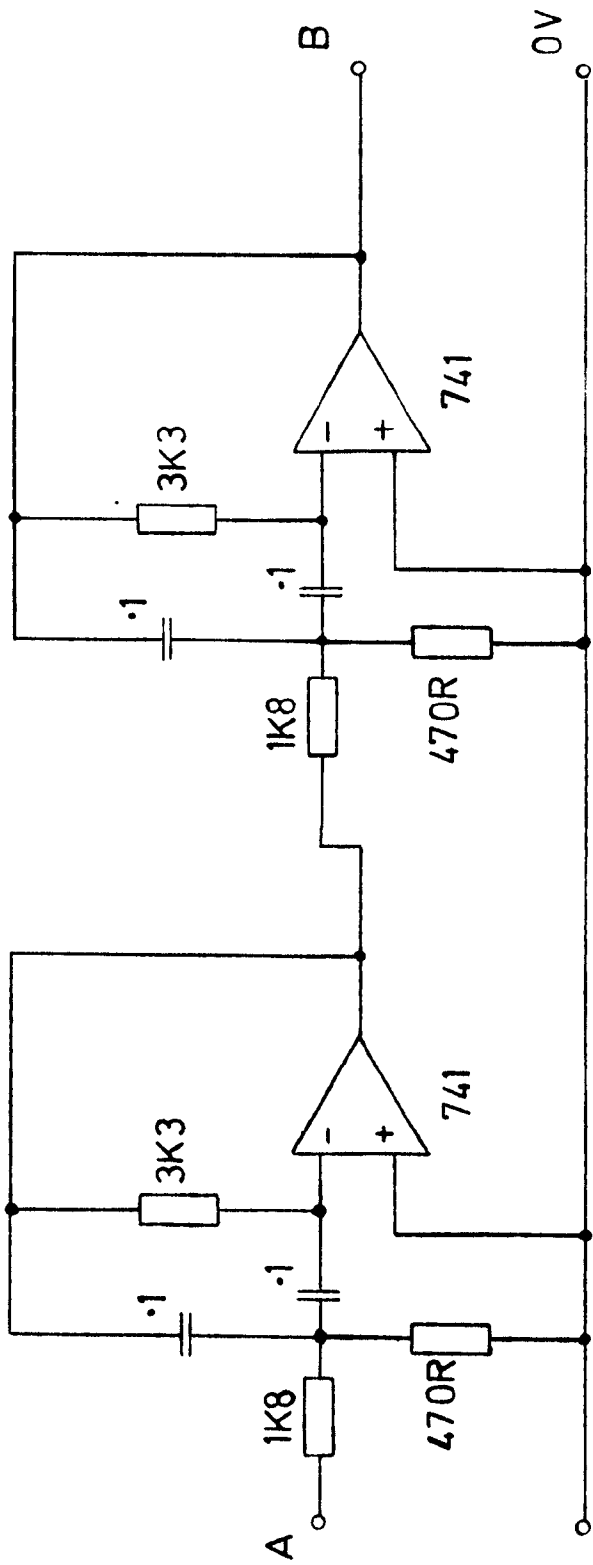


Figure 3.6 Bandpass amplifier

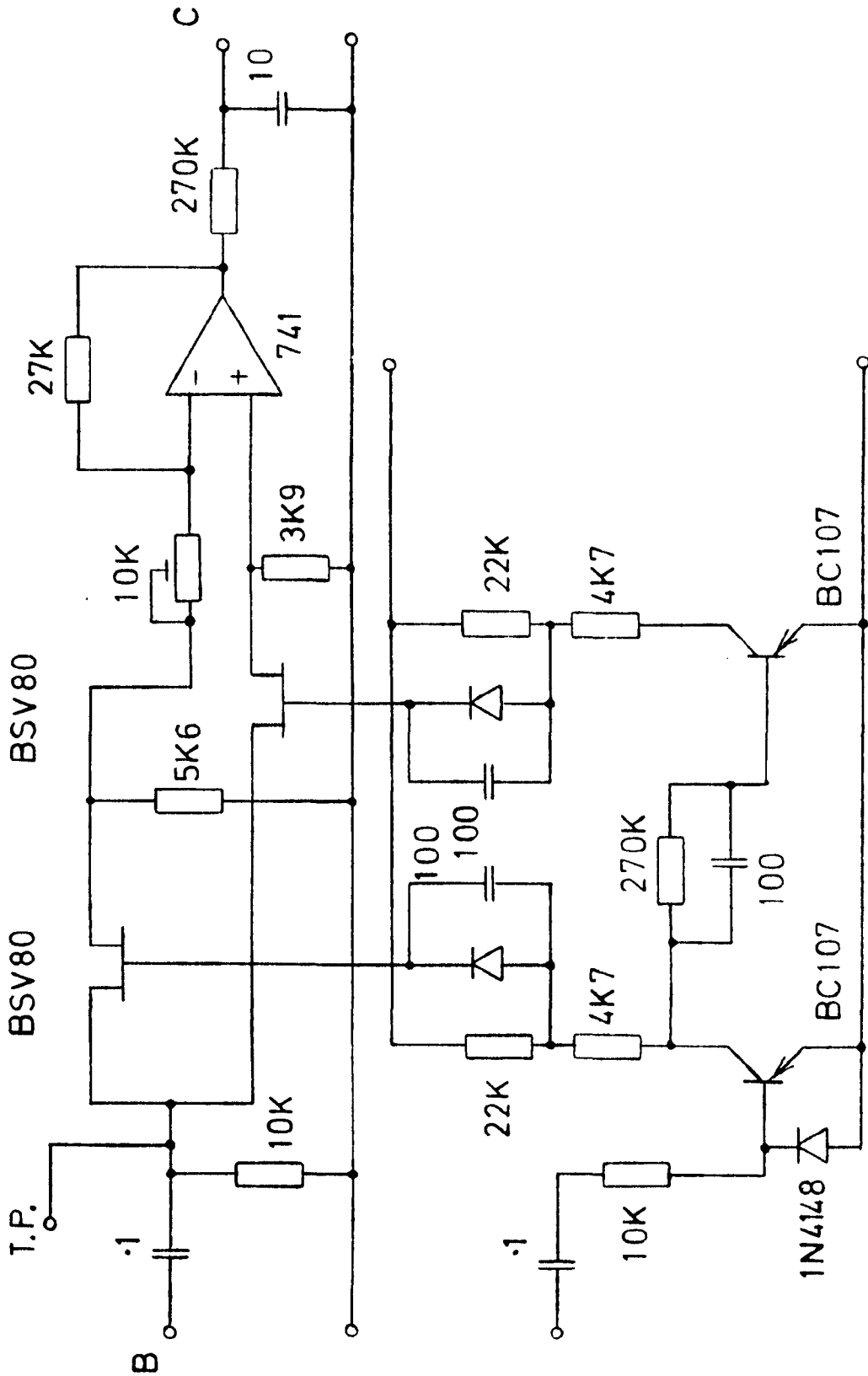
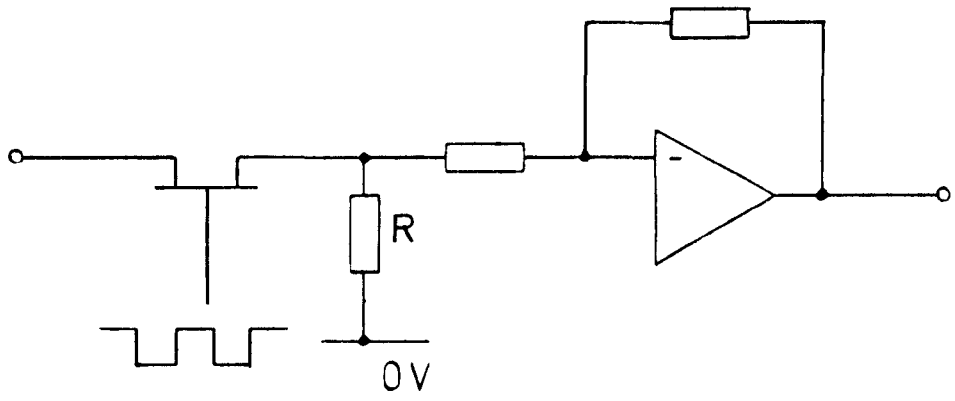
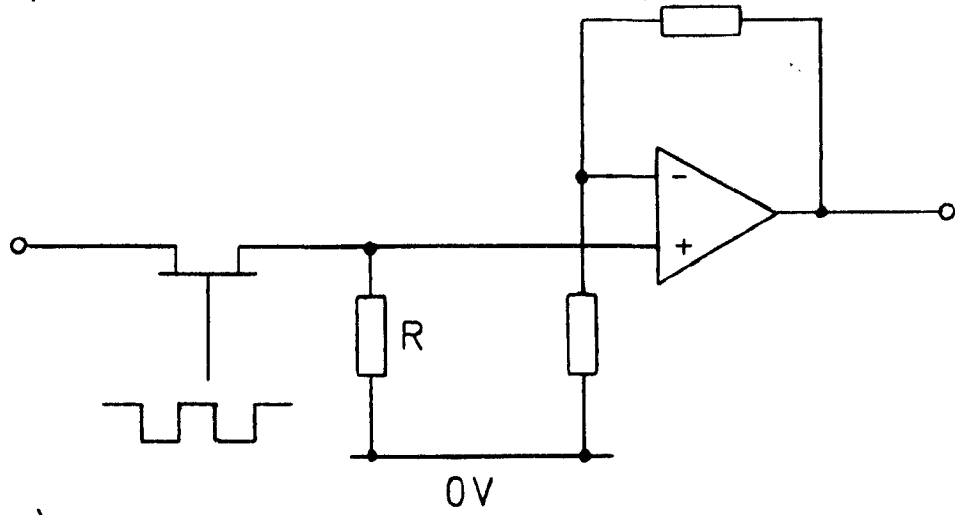


Figure 3.7 Phase - sensitive - rectifier (P.S.R.)



(a)



(b)

Figure 3.8 Operation of the P.S.R.

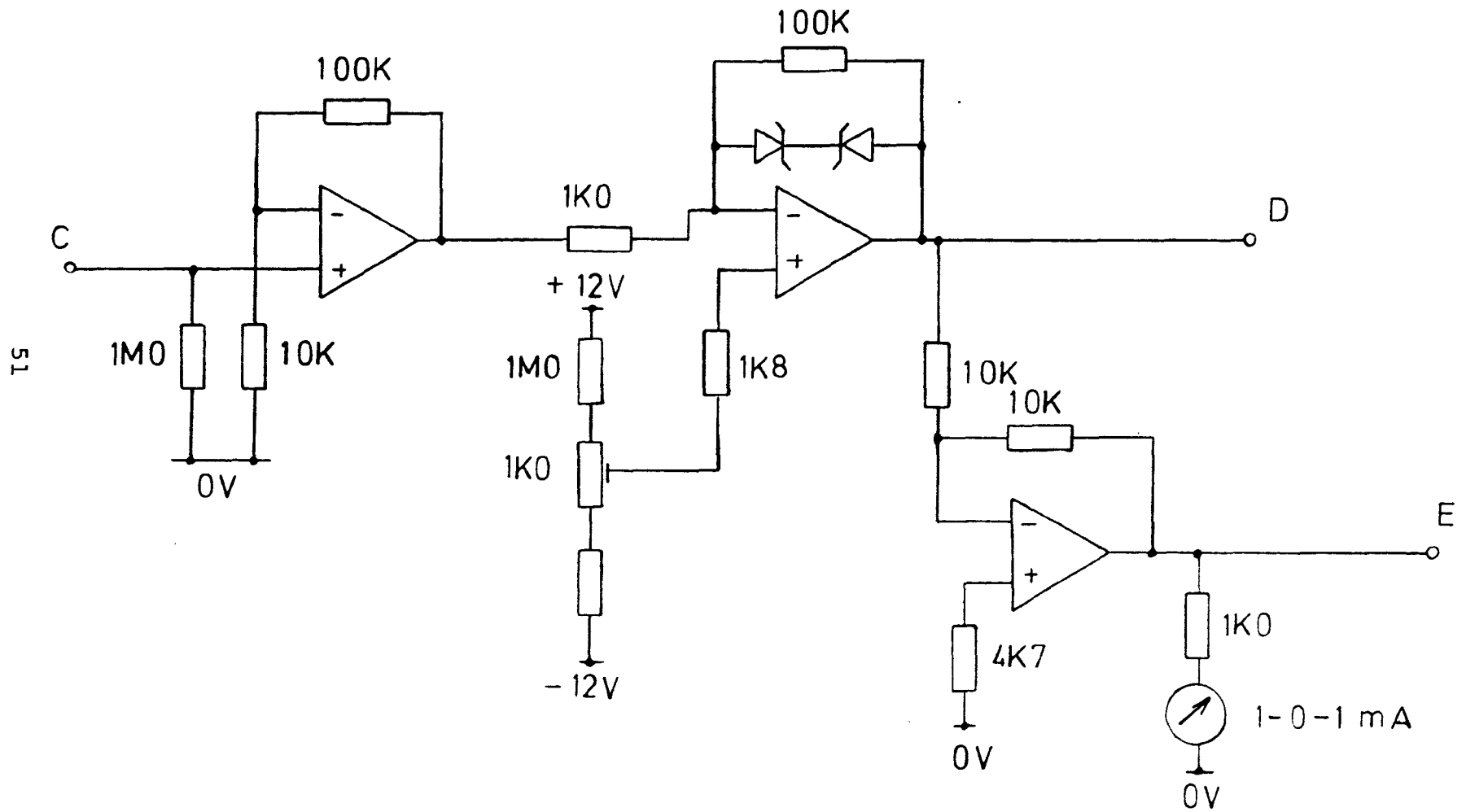
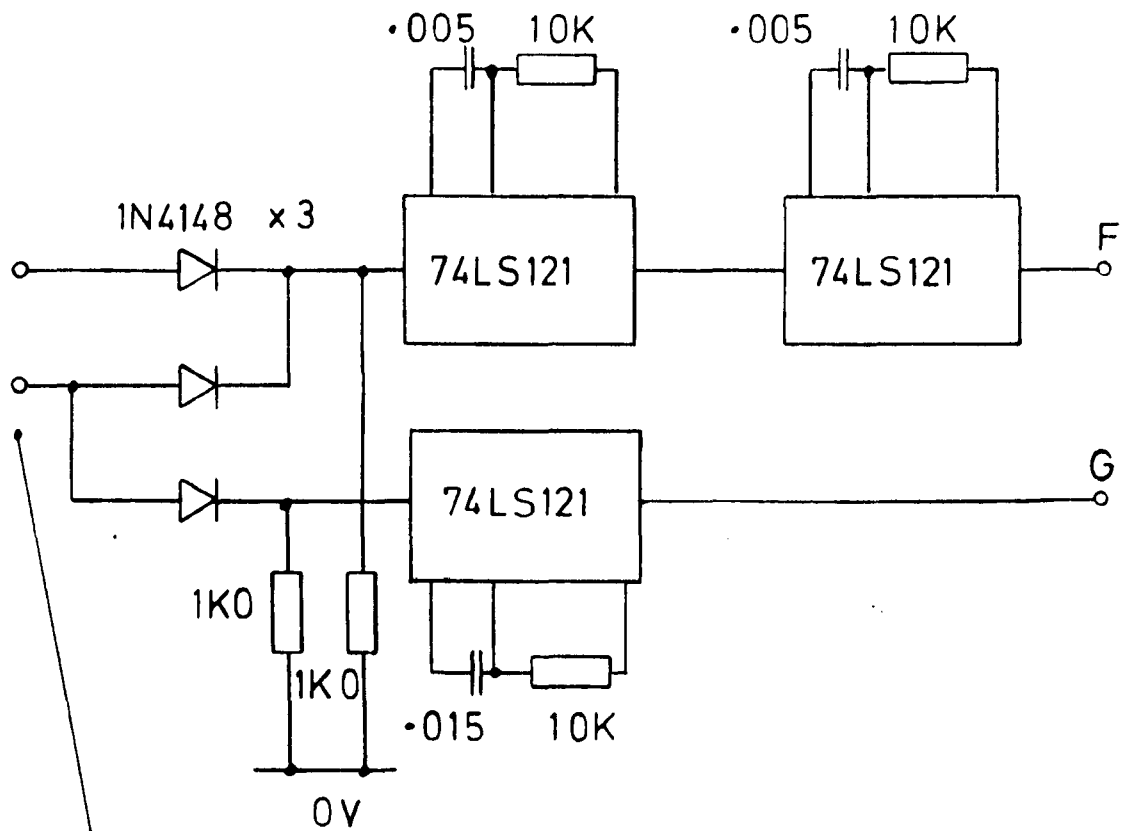


Figure 3.9 Linear amplifier



o/p from v/f converter (Meadows 1975)

Figure 3.10 Pulse converter

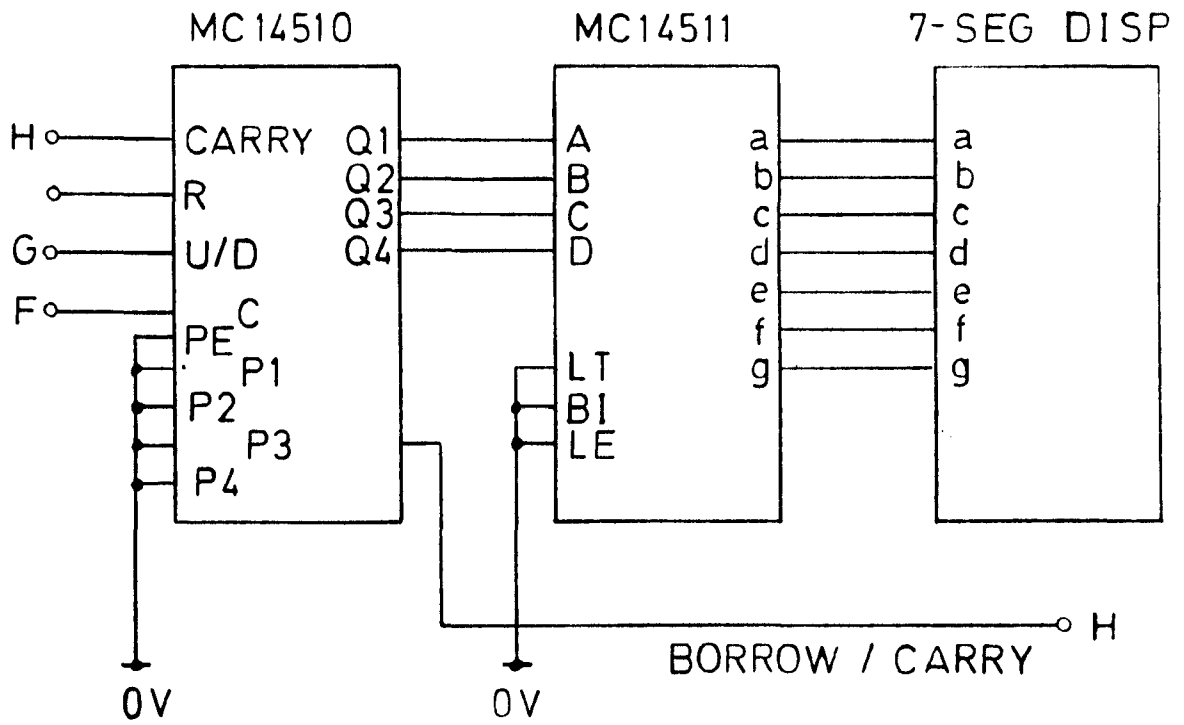


Figure 3.11 One decade of the step - counter

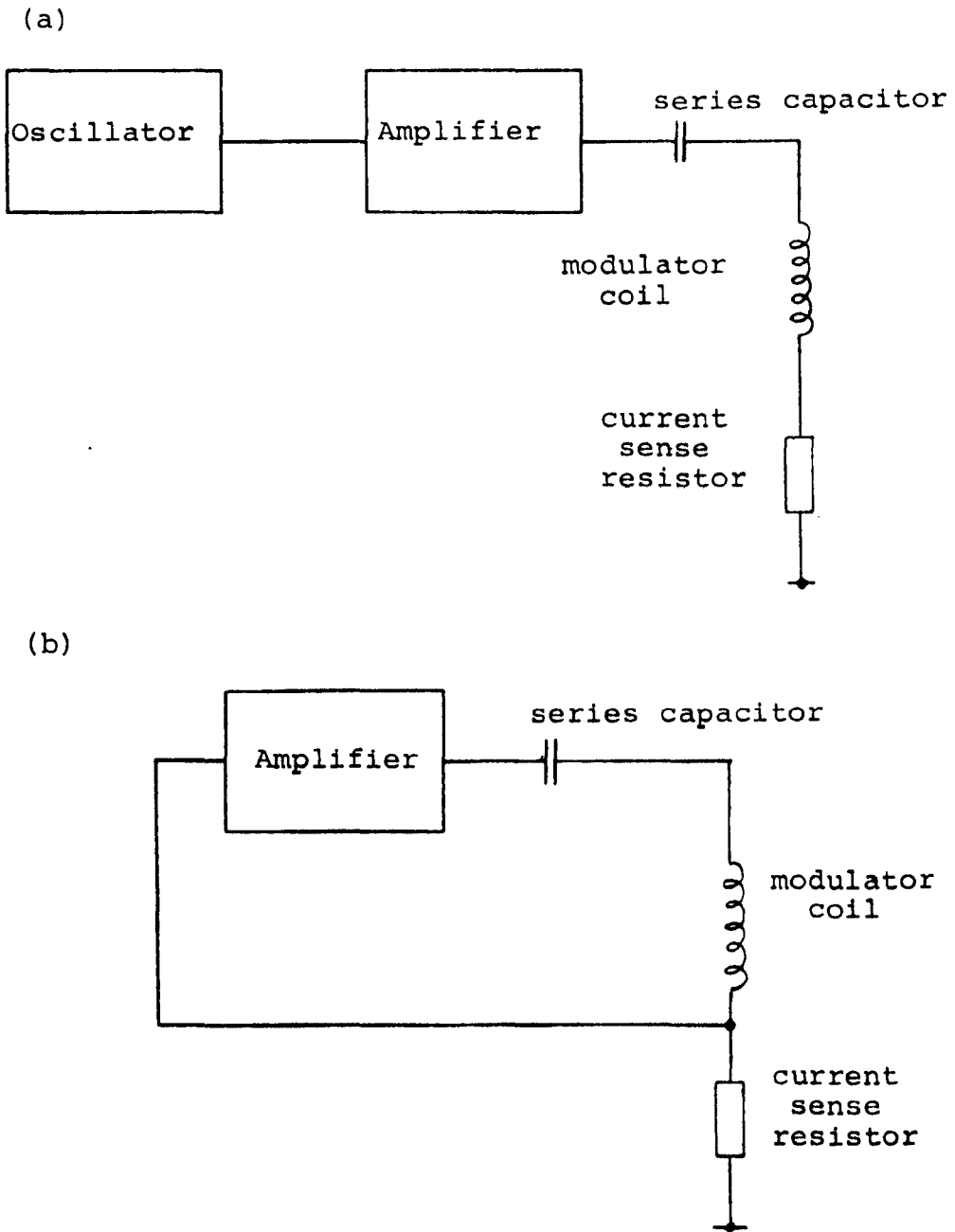


Figure 3.12 Faraday cell oscillator block diagram

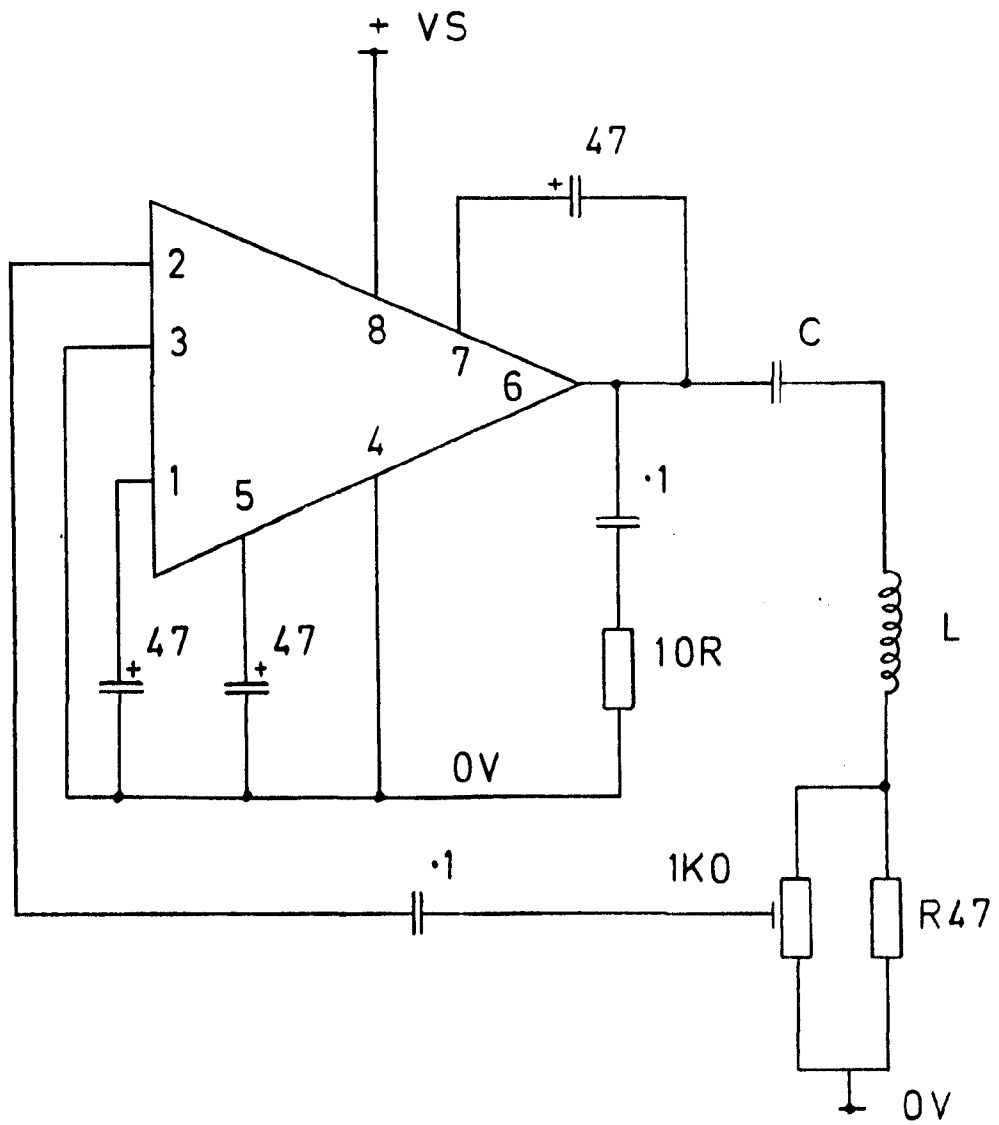
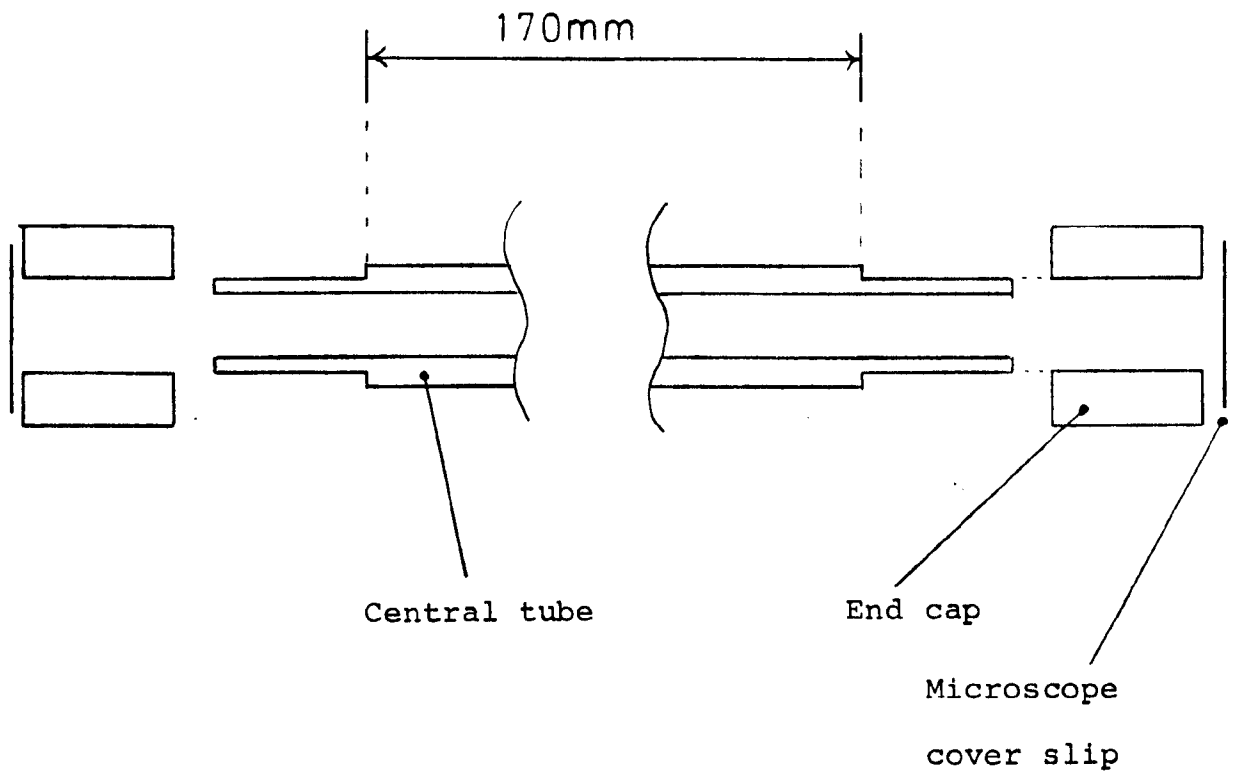


Figure 3.13 Faraday cell oscillator



Scale 1:1

Figure 3.15 Modulator core

CHAPTER FOUR
EXPERIMENTAL PROCEDURES

4.1 Ellipsometer Optical Alignment

The description of the polarisation state using the electric field vector \underline{E} requires there to be a set of reference axes relative to which the vector is determined. In general any set of orthogonal axes are sufficient and mutually equivalent. The optical components of an ellipsometer will define only one axis, that of optical transmission. Two orthogonal axes can then be defined within a plane perpendicular to the axis of transmission. These are the only constraints placed upon the axes. In the case of reflection ellipsometry it is convenient to place one further constraint upon the axes, namely that they are the same for any angle of incidence. This now limits the choice of axes to one orthogonal set. The set of axes is the normal to the plane of incidence at the point of reflection and the normal to the surface at the point of reflection.

The alignment of a reflecting ellipsometer will thus consist of:-

- a) identifying the reference axes in space
- b) determining the orientation of each optical component relative to the reference axes.

The greatest problems will be encountered in determining the orientation of each optical component as imperfections, such as ellipticity in the polariser, will give misleading results unless a specific alignment procedure is followed. A procedure will be developed to eliminate all first-order imperfections in the optical alignment.

4.1.1 Reference Axes (p-s)

The reference axes to be set are the optical axis, the plane of incidence (p) and the plane of the sample (s). To set these axes the arms of the ellipsometer are adjusted to be co-linear and all optical elements are removed. Four identical irises are now mounted, two on each arm, on the ellipsometer; and a low-power He-Ne laser adjusted such that its beam passes sequentially through all of the irises, figure 4.1. A plane front silvered mirror is now placed at the end of the reflection arm and adjusted to reflect the beam back through the irises to the laser. The laser beam is now travelling along the ellipsometer optical axis.

An alignment sample is now mounted on the sample stage (Meadows 1975) and the reflection arm rotated into an angled position. The sample alignment is adjusted such that the laser beam again passes through each iris in sequence and is reflected back to the laser. The normal to the sample surface in the plane of incidence and the normal to the plane of incidence in the sample surface define the p-s axes. The optical components will be aligned to these axes. The alignment sample must be optically flat and specularly reflecting.

The irises used had a diameter of 1 mm and the distance between the first iris next to the laser and the last next to the mirror was 1.6m. The optical axis is thus set to ± 0.015 deg. The p-s axes set by the sample are located to a greater accuracy by virtue of the three reflections,

two at the sample and one at the end mirror. The increase in accuracy is a factor of 8 i.e. ± 0.002 deg. These figures can be used as a general guide to the remainder of the alignment, requiring that the angle of incidence should be set to better than ± 0.015 deg. and component azimuth to ± 0.002 deg. The azimuth alignment will not, however, be as accurate as this due to goniometer imperfections (Meadows 1975), the achievable accuracy is limited to ± 0.01 deg.

4.1.2 Analyser/Polariser Azimuths

The orientation of the analyser and polariser azimuths is subject to component imperfection (McCrackin et al 1963, Hunter 1973), the principal imperfection being ellipticity of the polariser. The analysis will assume that each component is described by a (2x2) Jones matrix of the form

$$\begin{pmatrix} T_{11} & T_{12} \\ T_{21} & T_{22} \end{pmatrix}$$

the elements T_{ij} for each component are listed in table 4.1 In general any or all of the T_{ij} elements may be complex. The principal terms of interest are the T_{11} and T_{22} terms; these represent the major properties of the component. For example, a polariser which has a finite ellipticity, χ , has the matrix

$$\begin{pmatrix} 1 & 0 \\ 0 & j \tan \chi \end{pmatrix}$$

The off-diagonal terms T_{12} and T_{21} are cross-scattering terms and are likely to be caused by surface roughness and optical activity.

The first step of alignment is to mount both the analyser and polariser on to the ellipsometer without a sample and with the arms co-linear. The azimuths are adjusted such that they are orthogonal and nulled. In this condition the azimuths differ only by $\pi/2$ although their absolute values are undefined.

Secondly, the alignment sample is remounted and the reflection arm rotated into an angled position. The analyser and polariser, in general, will no longer be in the extinction position and must therefore be re-nulled. There are two methods by which the null can be located, either the analyser can be set and the polariser nulled or vice versa; until the azimuths again differ by $\pi/2$. These two methods are not equivalent (McCrackin et al 1963).

The transfer matrix of the system T is given by

$$T = T_A R(A) T_S R(P) T_P$$

where T_A - analyser principal frame matrix

T_S - alignment sample principal frame matrix

T_P - polariser principal frame matrix

$R(A)$ - analyser rotation matrix

$R(P)$ - polariser rotation matrix

The detected intensity, I , is given by

$$I = (T E_I)^\dagger (T E_I)$$

where E_I - source electric field matrix

\dagger - Hermite transpose matrix

the null condition is

$$\frac{\partial I}{\partial A} \quad \text{or} \quad \frac{\partial I}{\partial P} = 0$$

Hunter (1973) has solved these equations to first-order and deduces the near-extinction relations

$$\frac{\partial I}{\partial A} = 0 : \quad \mu_1 + \nu_1 \tan \Psi \cos \Delta = \beta_{2SR} + \beta_{1AI} \tan \Psi \sin \Delta$$

$$\begin{aligned} \frac{\partial I}{\partial P} = 0 : \quad \mu_1 \cos \Delta + \nu_1 \tan \Psi \\ = (\chi + \beta_{2SI}) \sin \Delta + \beta_{2SR} \cos \Delta \end{aligned}$$

$$\mu_1 = (-P + \pi/2 \pm \pi/2)$$

$$\nu_1 = A \pm \pi/2$$

The subscripts R and I denote the real and imaginary components; the alignment sample characteristics are

$$\rho = \tan \Psi \exp i\Delta$$

Nulling the polariser and setting the condition that the analyser and polariser are orthogonal gives

$$\frac{\partial I}{\partial P} = 0 : \quad A = P \pm \pi/2$$

substitution gives

$$-P + P \tan \Psi \cos \Delta = \beta_{2SR} + \beta_{1AI} \tan \Psi \cos \Delta$$

$$P (\tan \Psi \cos \Delta - 1) = \beta_{2SR} + \beta_{1AI} \tan \Psi \cos \Delta$$

This does not have a general solution at $P=0$. However, if the terms containing β_{2SR} and β_{1AI} are ignored then $P=0$ does become a general solution. The removal of the β terms can be justified by noting that they are off-diagonal terms and so correspond to optical activity; they do not describe the polariser/analyser/sample ellipticity. This result is the same as that derived by McCrackin et al (1963).

The alternative nulling technique is to null the analyser, thus giving the conditions:-

$$\frac{\partial I}{\partial A} = 0 : A = P \pm \pi/2$$

substitution gives

$$-P \cos \Delta + P \tan \Psi = (\chi + \beta_{2SI}) \sin \Delta + \beta_{2SR} \cos \Delta$$

again ignoring the off-diagonal β_{2SI} & β_{2SR} terms we have

$$P (\tan \Psi - \cos \Delta) = \chi \sin \Delta$$

This equation does not have a general solution $P=0$ unless χ , the polariser ellipticity, or $\sin \Delta$ is zero.

The two methods of nulling each have the disadvantage that off-diagonal terms are to be ignored if a $P=0$ solution is to be found. If the alignment sample is chosen with $\Delta \sim \pi/2$ then the effects of the terms β_{1AI} and β_{2SR} are minimised leaving only the β_{2SI} term to be ignored. Note that these three terms are representative of optical activity in the analyser and alignment sample.

Thus the procedure to be preferred is to set the analyser and null the polariser upon a sample which has the characteristic of $\Delta \sim \pi/2$

The analyser is rotated by a small amount until the polariser nulls at $P = A \pm \pi/2$; this occurs only when the analyser and polariser pass-planes are parallel with the p - s axes respectively.

4.1.3 Compensator Axes at $\pm \pi/4$

The ellipsometer is set into the polariser, compensator and analyser configuration with the incidence and reflection arms co-linear, and without the alignment sample. The polariser azimuth is set to be $+\pi/4$ and the analyser $-\pi/4$.

The transfer matrix for this configuration is:-

$$T = T_A R(-\pi/2) T_C R(\pi/4) T_P$$

T_C - compensator transfer matrix in its principal frame.

The configuration has two extinction azimuths for the compensator which correspond to zones 1 and 3, compensator fast axis at $-\pi/4$ and zones 2 and 4, compensator fast axis at $\pi/4$. Hunter (1973) has derived near extinction relations in which either the analyser, polariser or compensator is nulled. Again neglecting the off-diagonal β terms and writing the azimuths as:-

$$P = \pi/4 + \partial P$$

$$A = -\pi/4 + \partial A$$

$$C = \pm\pi/4 + \partial C$$

The three nulling options give the equations

$$\frac{\partial I}{\partial P} = 0 : -\partial C - \partial P = (\partial C - \partial A) \partial'/t$$

$$\frac{\partial I}{\partial C} = 0 : \quad \partial C + \partial A = \frac{-(\partial C + \partial P)}{t^2} - \frac{\chi}{t}$$

$$\frac{\partial I}{\partial A} = 0 : \quad \partial C + \partial A = \frac{-\partial'(\partial C + \partial P)}{t} - \frac{\chi}{t}$$

where the compensator matrix is

$$\begin{bmatrix} 1 & 0 \\ 0 & -it \exp i\theta' \end{bmatrix}$$

$$\theta = \pi/2 + \theta'$$

The object of the alignment is to reduce ∂C , the compensation azimuth error, to zero. Each equation has a similar sensitivity to ∂C , however, the options which null the analyser or compensator do not have a general solution $\partial C = 0$. Only the option which nulls the polariser has the required solution. Thus setting the analyser to $-\pi/4$ ($\partial A = 0$) gives the equation

$$\partial C = \partial P (1 + \partial'/t)^{-1}$$

This equation is independent of the polariser ellipticity χ and the compensator characteristics θ' & t are only a scale factor between ∂C & ∂P ; they do not affect the nulling azimuth.

The alignment procedure is thus to set the analyser azimuth to $-\pi/4$, position the compensator at an arbitrary azimuth and null the polariser. If the polariser does not null at $\pi/4$ then the compensator azimuth is adjusted and the polariser re-nulled. The procedure is repeated until the polariser nulls at an azimuth of $\pi/4$. When the polariser nulls at $\pi/4$ the compensator fast/slow areas are also at $\pm\pi/4$.

4.1.4 Summary of azimuth alignments for the polariser, analyser and compensator

It has been shown that the p - s axes, polariser, compensator and analyser azimuths can be located despite the presence of optical imperfections. The steps of the alignment are:-

- a) Null the analyser and polariser with the incidence and reflection arms parallel; the azimuths will differ by $\pi/2$. The compensator and alignment sample are not mounted.
- b) Mount and align a sample with the characteristics $\Psi \sim \pi/4$ and $\Delta \sim \pi/2$. The analyser and polariser are nulled by setting the analyser and nulling the polariser. If the azimuths do not differ by $\pi/2$ then the analyser azimuth is altered and the polariser re-nulled. This step is repeated until the polariser nulls at $A \pm \pi/2$. The pass-planes of the analyser and polariser are now co-linear with the p - s axes.
- c) Rotate the analyser to an azimuth of $-\pi/4$, the polariser to $\pi/4$ and mount the compensator. Null the polariser. If the polariser does not null to an azimuth of $\pi/4$, adjust the azimuth of the compensator and re-null the polariser. This step is repeated until the polariser nulls at $\pi/4$. The compensator fast/slow axes are now at $\pm \pi/4$.

The optical azimuths of each component are now aligned to $\pm \pi/4$ and the ellipsometer is ready to be used.

4.1.5 Compensator Calibration

Under ideal conditions where a four-zone experiment is performed the characteristics of the compensator do not affect the measured Ψ & Δ of the surface. However, it is often impractical to perform measurements in all four zones and thus corrections have to be made to measurements performed in two or a single zone. There is a large quantity of literature which describes methods by which compensators can be calibrated Jerrard (1952), very well documented, Holmes (1964, 1965), Azzam and Bashara (1971 d), Hunter (1973), Kothiyal (1975) and El-Hosseiny (1975).

The compensator used in the ellipsometer is a K-prism design of Oxley (1911) modified by Clapham, Downes and King (1969), figure 4.2. The retardation is produced by three total internal reflections at glass/air interfaces. The three reflections ensure that the entrance and exit optical axes are co-linear, Clapham et al (1969) adjusted the angles of the prism by a small amount and coated the long reflection face with a 275 \AA film of Mg F_2 . The modified compensator has a variation of less than 1 degree in retardation over the wavelength range 200 to 600 nm. Oxleys original design has a variation of 5.7 degrees.

The compensator was calibrated with a two-zone experiment upon a fine gold substrate. The data was taken as a normal spectral scan in zone 3; the ellipsometer was re-configured to operate in zone 1 and a second spectral scan taken. Due to the large amount of time required

to perform these measurements, approximately five - six hours, the substrate under examination should be as stable as possible; fine gold was considered to be suitable.

Hunter (1973) derives the relationship between the nulling azimuths A & P, compensator characteristic ρ_c and surface parameter ρ (compensator fast axis at $\pi/4$) as

$$\rho_c = \cot (P + \pi/4) \cdot (1 + \rho \tan A) / (1 - \rho \tan A)$$

where $\rho = \sin (A_1 - A_3) \sin (P_1 + P_3 + \pi/2)$
 $\pm j \{ [\sin (A_1 - A_3) \sin (P_1 + P_3 + \pi/2)]^2$
 $- \sin 2A_1 \sin 2A_3 \sin^2 (P_1 - P_3) \} \dagger$
 $/ [2 \sin 2A_1 \sin 2A_3 \sin (P_3 - P_1)]$

The order of calculation is thus to determine ρ from a two-zone experiment and using ρ with zone 3 data to determine ρ_c . A typical calibration curve of t_c & Δ_c is shown in figure 4.3

4.1.6 Monochromator Calibration

The spectral selection monochromator was a SPEX Minimate monochromator with a 1200 lines/mm grating blazed for 500 nm. The monochromator was calibrated using the configuration shown in figure 4.4. Light from a high-pressure Hg lamp is focused on to the entrance slit of the monochromator. The beam direction is defined by the two irises I_1 and I_2 from the incidence arm of the ellipsometer. The diffracted beam passes through the exit slit of the monochromator and is detected by a Si photodiode.

The calibration was performed by locating the peak detected signal for the five Hg lines which are in the visible region (Kaye & Laby) and noting the wavelength indicated by the monochromator. The error between the known wavelength and tabulated value was determined and is shown graphically in figure 4.5. It is apparent that the errors have a 2 nm spread with a 6.5 nm offset.

The 2 nm spread is consistent with the manufacturers data for this instrument, but the 6.5 nm offset is due to an internal offset caused by a small misalignment.

Thus the monochromator reading is 7 nm too high with a significance of ± 1 nm.

4.2 Alloy Fabrication

The ternary Au-Ag-Cu system was examined at an equilibrium temperature of 600°C. At this temperature the system contains a significant duplex phase region (McMullen and Norton 1949), figure 4.6. The examination required the alloys to be fabricated at 10% wt intervals over the whole of the ternary range. To this end 36 alloys were fabricated. The ternary alloys formed part of a set of alloys which included the binary systems Au-Ag, Ag-Cu & Au-Cu (Clarke 1980). In order to avoid confusion with the earlier work, the samples were numbered from 31 to 66 inclusive.

Each alloy was fabricated in a quantity of 10 gm from granules of spectroscopically pure metal. The processing of each alloy was:-

- 1) bulk granules were weighed out in proportion for a 10 gm sample
- 2) the granules were mixed and melted together in a graphite crucible by a R.F. induction furnace under an inert gas into a billet
- 3) the billet was worked into a flat sheet 1 mm thick with several annealings to remove stress and to homogenise the sheet
- 4) the sheet was cut into two plaquettes 10x20x1 mm
- 5) the plaquettes were annealed for 2 hours at 600°C in either a vacuum or salt bath and then air/water quenched
- 6) each plaquette was mounted in thermosetting resin ready for polishing

The mounted plaquettes were polished by hand on a series of abrasive papers starting with grade 150 and finishing with grade 600. The polishing was performed while a stream of water flowed over the abrasive paper to remove loose grit and swarf. This water was filtered to remove the gold and silver swarf for recycling. The surfaces were then given a final high finish with diamond abrasives on a lapping wheel. The abrasives were of size 6μ , 1μ and $1/4\mu$.

The polishing was performed by hand at each stage to ensure a good quality surface finish. When polishing soft metals there is always a danger of burnishing the surface rather than abrasive polishing. Burnishing is characteristic of causing the surface to flow. This is highly undesirable as there is a risk of embedding the abrasive compound within the surface and of destroying the phase proportions of the surface leaving a Beilby-type layer of deformed material. To avoid these dangers each alloy was polished singly, by hand, with the minimum pressure and slowest wheel speed to achieve abrasion and frequently inspected under a microscope for burnishing.

Finally, offcuts of each alloy were taken during the cutting of the plaquettes and these were chemically assayed by the Worshipful Company of Goldsmiths. Two alloys, 45 and 46, were of unsatisfactory composition and were repeated as 45R and 46R. The assayed compositions are detailed in table 4.2, and are shown on the phase diagram in figure 4.6.

4.3.1 Ellipsometric Data Reduction

The ellipsometer constructed and aligned according to the procedure described above is capable of producing data which is not subject to azimuth uncertainties, only to component imperfections. The data reduction procedure is required to calculate the Ψ and Δ values of a surface from the nulling azimuths of the polariser and analyser in the presence of optical imperfections, the principal imperfections being associated with the compensator.

McCrackin et al (1963) noted that if an average of Ψ and Δ is formed by averaging complementary zones, then the averages agree to within experimental error. In our case it was not possible to perform a four-zone measurement as the compensator could not be rotated by $\pi/2$. This constrained measurements to two-zones (1 and 3) at best, in practice a two-zone experiment was used only for calibrating the compensator as it produced considerable operator fatigue. The normal method of measurement was therefore a single-zone measurement (zone 3).

The equations for deducing Ψ and Δ from a single zone measurement with compensator corrections are described by many authors, Holmes & Feucht (1967), Azzam & Bashara (1971), Hunter (1972), Kothiyal (1975); the analysis used is that due to Holmes & Feucht (1967).

The angles measured by the ellipsometer are not azimuths but angles relative to the $\pm\pi/4$ azimuths. This is due to the nature of the control electronics which are only capable of measuring angular changes rather than absolute angles, the

polariser/analyser being returned to $\pm\pi/4$ fiducial positions at the beginning/end of each experiment.

The equations to calculate the azimuths are:-

$$A = \pi/4 + A_R$$

$$P = -\pi/4 + P_R$$

where A & P - component azimuths

A_R & P_R - indicated angular change from $\pm\pi/4$ fiducial position.

Assuming that the compensator can be described by $\rho_c = \tan \psi_c \exp i\Delta_c$, for an ideal compensator with $\psi = \pi/4$ and $\Delta = \pi/2$, $\rho_c = i$, Holmes & Feucht (1967) derive the equation between the nulling azimuths A and P, and the surface parameter ρ_s for zone 3 as

$$\rho_s = \frac{\cot P - \rho_c}{\rho_c \tan A (\cot P - 1)}$$

The surface complex refractive index n is then calculated as (McCrackin et al 1963)

$$\hat{n} = \tan \phi \left(1 - \frac{4 \rho_s \sin^2 \phi}{(\rho_s + 1)^2} \right)^{\frac{1}{2}}$$

where ϕ - angle of incidence

ρ_s - ellipsometric parameter, $\tan \psi_s \exp i\Delta_s$

\hat{n} - surface complex refractive index, $n - ik$

The final step is to calculate the normal reflectance for the surface as (Wooten 1972)

$$R_n = \frac{(1 - n)^2 + k^2}{(1 + n)^2 + k^2}$$

Thus the normal reflectance at a given wavelength is calculated from a single-zone measurement with a correction for the compensator imperfections.

4.3.2 Calculation of Colour Co-ordinates (CIE 1931)

The colour of an object can be described using a co-ordinate system based on the human eye's sensitivity to the visible spectrum (Bouma 1971); the sensation of colour is due to radiation falling upon the cones which form part of the retina. The definition of colour is based upon the levels at which the three types of cone, which have responses peaking at 430 nm, 540 nm, and 590 nm, McNichol (1964 a,b), Wold (1957), Rushton (1955), are stimulated. The stimulation depends upon the quantities of source luminance, object reflectance and eye sensitivity. This method yields the tristimulus values of colour for any coloured object in a known illumination. The tristimulus values are calculated according to the CIE 1931 convention as:-

$$X = k \int R(\lambda) I(\lambda) E_x(\lambda) d\lambda$$

$$Y = k \int R(\lambda) I(\lambda) E_y(\lambda) d\lambda$$

$$Z = k \int R(\lambda) I(\lambda) E_z(\lambda) d\lambda$$

where $R(\lambda)$ - reflectivity of object

$I(\lambda)$ - illuminance at object

$E_x(\lambda), E_y(\lambda), E_z(\lambda)$ - response of the eye

The integration limits are the bounds of the visible spectrum, 380 nm - 780 nm.

The response curves $E_x(\lambda)$, $E_y(\lambda)$ and $E_z(\lambda)$ are shown in figure 4.7. The description of colour by the tristimulus value (X,Y,Z) forms a three-dimensional space in which any colour is represented by a unique point (X,Y,Z) , figure 4.8. The CIE convention describes a two-dimensional colour co-ordinate plot derived from the (X,Y,Z) tristimulus value using the normal relations

$$x = \frac{X}{X + Y + Z}$$

$$y = \frac{Y}{X + Y + Z}$$

$$z = \frac{Z}{X + Y + Z}$$

noting that $x+y+z = 1$

This normalising of the colour space XYZ to xyz is equivalent to the projection of the origin through the colour point in XYZ space and intersecting with a plane of constant luminance (Bouma 1971), figure 4.8. Each point on the plane of constant luminance will correspond to all points (X,Y,Z) which have their components in a constant ratio. The complete description of a colour is thus a pair of co-ordinates (x,y) and a luminance L.

Using this description the locus of the monochromatic radiations can be constructed, figure 4.9; the position of the 'white' point is also marked. It is possible to construct two types of contour upon the colour plane, those of constant

hue, which are radial from the white point to the monochromatic locus and those of constant saturation which are parallel to the monochromatic locus.

The colour of any object is thus calculated by means of the three XYZ integrals which integrate the source luminance, object reflectance and eye's response over the visible region, and the colour co-ordinates x, y and luminance derived from the normalising relations described above.

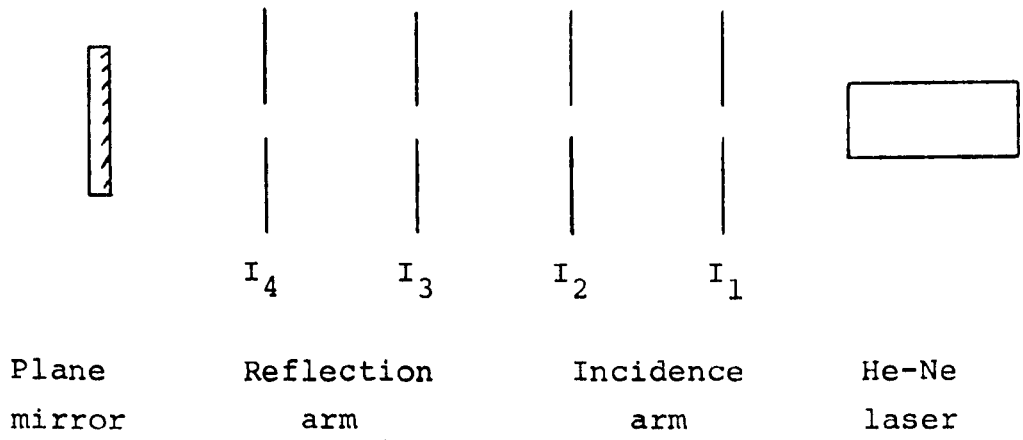


Figure 4.1 Alignment of the optical axis

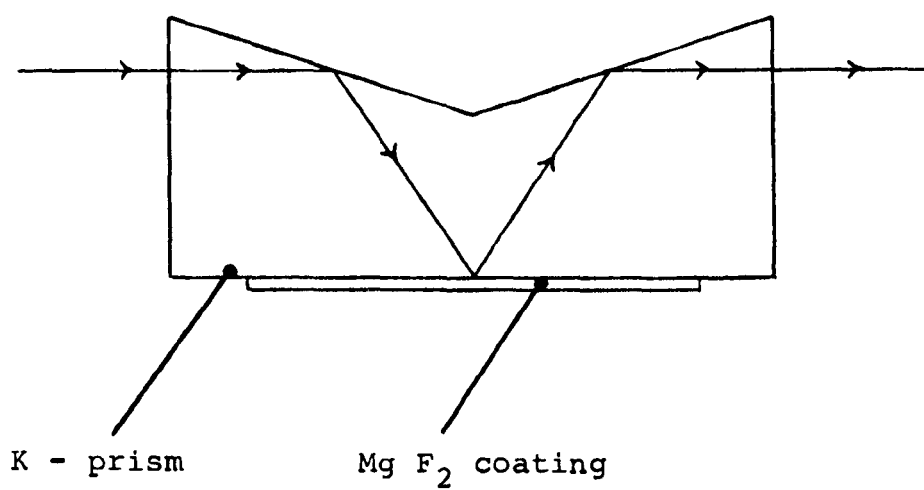


Figure 4.2 Compensator prism

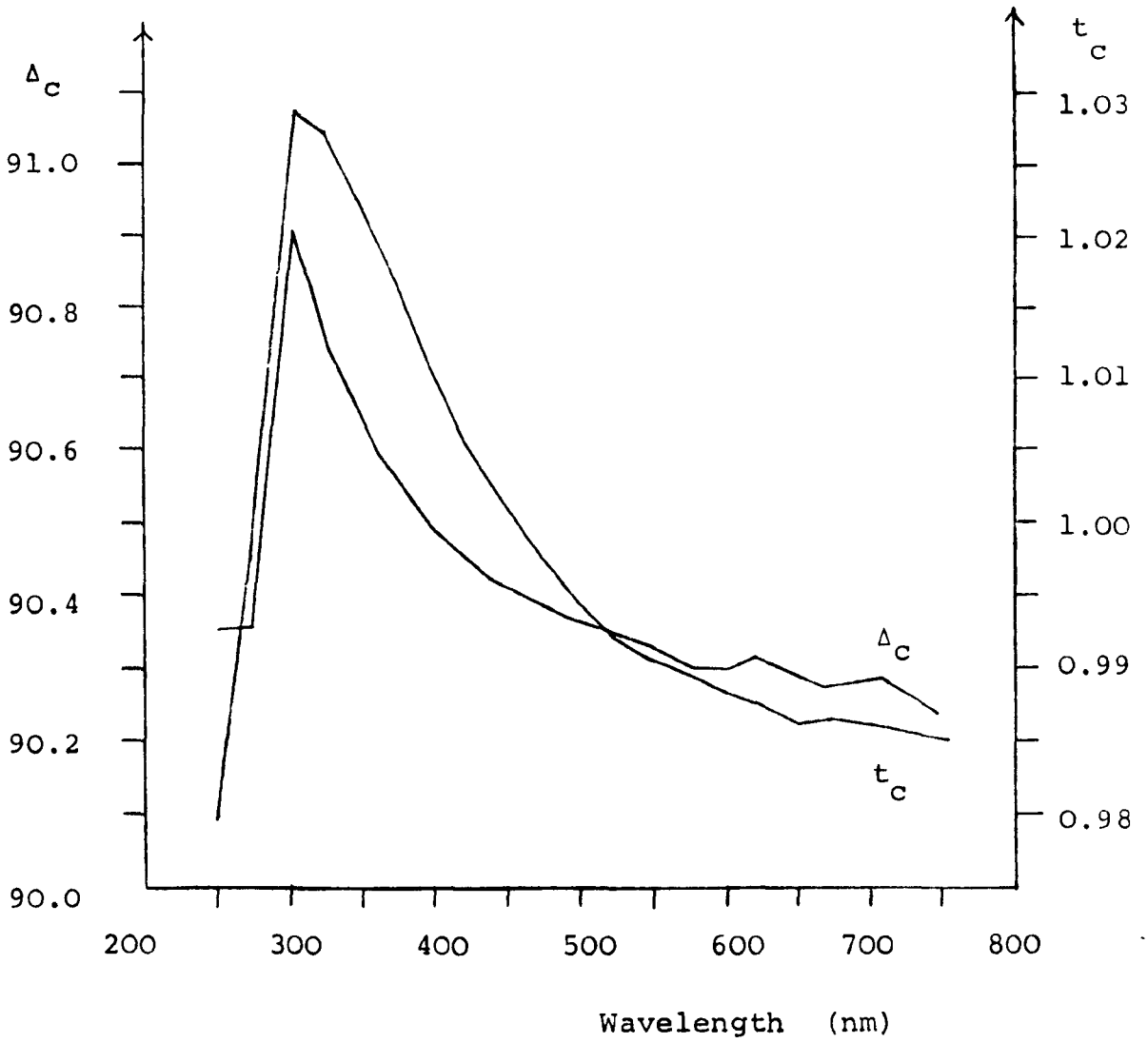


Figure 4.3 Compensator calibration

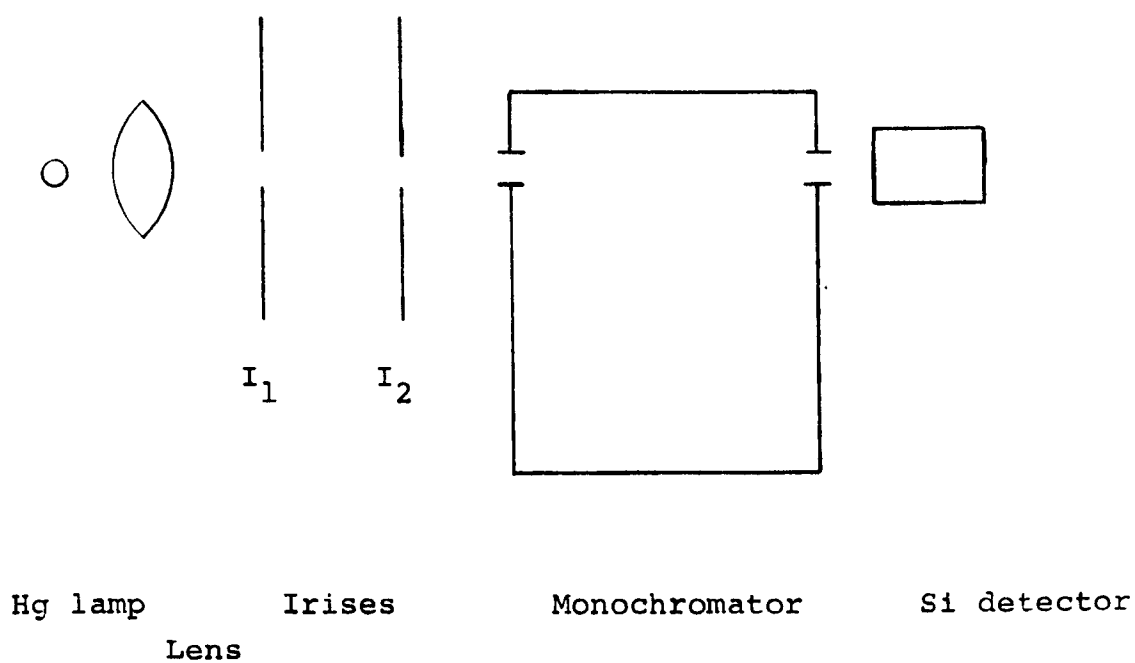


Figure 4.4 Experimental configuration for calibration of the monochromator

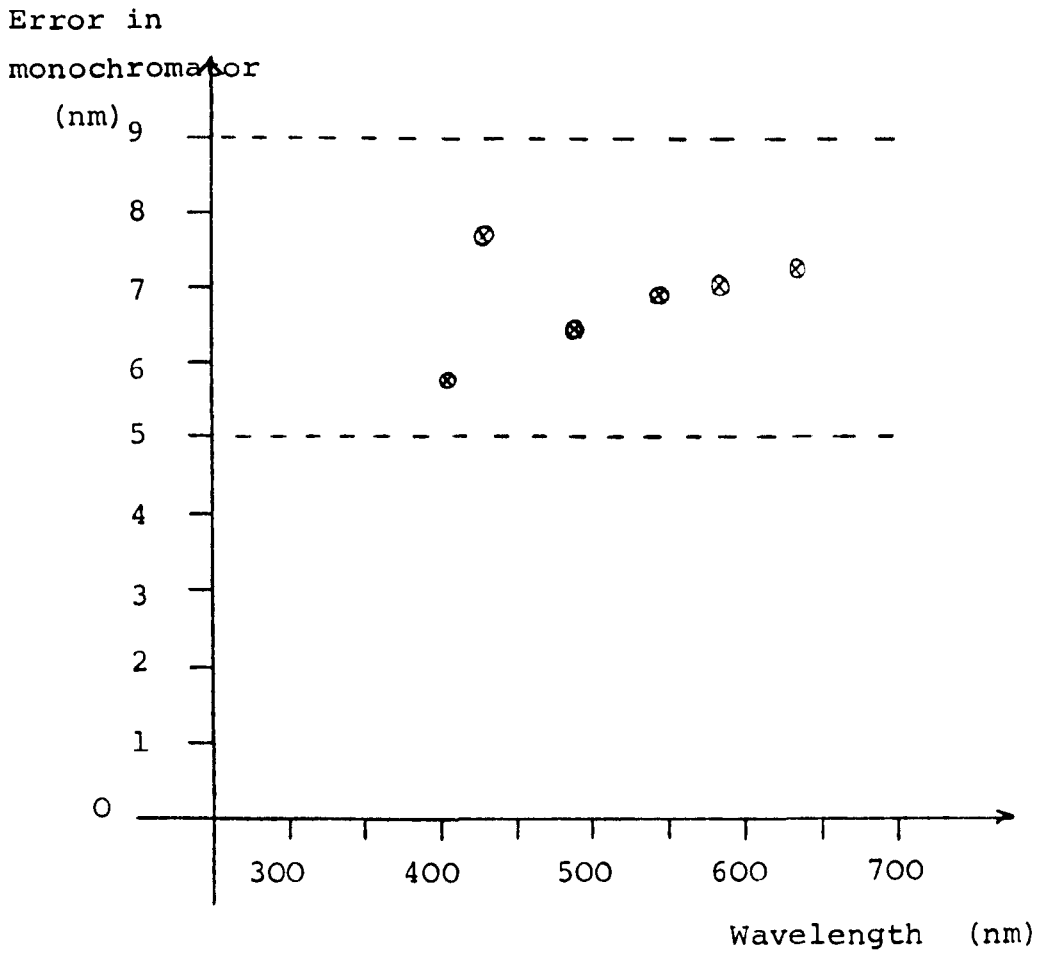


Figure 4.5 Monochromator calibration with the manufacturers tolerance indicated

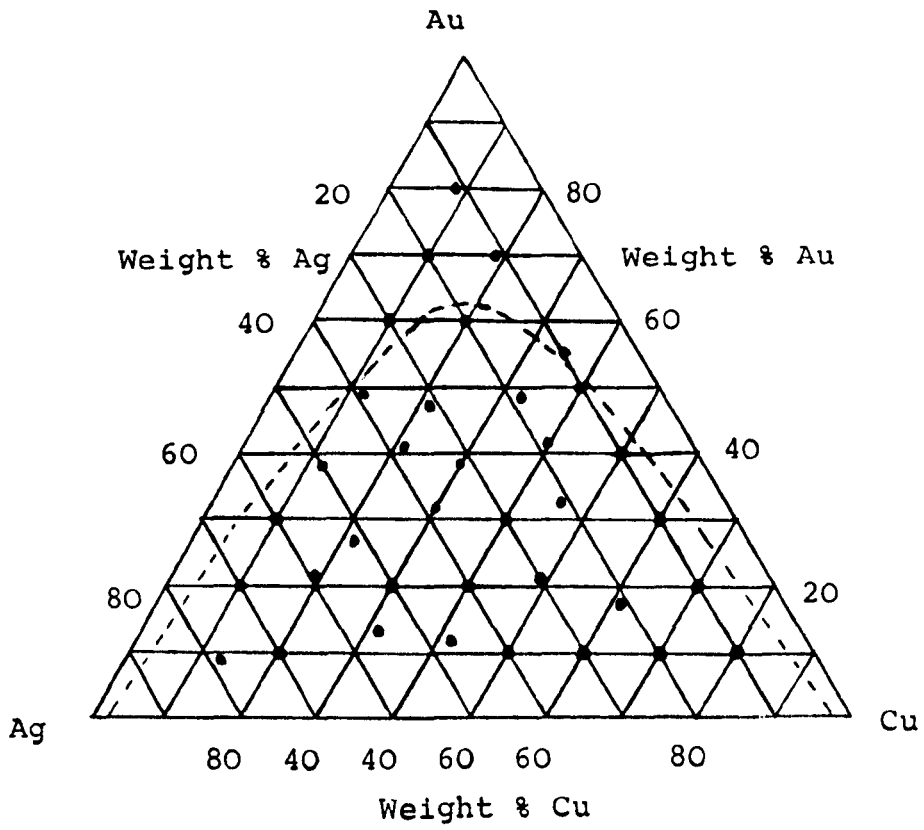


Figure 4.6 Au-Ag-Cu ternary phase diagram @ 600 C showing the compositions of the alloys

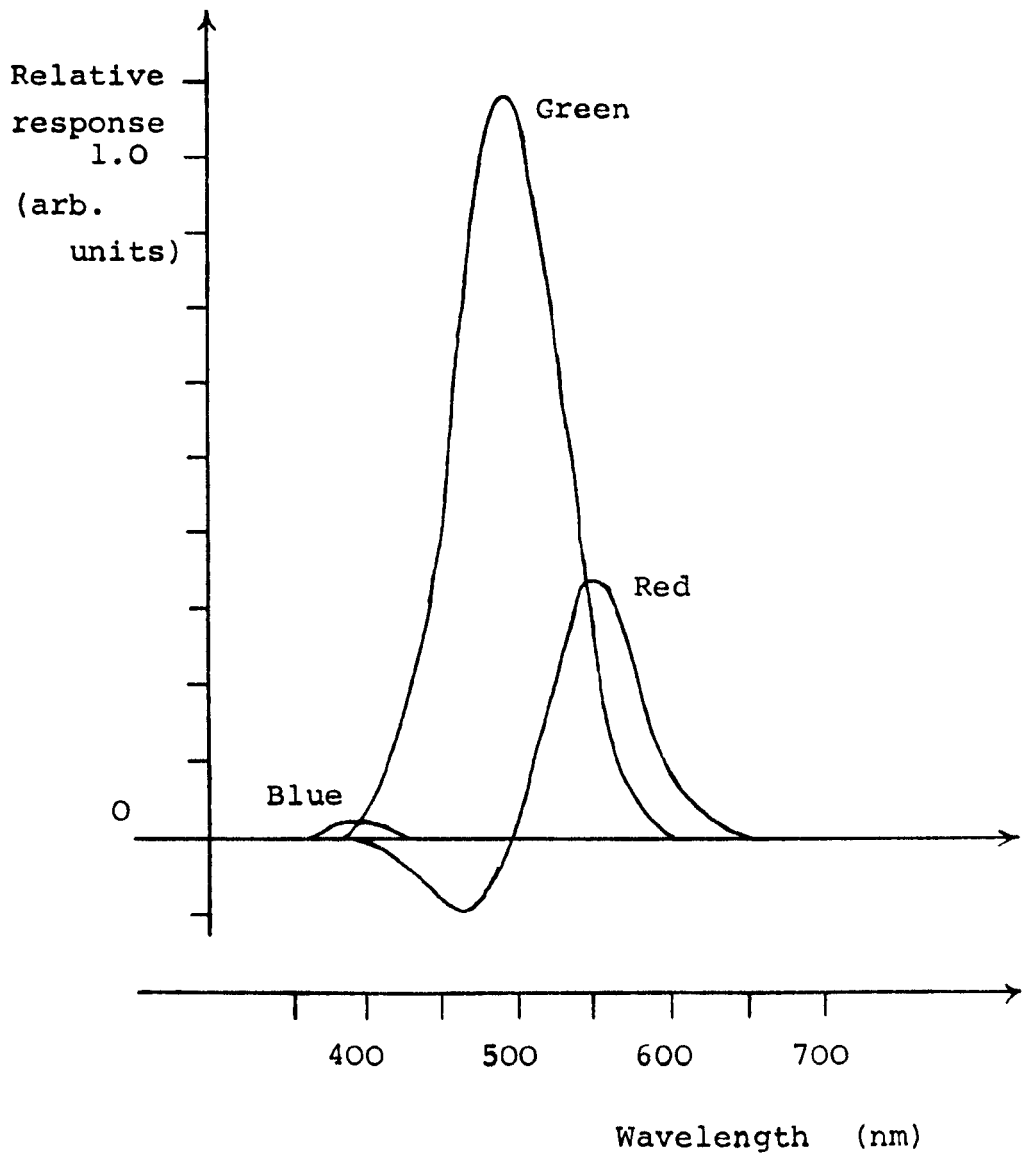


Figure 4.7 Tri-stimulus matching functions of the eye

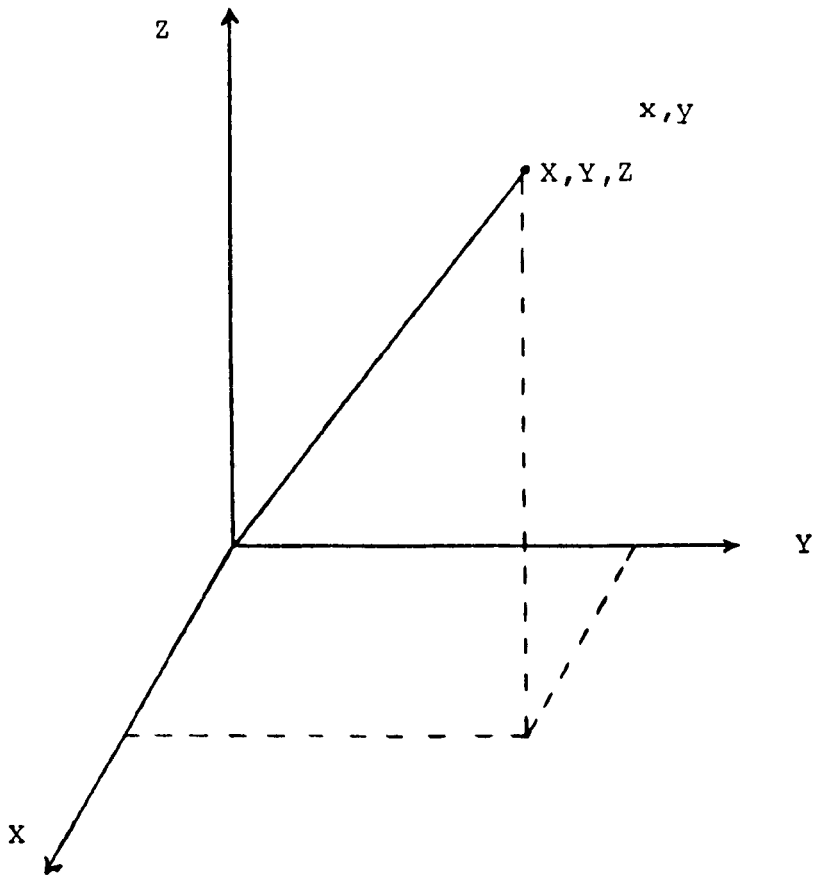


Figure 4.8 Projection of a colour point onto a plane of constant luminance

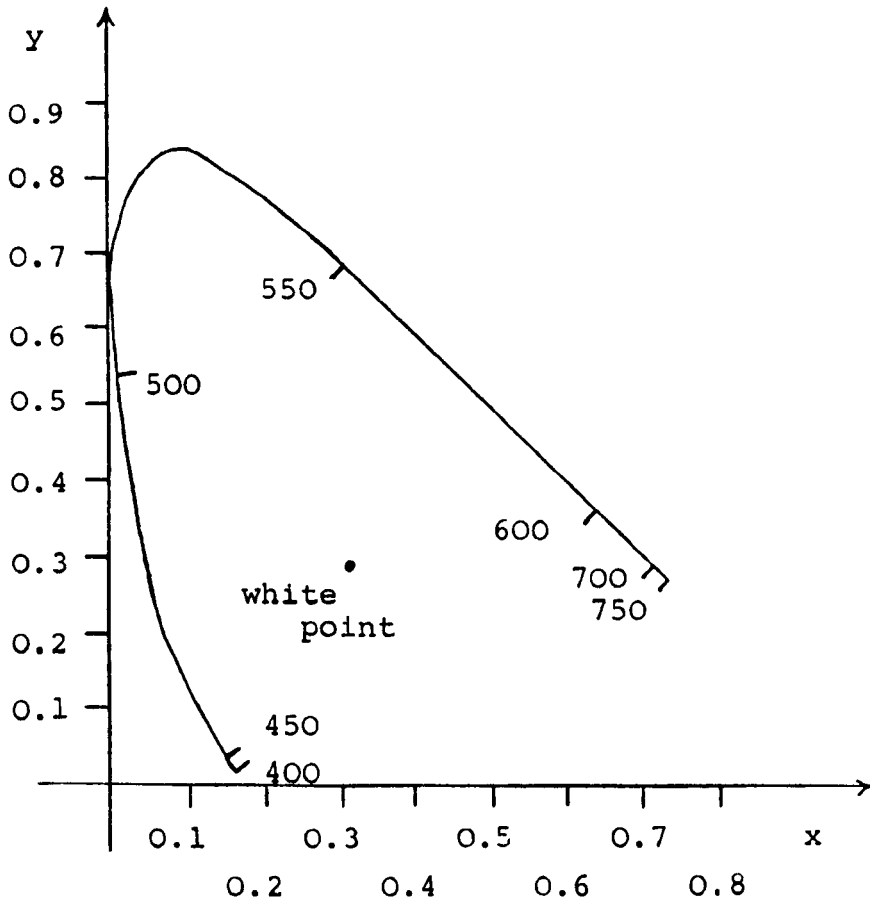


Figure 4.9 Mono-chromatic locus of colour in the CIE (1931) convention

Principal frame matrix

$$\begin{pmatrix} T_{11} & T_{12} \\ T_{21} & T_{22} \end{pmatrix}$$

| Element | Polariser/ Analyser | Compensator | Sample |
|----------|------------------------|----------------------|--------------------------|
| T_{11} | 1 | 1 | $\tan \psi \exp i\Delta$ |
| T_{12} | β_{1P} | β_{1C} | β_{1S} |
| T_{21} | β_{2P} | β_{2C} | β_{2S} |
| T_{22} | β_{3P} | $t_C \exp i\Delta_C$ | β_{3S} |

Table 4.1 Jones matrices of the ellipsometric components in their principal frames

| Sample number | Wt % Au | Wt % Ag | Wt % Cu |
|---------------|-----------|-----------|------------------|
| 31 | 78.9 (80) | 10.4 (10) | <u>10.7</u> (10) |
| 32 | 69.9 (70) | 10.6 (10) | <u>19.5</u> (20) |
| 33 | 69.8 (70) | 20.3 (20) | <u>9.8</u> (10) |
| 34 | 59.6 (60) | 29.8 (30) | <u>10.6</u> (10) |
| 35 | 60.1 (60) | 20.0 (20) | <u>19.9</u> (20) |
| 36 | 56.2 (60) | 9.7 (10) | <u>34.2</u> (30) |
| 37 | 49.0 (50) | 40.4 (40) | <u>10.6</u> (10) |
| 38 | 48.1 (50) | 31.2 (30) | <u>20.7</u> (20) |
| 39 | 49.4 (50) | 18.8 (20) | <u>31.8</u> (30) |
| 40 | 50.2 (50) | 9.9 (10) | <u>39.9</u> (40) |
| 41 | 39.3 (40) | 51.2 (50) | <u>9.5</u> (10) |
| 42 | 40.4 (40) | 39.0 (40) | <u>20.6</u> (20) |
| 43 | 39.0 (40) | 30.8 (30) | <u>30.2</u> (30) |
| 44 | 40.4 (40) | 19.6 (20) | <u>40.0</u> (40) |
| 45R | 39.9 (40) | 10.7 (10) | <u>49.5</u> (50) |
| 46R | 29.9 (30) | 59.9 (60) | <u>10.1</u> (10) |
| 47 | 27.3 (30) | 51.0 (50) | <u>21.5</u> (20) |
| 48 | 30.5 (30) | 39.7 (40) | <u>29.8</u> (30) |
| 49 | 30.0 (30) | 29.9 (30) | <u>40.1</u> (40) |
| 50 | 33.3 (30) | 20.7 (20) | <u>46.8</u> (50) |
| 51 | 29.9 (30) | 9.6 (10) | <u>60.5</u> (60) |
| 52 | 20.2 (20) | 69.7 (70) | <u>10.1</u> (10) |
| 53 | 21.0 (20) | 59.6 (60) | <u>19.4</u> (20) |
| 54 | 19.9 (20) | 49.8 (50) | <u>30.3</u> (30) |
| 55 | 20.2 (20) | 39.6 (40) | <u>40.4</u> (40) |
| 56 | 20.5 (20) | 29.8 (30) | <u>49.7</u> (50) |
| 57 | 19.7 (20) | 20.1 (20) | <u>60.2</u> (60) |
| 58 | 20.0 (20) | 9.8 (10) | <u>69.2</u> (70) |
| 59 | 9.4 (10) | 79.0 (80) | <u>11.6</u> (10) |
| 60 | 9.9 (10) | 69.9 (70) | <u>20.2</u> (20) |
| 61 | 13.6 (10) | 55.7 (60) | <u>30.7</u> (30) |
| 62 | 11.5 (10) | 46.4 (50) | <u>42.1</u> (40) |
| 63 | 9.9 (10) | 39.8 (40) | <u>50.3</u> (50) |
| 64 | 9.9 (10) | 29.8 (30) | <u>60.3</u> (60) |
| 65 | 10.1 (10) | 20.0 (20) | <u>69.9</u> (70) |
| 66 | 9.8 (10) | 10.3 (10) | <u>79.9</u> (80) |

Table 4.2 Assayed composition in wt % of the ternary Au-Ag-Cu alloys. (Figures in brackets are nominal compositions, figures underlined are determined by difference.)

CHAPTER FIVE

RESULTS

5.1 Absorption Edges

The optical properties of the Au-Ag-Cu system were examined at 10 wt% intervals using 36 alloys. An additional set of 7 DIN8328 alloys numbered ON, 1N, 2N, 3N, 4N, 5N & 8N used as colour standards for watchcases were also examined. The optical properties were examined ellipsometrically over the wavelength range of 250 nm to 850 nm at an incremental resolution of 5 nm. The data was recorded as an analyser/polariser nulling azimuths and wavelength. The data was reduced to a spectral refractive index $n-ik$ and thus to a normal reflectance spectrum. To identify the position of absorption edges the normal reflectance spectrum $R_n(\lambda)$ was calculated and zeros in the derivative $\partial^2 R_n / \partial \lambda^2$ located. Finally the colour co-ordinates were calculated by the CIE 1931 convention under illuminant 'C'. The details of the data reduction are given in Chapter 4.

The reflectance spectra of the 36 ternary alloys are shown in figures 5.1 to 5.9 inclusive. They show two distinct absorption edges due to the silver- and copper- rich phases at approximately 310 nm and 570 nm respectively. The general characteristics of the reflectance spectra being that of a high reflectance at wavelengths longer than 570 nm, a distinct absorption edge at 570 nm followed by a plateau region where the height depends upon alloy composition followed by a second

absorption edge at 310 nm. All of the duplex-phase alloys exhibited this structure with the exact wavelengths of absorption, plateau height and width depending upon the precise alloy composition. The absorption of the single-phase alloys is distinct at 570 nm but there is no plateau region or second edge. The reflectance decreases gradually with decreasing wavelength after the 570 nm edge.

The exact positions of the absorption edges were determined by the location of zeros in $\partial^2 R_n / \partial \lambda^2$. These zeros correspond to the wavelengths at which absorption due to bound electrons commence. The absorption edges were located for each of the 36 alloys and are plotted collectively in figure 5.10, and in constant gold wt% groupings in figures 5.11 to 5.23 inclusive. Additionally the edge wavelengths are tabulated in table 5.1. To improve the clarity with which alloying effects are derived the edge wavelengths are plotted as functions of both gold- and silver-proportion.

Three absorption edges were located at nominal wavelengths of 570 nm, 440 nm and 310 nm. The 440 nm and 570 nm edges exhibited a smooth monotonically changing locus dependant upon the silver proportion. The 570 nm edge was located in all of the duplex-phase alloys and ranged in magnitude from 0.2 to 0.5 nm/wt% silver; detailed values are given in table 5.2. A weak edge was located at 440 nm in the 20, 30 and 40 wt% gold alloys. In the case of the 20 wt% gold alloys sufficient data was available

to estimate the edge shift to be 0.3 nm / wt% silver.

The 310 nm edge did not exhibit a monotonic shift with silver proportion but showed both a positive and negative shift coefficient upon alloying. The maximum shift occurs for all of the alloys at a silver wt% of approximately 30 %. The alloying effect can be described as a linear relationship upon which is superimposed a spread function. The spread function is centred at 30 wt% silver and extends from 20 wt% to 50 wt%. This structure was identified in the 10 wt% to 50 wt% gold groupings. The maximum peak shift was estimated by taking a linear interpolation between alloys at the end of the locus and determining the peak height above this linear interpolation. The peak shift was estimated for all the duplex-phase alloys and are presented in figure 5.23. The peak shift has a negative gradient with respect to gold proportion and decreases at a rate of 0.5 nm / wt% gold.

5.2 Colorimetry

The colours of the 36 ternary alloys and 7 DIN8328 alloys were calculated under the CIE 1931 convention for illuminant 'C' in the L-x-y system using the normal reflectance spectra already derived. The colour co-ordinates are presented both graphically in figure 5.24 and in tabular form in table 5.3. The colour region of the alloys is very close to the 'white' point and are characterised by a high luminance, 70 to 90 %,

and low saturation, 6 to 25 %.

The loci of constant gold proportion show that the colour co-ordinates of some duplex-phase alloys do not lie upon straight lines but show a distinct curvature towards greater saturation. This effect is quite marked for the 10 and 20 wt% gold alloys. These groupings have been plotted on an extended scale in figure 5.25.

Additionally, the colour co-ordinates of the DIN8328 alloys were made available by the Worshipful Company of Goldsmiths. The colour co-ordinates were determined under illuminant 'D' using a normal reflectometer. The colour co-ordinates were also determined ellipsometrically under illuminant 'D' and are tabulated in table 5.5.

It is not possible to directly compare the colour co-ordinates under illuminant 'C' of the DIN8328 alloys to the Au-Ag-Cu ternary alloys as the surface preparation and annealing processes used in the production of the DIN8328 alloys was unknown. It is notable that under illuminant 'D' the normal reflectometer gave consistently higher luminances than those determined ellipsometrically.

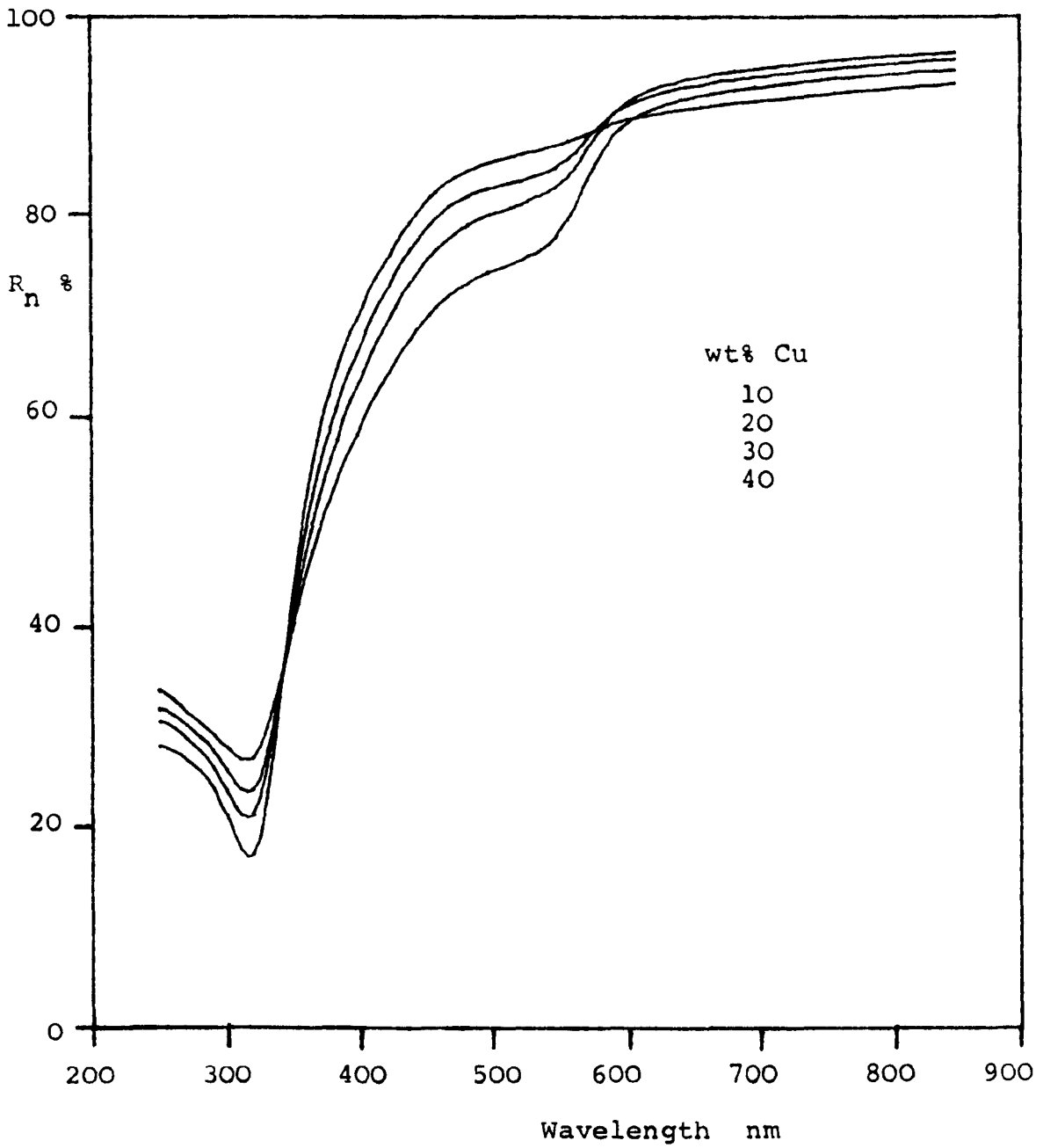


Figure 5.1 Normal reflectance spectra of 10 wt% Au alloys.

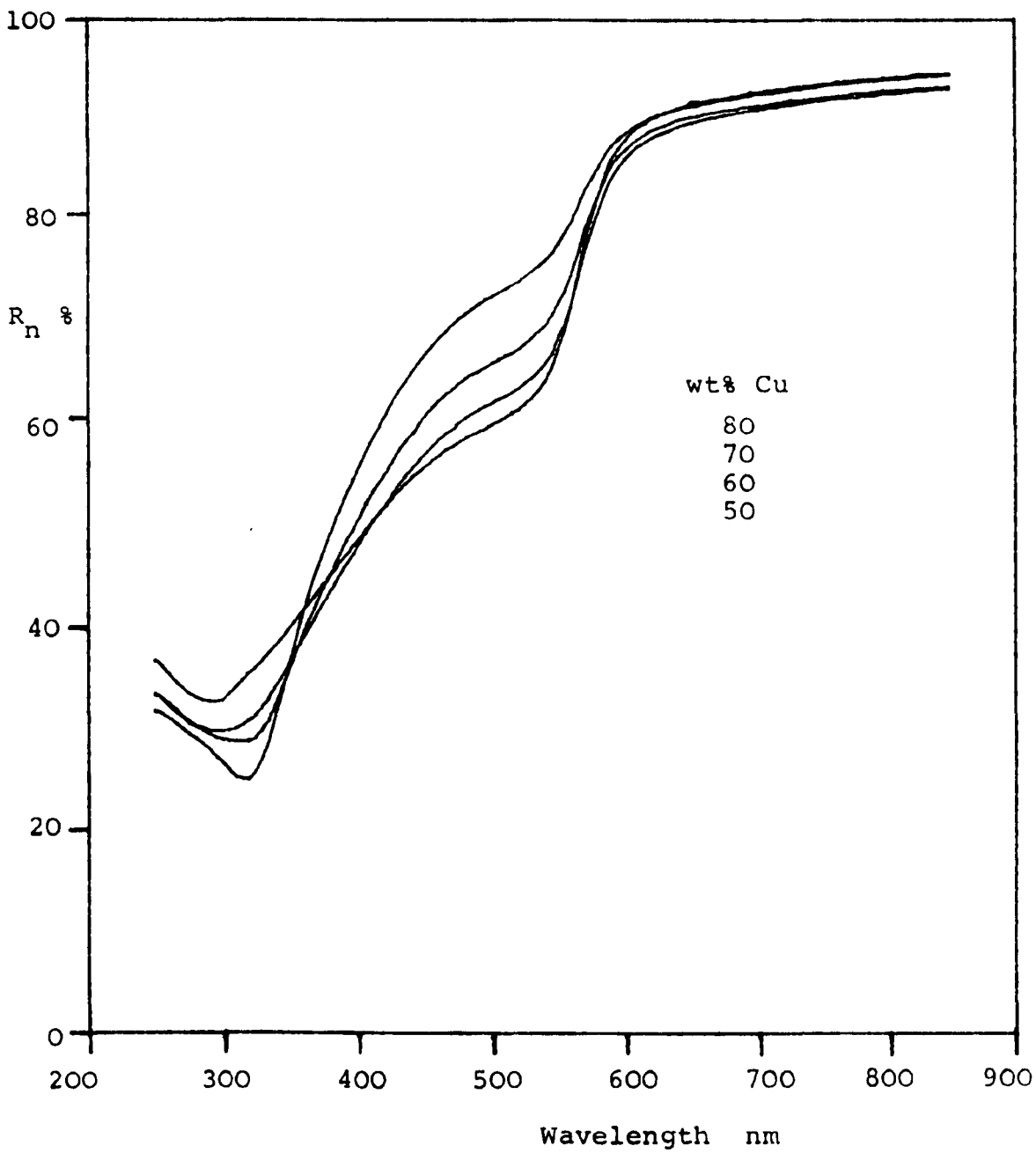


Figure 5.2 Normal reflectance spectra of 10 wt% Au alloys.

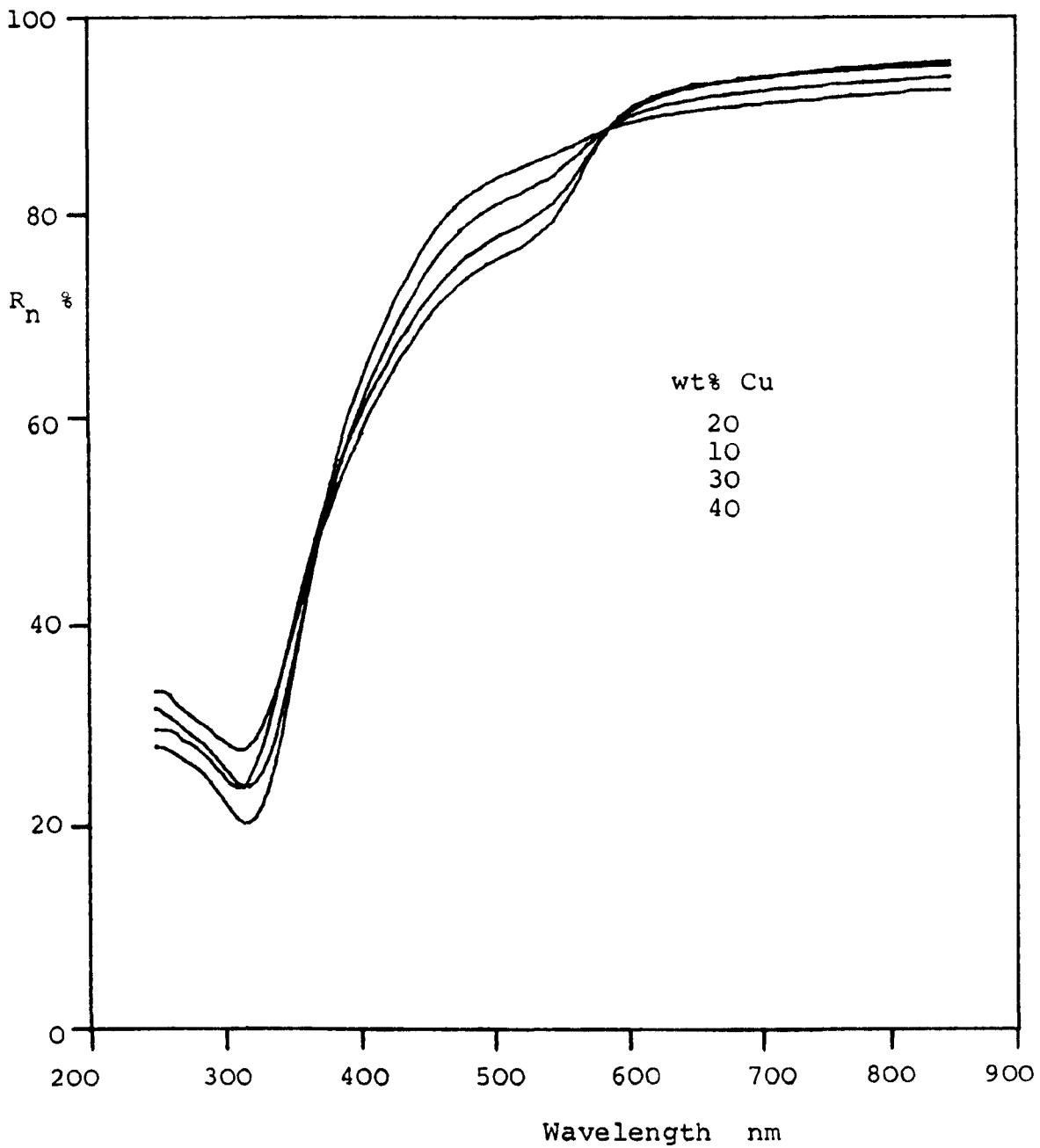


Figure 5.3 Normal reflectance spectra of 20 wt% Au alloys.

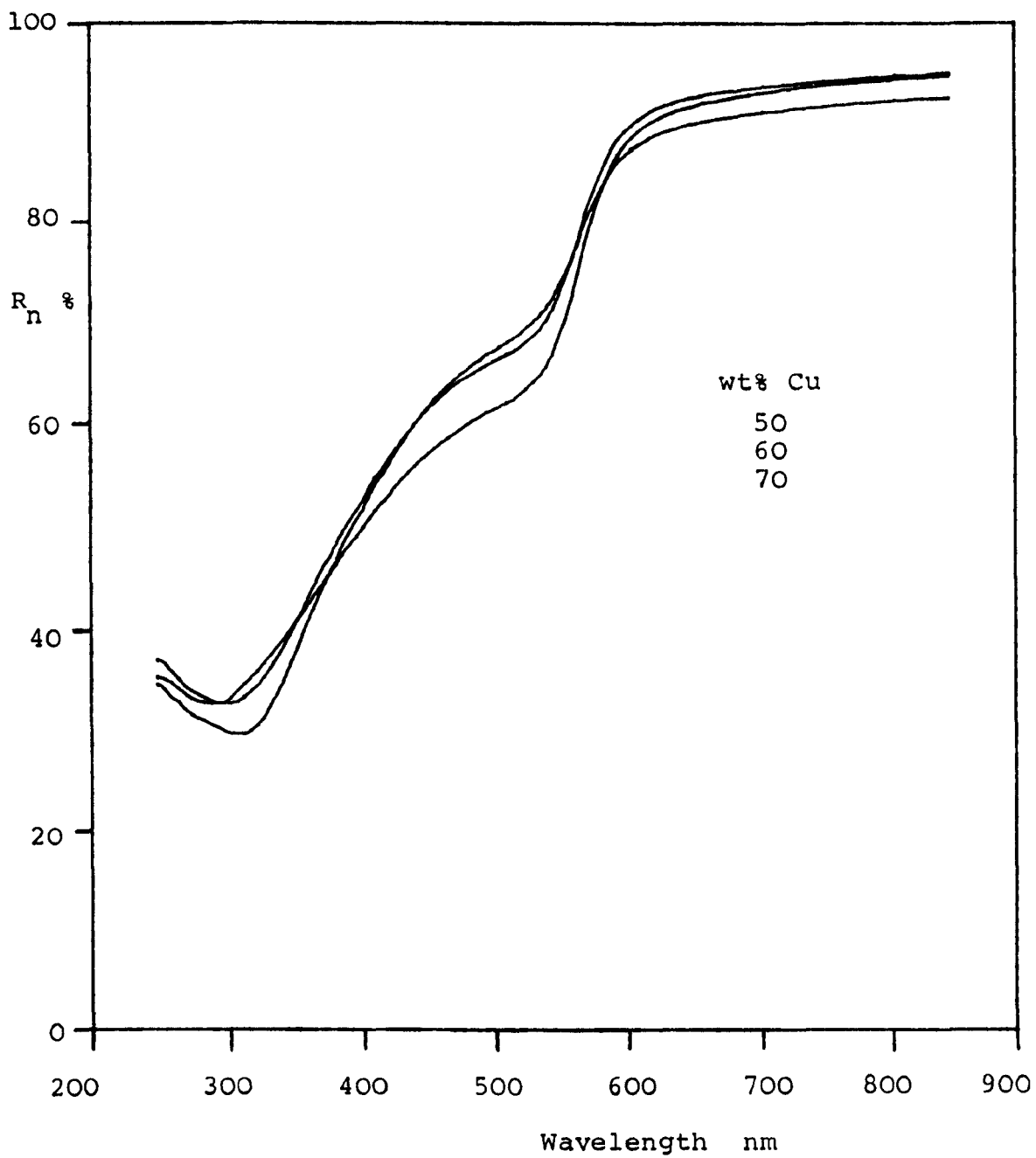


Figure 5.4 Normal reflectance spectra of 20 wt% Au alloys.

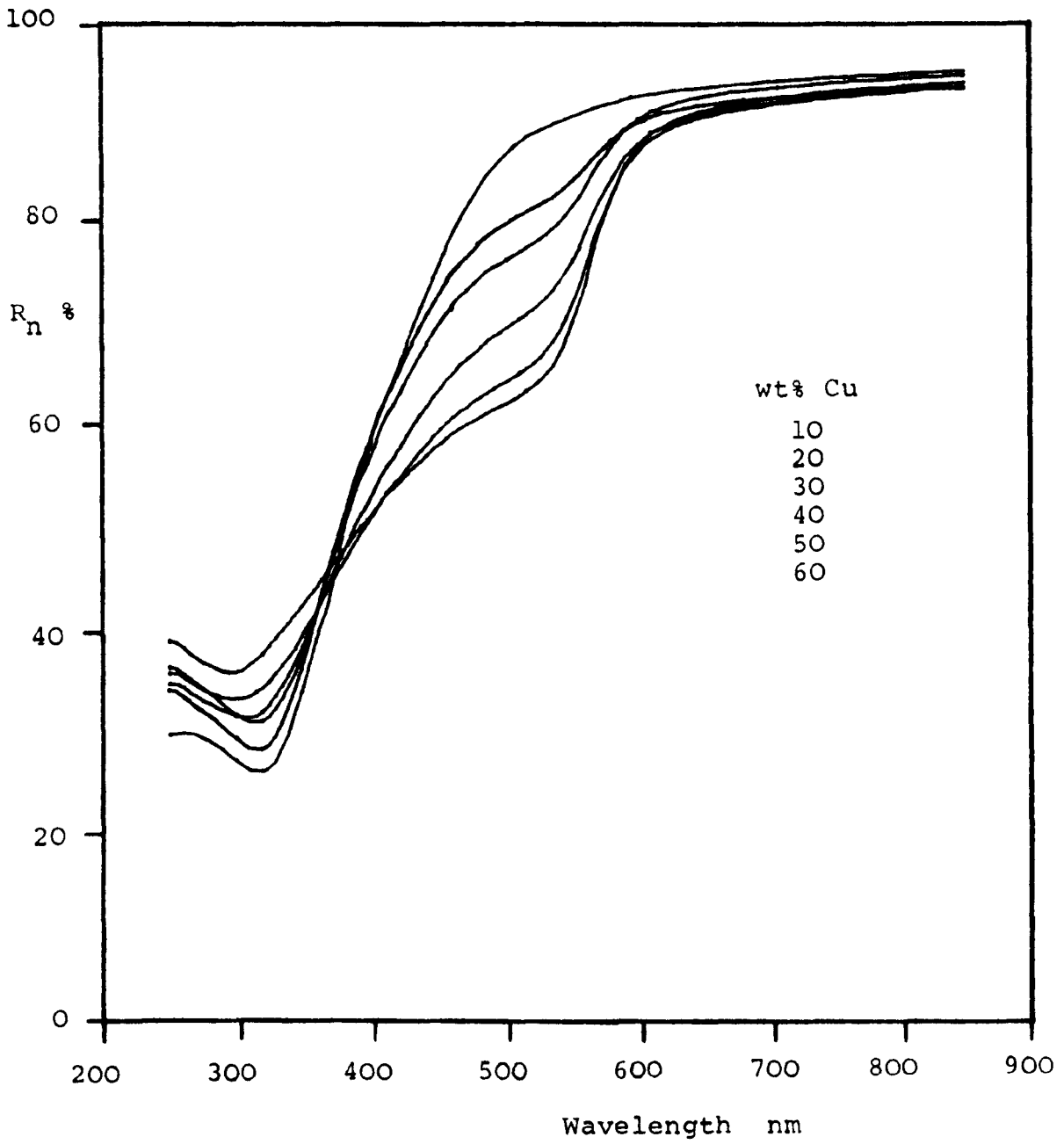


Figure 5.5 Normal reflectance spectra of 30 wt% Au alloys.

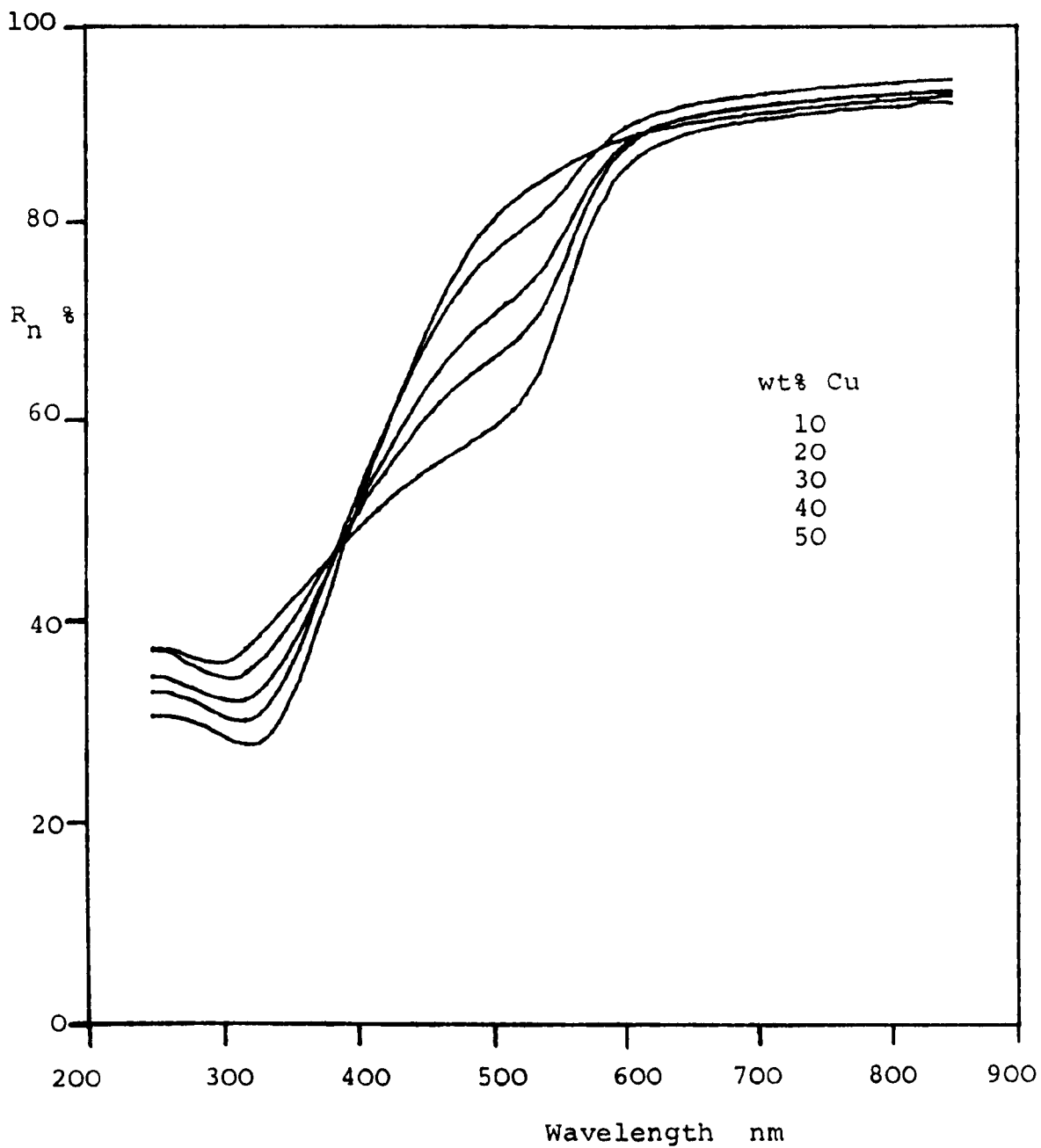


Figure 5.6 Normal reflectance spectra of
40 wt% Au alloys.

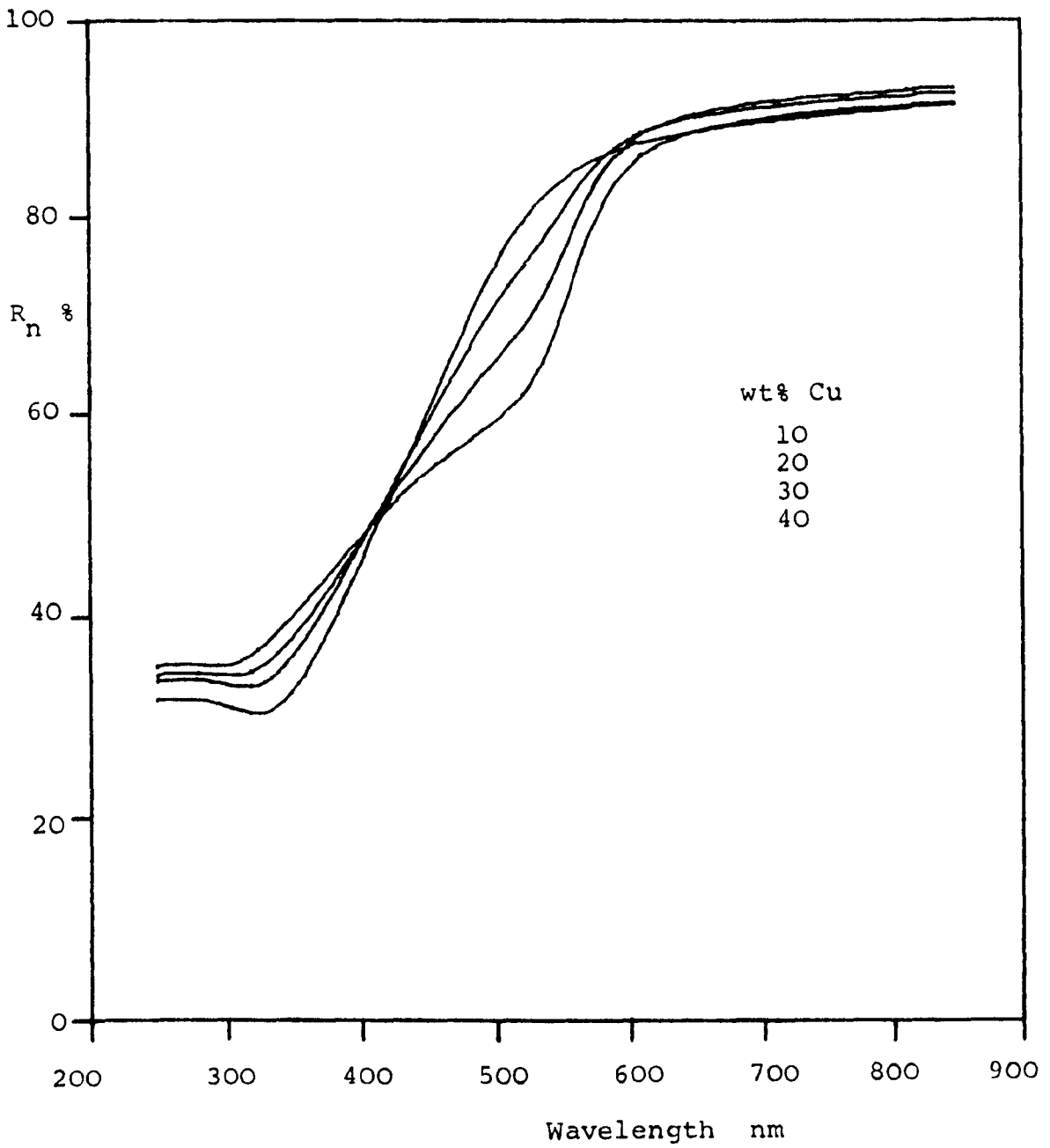


Figure 5.7 Normal reflectance spectra of 50 wt% Au alloys.

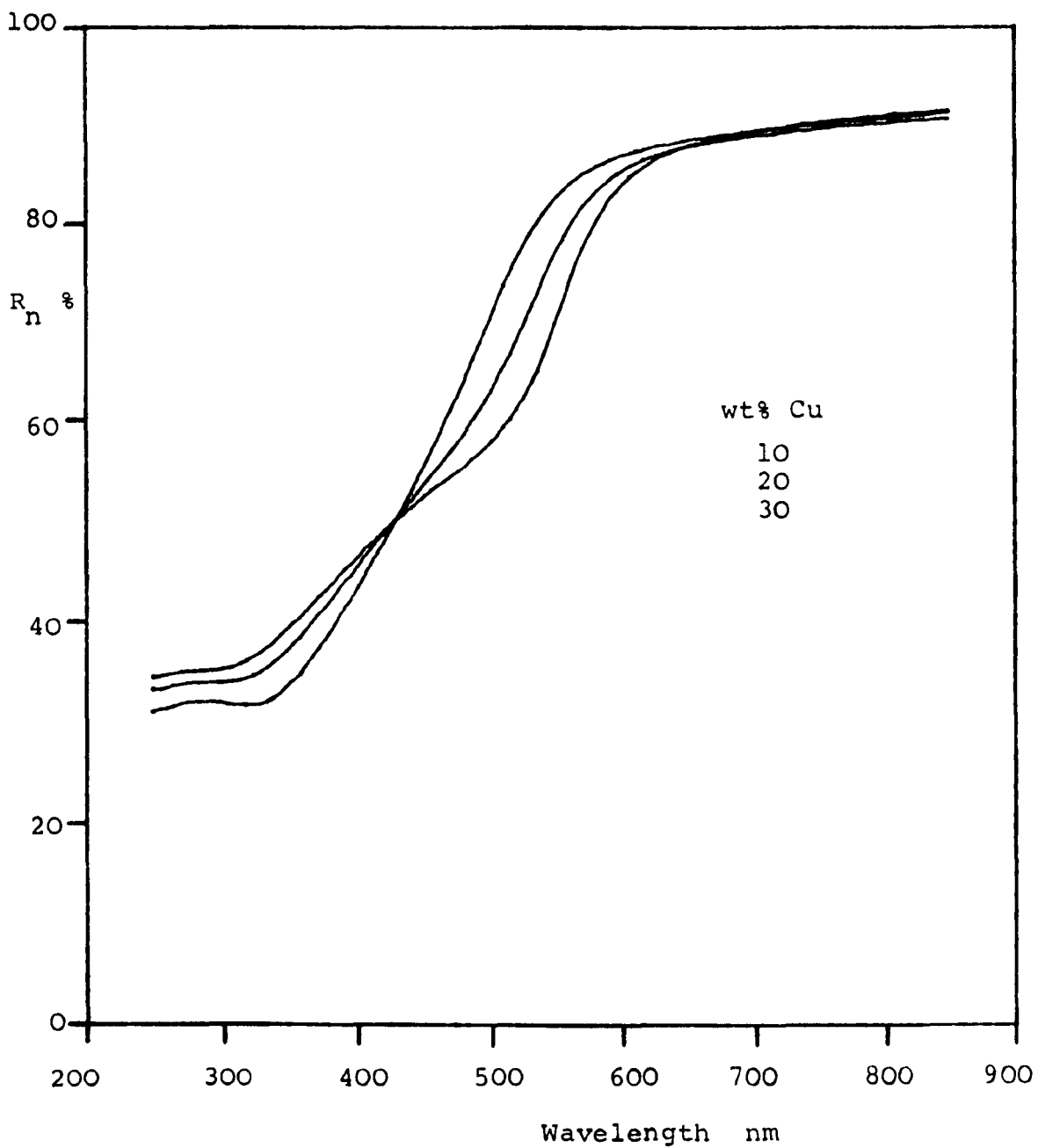


Figure 5.8 Normal reflectance spectra of 60 wt% Au alloys.

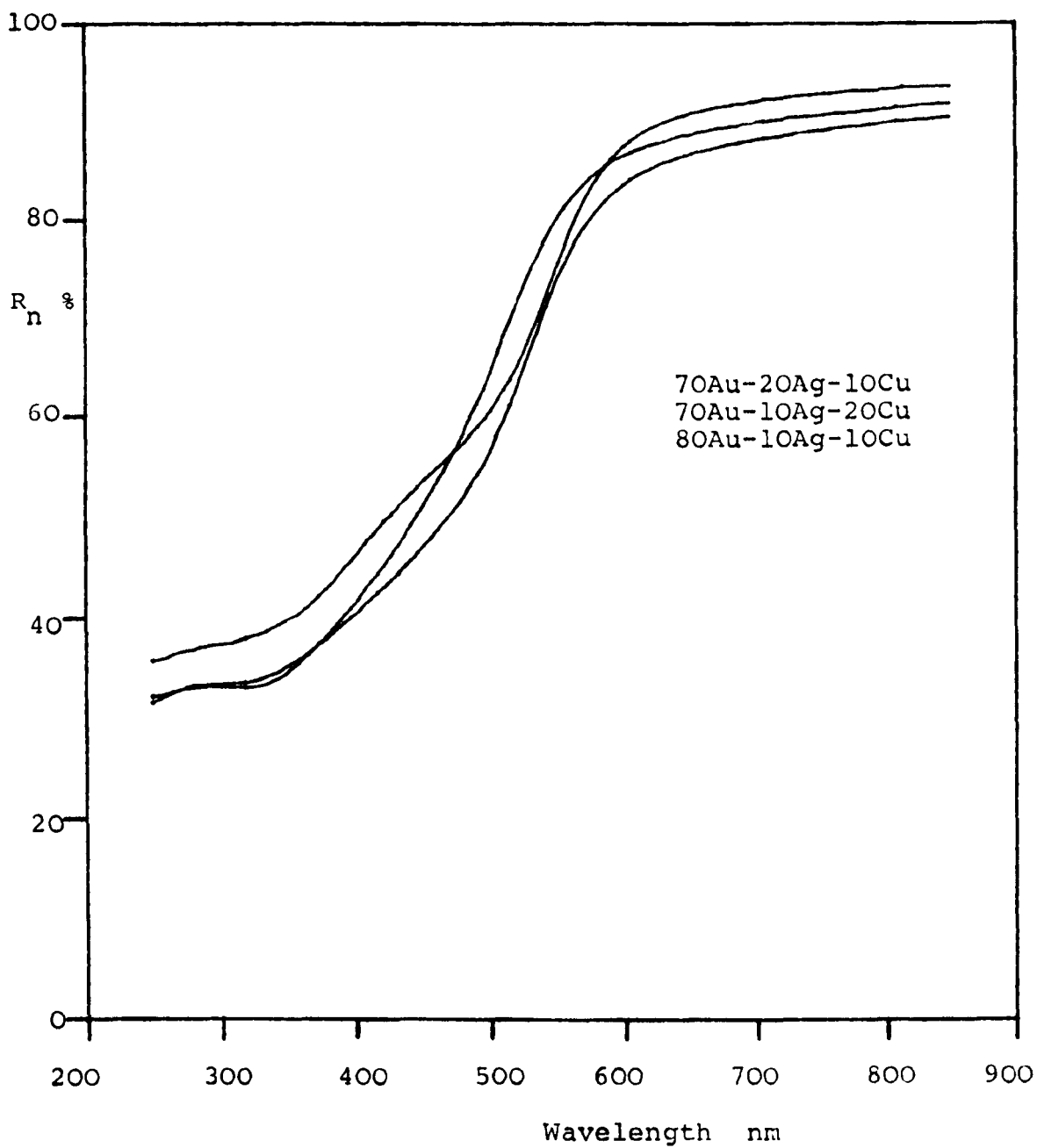


Figure 5.9 Normal reflectance spectra of alloys
70Au-20Ag-10Cu, 70Au-10Ag-20Cu &
80Au-10Ag-10Cu.

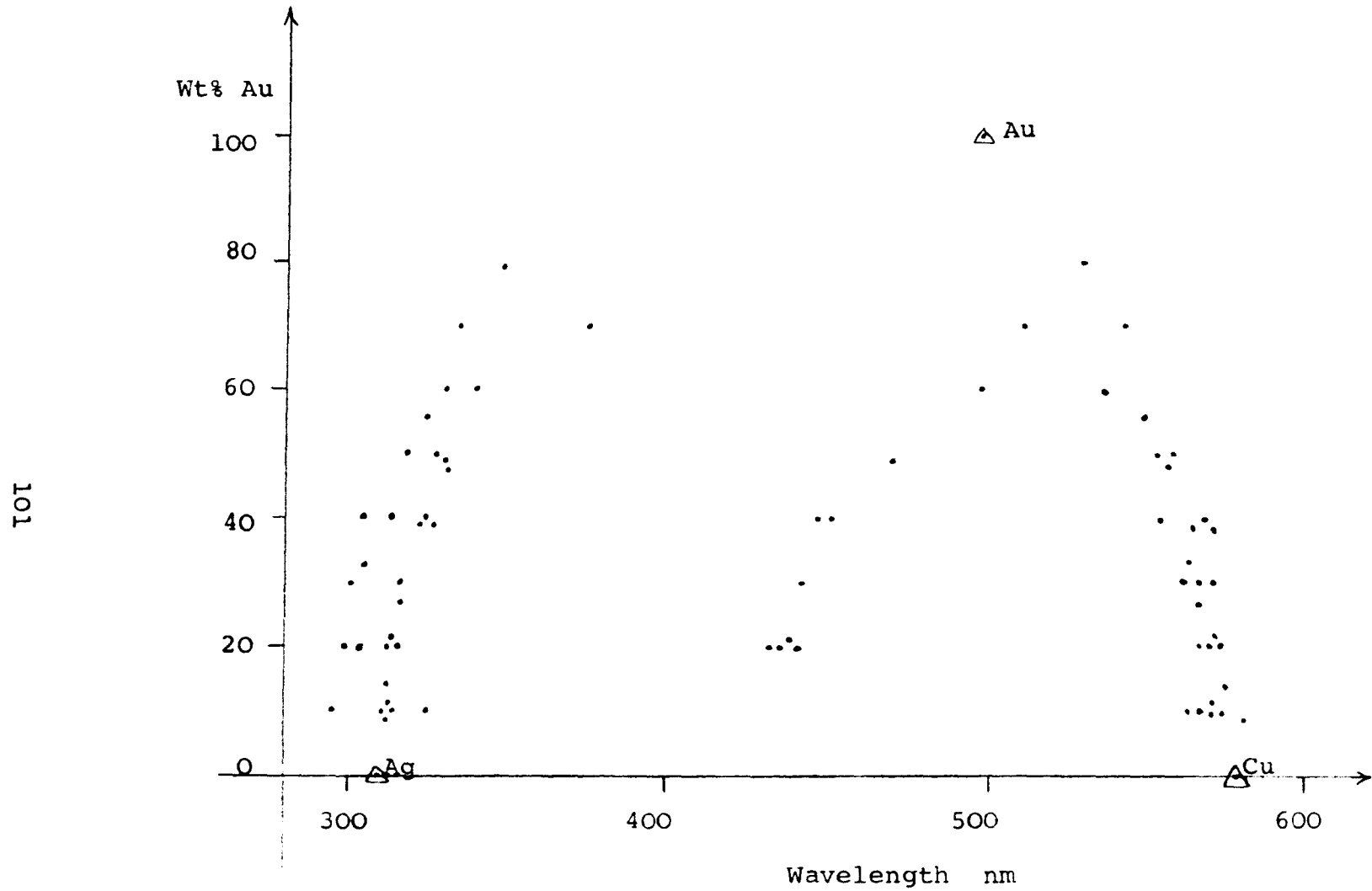


Figure 5.10 Wavelengths of absorption edges in the Au-Ag-Cu ternary system at an annealing temperature of 600 °C.

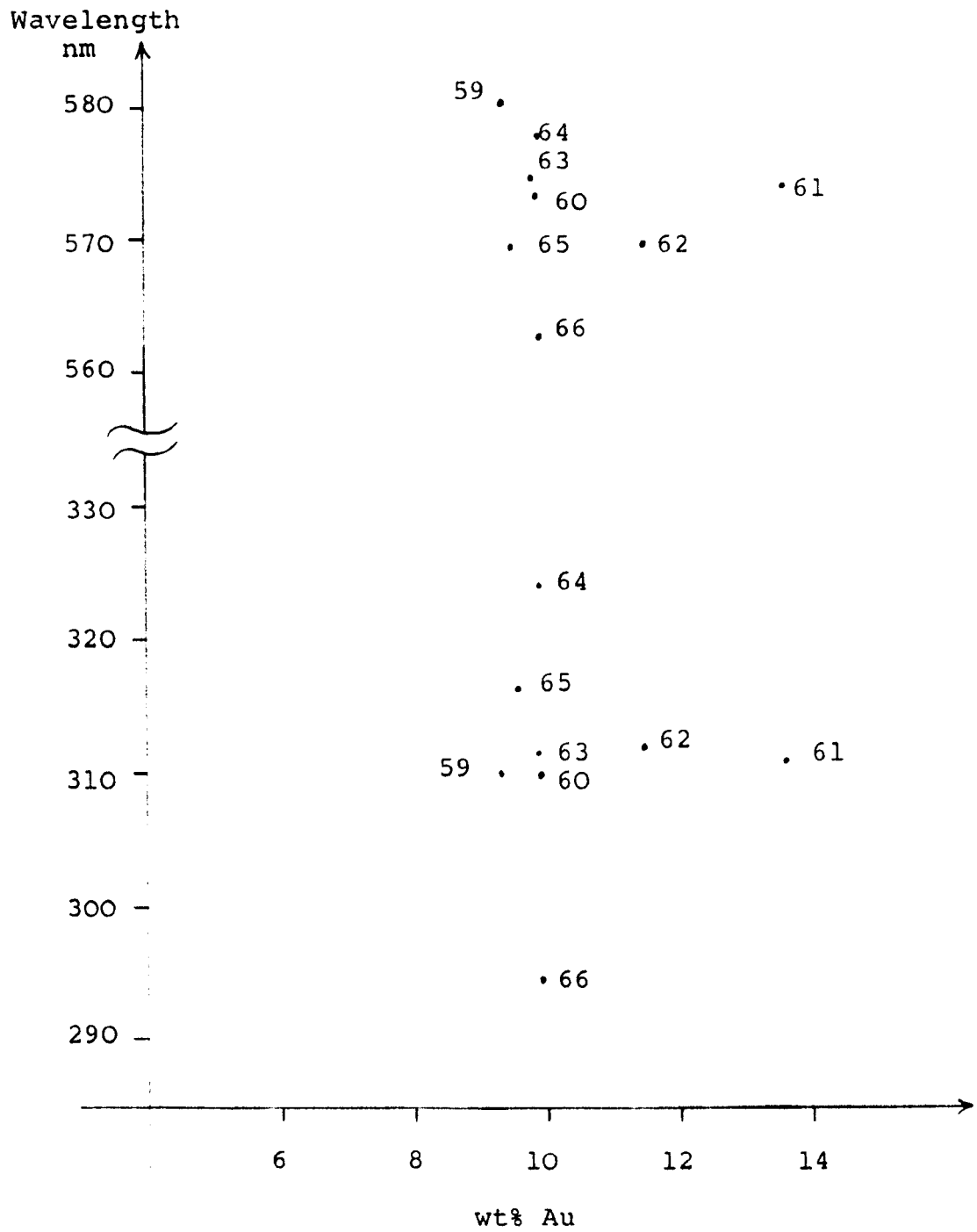


Figure 5.11 Absorption edge wavelengths of 10 wt% Au alloys.

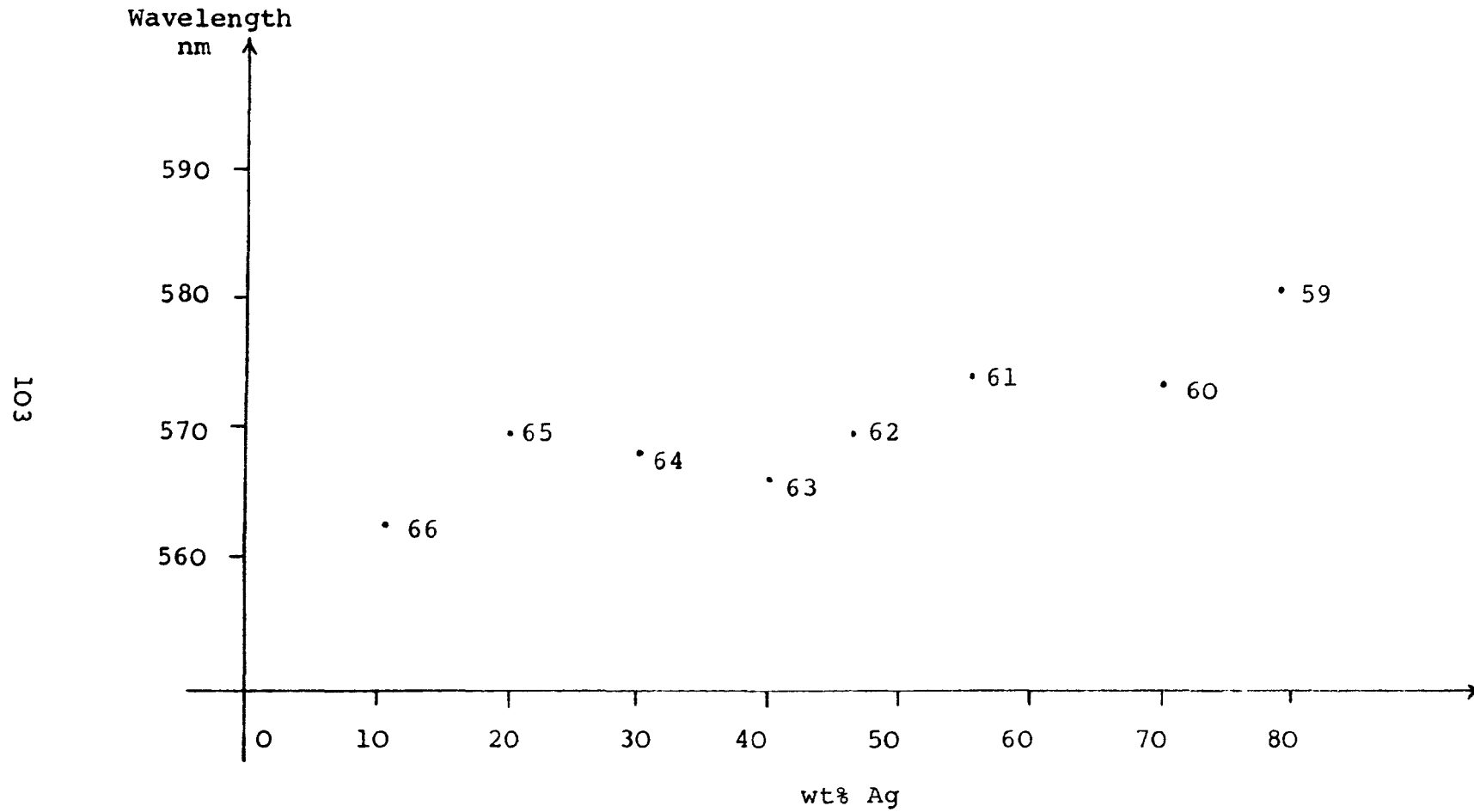


Figure 5.12 Absorption edge wavelengths of 10 wt% Au alloys.

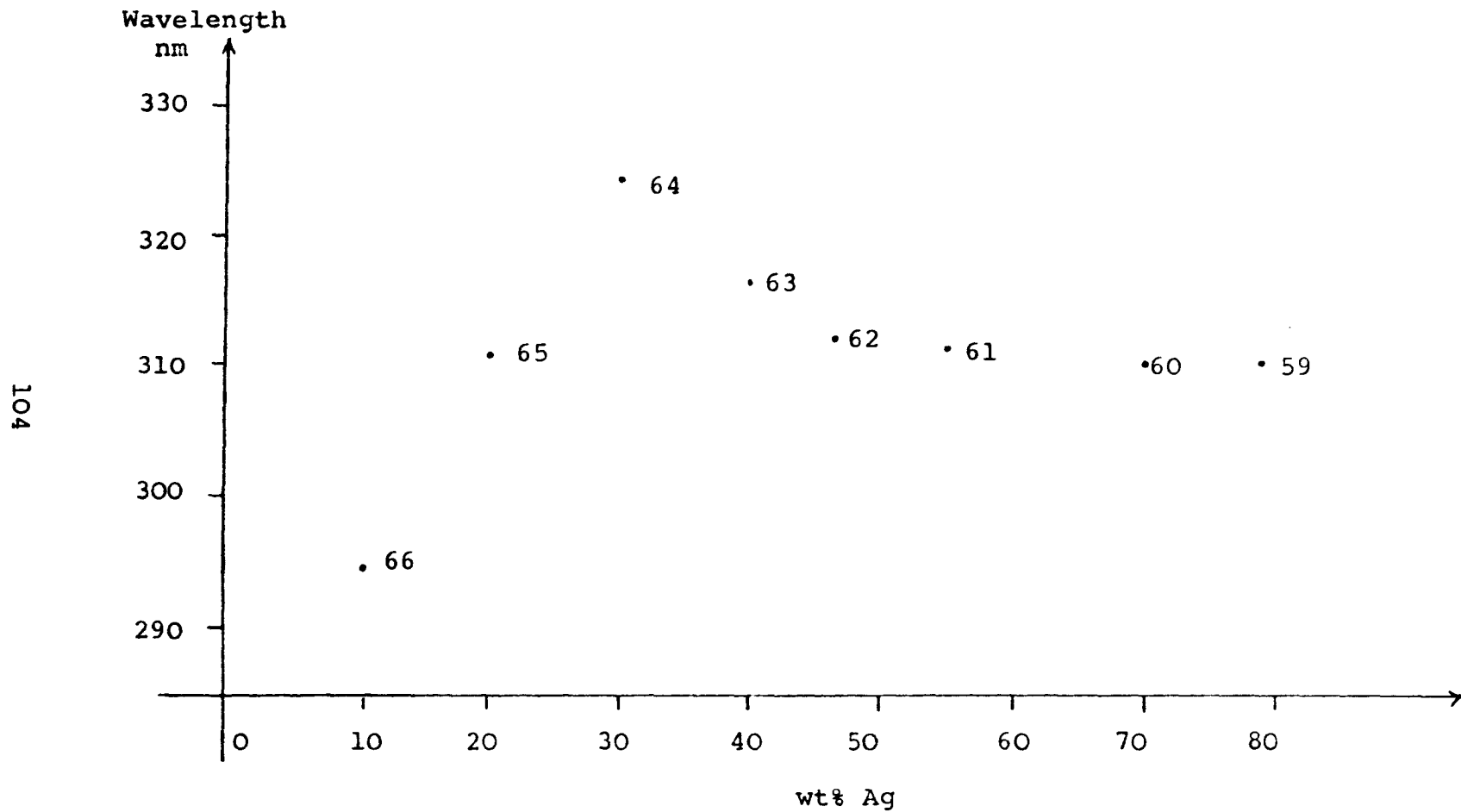


Figure 5.13 Absorption edge wavelengths of 10 wt% Au alloys.

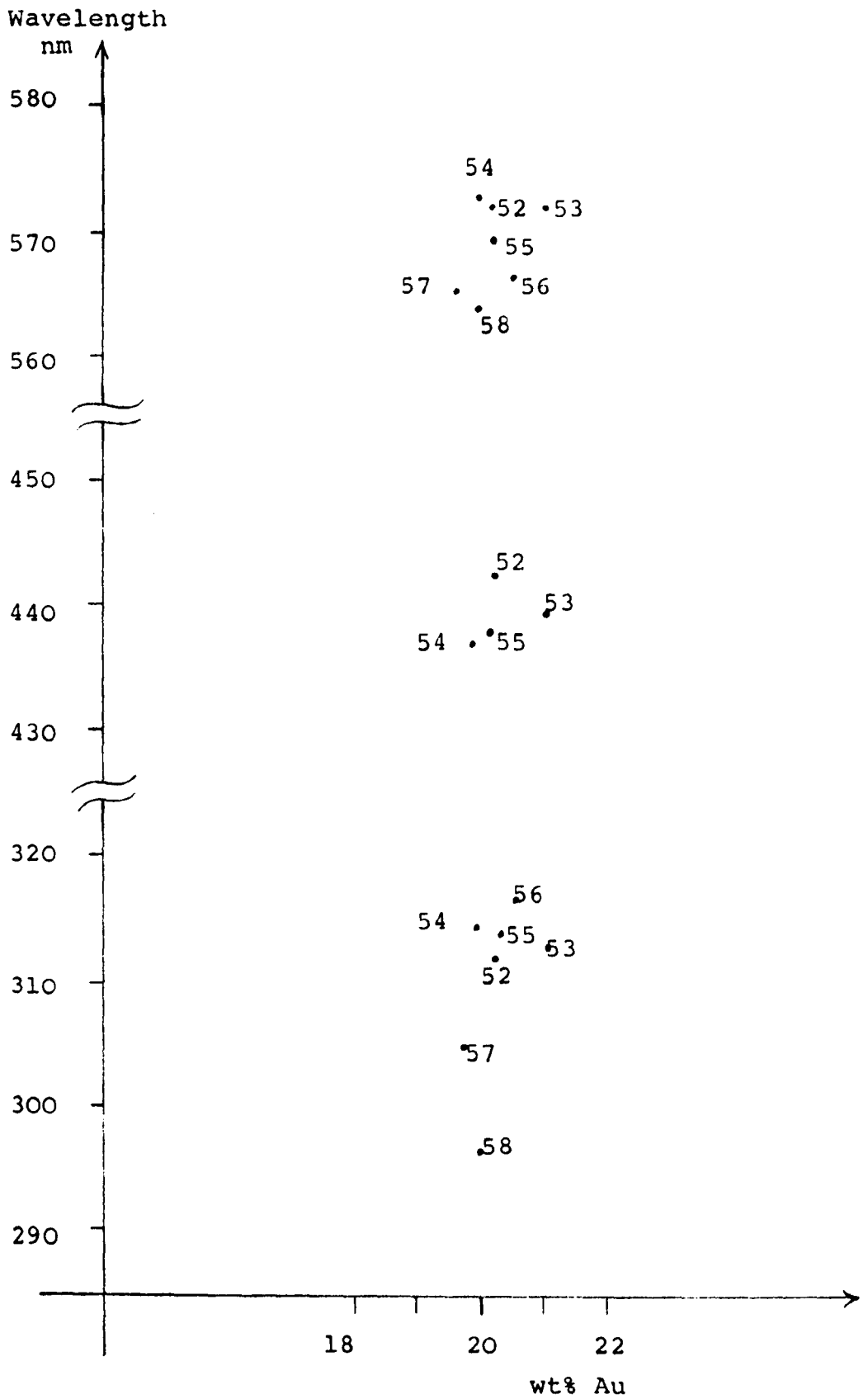


Figure 5.14 Absorption edge wavelength of 20 wt% Au alloys.

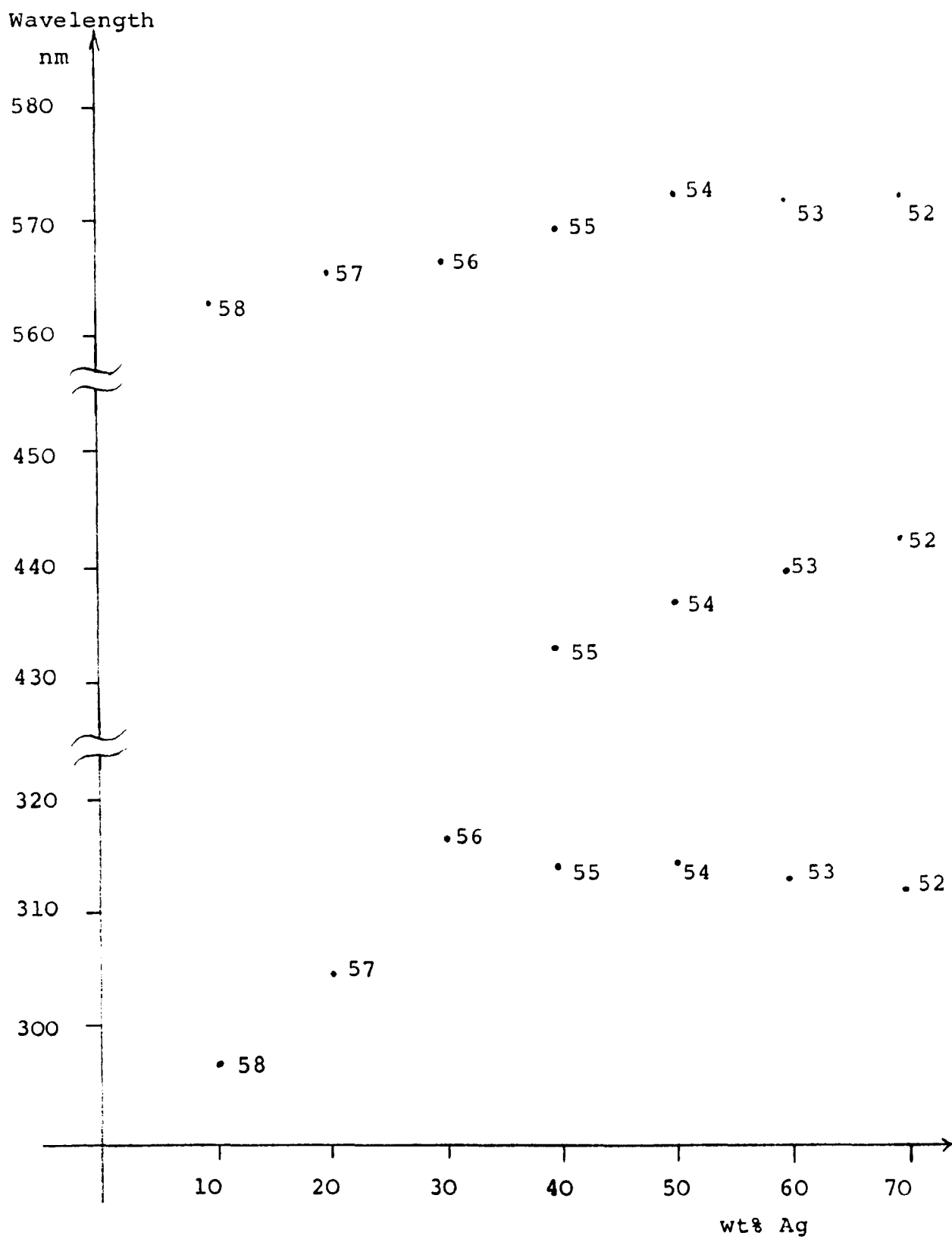


Figure 5.15 Absorption edge wavelength of 20 wt% Au alloys.
106

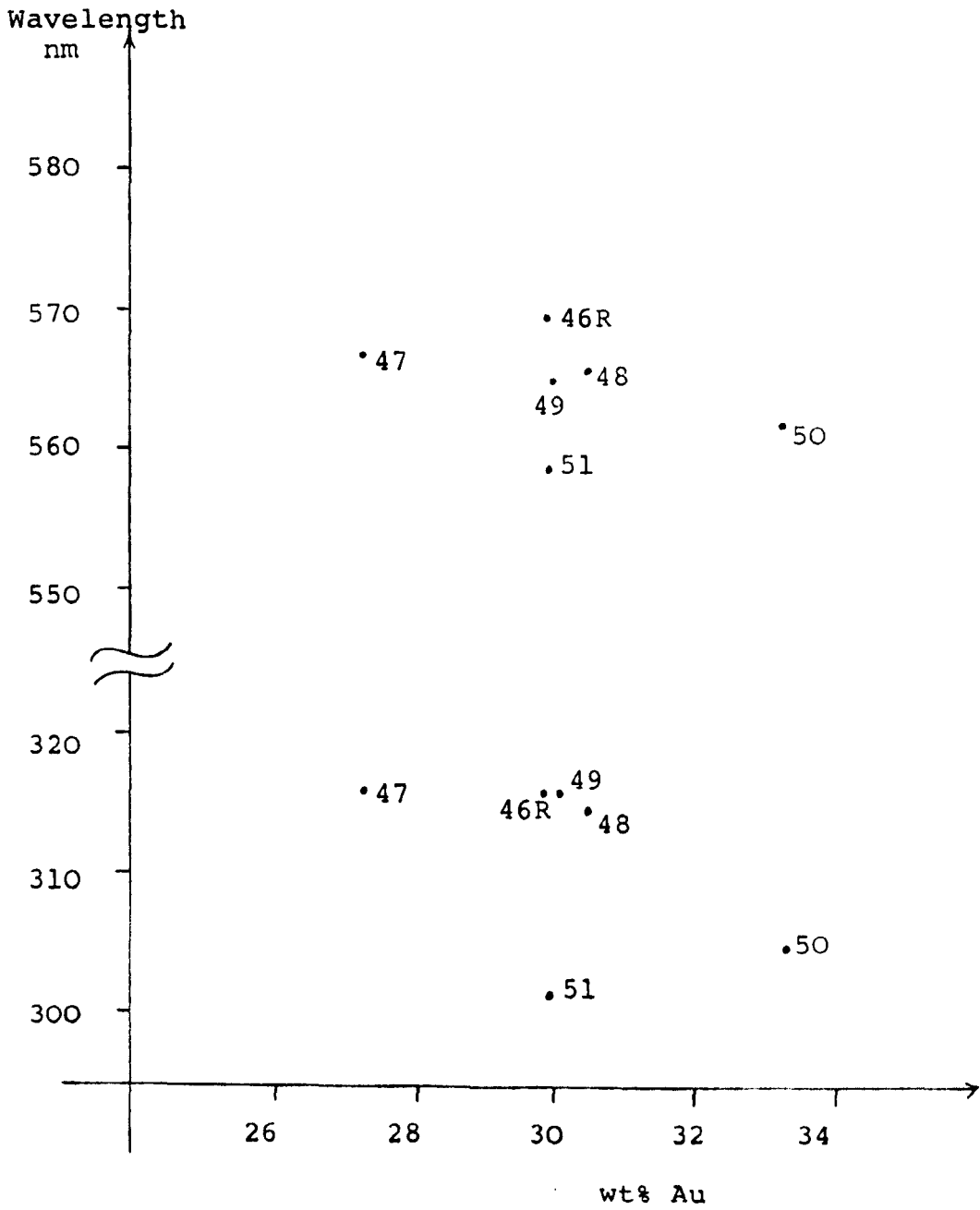


Figure 5.16 Absorption edge wavelengths of 30 wt% Au alloys.

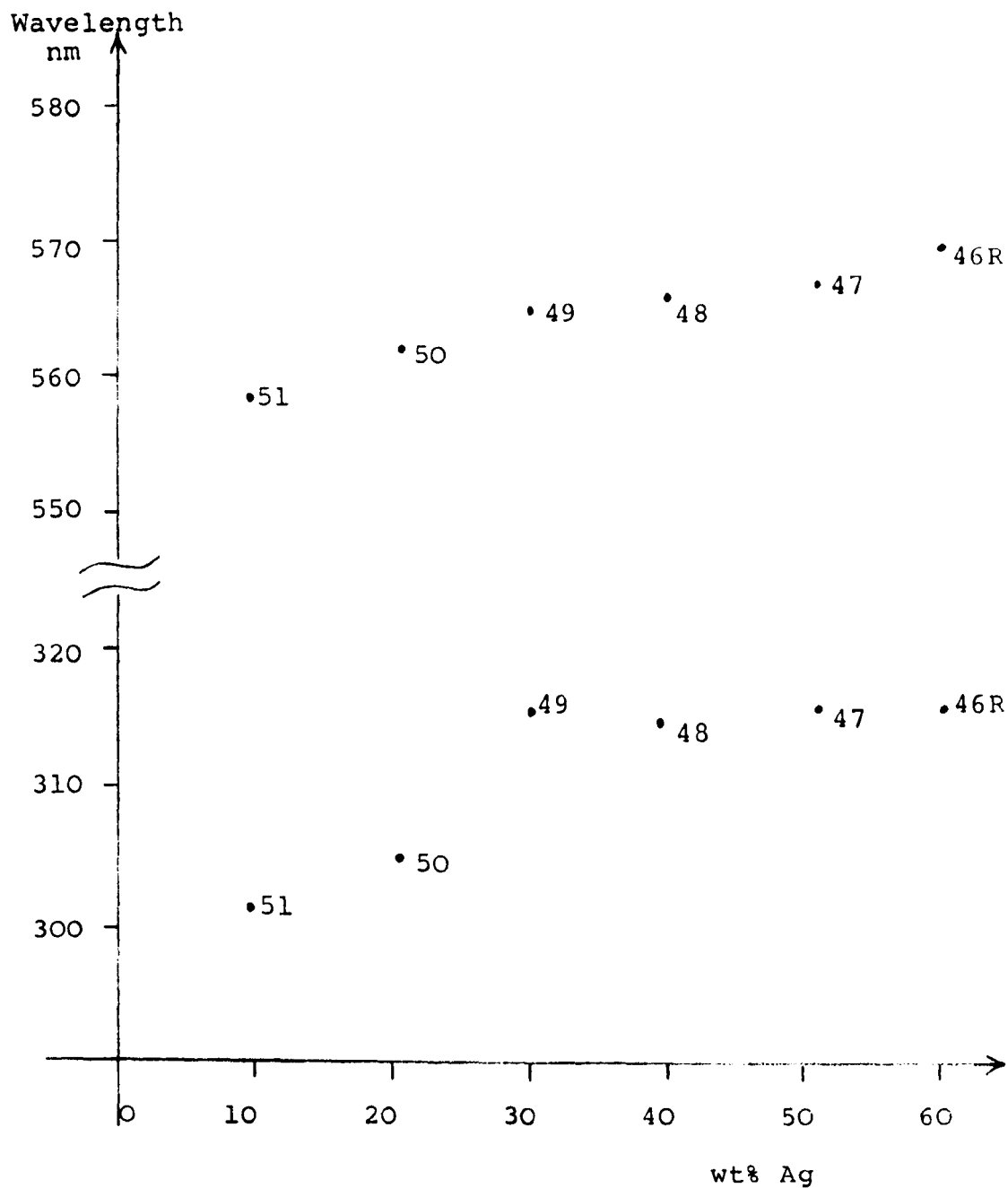


Figure 5.17 Absorption edge wavelength of 30 wt% Au alloys.

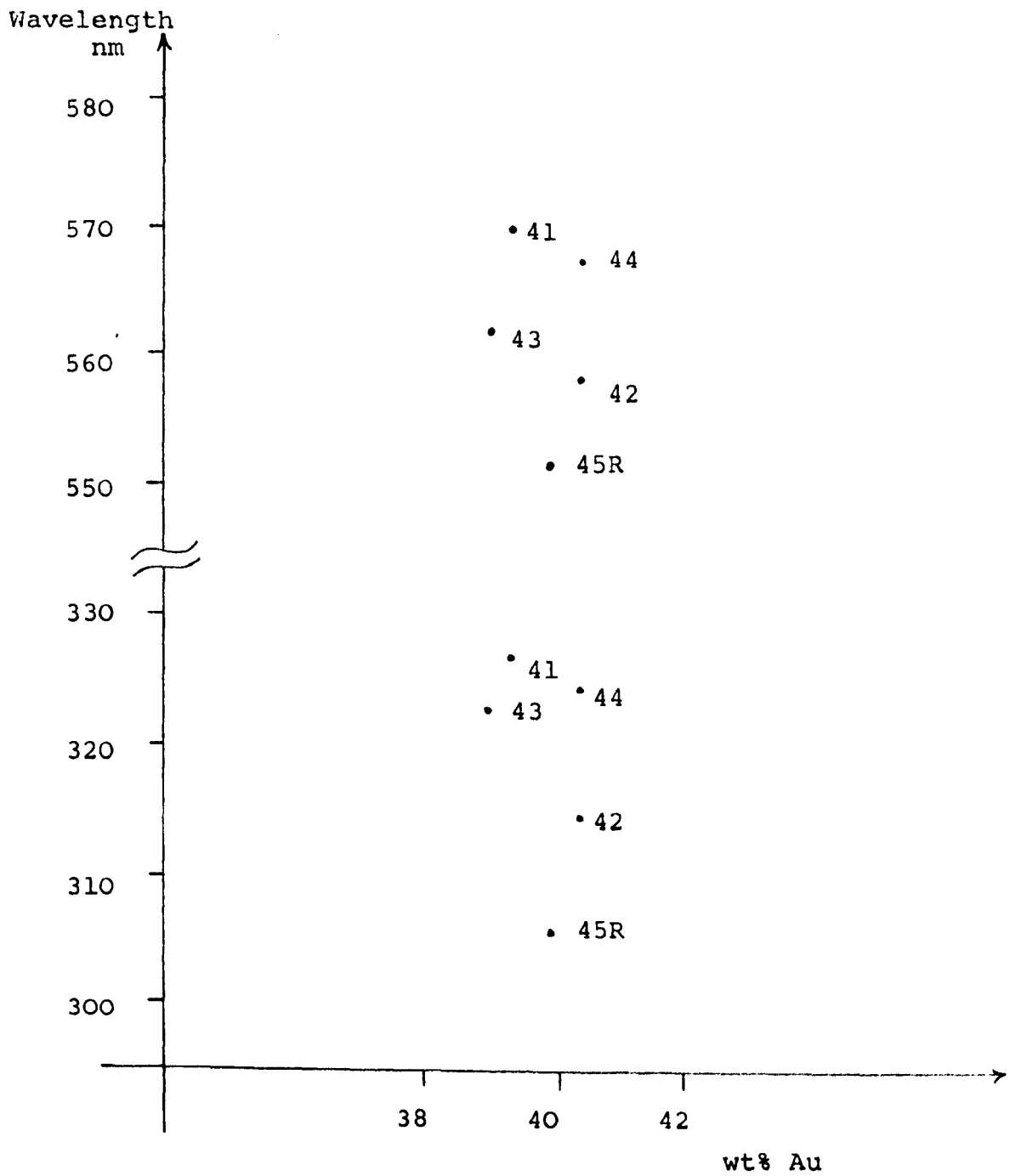


Figure 5.18 Absorption edge wavelength of 40 wt% Au alloys.

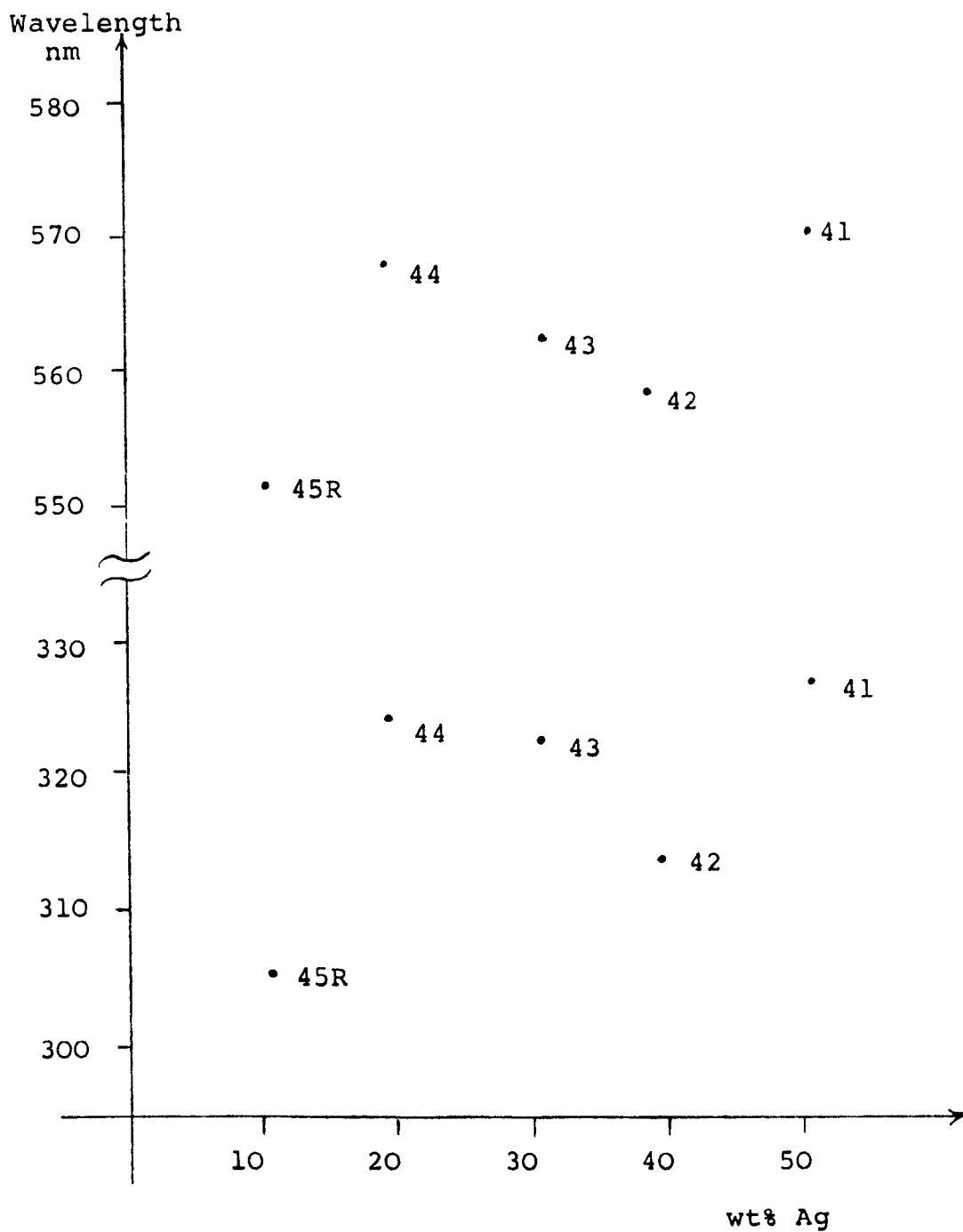


Figure 5.19 Absorption edge wavelength of 40 wt% Au alloys.

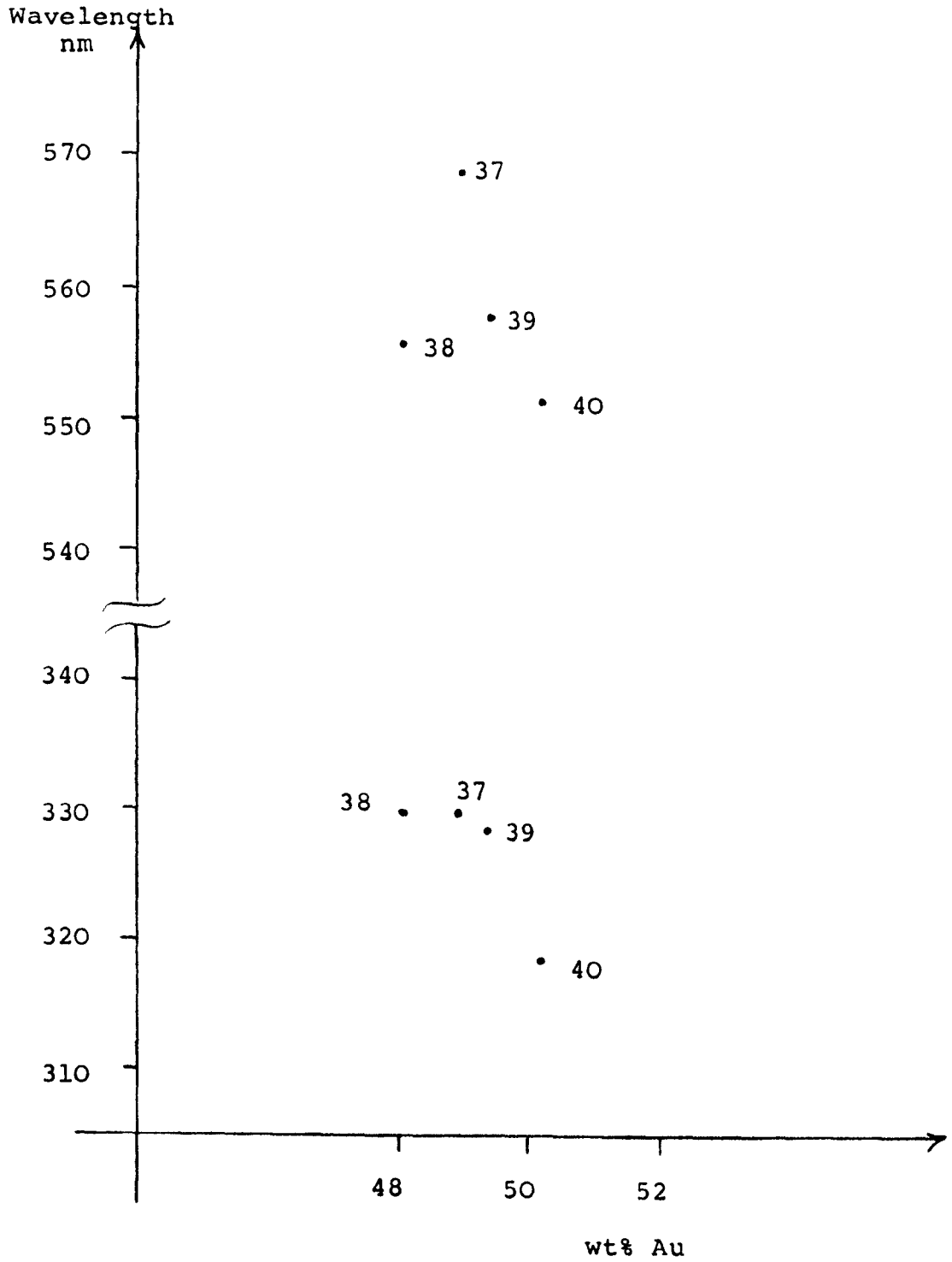


Figure 5.20 Absorption edge wavelength of 50 wt% Au alloys.

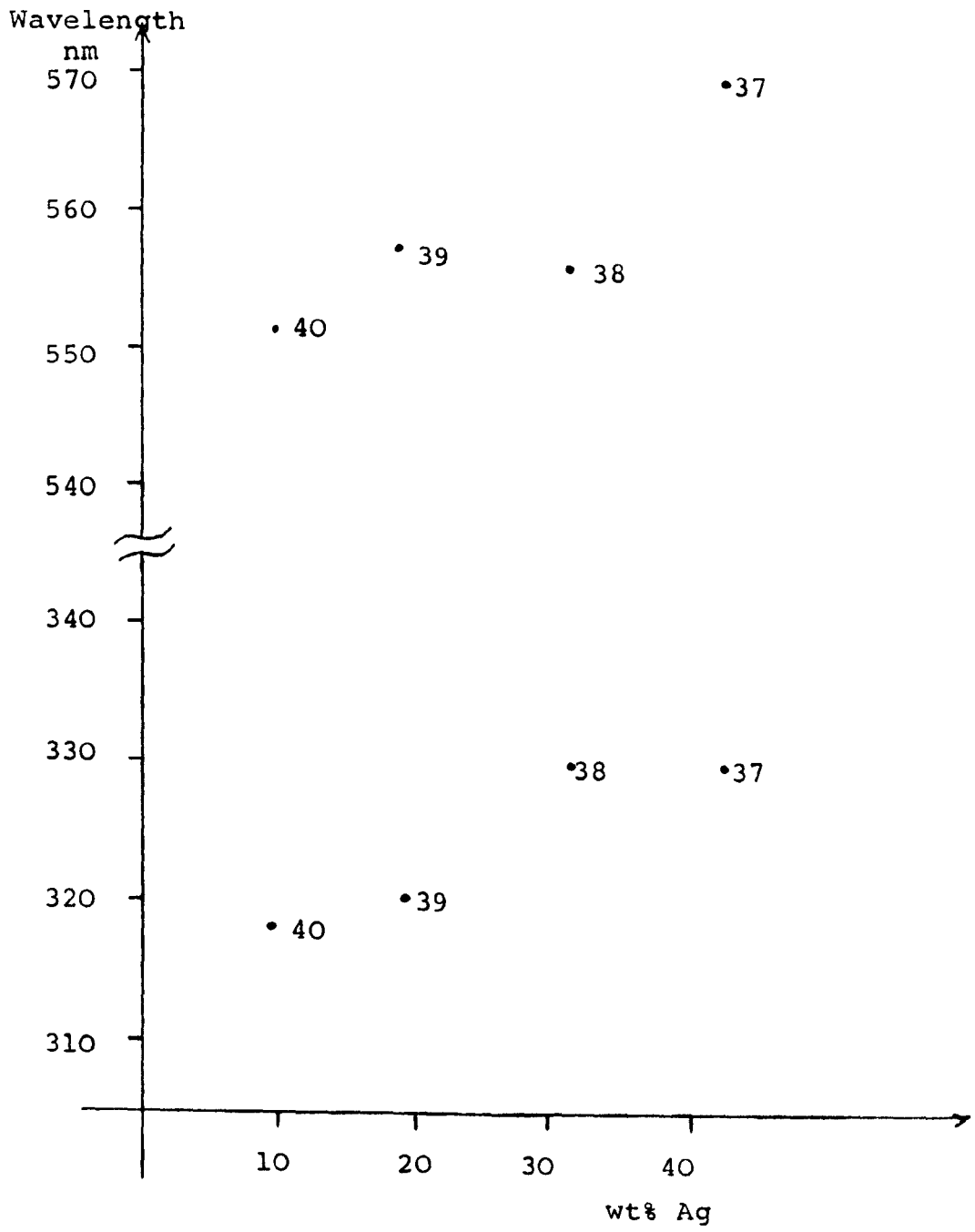


Figure 5.21 Absorption edge wavelength of 50 wt% Au alloys.

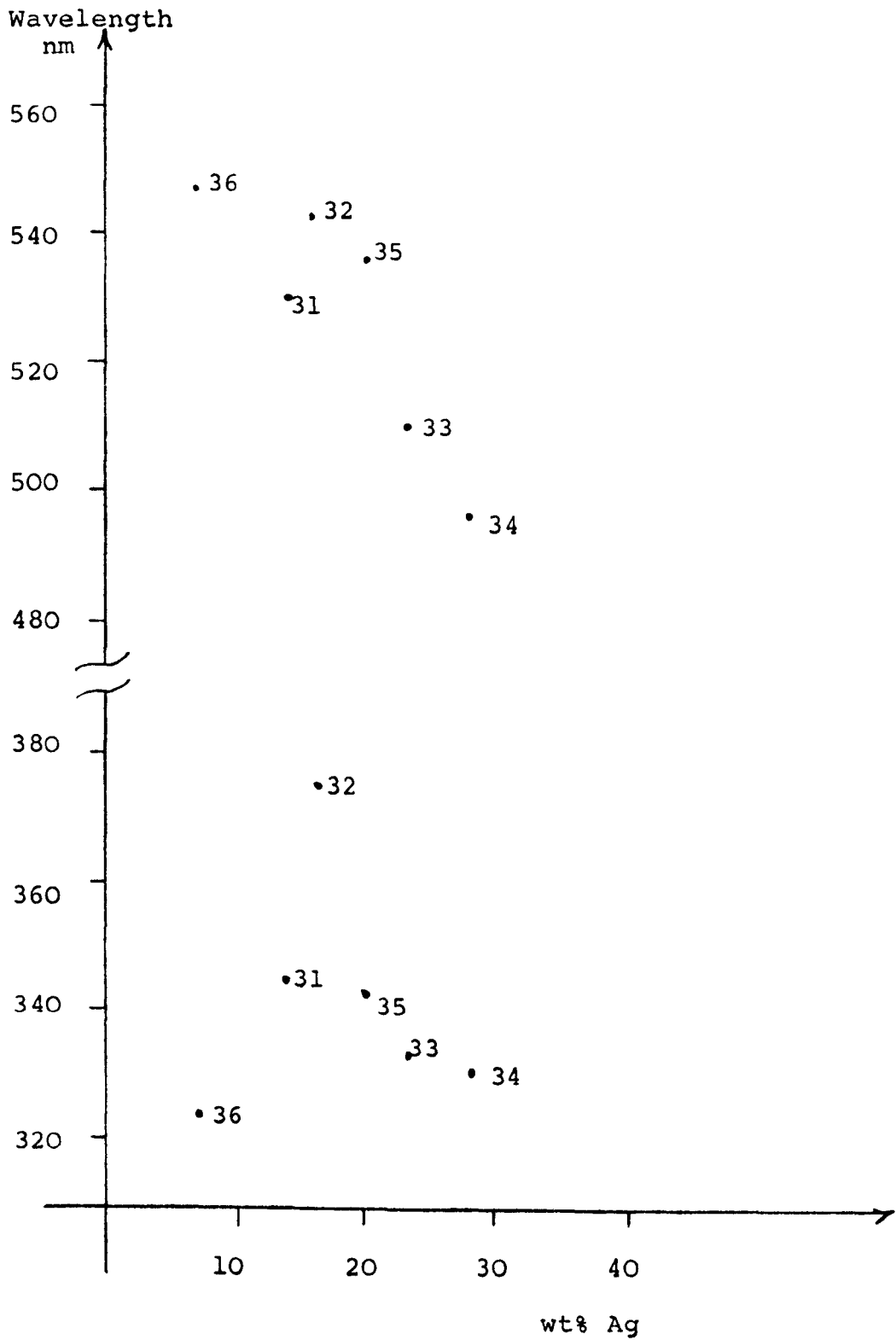


Figure 5.22 Absorption edge wavelength of
60, 70, & 80 wt% Au alloys.
(single phase)
113

Excess wavelength
shift nm

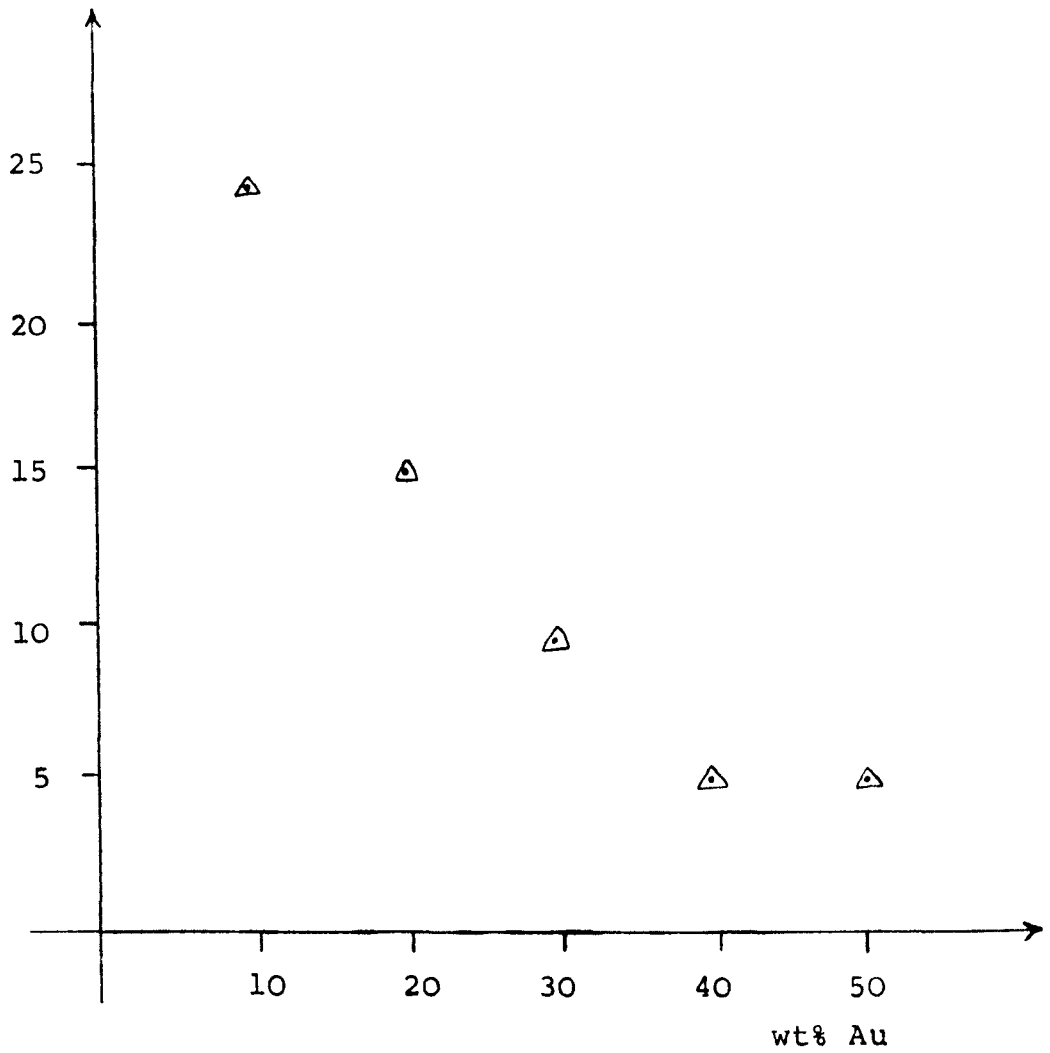


Figure 5.23 Excess shift in absorption wavelength of alloys with 30 wt% Ag.

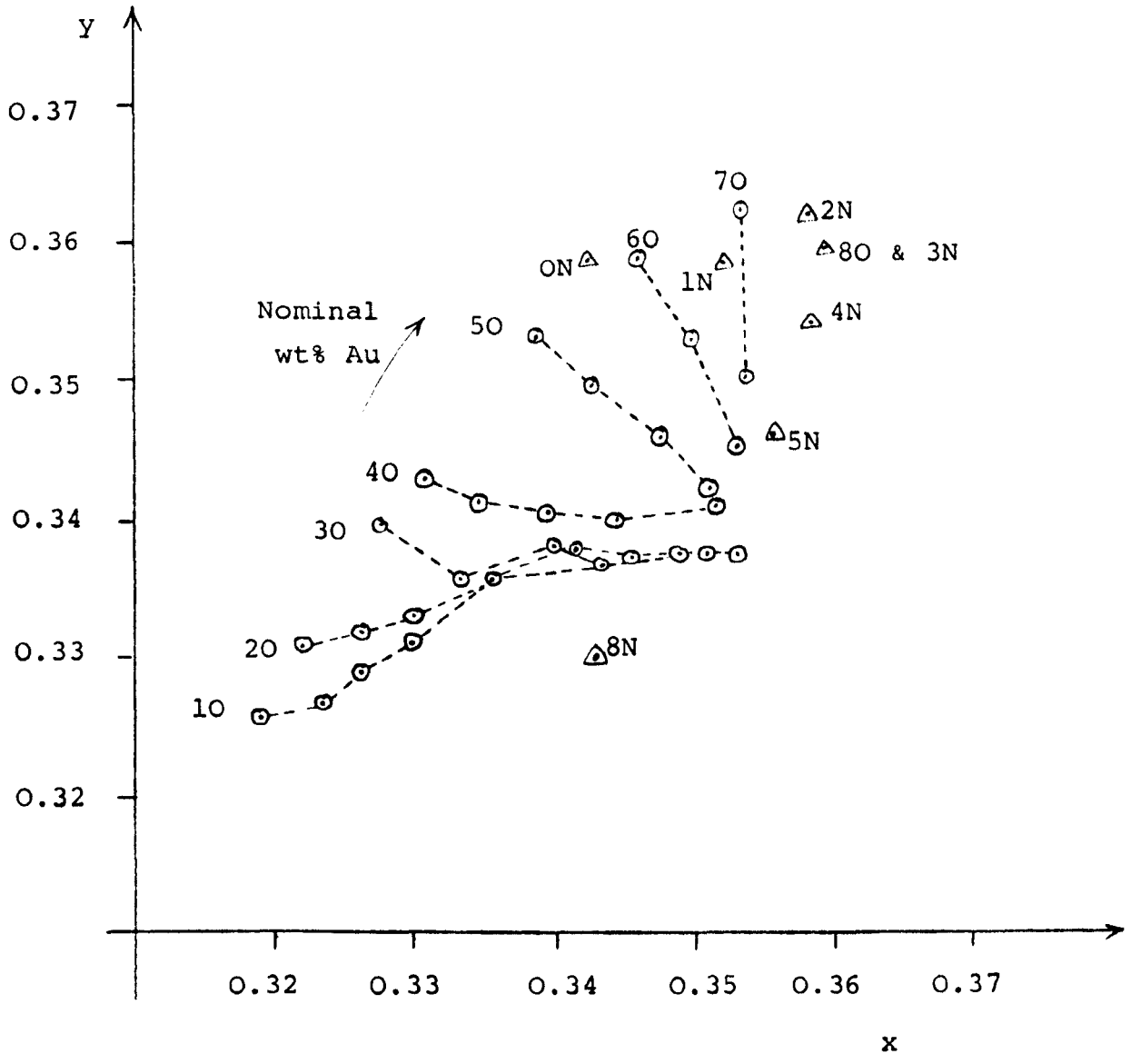


Figure 5.24 Colour diagram of all ternary Au-Ag-Cu and DIN8328 alloys under illuminant 'C'

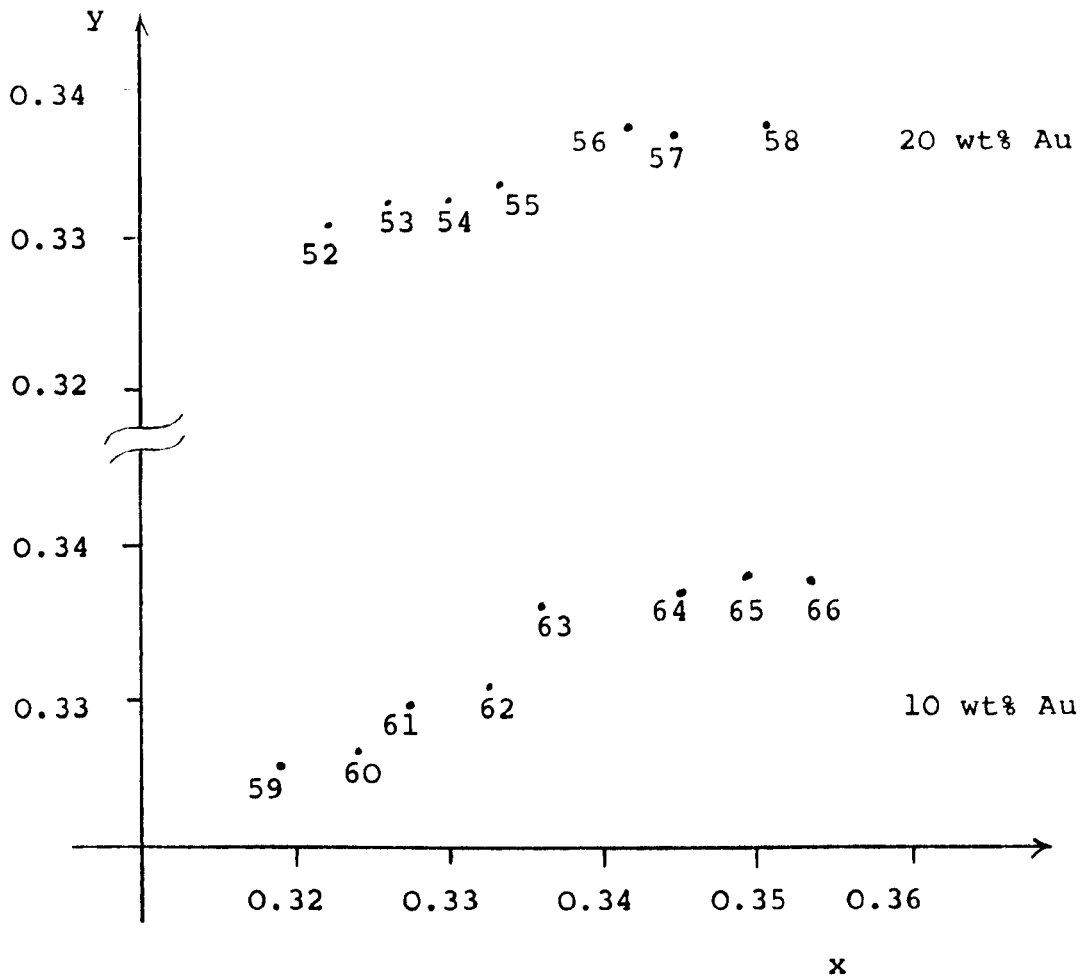


Figure 5.25 Colour diagram of 10 & 20 wt% Au alloys on an expanded scale.

| Sample Number | Absorption Wavelengths (nm) | | |
|------------------|----------------------------------|-------|-------|
| | | | |
| 31 | 345.9 | | 531.2 |
| 32 | 374.5 | | 543.0 |
| 33 | 334.4 | | 509.7 |
| 34 | 330.7 | | 497.2 |
| 35 | 342.6 | | 536.9 |
| 36 | 324.1 | | 547.9 |
| 37 | 330.0 | | 469.6 |
| 38 | 329.8 | | 556.2 |
| 39 | 328.4 | | 557.8 |
| 40 | 318.7 | | 551.7 |
| 41 | 326.8 | 451.5 | 570.5 |
| 42 | 314.3 | | 558.6 |
| 43 | 322.9 | | 562.5 |
| 44 | 324.7 | 446.9 | 568.0 |
| 45R | 305.5 | | 551.8 |
| 46R | 315.9 | 441.7 | 569.7 |
| 47 | 316.2 | | 567.2 |
| 48 | 314.9 | | 565.9 |
| 49 | 315.9 | | 564.9 |
| 50 | 305.1 | | 562.0 |
| 51 | 301.7 | | 558.5 |
| 52 | 312.2 | 442.5 | 572.0 |
| 53 | 313.2 | 439.3 | 572.2 |
| 54 | 314.5 | 436.9 | 572.6 |
| 55 | 313.8 | 433.0 | 569.6 |
| 56 | 316.5 | | 566.7 |
| 57 | 304.6 | | 565.6 |
| 58 | 296.7 | | 564.2 |
| 59 | 309.8 | | 580.7 |
| 60 | 310.2 | 573.4 | |
| 61 | 311.0 | | 573.9 |
| 62 | 312.2 | | 569.6 |
| 63 | 311.5 | | 566.2 |
| 64 | 324.2 | | 568.0 |
| 65 | 316.4 | | 569.4 |
| 66 | 294.6 | | 562.7 |

Table 5.1 Absorption Wavelengths of Au-Ag-Cu Alloys

| Wt% gold (nominal) | Edge λ (nm) | Alloying Shift nm / wt% Ag |
|-------------------------|--------------------------|-------------------------------|
| 10 | 570 | 0.26 |
| | 310 | 0.23 |
| 20 | 565 | 0.11 |
| | 440 | 0.30 |
| | 305 | 0.22 |
| 30 | 565 | 0.21 |
| | 310 | 0.29 |
| 40 | 560 | 0.46 |
| | 315 | 0.53 |
| 50 | 560 | 0.55 |
| | 325 | 0.35 |

Table 5.2 Nominal edge wavelengths and changes upon alloying.

| Sample Number | x | y | Sat. % | L % |
|---------------|--------|--------|--------|------|
| 31 | 0.3602 | 0.3595 | 25.1 | 72.6 |
| 32 | 0.3545 | 0.3495 | 20.9 | 75.4 |
| 33 | 0.3538 | 0.3619 | 24.0 | 78.2 |
| 34 | 0.3464 | 0.3591 | 21.3 | 81.0 |
| 35 | 0.3506 | 0.3528 | 20.7 | 76.2 |
| 36 | 0.3537 | 0.3451 | 19.5 | 71.5 |
| 37 | 0.3392 | 0.3529 | 17.7 | 82.6 |
| 38 | 0.3430 | 0.3495 | 17.8 | 80.5 |
| 39 | 0.3478 | 0.3462 | 18.2 | 76.9 |
| 40 | 0.3515 | 0.3418 | 18.0 | 72.1 |
| 41 | 0.3312 | 0.3432 | 12.9 | 85.2 |
| 42 | 0.3348 | 0.3410 | 13.3 | 83.5 |
| 43 | 0.3401 | 0.3406 | 14.6 | 79.3 |
| 44 | 0.3447 | 0.3402 | 15.7 | 76.7 |
| 45R | 0.3519 | 0.3411 | 17.9 | 72.3 |
| 46R | 0.3276 | 0.3401 | 11.1 | 90.3 |
| 47 | 0.3293 | 0.3352 | 10.3 | 84.8 |
| 48 | 0.3334 | 0.3353 | 11.4 | 82.9 |
| 49 | 0.3404 | 0.3378 | 13.9 | 78.0 |
| 50 | 0.3466 | 0.3381 | 15.7 | 74.5 |
| 51 | 0.3497 | 0.3378 | 16.3 | 73.1 |
| 52 | 0.3224 | 0.3310 | 7.3 | 86.8 |
| 53 | 0.3265 | 0.3327 | 8.9 | 85.5 |
| 54 | 0.3306 | 0.3331 | 10.1 | 83.6 |
| 55 | 0.3336 | 0.3338 | 11.0 | 82.5 |
| 56 | 0.3419 | 0.3375 | 14.3 | 76.0 |
| 57 | 0.3452 | 0.3364 | 14.9 | 76.1 |
| 58 | 0.3511 | 0.3374 | 16.7 | 72.6 |
| 59 | 0.3184 | 0.3254 | 4.7 | 87.8 |
| 60 | 0.3231 | 0.3268 | 6.4 | 86.7 |
| 61 | 0.3271 | 0.3290 | 8.0 | 85.2 |
| 62 | 0.3325 | 0.3311 | 10.0 | 81.1 |
| 63 | 0.3360 | 0.3349 | 12.0 | 79.8 |
| 64 | 0.3437 | 0.3366 | 14.5 | 75.0 |
| 65 | 0.3488 | 0.3376 | 16.1 | 72.1 |
| 66 | 0.3536 | 0.3376 | 17.4 | 71.8 |

Table 5.3 L-x-y colour co-ordinates under illuminant 'C' of the Au-Ag-Cu ternary alloys.

| Sample Number | x | y | L % |
|---------------|--------|--------|------|
| 0N | 0.3431 | 0.3590 | 83.2 |
| 1N | 0.3524 | 0.3590 | 80.5 |
| 2N | 0.3586 | 0.3627 | 76.9 |
| 3N | 0.3597 | 0.3597 | 76.2 |
| 4N | 0.3590 | 0.3546 | 75.8 |
| 5N | 0.3557 | 0.3466 | 73.7 |
| 8N | 0.3241 | 0.3303 | 68.4 |

Table 5.3 Contd.

L-x-y colour co-ordinates under illuminant 'C' of the DIN8328 alloys.

| Sample Number | Gold | Silver | Copper | Nickel | Zinc |
|---------------|------|--------|--------|--------|------|
| 0N | 58.5 | 34.0 | 7.5 | - | - |
| 1N | 58.5 | 26.5 | 15.0 | - | - |
| 2N | 75.0 | 16.0 | 9.0 | - | - |
| 3N | 75.0 | 12.5 | 12.5 | - | - |
| 4N | 75.0 | 9.0 | 16.0 | - | - |
| 5N | 75.0 | 4.5 | 20.5 | - | - |
| 8N | 59.0 | - | 22.0 | 12.0 | 7.0 |

Table 5.4 Composition in wt% of the DIN8328 alloys.

| Sample Number | Ellipsometry | | | Normal Reflectometer | | |
|---------------|--------------|--------|------|----------------------|-------|-----|
| | x | y | L % | x | y | L % |
| 0N | 0.3447 | 0.3705 | 83.1 | 0.339 | 0.367 | 90 |
| 1N | 0.3542 | 0.3702 | 80.4 | 0.352 | 0.370 | 82 |
| 2N | 0.3603 | 0.3736 | 76.8 | 0.359 | 0.377 | 82 |
| 3N | 0.3615 | 0.3706 | 76.1 | 0.360 | 0.373 | 79 |
| 4N | 0.3610 | 0.3654 | 75.6 | 0.360 | 0.366 | 76 |
| 5N | 0.3580 | 0.3575 | 73.5 | 0.360 | 0.361 | 74 |
| 8N | 0.3204 | 0.3425 | 68.4 | - | - | - |

Table 5.5 Colour co-ordinates of the DIN8328 alloys under illuminant 'D' by ellipsometry and normal reflectometry. Normal reflectance data by permission of the Worshipful Company of Goldsmiths.

CHAPTER SIX

DISCUSSION

6.1 Introduction

Colorimetry can be divided into the two sections of physical and visual colorimetry. The former is a definition of colour space and allows a description of colour which is independent of the particular observer. Although the properties of a 'standard' observer are used, they are tabulated and thus allow any laboratory to derive colour co-ordinates in a consistent way. A description of colour is thus possible on a basis which in principle will permit all laboratories to attribute the same colour co-ordinates to a particular coloured sample. The use of an ellipsometer as a physical colorimeter had not been reported before this work was undertaken; its use does have several potential advantages. Firstly that the calibration of an ellipsometer is in terms of determining azimuth angles to a high precision at a known working wavelength, both of these requirements are readily fulfilled by a well established technology. Secondly, the ellipsometer does not rely upon a reference surface, it measures the optical properties of the sample directly and not by comparison. Thirdly, it does not require that the optical detector is a linear device. Finally, the ellipsometer is relatively insensitive to light which is scattered out of the field of view, the principal effect is a reduction in the signal to noise ratio and not a change in the nulling azimuth. In the light of these advantages the Worshipful Company of Goldsmiths sponsored the colorimetric

examination of the Au-Ag-Cu system by a nulling ellipsometer.

The optical properties of the Au-Ag-Cu systems are governed by the proportion of the individual elements and by the manner in which they combine to form the ternary system. Individually each element has a face centred cubic crystalline structure and is a Group I element. When alloyed, however, the three elements display distinct and varied solubility characteristics, Norton and M^CMullon (1949).

A mechanism to explain this structure has been proposed by Rivory (1977) based on the overlapping of the atomic d-bands. The mutual affinity of the elements is proposed to depend proportionally on the d-band overlap. Thus for an Ag-Cu alloy the solubility is predicted to be small (little d-band overlap), while for both Au-Cu and Au-Ag the solubility is very great (large d-band overlap). The known phase structure supports this model. The Ag-Cu solubility is limited at an equilibrium temperature of 600 C to a few percent while both Au-Cu and Au-Ag exhibit complete solubility. The d-band mixing is important not only for the physical structure of the alloys but also because the principal absorption edges which govern the colour of each element are due to d-band transition, Fukatani (1971), Erlbach (1969 a & b), Rivory (1969, 1977), Hollstein (1977) and Nielsen (1974). The wavelengths of these

absorption edges and the particular atomic transitions are given in table 6.1. The binary Ag-Au and Au-Cu alloys show complete solubility and the normal reflectance spectra and absorption edge wavelengths are a continuous locus between the extremes of the component elements, Clarke (1980), Rivory (1976). In the case of the duplex phase alloys in the Au-Ag-Cu system it is necessary to re-examine the phase diagram in order to predict the alloys behaviour. Consider the equilibrium phase diagram in figure 6.1 of a duplex phase system. The alloy system consists of three regions, the single-phase α and β phases, each consisting of a region where the elemental components have complete miscibility and the duplex phase region where both α and β phases exist together. The phase composition of the alloy system for a given temperature is derived from the phase diagram by taking a section through the diagram at the equilibrium temperature, T . All possible compositional and phase structures are represented by points on the straight line CD. In the case of the single phase alloys these are represented by the line segments CP and RD. While the duplex region is PR. The duplex phase region contains an important symmetry, which is that all of the possible alloys represented by points on the line PR are composed of the same α and β phases in different proportions. Consider the point Q in figure 6.1. The proportion of α to β phase is given by the lever rule as QR: PQ. As the point Q moves to the left then the α phase proportion increases, until at P

the alloy is entirely α phase. Similarly, if Q moves to the right the β phase proportion will increase until at R the alloy is entirely β phase. The colorimetry of such a duplex phase region can now be derived from the phase structure and Graussmanns' Third Law of Colorimetry.

Both the α and β phase alloys will have a colour locus with composition shown in figure 6.2; this locus may be linear or not. However, once a duplex phase alloy is considered then the form of the locus can be predicted. The duplex phase region contains only two different phases in a range of varying proportions; thus the colour locus of such a mixture in the L-x-y convention will be a straight line, PR in figure 6.2.

The principal colorimetric property of the duplex phase region is thus expected to be a linear colour locus, which in the Au-Ag-Cu system will be when alloys of a constant weight % of gold are considered.

The observed behaviour of the alloys clearly does not agree with this prediction. Firstly, the colour loci are distinctly curved towards greater saturation relative to linear mixing. Secondly, the absorption edge positions show a dependence upon silver content; this is shown clearly in figure 5.10. These deviations may be due to two causes. Firstly, that there is some 'averaging' process involved at the atomic level between the two phases or secondly, that the observed deviations are an instrumental artifact.

6.2 Comparison with published data

Several authors have published colorimetric data on the Au-Ag-Cu ternary system against which a comparison is possible. They are German et al (1980), Starenko (1974) and a private communication from the Worshipful Company of Goldsmiths of colour co-ordinates derived via a normal spectro-reflectometer. Additionally a limited comparison is possible with Clarke (1980) who examined the Ag-Cu, Cu-Au and Au-Ag binary systems.

German et al (1980) examined a small (unstated) number of alloys with the same equilibrium temperature and compositions to alloys used in this study with a spectrophotometer. Their results are presented in the CIE L*a*b system of co-ordinates, Kuchni (1976). The L*a*b system is intended as a uniform colour space in which perceived colour differences are quantitatively represented by comparable co-ordinate differences. The transformation between tristimulus co-ordinates XYZ and L*a*b co-ordinates is;

$$L = 116 \left[(Y/Y_0)^{1/3} \right] - 16$$

$$a = 500 \left[(X/X_0)^{1/3} - (Y/Y_0)^{1/3} \right]$$

$$b = 200 \left[(Y/Y_0)^{1/3} - (Z/Z_0)^{1/3} \right]$$

X,Y,Z - tristimulus co-ordinates of colour

X₀, Y₀, Z₀ - tristimulus co-ordinates of illumination

Colour differences are characterised by the parameter

ΔE where

$$\Delta E = (\Delta L^2 + \Delta a^2 + \Delta b^2)^{\frac{1}{2}}$$

ΔL , Δa , Δb - incremental differences in L*a*b co-ordinates

It is apparent that the transformation between these two sets of co-ordinate systems is non-linear and that deviation from linear colour mixing is difficult to detect.

The German data is presented as a series of loci in the co-ordinates L, a and b as a function of both atomic and weight percentage. They do not distinguish between their own data and this work, Roberts (1980). When constructing the loci comparison is thus limited to their statement that 'where alloy compositions that had been investigated by Roberts and Clarke were restudied in the present work, the results agreed to within these ranges of error' (± 0.8 in L, ± 0.2 in a and ± 0.5 in b). This measure of uncertainty in colour co-ordinates is insufficient to show the observed deviation from linear colour mixing.

An independent measurement of the Au-Ag-Cu system colorimetry has been performed by Starenko (1974) by an ellipsometric method. The colorimetric data is presented as a series of loci in the u v w uniform colour space. Sample preparation and equilibrium temperature are not reported. The loci are constructed as lines with constant atomic weight percentage. A direct comparison is possible if the colour co-ordinates in this study are transformed

into the CIE 1960 UCS scheme. The transformation used was

$$u = \frac{4x}{-2x + 12y + 3}$$

$$v = \frac{6y}{-2x + 12y + 3}$$

x, y - colour co-ordinates in the 1931 L x y system.

The particular alloys selected for comparison were chosen to have an atomic weight percentage of gold lying on or close to the Starenko loci. Five alloys were found to fulfill this criterion and their precise atomic weight percentage of gold and u v colour co-ordinates are detailed in table 6.2. The data is also presented graphically in figure 6.3 superimposed on the loci derived by Starenko. It is apparent that, while only five alloys can be directly compared, the agreement is better than 0.001 to 0.0005 in colour co-ordinates for these alloys and that no systematic differences are apparent.

The colour co-ordinates of the DIN 8328 series of alloys were derived under illuminant 'D' for comparison with data made available in a private communication by the Worshipful Company of Goldsmiths via reflectance measurements.

The data, table 5.5 are compared by colour difference plots in figure 6.4. A direct comparison is justified because the same samples were used in both the ellipsometric

and reflectance studies although the equilibrium temperature and phase composition are unknown. Each alloy was washed in alcohol before measurement by ellipsometry; other than this no surface preparation was attempted. It is apparent that for the 75 wt % Au alloys there is a systematic bias to a significance of ~ 0.01 in colour differences of each alloy. The presence of this bias requires further examination of the reflectometer data. In particular if the reflectometer used a barium sulphate reference, then it will give a positive bias to the reflectance unless a correction is applied (Wyszecki 1970). Additionally the alloy surface finish in terms of roughness and films is uncertain. Both of these effects can cause significant apparent colour shifts (Clarke 1980). The detailed experimental procedure of the reflectance measurements was unknown and the factors described cannot be discounted as the cause of the colour differences.

Clarke (1980) examined the Ag-Au, Au-Cu, and Ag-Cu binary systems observed a similar curvature in the Ag-Cu binary duplex-phase alloys. The experimental method used by Clarke was the same ellipsometric method as used in this work. The increased saturation was observed and analysed in terms of surface roughness, surface films, multiple reflections and dielectric mixing but Clarke was unable to quantify the effect. The presence of the curvature was expected as the method of alloy preparation and ellipsometric procedures were very similar to this work.

In summary, the colour co-ordinates of the Au-Ag-Cu alloys derived ellipsometrically have been found to be consistent with those derived independently. However, the presence of the curvature in the colour locus of the duplex-phase alloys has been undetected by other workers.

This work will attempt to quantify the curvature in the colour locus and propose a model based upon the addition of optical wavefronts at the sample under examination to produce a pseudo single-phase wavefront. The curvature is demonstrated as being an instrumental artifact.

6.3 Optical Model

The substrate to be modelled is a duplex-phase substrate composed of phases α and β on volume fractions Q_α and Q_β ($Q_\alpha + Q_\beta = 1$). The surfaces are considered to be perfectly flat, specularly reflecting and the exposed surface area fractions to be equal to the volume fractions.

When polarised light of known ellipticity is incident upon the substrate two wavefronts of different ellipticities are produced by reflection; this is shown diagrammatically in figure 6.5. The reflected beams then combine to form an 'average' of the two polarisation states.

Assuming that the incident light is incoherent then the reflected beams will be described by a Stokes vector equal to the weighted sums of the Stokes vectors of the beams reflected from each phase (Klein 1970).

$$S_R = Q_\alpha S_\alpha + Q_\beta S_\beta$$

where S_R - Stokes vector of the reflected beam

S_α and S_β - Stokes vectors of the reflected beams from each phase

Q_α and Q_β - Surface area proportions of α and β phases

The two Stokes vectors S_α and S_β are represented in the Mueller matrix formulation (Gerrard and Burch 1975) by the products of the incident beam vector S_I and the Mueller matrix of each phase M_α and M_β respectively. Thus

$$S_\alpha = M_\alpha S_I$$

$$S_\beta = M_\beta S_I$$

substitution gives

$$S_R = (Q_\alpha M_\alpha + Q_\beta M_\beta) S_I$$

The factor $(Q_\alpha M_\alpha + Q_\beta M_\beta)$ may now be equated with the pseudo single-phase surface characterised by M_S

$$M_S = Q_\alpha M_\alpha + Q_\beta M_\beta$$

The matrices M_α and M_β can be derived for a surface with a Jones matrix

$$\begin{pmatrix} r_s & 0 \\ 0 & r_p \end{pmatrix}$$

$$M_g = \frac{1}{2} \begin{pmatrix} (r_s r_s^* + r_p r_p^*) & (r_s r_s^* - r_p r_p^*) & 0 & 0 \\ (r_s r_s^* - r_p r_p^*) & (r_s r_s^* + r_p r_p^*) & 0 & 0 \\ 0 & 0 & (r_s^* r_p + r_p^* r_s) & i(r_s^* r_p - r_p^* r_s) \\ 0 & 0 & i(r_s^* r_p - r_p^* r_s) & (r_s^* r_p + r_p^* r_s) \end{pmatrix}$$

where $g = \alpha, \beta, S$.

The factor $(Q_\alpha M_\alpha + Q_\beta M_\beta)$ may now be evaluated and equated to M_S giving the equations

$$r_s r_s^* + r_p r_p^* = Q_\alpha (r_{s\alpha} r_{s\alpha}^* + r_{p\alpha} r_{p\alpha}^*) + Q_\beta (r_{s\beta} r_{s\beta}^* + r_{p\beta} r_{p\beta}^*)$$

$$r_s r_s^* - r_p r_p^* = Q_\alpha (r_{s\alpha} r_{s\alpha}^* - r_{p\alpha} r_{p\alpha}^*) + Q_\beta (r_{s\beta} r_{s\beta}^* - r_{p\beta} r_{p\beta}^*)$$

$$r_s^* r_p + r_p^* r_s = Q_\alpha (r_{s\alpha}^* r_{p\alpha} + r_{p\alpha}^* r_{s\alpha}) + Q_\beta (r_{s\beta}^* r_{p\beta} + r_{p\beta}^* r_{s\beta})$$

$$r_s^* r_p - r_p^* r_s = Q_\alpha (r_{s\alpha}^* r_{p\alpha} - r_{p\alpha}^* r_{s\alpha}) + Q_\beta (r_{s\beta}^* r_{p\beta} - r_{p\beta}^* r_{s\beta})$$

adding the first two equations gives

$$r_s r_s^* = Q_\alpha r_{s\alpha} r_{s\alpha}^* + Q_\beta r_{s\beta} r_{s\beta}^*$$

subtraction gives

$$r_p r_p^* = Q_\alpha r_{p\alpha} r_{p\alpha}^* + Q_\beta r_{p\beta} r_{p\beta}^*$$

thus

$$\begin{aligned} \frac{r_p r_p^*}{r_s r_s^*} &= \frac{Q_\alpha r_{p\alpha} r_{p\alpha}^* + Q_\beta r_{p\beta} r_{p\beta}^*}{Q_\alpha r_{s\alpha} r_{s\alpha}^* + Q_\beta r_{s\beta} r_{s\beta}^*} \\ &= \tan^2 \psi_S \end{aligned}$$

Similarly adding the third and fourth equations from the factor $(Q_\alpha M_\alpha + Q_\beta M_\beta)$ gives

$$r_s^* r_p = Q r_s^* r_p + Q r_s^* r_p$$

substituting $r_s^* = |r_s| \exp i(-\Delta_s)$

$$r_p = |r_p| \exp i(\Delta_p)$$

$$r_s^* r_p = |r_s| |r_p| \exp i(\Delta_p - \Delta_s)$$

$$= |r_s| |r_p| \exp i\Delta$$

$$= Q_\alpha |r_{s\alpha}| |r_{p\alpha}| \exp i(\Delta_{p\alpha} - \Delta_{s\alpha})$$

$$+ Q_\beta |r_{s\beta}| |r_{p\beta}| \exp i(\Delta_{p\beta} - \Delta_{s\beta})$$

noting that two complex numbers are equal when both the real and imaginary components are equal, the expansion of the above equation into real and imaginary components gives

$$|r_s| |r_p| \cos\Delta = Q_\alpha |r_{s\alpha}| |r_{p\alpha}| \cos\Delta_\alpha + Q_\beta |r_{s\beta}| |r_{p\beta}| \cos\Delta_\beta$$

$$|r_s| |r_p| \sin\Delta = Q_\alpha |r_{s\alpha}| |r_{p\alpha}| \sin\Delta_\alpha + Q_\beta |r_{s\beta}| |r_{p\beta}| \sin\Delta_\beta$$

dividing these two equations gives

$$\tan\Delta = \frac{Q_\alpha |r_{s\alpha}| |r_{p\alpha}| \sin\Delta_\alpha + Q_\beta |r_{s\beta}| |r_{p\beta}| \sin\Delta_\beta}{Q_\alpha |r_{s\alpha}| |r_{p\alpha}| \cos\Delta_\alpha + Q_\beta |r_{s\beta}| |r_{p\beta}| \cos\Delta_\beta}$$

The model proposed relates the averaged or pseudo single-phase substrate observed by a nulling ellipsometer to the phase composition and properties of its component phases. The Au-Ag-Cu ternary system was examined at 10% wt. intervals and the alloys available did not contain the terminal solid solutions to assess the model. However, an earlier worker (Clarke 1980) had examined the Ag-Cu alloys as a binary system which included the terminal solid solutions.

The alloys used to examine the model were the two terminal solid solutions 96 Ag 4 Cu and 2 Ag 98 Cu and the duplex alloys 70 Ag 30 Cu ($Q_{\beta} = 0.324$), 60 Ag 40 Cu ($Q_{\beta} = 0.419$) and 30 Ag 70 Cu ($Q_{\beta} = 0.738$). The alloys were measured over a range of wavelengths which avoided the main absorption edges but which showed significant differences on Ψ and Δ . The wavelength range 400 to 500nm was selected as fulfilling these criteria.

The model was tested in two ways;-

- 1) given the terminal solid solutions and two-phase alloy data, the volume fractions of each two-phase alloy was determined by using the model to predict

ψ and Δ values of an alloy and adjusting the volume fraction to produce the best fit between experimental data and modelled data.

ii) three duplex phase alloys of known volume fraction were used with the model to predict the ψ and Δ values of the terminal solid solutions. These ψ and Δ values were then compared with experimental data.

The first test required the model to predict the ψ and Δ values of a two-phase alloy given the terminal solid solutions. The modelled ψ and Δ values were derived for a trial value of volume fraction Q_β and the modelled and experimental ψ and Δ values compared. The volume fraction Q_β was then adjusted to minimise the error between the two sets of data. A Fortran IV program was written to perform this calculation (Appendix A) and minimise the error function.

$$(\psi_{\text{calc}} - \psi_{\text{exp}})^2 + (\Delta_{\text{calc}} - \Delta_{\text{exp}})^2$$

by adjusting the volume fraction Q_β of the calculated data point.

This calculation was performed at 11 wavelengths from 400 to 500 nm in 10 nm steps. The mean and root variance of the calculated values of Q_β were then formed. The volume fractions of the three two-phase alloys were calculated by this method and compared with values calculated from the

phase diagram (Clarke 1980), the data is presented in table 6.3. It can be seen that in two out of the three cases the experimentally determined values agree with the phase diagram calculated values to within one root variance and in the third case to within two root variances.

The second test required the model to predict the properties of the terminal solid solutions from experimental data of three two-phase alloys. A second Fortran IV program (Appendix B) was written to perform this function. It used the algorithm:-

1. Using initial estimates of ψ and Δ for the α and β phase terminal solutions, use the model to calculate the ψ and Δ values of each two-phase alloy.
2. Form the error function

$$\sum_{i=1}^3 \{ (\psi_{\text{calc}} - \psi_{\text{exp}})^2 + (\Delta_{\text{calc}} - \Delta_{\text{exp}})^2 \}_i$$

the summation extends over the three two-phase alloys.

3. Adjust the values of ψ_{α} , Δ_{α} and ψ_{β} , Δ_{β} and repeat operation 2.
4. Compare the two error values produced by successive ~~interactions~~ ^{iterations} and repeated until the error is minimised.

The ψ and Δ values of the Ag-Cu and Cu-Ag terminal solutions were derived by this method and the results are shown in table 6.4, it contains both both experimentally determined ψ and Δ values as well as those derived via the model. The agreement between the calculated and experimental results is seen to be an average of 0.37 degrees in ψ and 0.72 degrees in Δ

The predicted locus of Ψ and Δ between the terminal solid solution values is shown in figure 6.6. The model has correctly predicted the magnitude and direction of the curvature in the locus as shown by the data plotted from the two-phase alloys.

The equations used in the model have been published without derivation by Roberts, Clarke and Hunt (1980), and with the derivation by Roberts and Hunt (1982). It should be noted that in the second paper an error exists in the derivation, the omission of a scale factor $|r_p|$ in the Stokes vector of each phase. This error was also pointed out by D.E.Aspnes (private communication). A correction has been submitted to the publishers.

The effect of the averaging process upon normal reflectance was examined using the Ag-Cu Cu-Ag data at a wavelength of 500 nm. The model was used to calculate sufficient Ψ and Δ pairs at varying volume fractions to construct a locus of normal reflectance as a function of volume fraction between the terminal solid solutions. This locus is shown in figure 6.7. The locus is non-linear and shows a distinct curvature with the reflectance biased to a higher level than to be expected from a linear interpolation. The difference peaking at $Q_\beta = 0.5$ with a difference of 3.5%

The positive biasing of normal reflectance has a very important effect upon the calculated colour. The two-phase alloy will appear to have a more saturated colour with a higher luminance than is predicted by linear, (Graussman's Third Law) mixing. This linear mixing is characteristic

of a normal reflectometer (Butcher 1961). Thus the colour locus of two-phase alloys is expected to be curved away from the 'white' point and towards the monochromatic locus. This curvature is clearly visible on the 10%, 20% wt Au alloys whose colour plots are shown in figure 5.25.

In summary, at this stage, the colour locus of the two-phase alloys determined by nulling ellipsometry is observed to be curved when it is reasonably expected to be straight. A model to explain the manner in which nulling ellipsometry averages the optical properties of component phases has been developed and tested upon the Ag-Cu Cu-Ag system. The model correctly predicted the presence of curvature in the colour locus of low-phase alloys.

The model was then used to re-assess the two-phase alloy data and calculate the colours of the terminal solid solutions for alloys of constant gold composition and compare predicted and experimental values.

The re-assessment of the ternary duplex-phase alloys consisted of selecting three alloys from each grouping of constant gold composition and using these alloys of known phase proportions to calculate the Ψ and Δ values of the terminal solid solutions.

Three alloys were used as this overdetermined the data for the terminal solid solution. The solid solutions were then used to predict the colour locus of the three

two-phase alloys used for each gold proportion. The alloys selected were:-

| | | |
|--------------|--------|---------------------|
| 1. 10% wt Au | No 60 | $Q_{\beta} = 0.225$ |
| | No 63 | $Q_{\beta} = 0.585$ |
| | No 66 | $Q_{\beta} = 0.920$ |
| 2. 20% wt Au | No 52 | $Q_{\beta} = 0.085$ |
| | No 55 | $Q_{\beta} = 0.510$ |
| | No 58 | $Q_{\beta} = 0.920$ |
| 3. 30% wt Au | No 46R | $Q_{\beta} = 0.075$ |
| | No 49 | $Q_{\beta} = 0.570$ |
| | No 51 | $Q_{\beta} = 0.920$ |
| 4. 39% wt Au | No 41 | $Q_{\beta} = 0.085$ |
| | No 43 | $Q_{\beta} = 0.480$ |
| | No 45R | $Q_{\beta} = 0.895$ |

The computer program used to derive the terminal solution data was the same as that used to analyse the Ag-Cu Cu-Ag data. (Appendix B).

The data is presented as derived α and β phase terminal solid solution reflectance spectra with the 1st derivative of reflectance w.r.t. wavelength to identify the absorption edges.

As an internal check of the accuracy with which the terminal solid solutions were calculated, the model was used to predict the reflectance spectra of the duplex-phase alloys, and spectra of the deconvoluted then convoluted alloys were compared to the original spectra. The terminal solid solution and comparative spectra are shown in figures 6.16 to 6.27 inclusive.

The terminal solid solutions are characterised by a single dominant absorption edge in each phase corresponding to either the silver- or copper-rich phase. The edges shift monotonically with increasing gold proportion to longer wavelengths for the silver edge, and to shorter wavelengths for the copper edge. The comparison between the deconvoluted - convoluted reflectance spectra and experimental data shows a good agreement, typically 1/2 % except in the regions of an absorption edge. The poorer fit in these regions is thought to be due to wavelength and angle of incidence alignment errors which are exaggerated by the large gradient between the reflectance and wavelength.

The effect of the increased reflectance of the duplex-phase alloys is to increase the apparent saturation and luminance. The colour loci predicted by the model between the terminal solid solutions are shown in figures 6.28 and 6.29. The loci are constructed in 10 % increments in β -phase proportion in the 1931 Lxy system, illuminant 'C'

The graphs also show the colour points of the alloys used in the modelling. The experimentally determined points are labelled 'E' and the modelled points 'M' with the remainder of the index as the alloy number. It is apparent that the model has correctly predicted the colour co-ordinates to within 0.0007 in x and y in 11 cases out of the 12 considered, compared to a maximum co-ordinate difference of 0.002 between observed and linear colour mixing. In each case both the direction and magnitude of the curvature are quantitatively correct. It is therefore considered that the observed curvature in the colour locus towards greater saturation for the duplex phase alloys is an instrumental effect and would not be present in a physical colorimeter. Under this premise it is proposed that the α and β phase terminal solid solution data are representative of the correct terminal solid solutions and that a revised colour map be calculated. The colour co-ordinates of the terminal solid solutions are given in table 6.5 and are shown graphically in figure ~~6.29~~^{6.30}. This data together with the single-phase alloy data constitute the revised colour map. In the revised colour map the colour loci of the duplex-phase alloys of constant weight percentage in gold are straight lines thus fulfilling Graussmans Third Law.

6.4 Conclusion

Ellipsometry has been applied to the colorimetric measurement of the AuAgCu ternary system. The colorimetric results have been compared to published data derived using reflectometry and where comparable alloys were examined the agreement is within the accuracy of the published data. However a deviation, smaller than the accuracy of the published data, was observed in the measured colorimetric loci from linear mixing of alloys with a constant Au weight percentage. The loci were expected to be straight lines in the CIE 1931 Lxy scheme but a small curvature towards a greater saturation was observed. The use of ellipsometry as a technique to examine surfaces explicitly states that the surface is homogeneous. The surface may be characterised by a substrate, film system and ambient environment but each factor is homogeneous. The AuAgCu system has provided an interesting problem in that the majority of the alloys examined were duplex-phase, that is, the surfaces were heterogeneous not homogeneous. The ellipsometer was found to locate a single well-defined null by averaging the surface optical properties, even when the duplex-phase alloys had phases which were markedly different. An optical model which described the averaging process was proposed and tested on the AgCu-CuAg binary duplex-phase system. This system was used as both duplex-phase and terminal solid solution alloys were available (no terminal solid solution alloys were available for the AuAgCu ternary system). The

optical model proposed that the light reflected from a poly-phase surface can be described by the weighted addition of the Stokes vectors of the light reflected from each phase. The model was tested by comparing the experimental and predicted optical properties and they were found to be in good agreement. The model quantitatively predicted the curvature in the colour loci and thus showed it to be an instrumental artifact present when examining poly-phase surfaces. The model was then used to predict the colorimetric properties of the AuAgCu duplex-phase system.

Finally, the optical model was derived for the condition of incoherent illumination, if coherent illumination is used then the weighted Jones and not Stokes vectors must be added. The two methods produce different results and Chapter Seven 'Further Work' expands on this difference as a possible technique for examining phase boundary positions without the need to know the compositions of the terminal solid solutions.

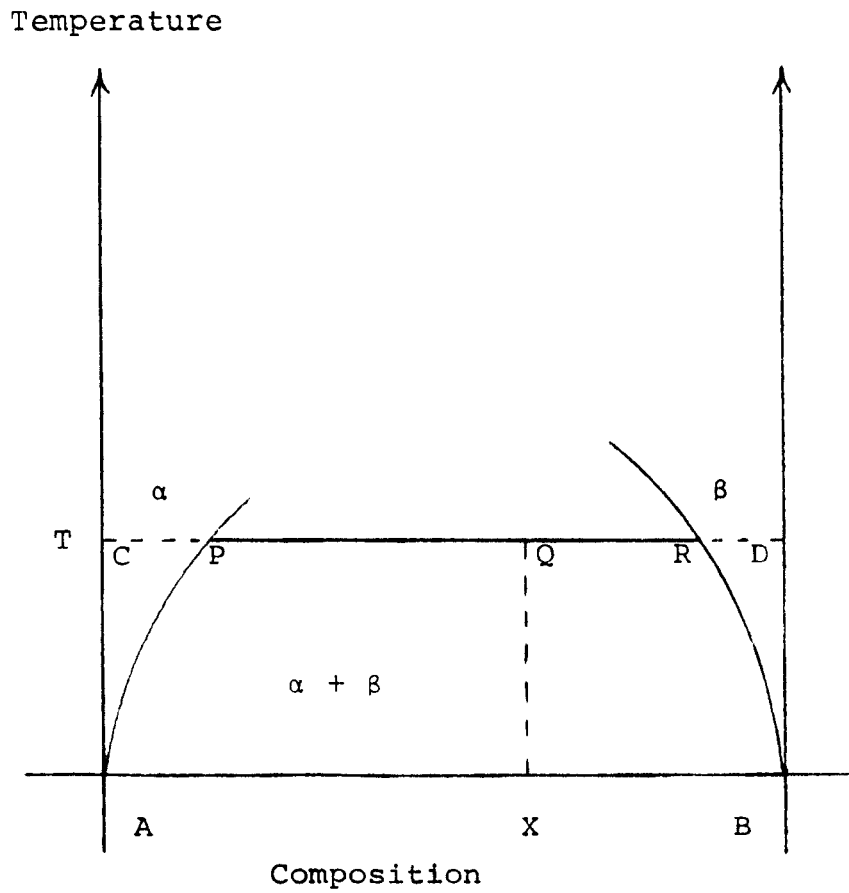


Figure 6.1 Phase diagram of a duplex-phase alloy with composition X at an equilibrium temperature T

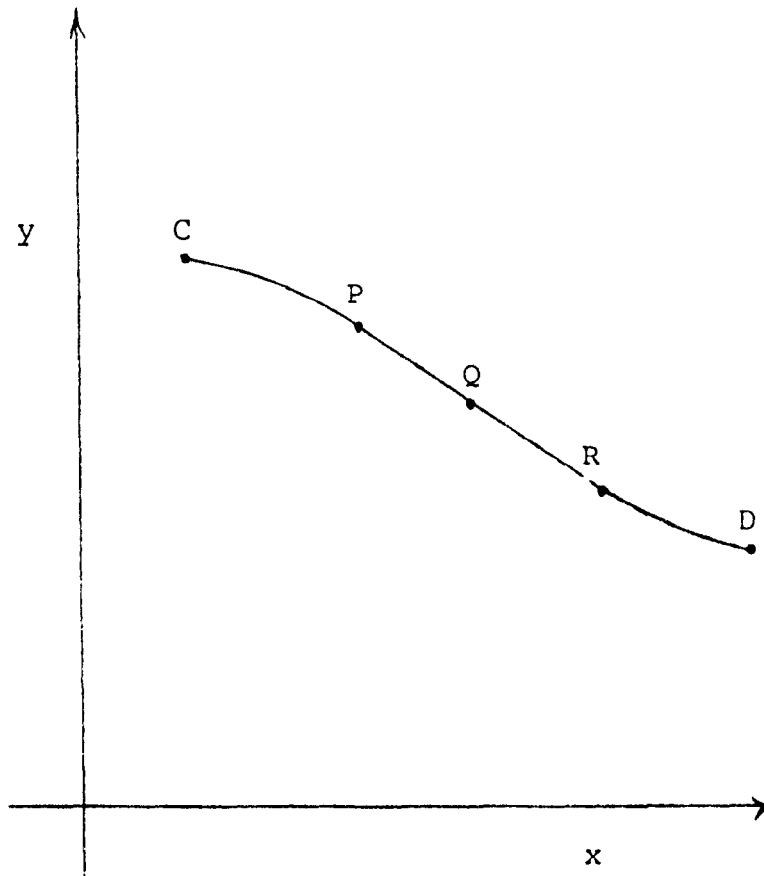


Figure 6.2 Colour locus of an alloy with both single- and duplex-phase regions in the CIE 1931 L-x-y colour diagram.

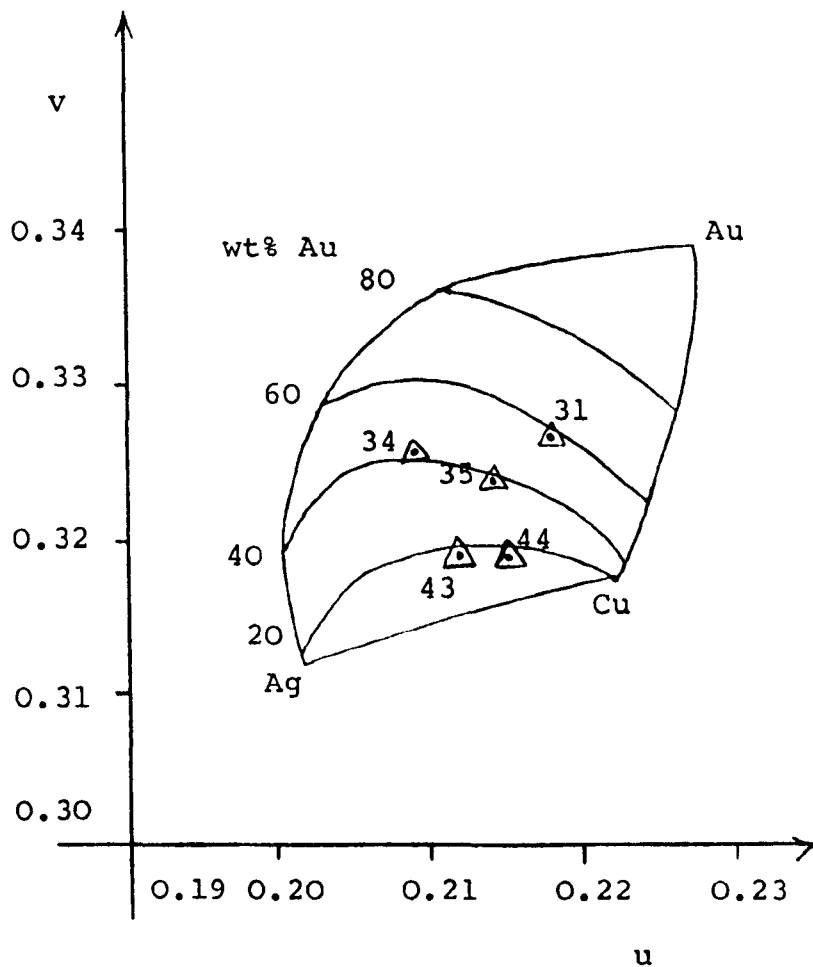


Figure 6.3 Comparison of colour co-ordinates in the 1960 UCS scheme between this work and Starenko and Lifshits (1974)

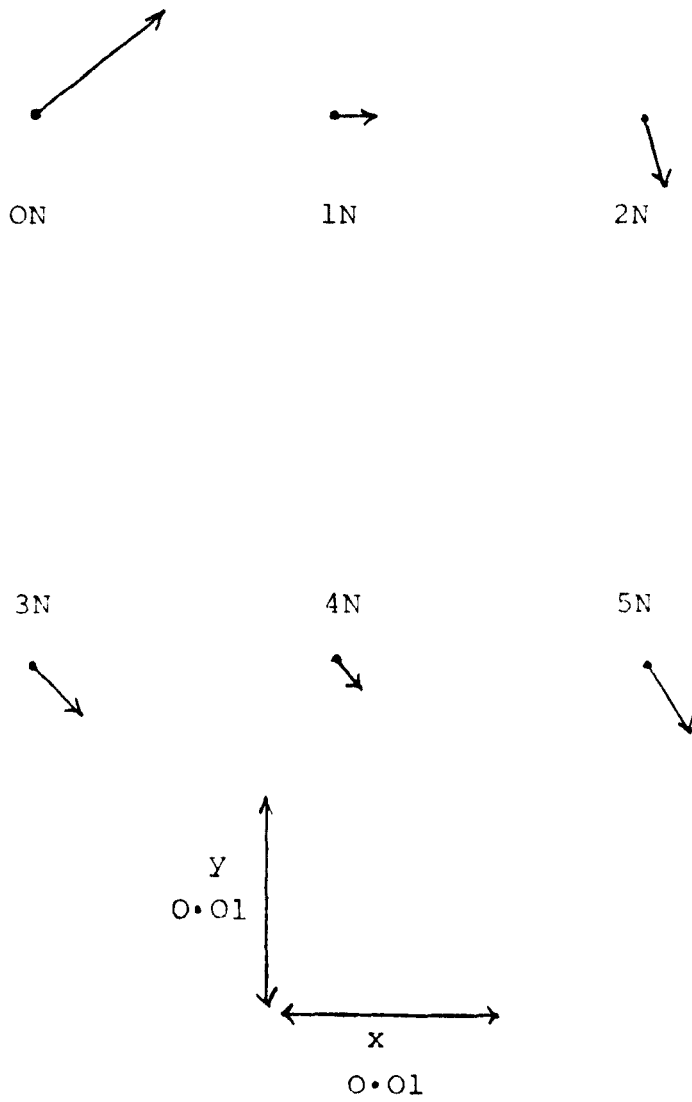


Figure 6.4 Colour difference vectors for the DIN8328 samples.

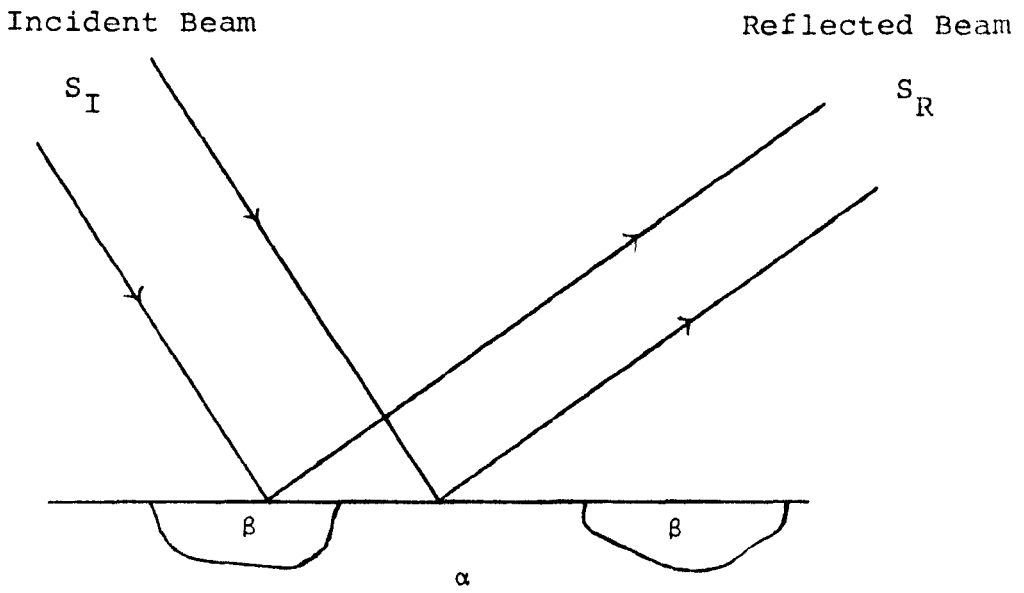


Figure6.5 Reflection of light from the two phases of a duplex alloy.

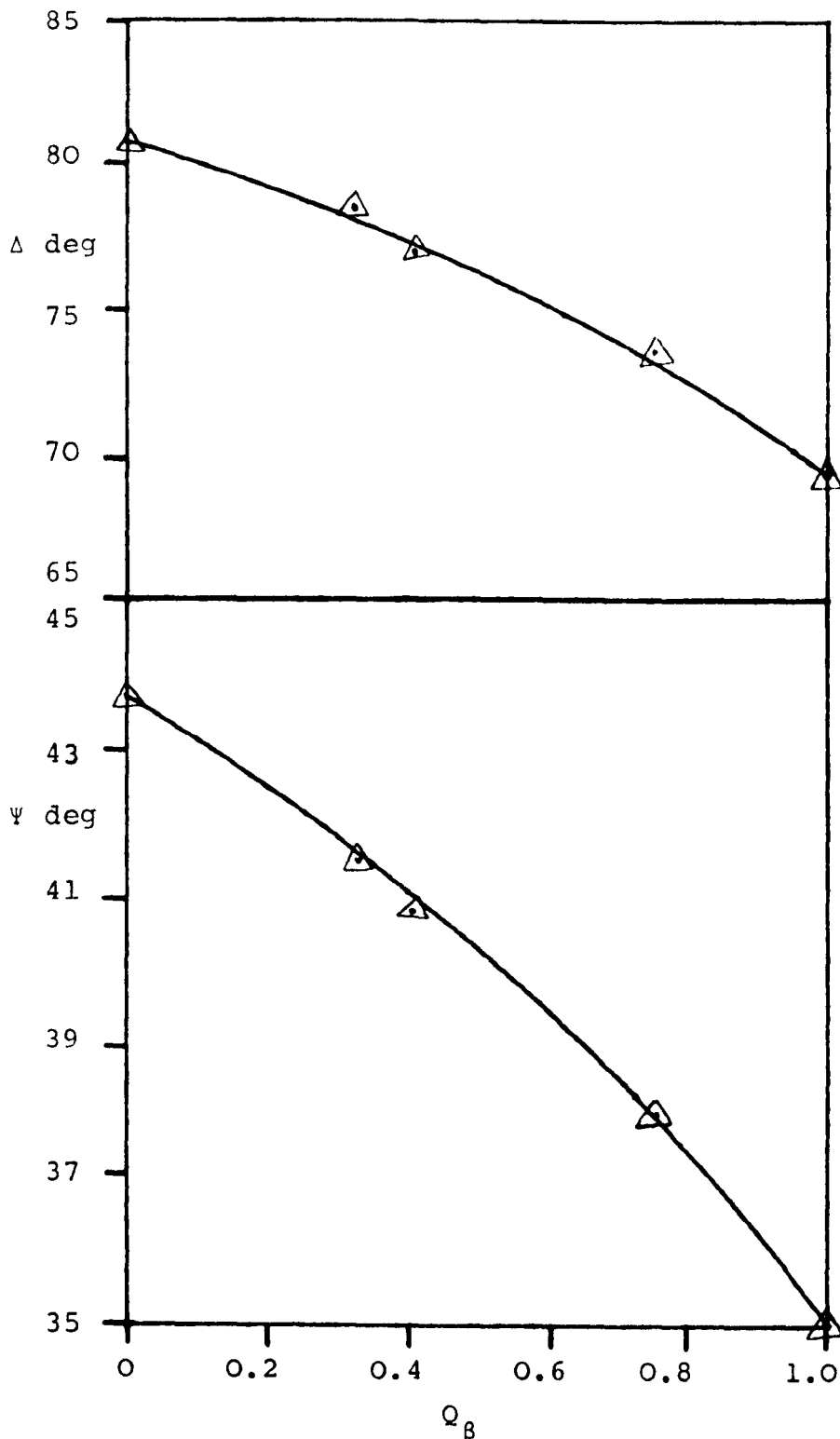


Figure 6.6 Variation of Ψ and Δ with volume fraction of β -phase predicted by the model. Data points from the AgCu data at $\lambda=500\text{nm}$.

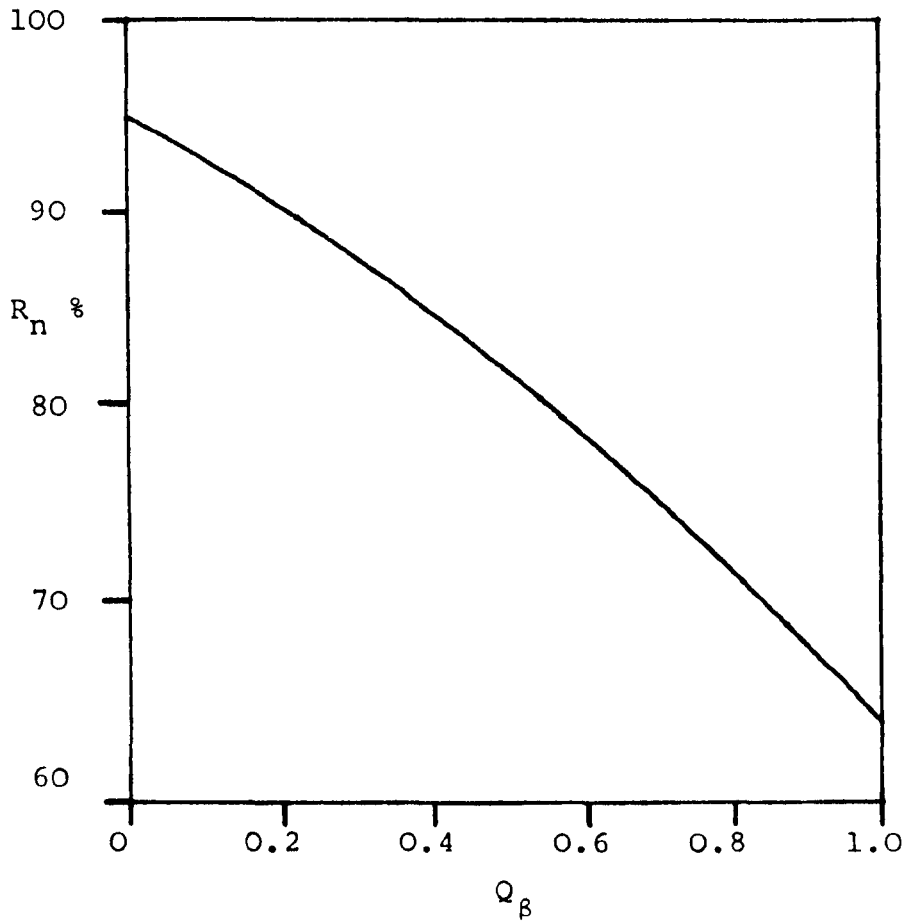


Figure 6.7 Variation of normal reflectance predicted by the model between the AgCu and CuAg terminal solid solutions at $\lambda=500$ nm.

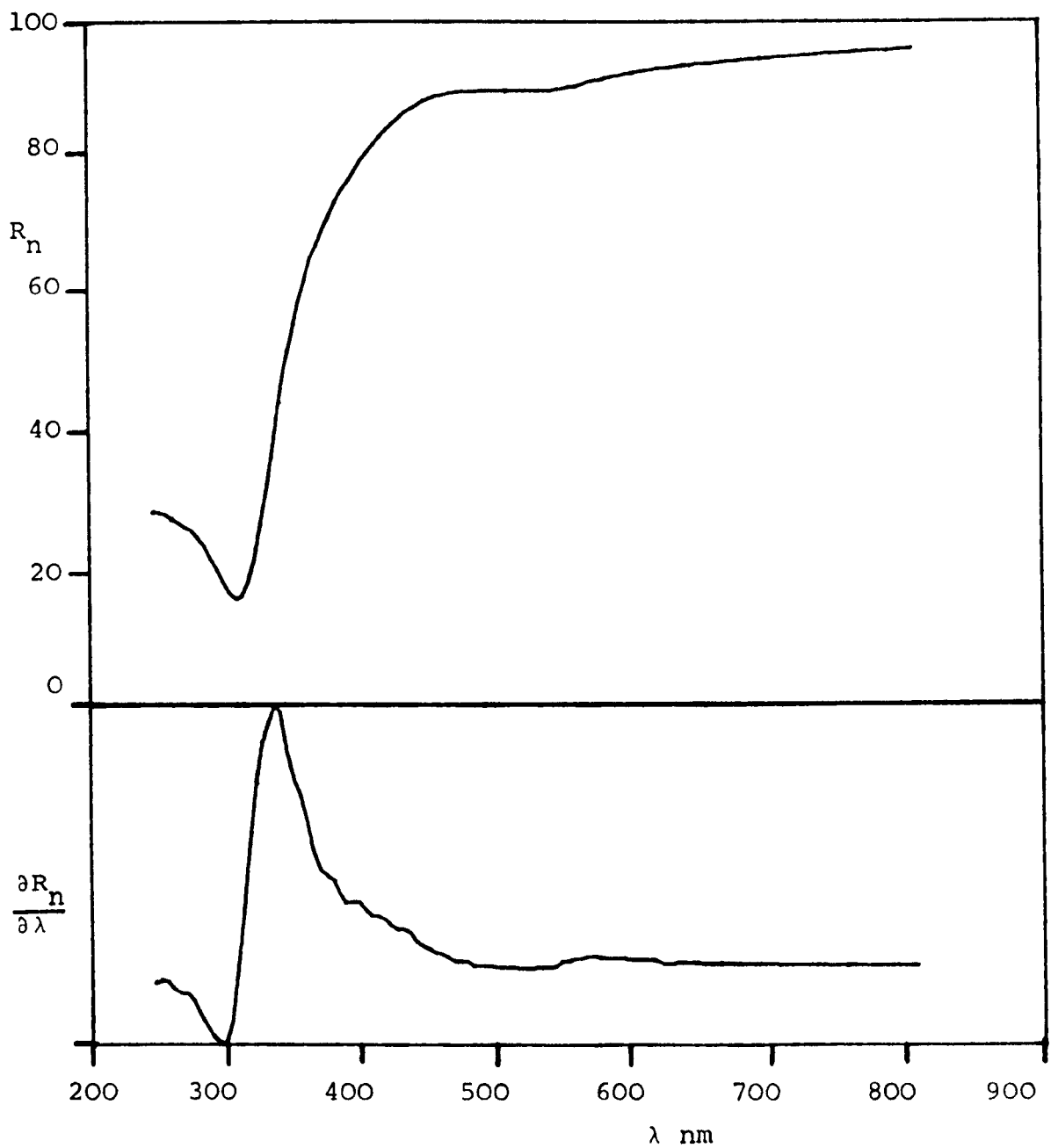


Figure 6.8 Normal and derivative reflectance spectra of 10 wt% α -phase terminal solid solution predicted by the model from duplex-phase data.

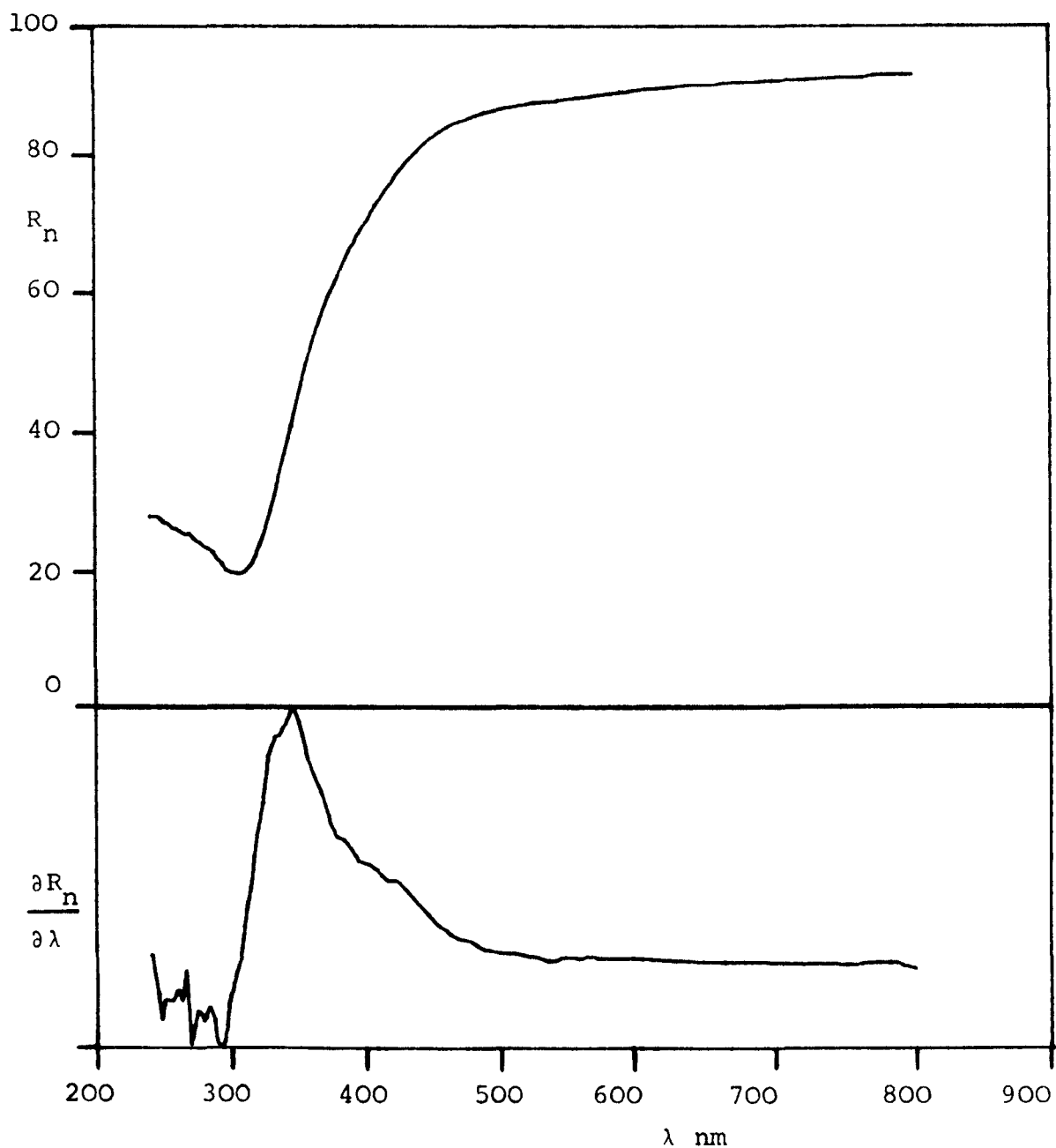


Figure 6.9 Normal and derivative reflectance spectra of
 20 wt% Au α -phase terminal solid solution predicted
 by the model from duplex-phase alloy data.

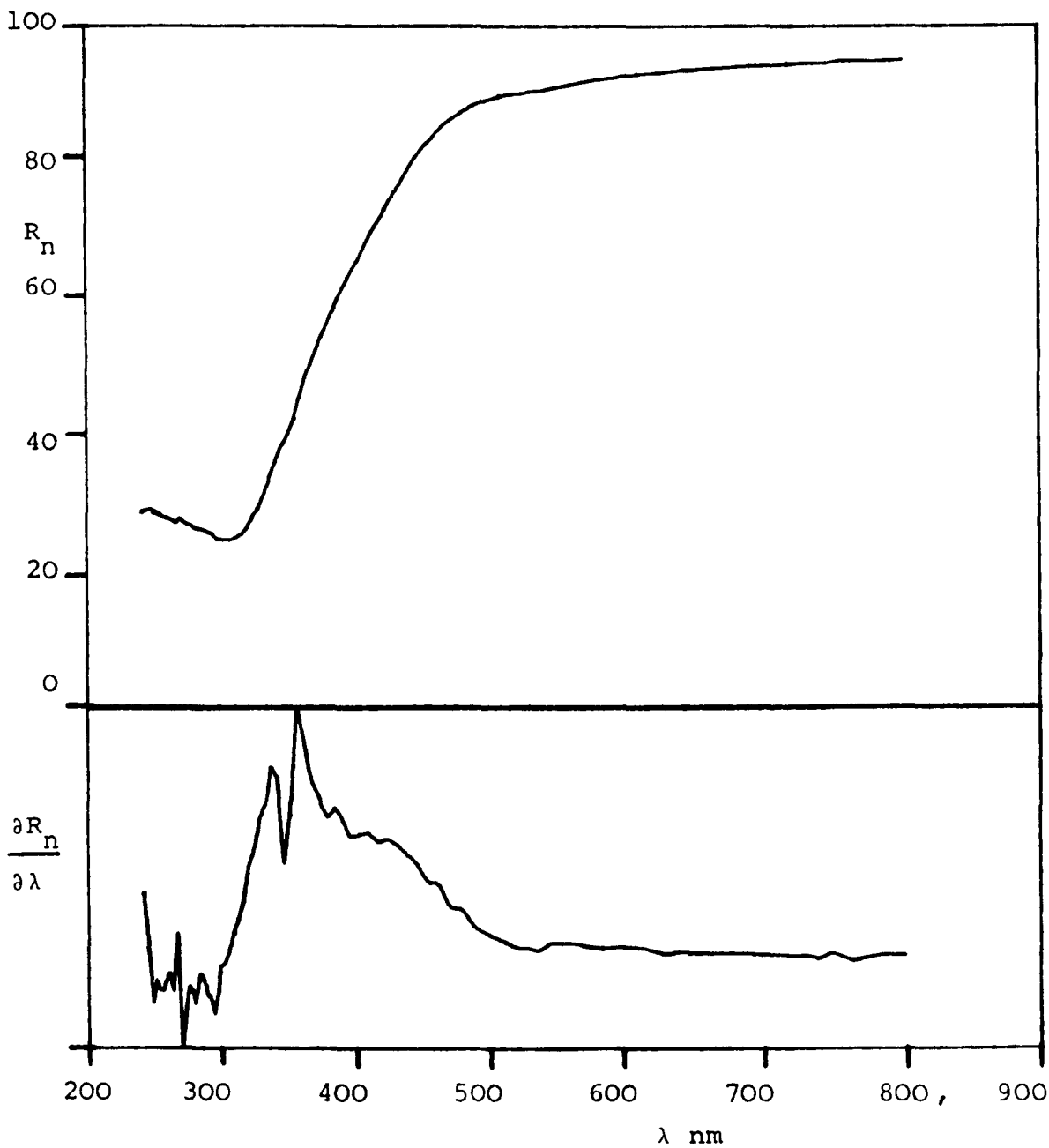


Figure 6.10 Normal and derivative reflectance spectra of 30 wt% Au α -phase terminal solid solution predicted by the model from duplex-phase alloy data.

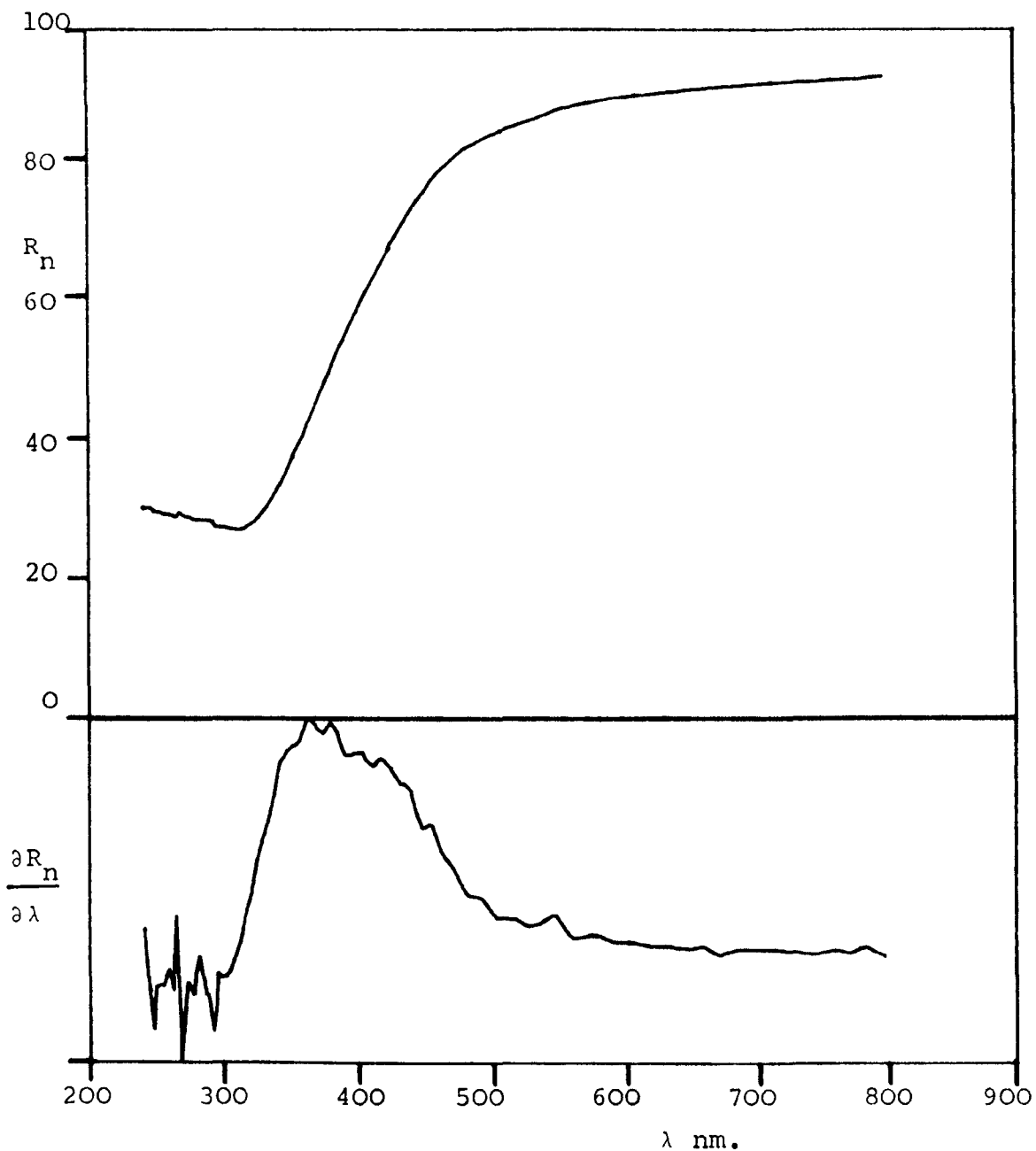


Figure 6.11 Normal and derivative reflectance spectra of 39 wt% Au α -phase terminal solid solution predicted by the model from duplex-phase alloy data.

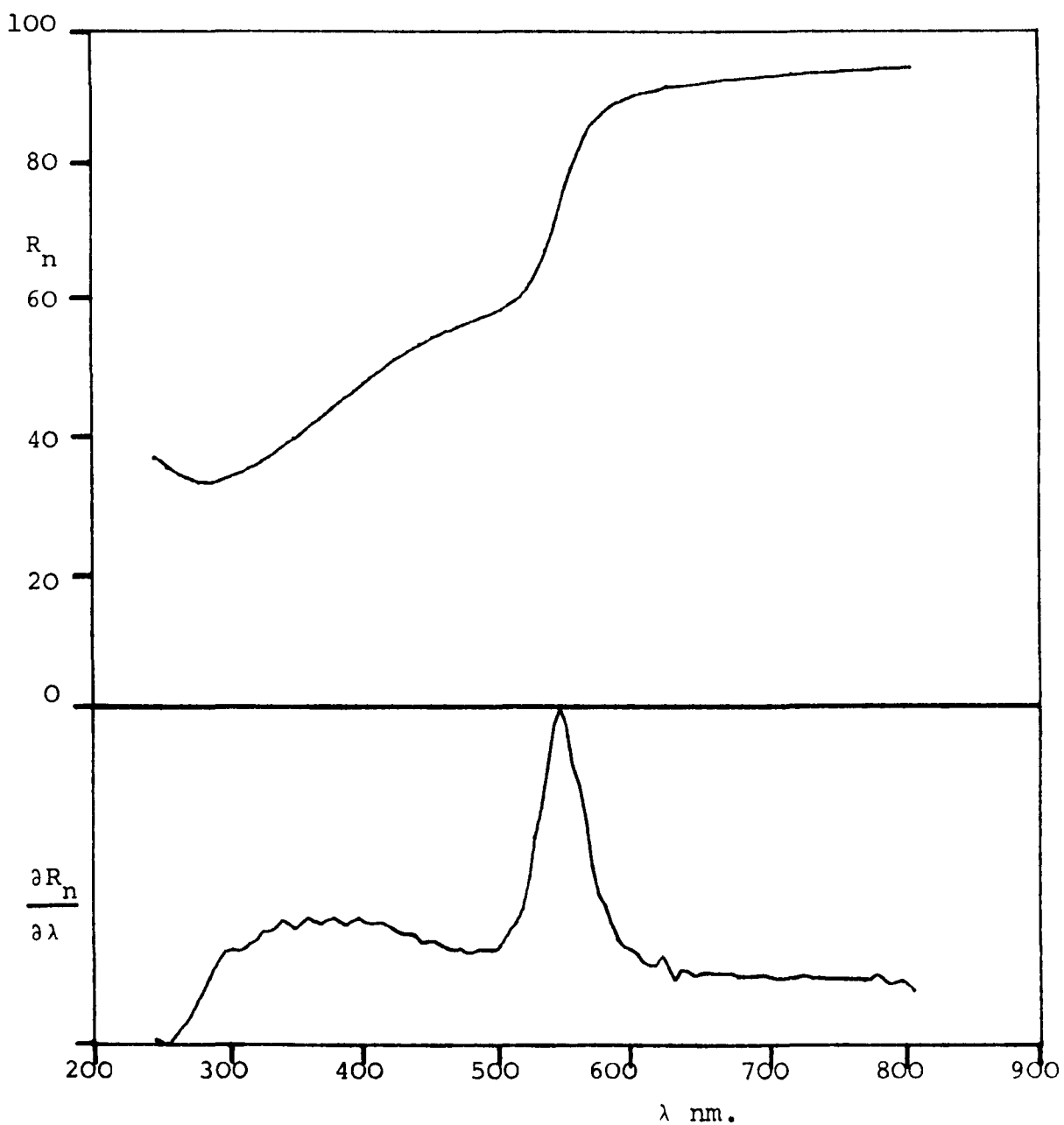


Figure 6.12 Normal and derivative reflectance spectra of 10 wt% Au β -phase terminal solid solution predicted by the model from duplex-phase alloy data.

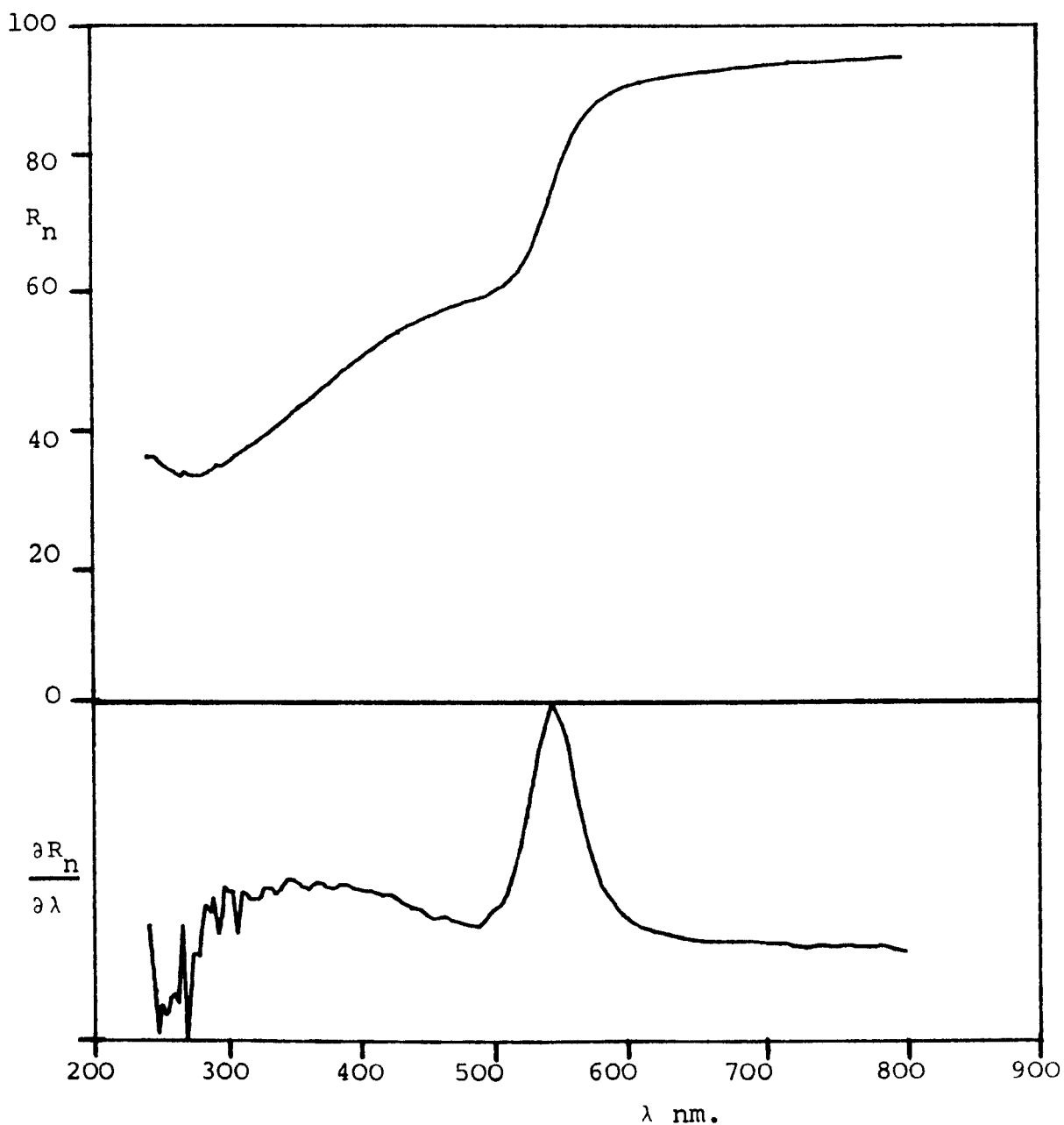


Figure 6.13 Normal and derivative reflectance spectra of 20 wt% Au β -phase terminal solid solution predicted by the model from duplex-phase alloy data.

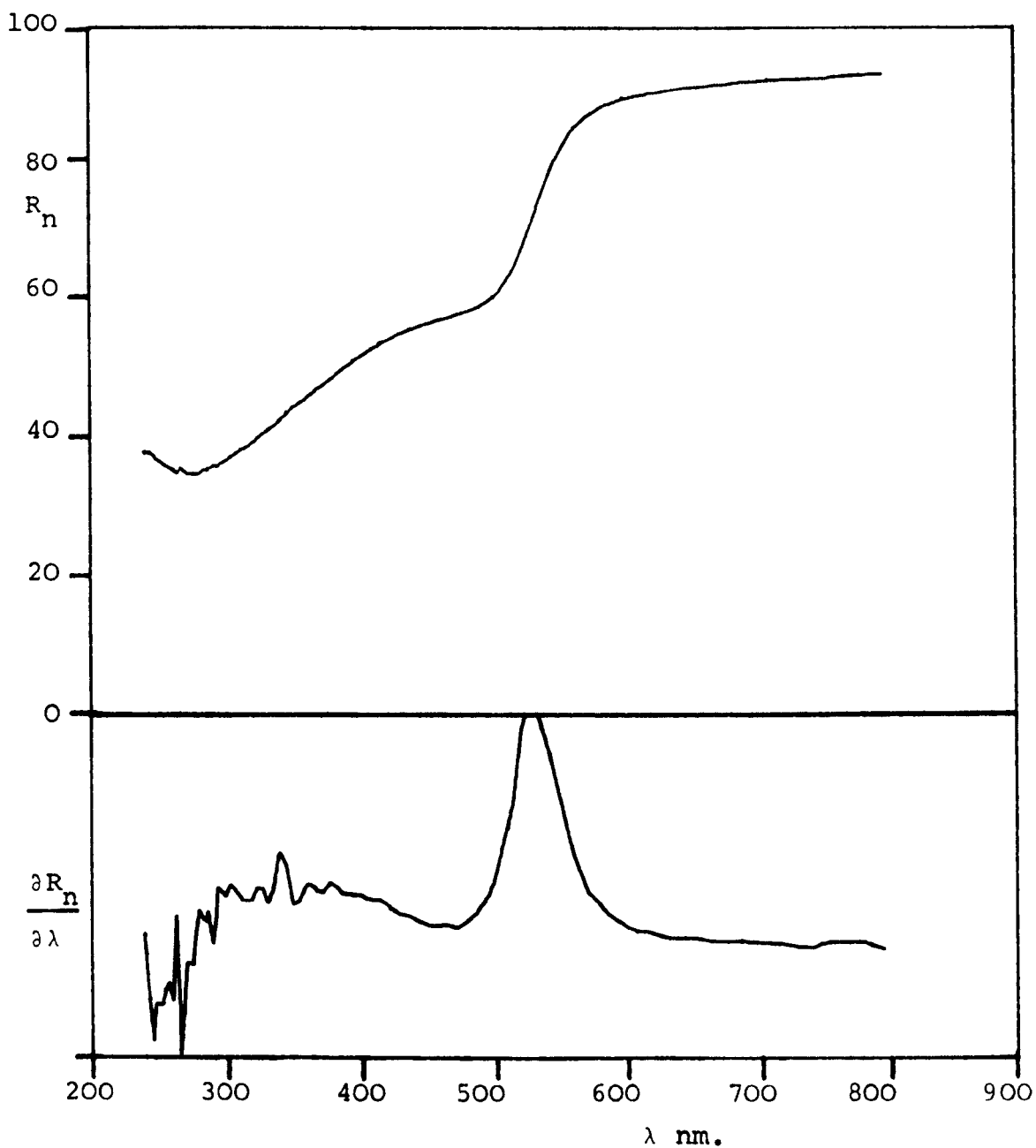


Figure 6.14 Normal and derivative reflectance spectra of 30 wt% Au β -phase terminal solid solution predicted by the model from duplex-phase alloy data.

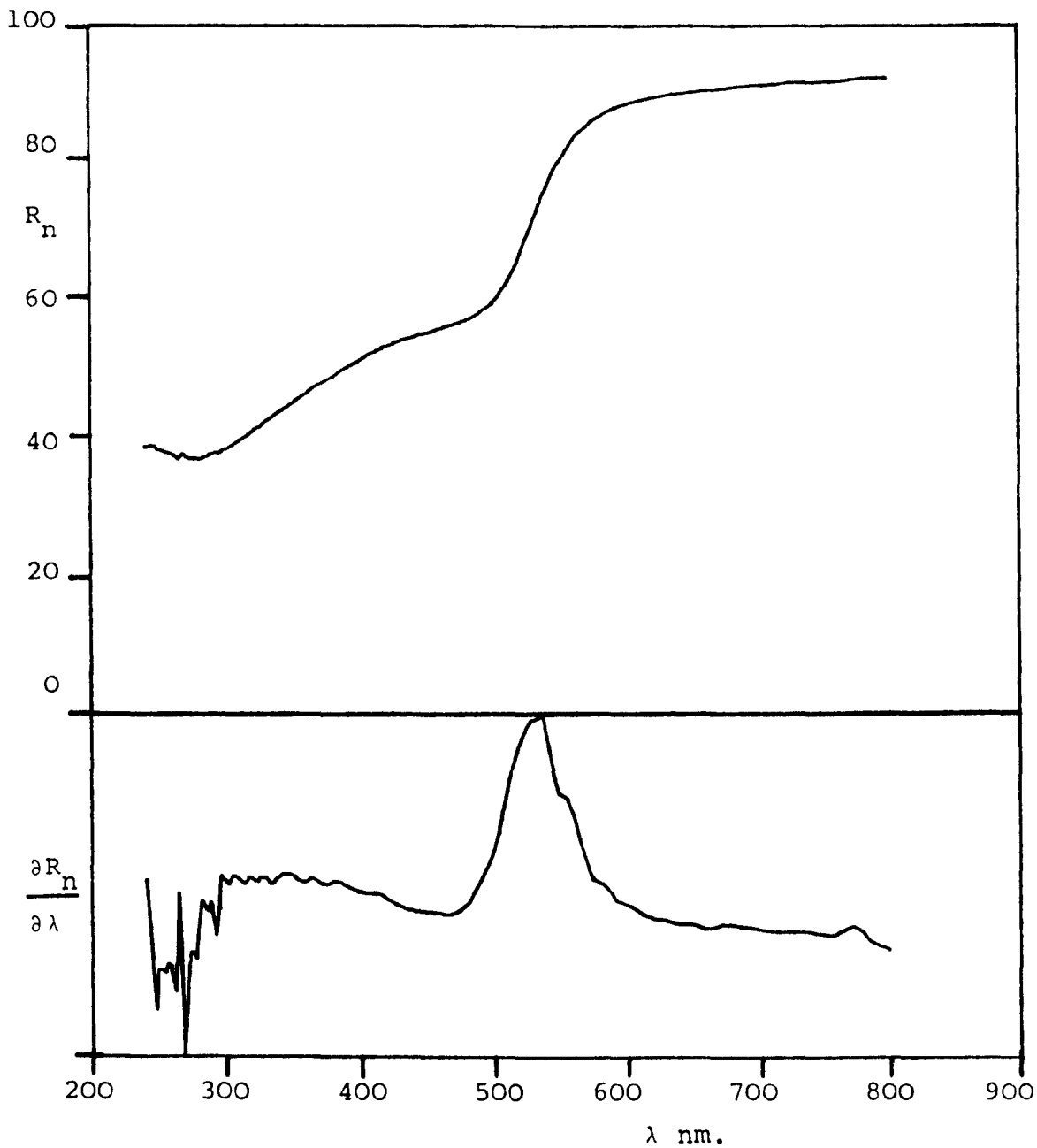


Figure 6.15 Normal and derivative reflectance spectra of
 39 wt% Au β -phase terminal solid solution predicted
 by the model from duplex-phase alloy data.

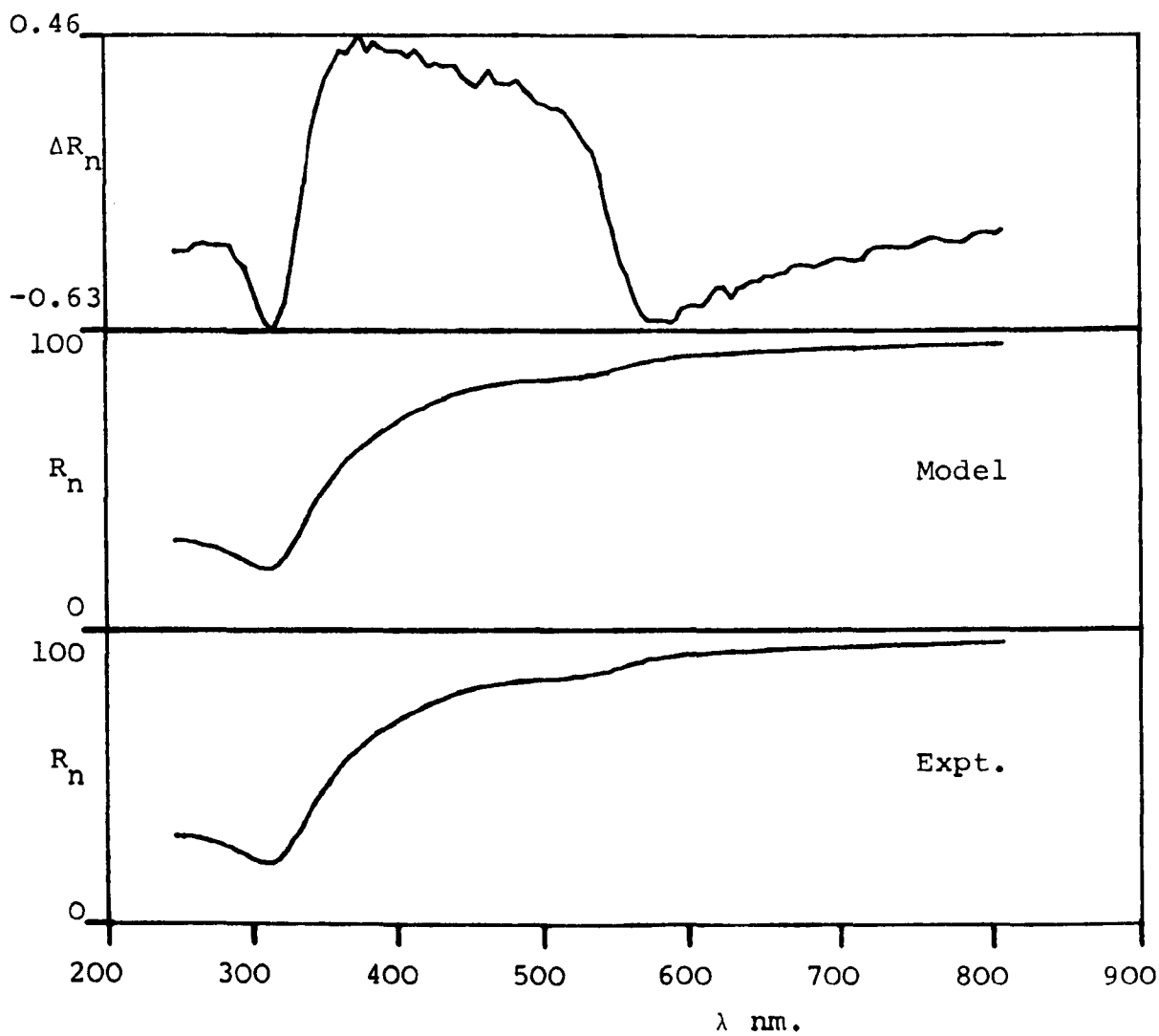


Figure 6.16 Comparison between modelled and experimental normal reflectance spectra of alloy number 60.

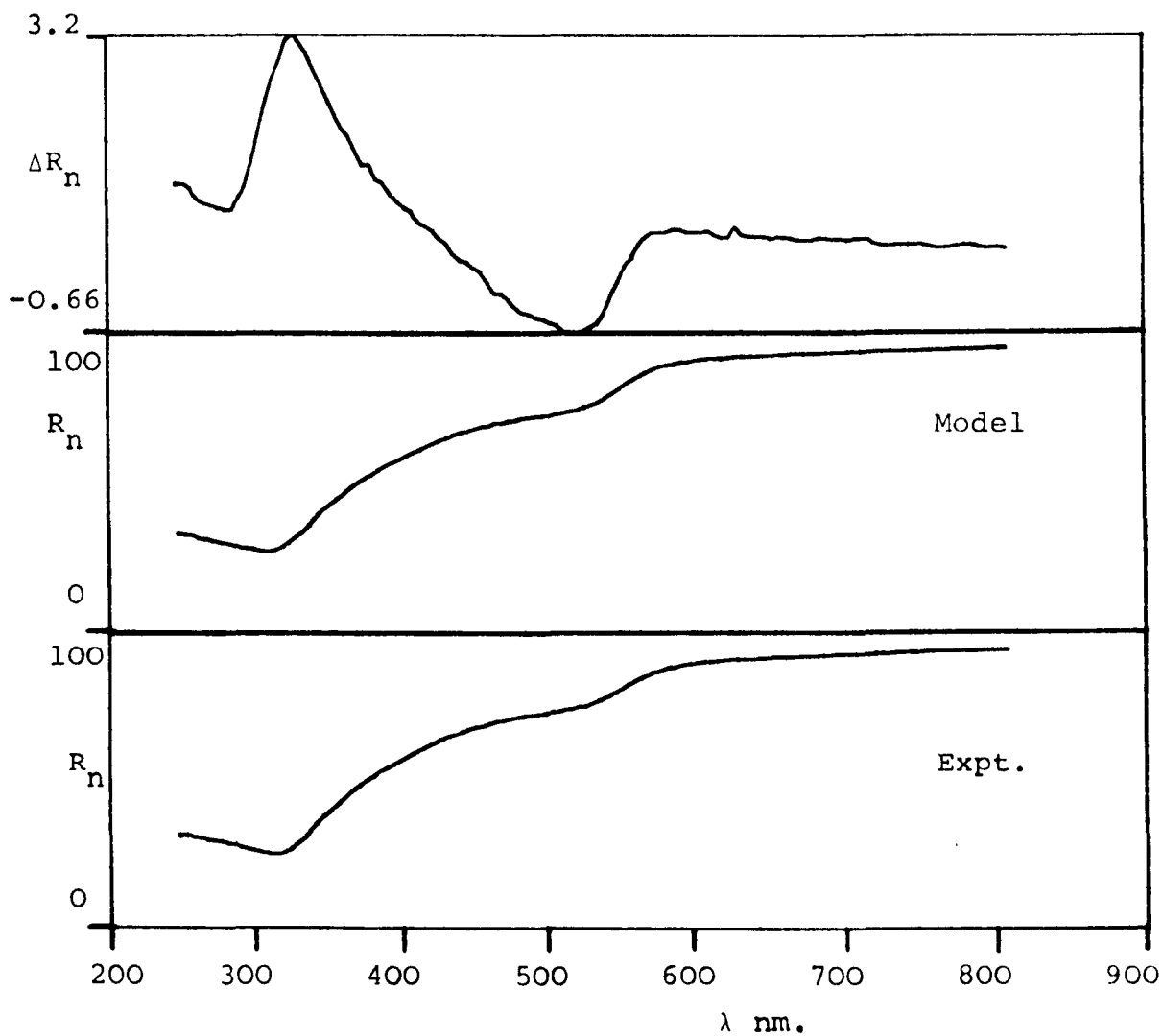


Figure 6.17 Comparison between modelled and experimental normal reflectance spectra of alloy number 63.

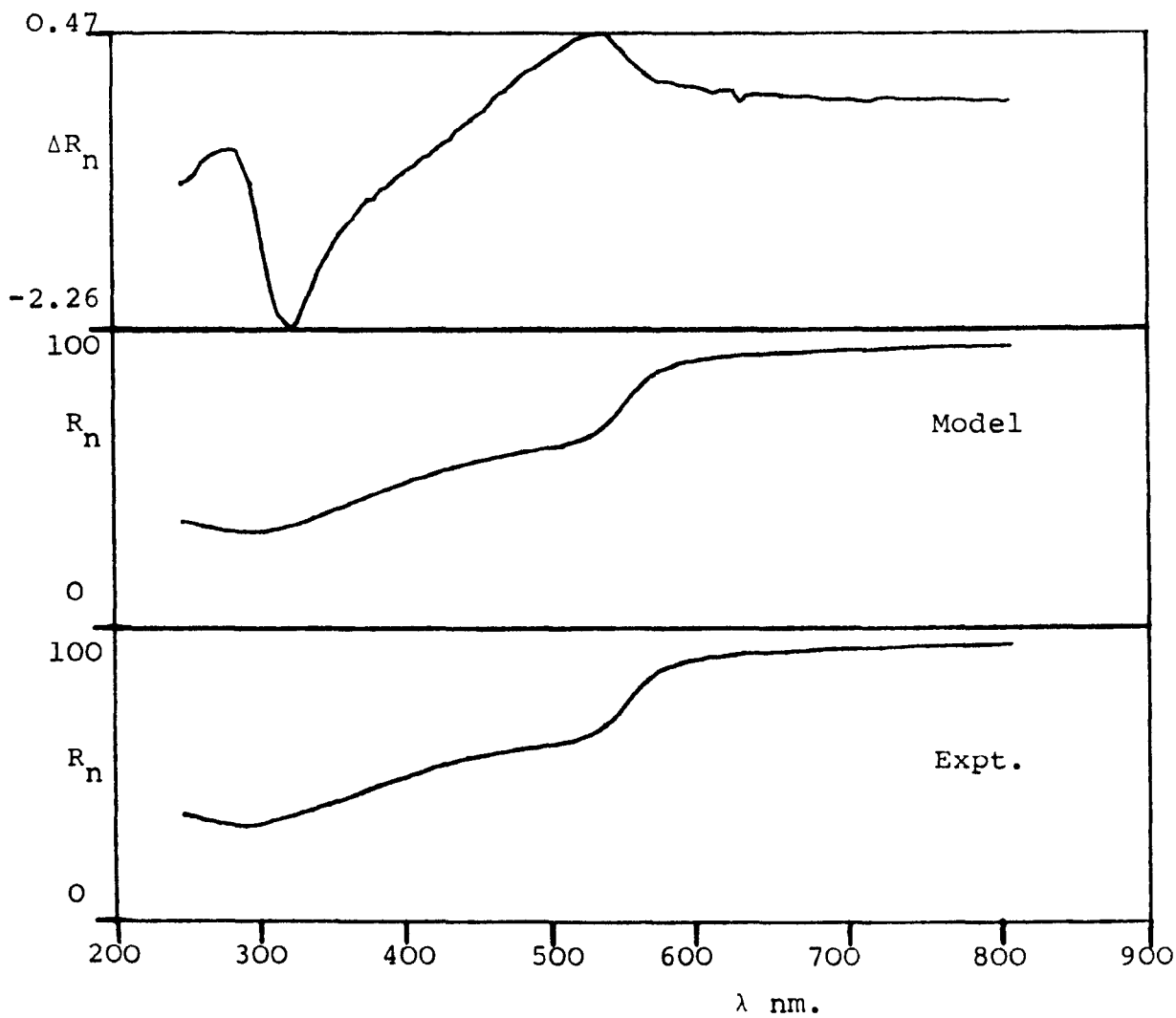


Figure 6.18 Comparison between modelled and experimental normal reflectance spectra of alloy number 66.

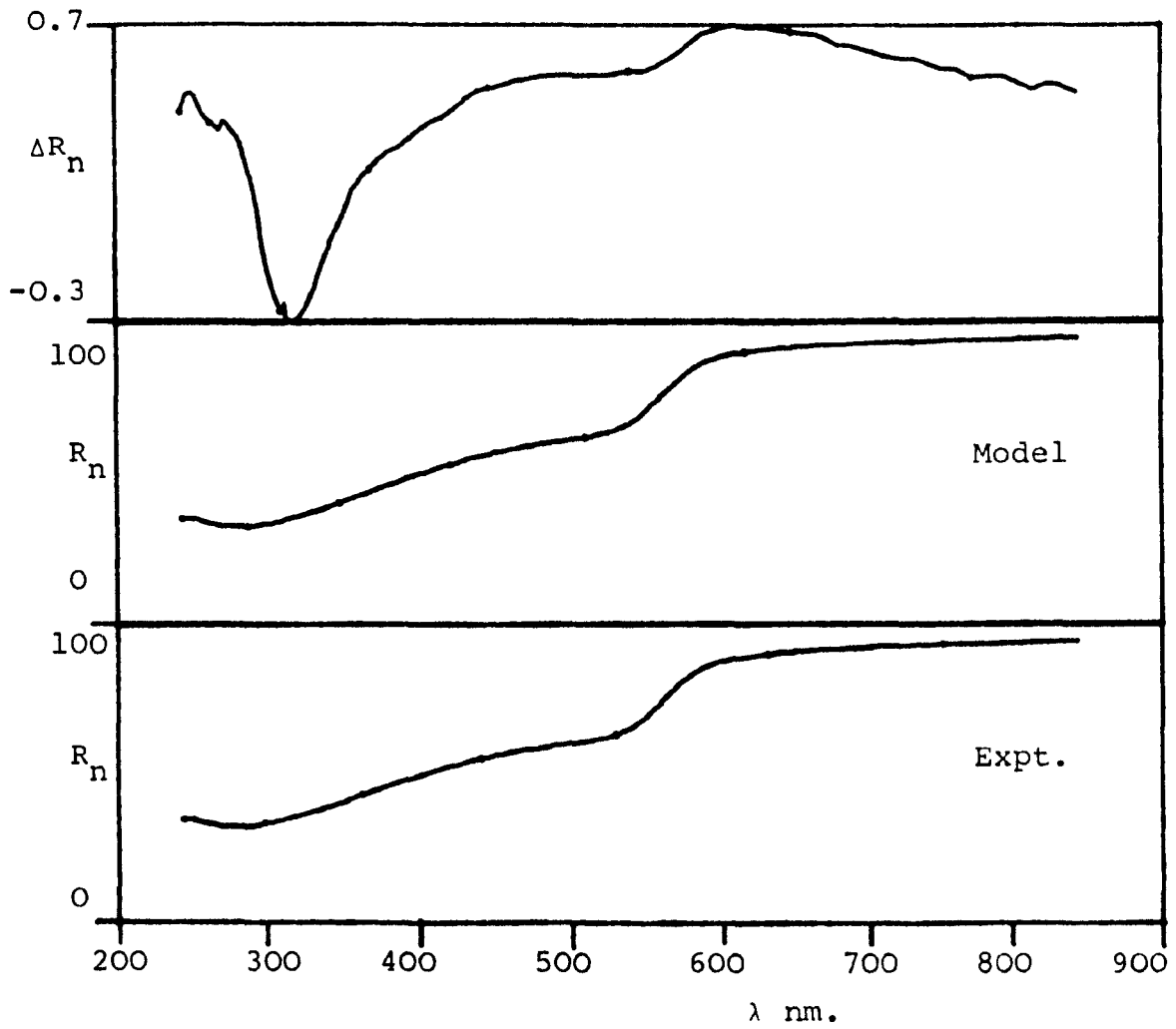


Figure 6.19 Comparison between modelled and experimental normal reflectance spectra of alloy number 58.

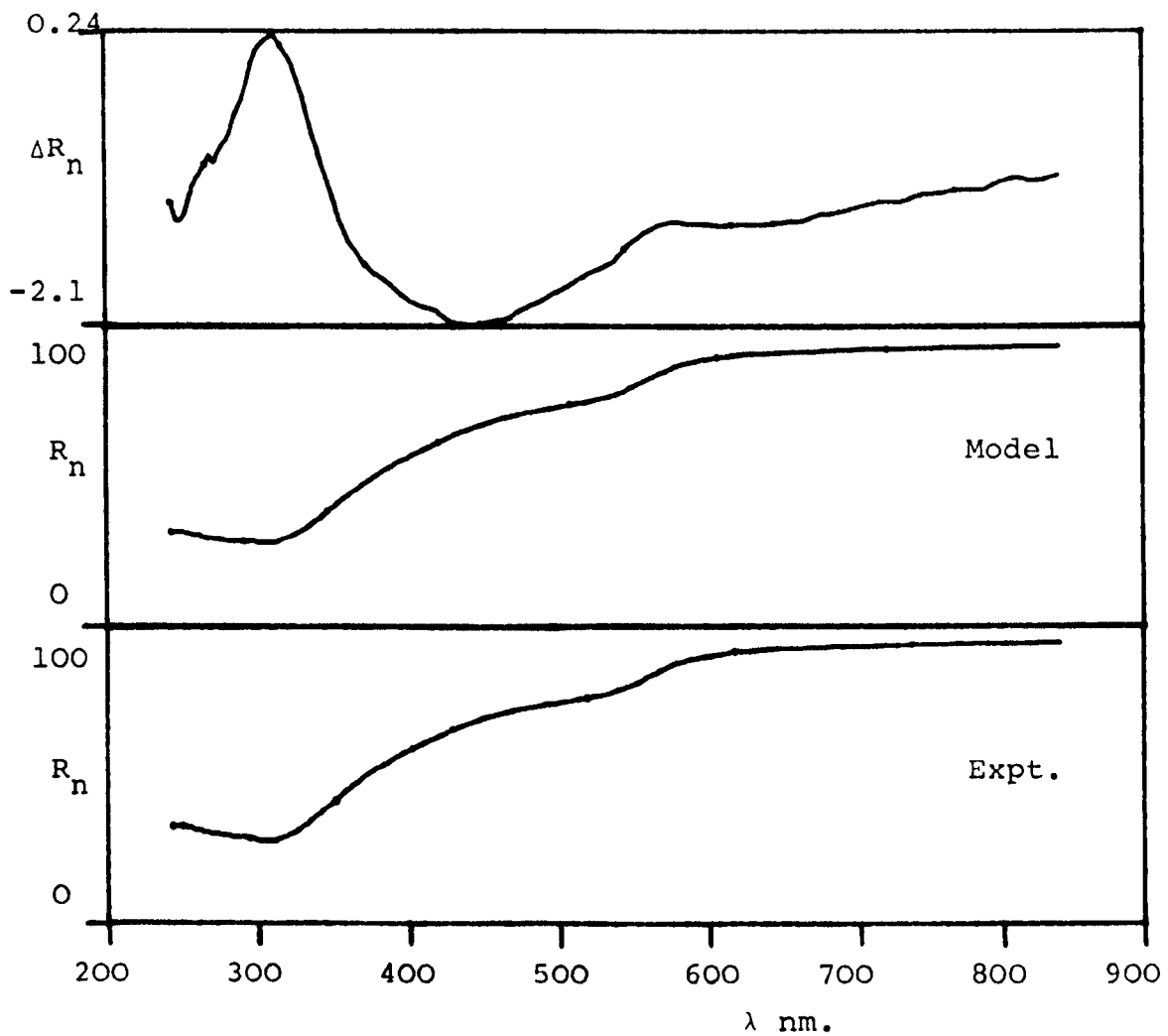


Figure 6.20 Comparison between modelled and experimental normal reflectance spectra of alloy number 55.

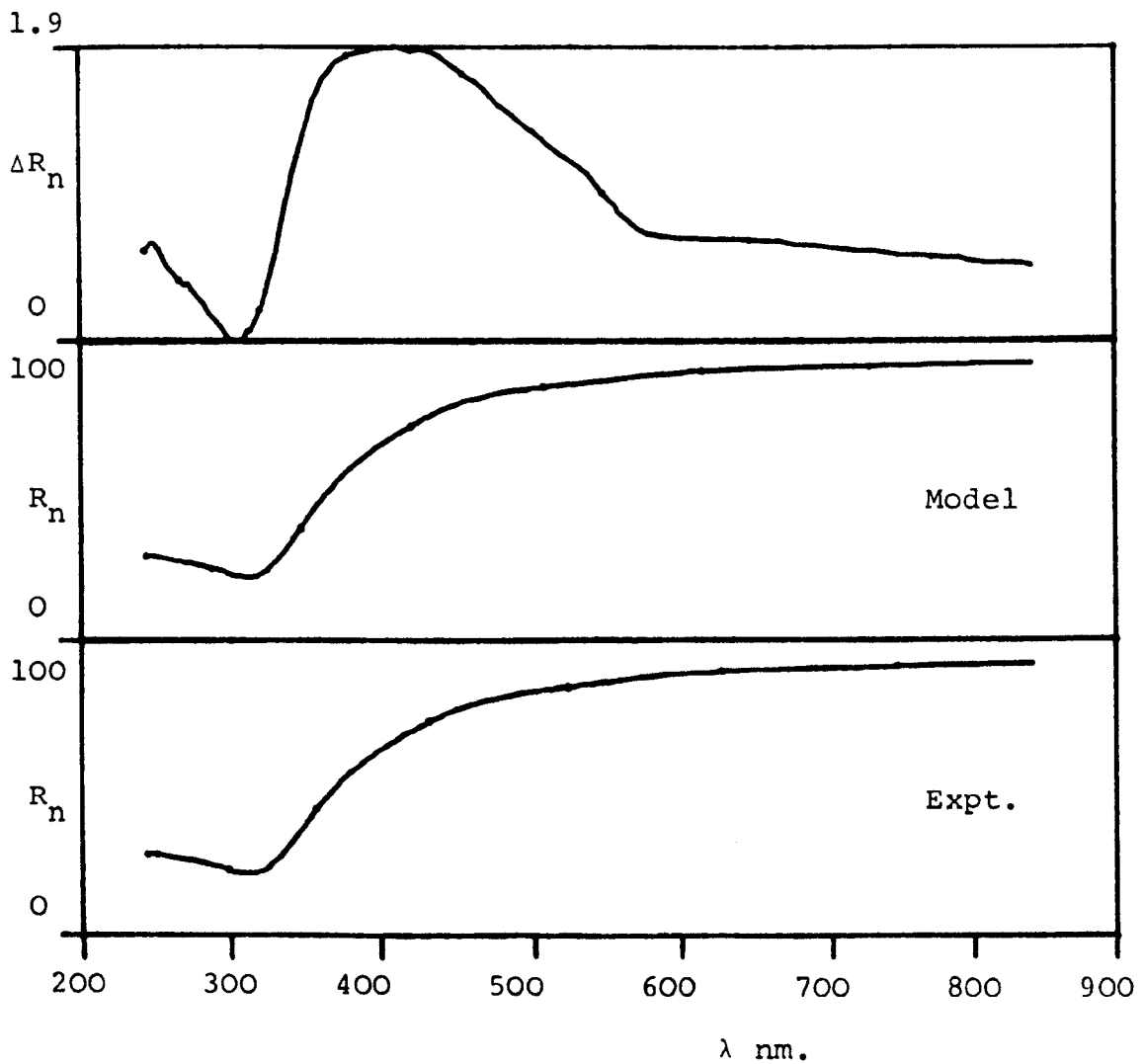


Figure 6.21 Comparison between modelled and experimental normal reflectance spectra of alloy number 52.

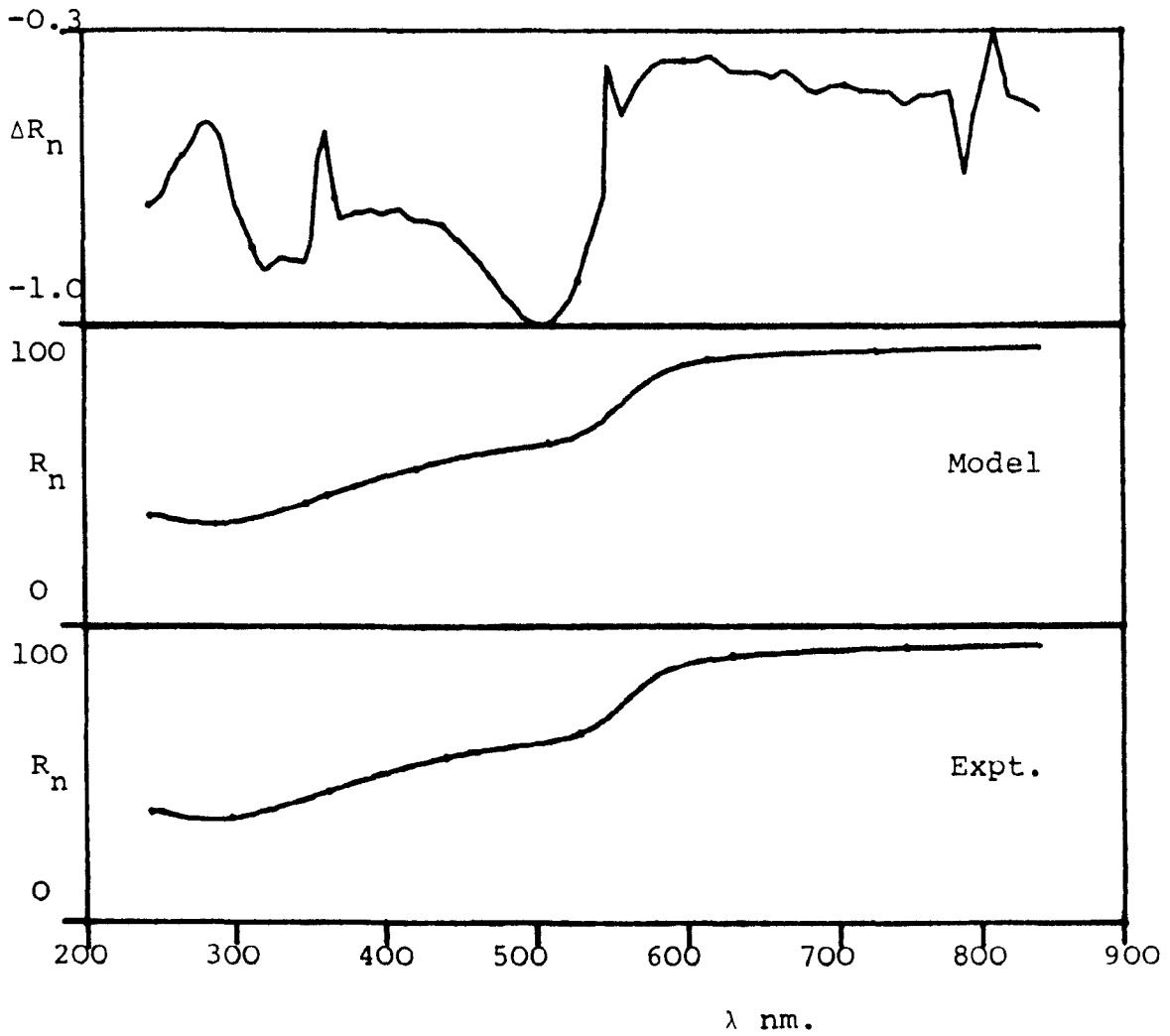


Figure 6.22 Comparison between modelled and experimental normal reflectance spectra of alloy number 51.

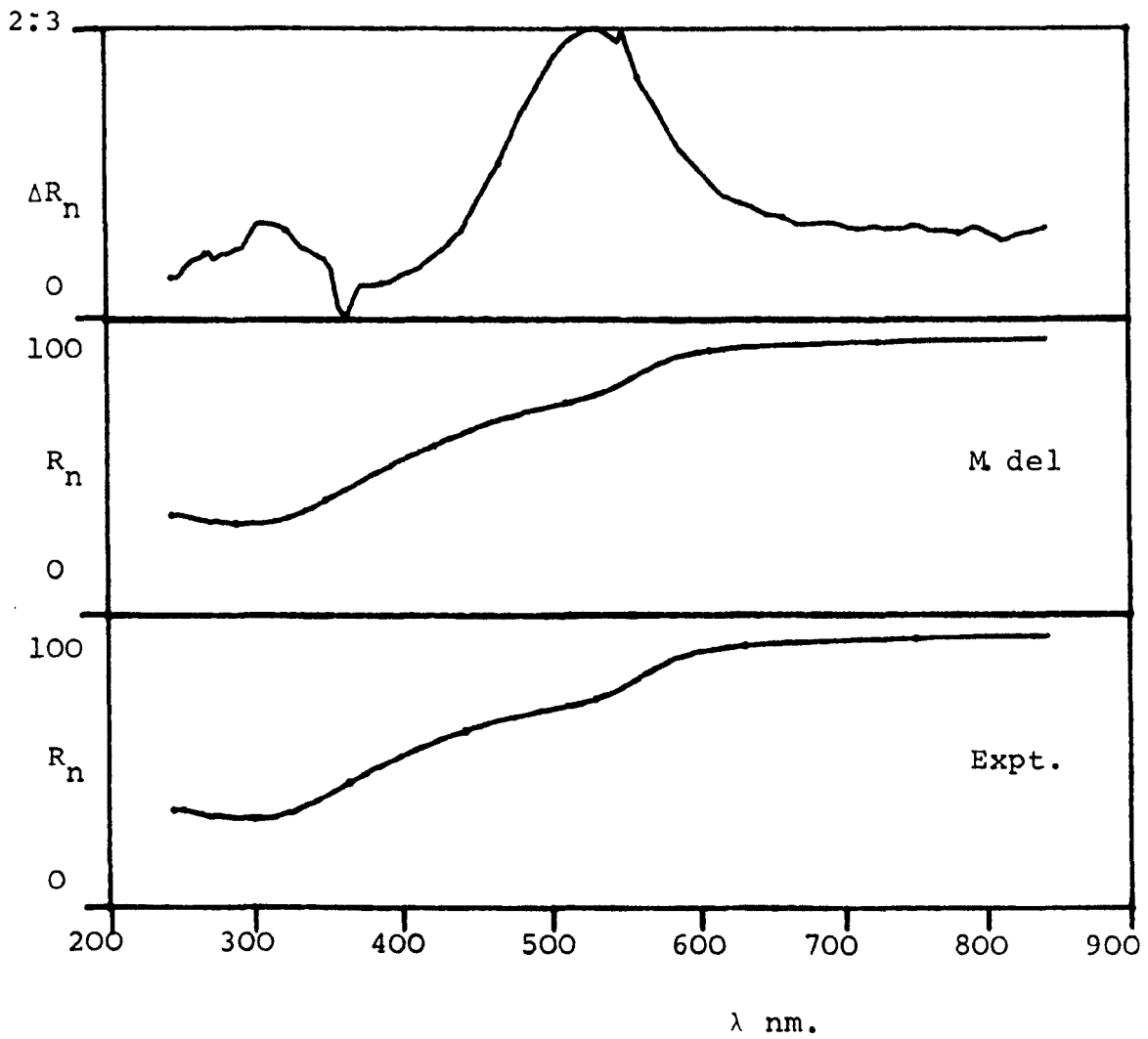


Figure 6.23 Comparison between modelled and experimental normal reflectance spectra of alloy number 49.

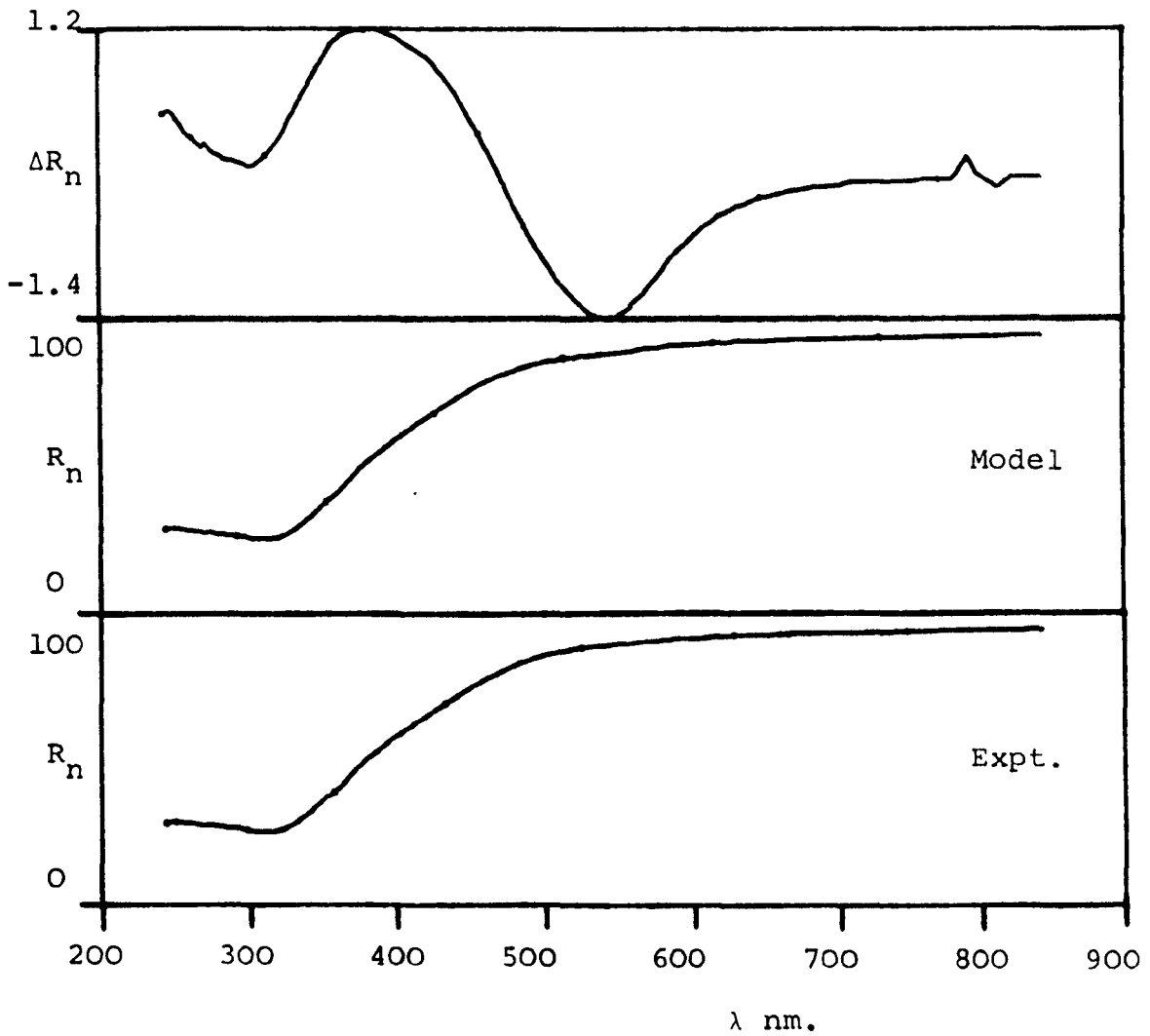


Figure 6.24 Comparison between modelled and experimental normal reflectance spectra of alloy number 46R.

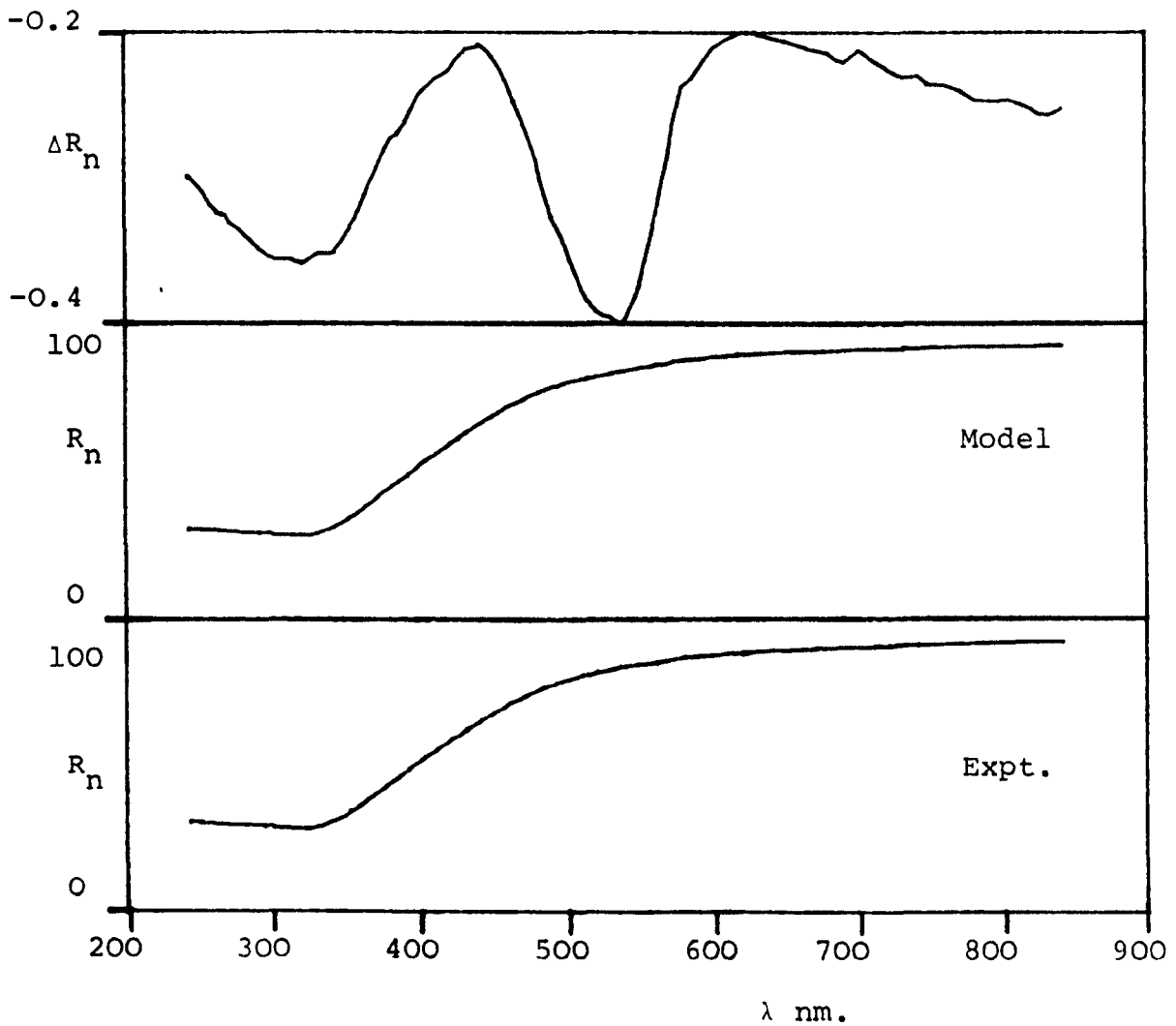


Figure 6.25 Comparison between modelled and experimental normal reflectance spectra of alloy number 41.

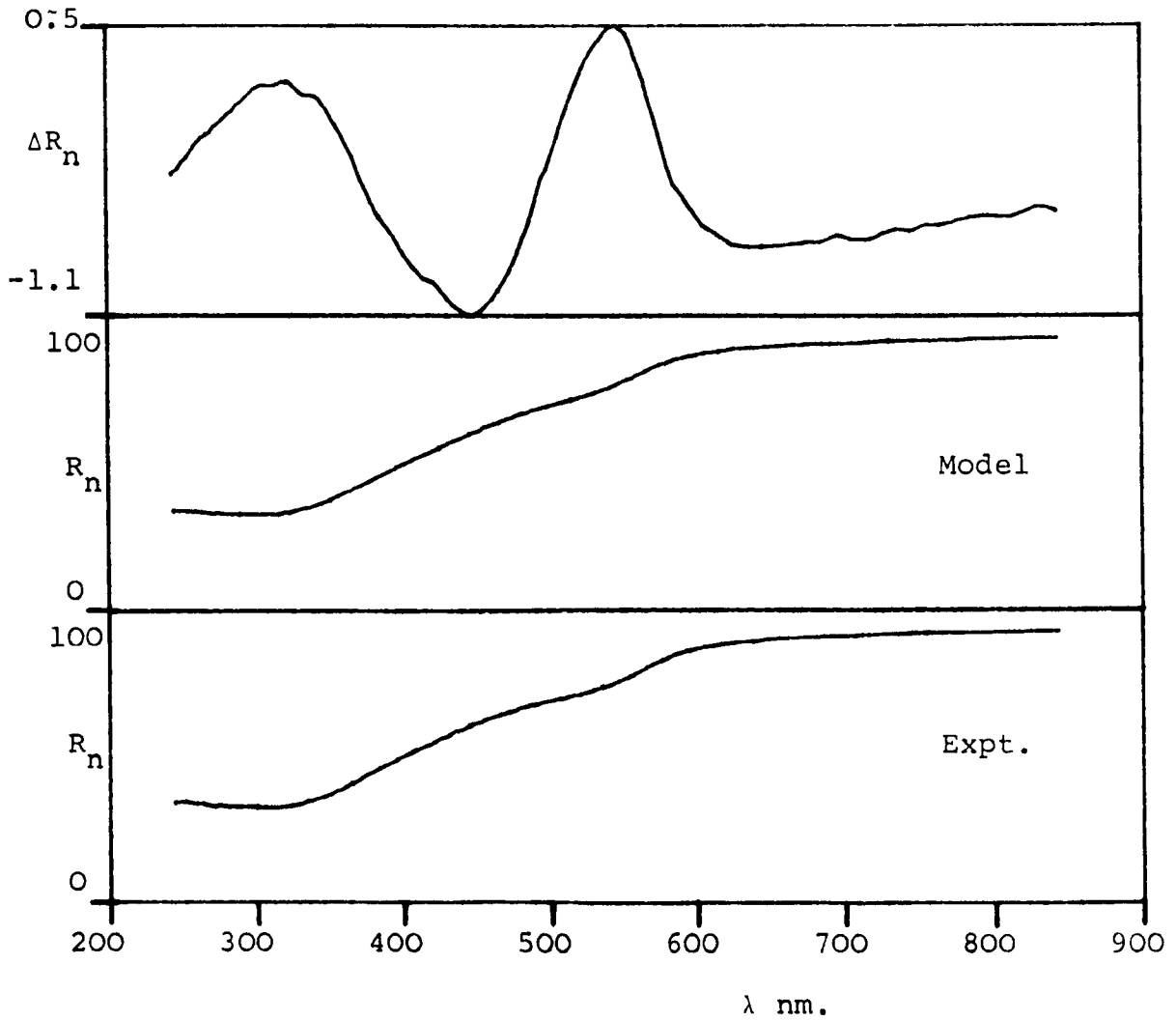


Figure 6.26 Comparison between modelled and experimental normal reflectance spectra of alloy number 43.

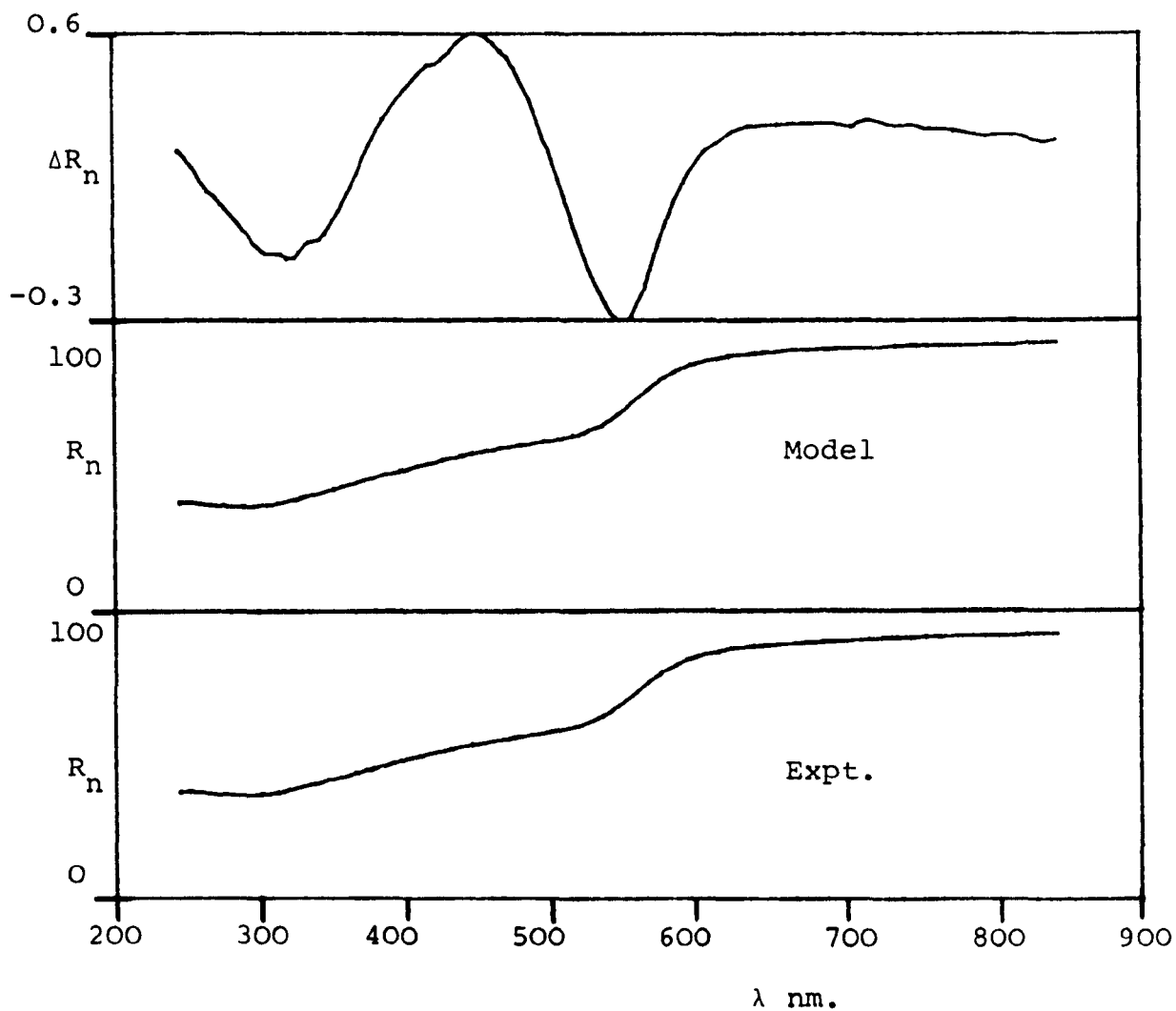


Figure 6.27 Comparison between modelled and experimental normal reflectance spectra of alloy number 45R.

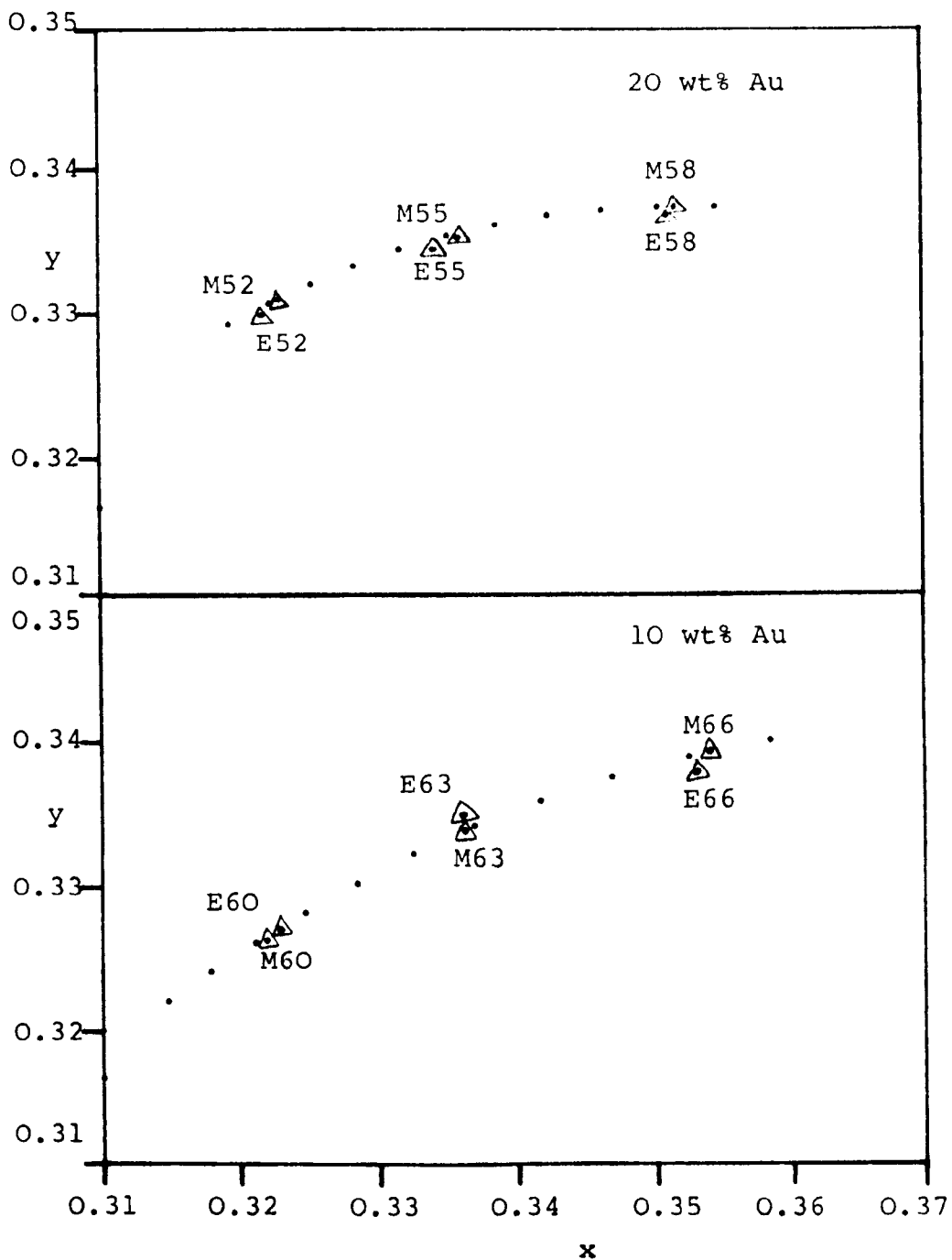


Figure 6.28 Colour locus in the 1931 CIE Lxy chromaticity diagram between the terminal solid solutions predicted by the model (prefixed M) in 10% volume fraction increments compared to experimentally determined values (prefixed E).

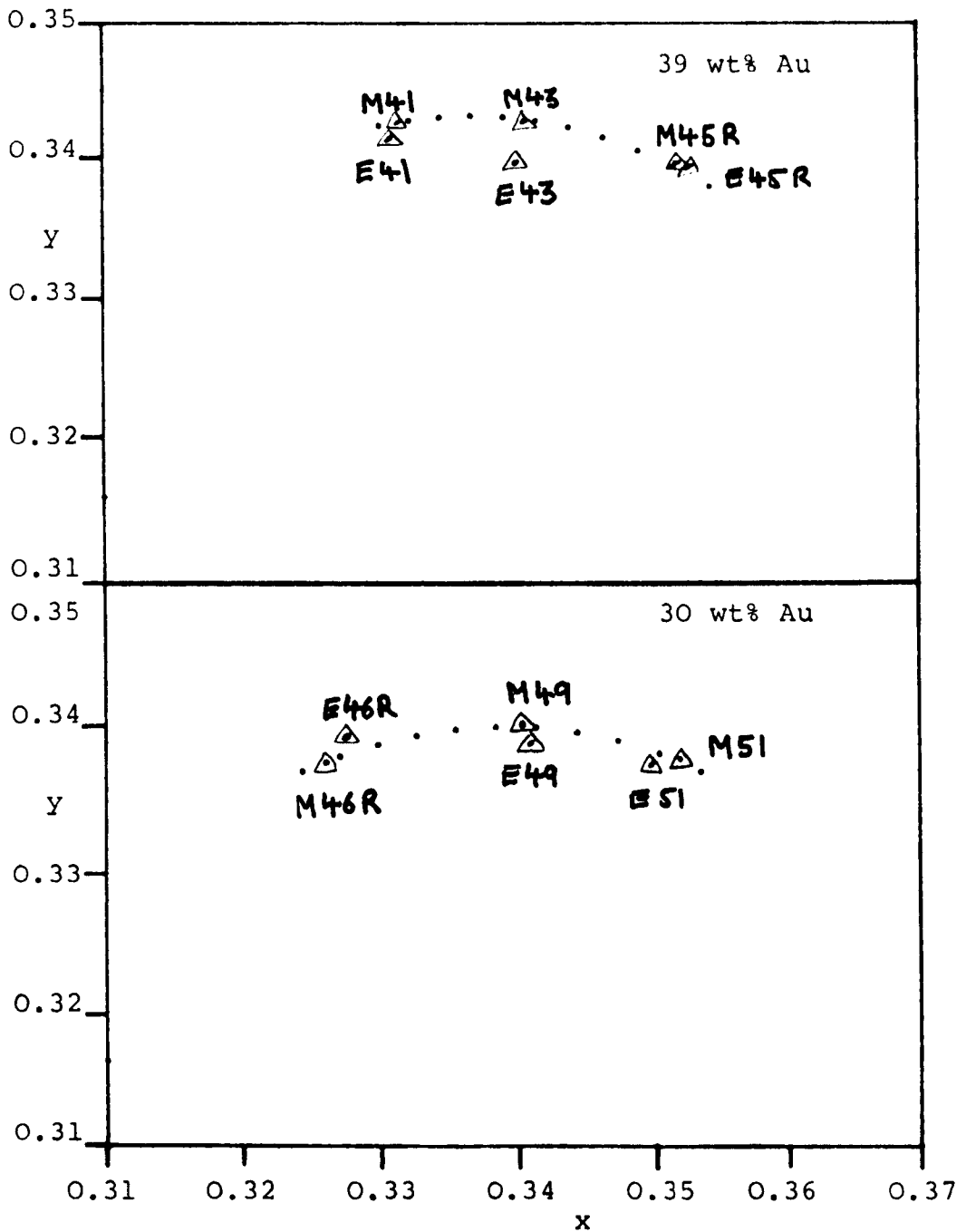


Figure 6.29 Colour locus in the 1931 CIE Lxy I11. 'C' colour diagram between the terminal solid solutions predicted by the model (prefixed M) in 10% volume fraction increments compared to experimentally determined values (prefixed E).

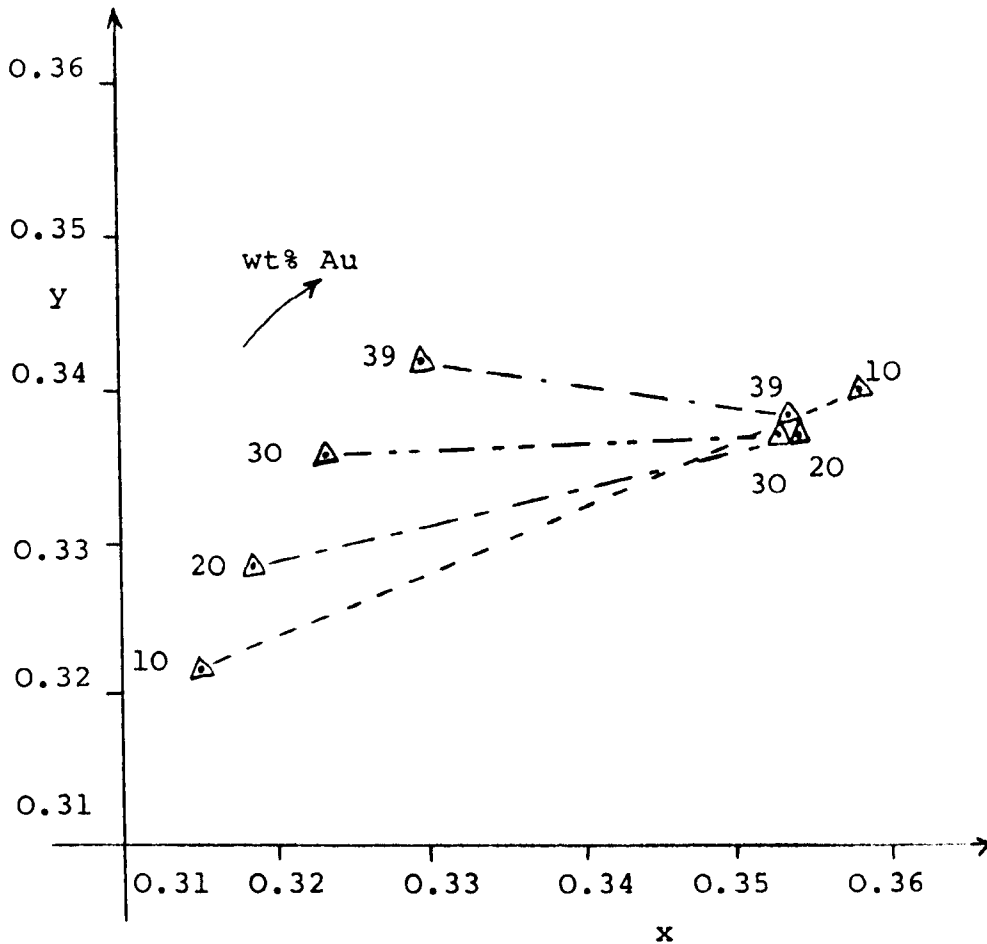


Figure 6.30 Revised colour loci of the duplex-phase alloys in the 1931 CIE Lxy Ill. 'C' diagram.

| | | |
|---------|-----------------|---|
| Gold: | 2.5 eV (496nm) | Erlbach (1969a) |
| | | d-band to Fermi surface. |
| | 3.5 eV (354nm) | Erlbach (1969b) |
| | | upper conduction band to Fermi surface. |
| Silver: | 3.85 eV (320nm) | Rivory (1969) |
| | | d-band to Fermi surface. |
| Copper: | 2.15 eV (577nm) | Hollstein (1977) |
| | | d-band to Fermi surface. |

Table 6.1 Energies and wavelengths of the absorption edges present in gold, silver and copper in the visible wavelength range.

| Nominal At% Au | Alloy No. | At% Au | u | v |
|-------------------|-----------|--------|--------|--------|
| 60 | 31 | 60.3 | 0.2185 | 0.3271 |
| 40 | 34 | 40.7 | 0.2094 | 0.3256 |
| | 35 | 38.1 | 0.2147 | 0.3240 |
| 20 | 43 | 20.7 | 0.2123 | 0.3190 |
| | 44 | 20.3 | 0.2157 | 0.3193 |

Table 6.2 Colour co-ordinates in the 1960 UCS scheme of alloys in this study similar in composition to the loci of Starenko and Lifshits (1974).

| Alloy Composition (nominal) | Proportion of α -phase | |
|--------------------------------|--------------------------------|----------------|
| | Phase diagram Clarke (1980) | Ellipsometry |
| 30Ag-70Cu | 26.2 | 25.1 \pm 2.1 |
| 60Ag-40Cu | 58.3 | 55.1 \pm 1.4 |
| 70Ag-30Cu | 67.6 | 67.3 \pm 2.7 |

Table 6.3 Comparison between the phase proportions of three Ag-Cu alloys derived from the phase diagram and by ellipsometry using the two-phase model.

| Wavelength (nm) | α -phase | | | |
|--------------------|-----------------|--------|----------|----------|
| | Model | Expt. | Model | Expt. |
| | Ψ | Ψ | Δ | Δ |
| 400 | 42.17 | 42.46 | 61.08 | 62.30 |
| 410 | 42.45 | 42.67 | 63.34 | 64.44 |
| 420 | 42.68 | 42.84 | 65.34 | 66.36 |
| 430 | 42.91 | 43.01 | 67.40 | 68.38 |
| 440 | 43.12 | 43.20 | 69.40 | 70.39 |
| 450 | 43.30 | 43.34 | 71.45 | 72.24 |
| 460 | 43.39 | 43.52 | 73.45 | 74.02 |
| 470 | 43.44 | 43.52 | 75.34 | 75.80 |
| 480 | 43.42 | 43.62 | 77.32 | 77.50 |
| 490 | 43.38 | 43.62 | 79.08 | 79.20 |
| 500 | 43.48 | 43.65 | 80.80 | 80.70 |

Table 6.4 Comparison between experimental and modelled data of the AgCu and CuAg terminal solid solutions.

contd./

| Wavelength (nm) | β -phase | | | |
|--------------------|----------------|--------|----------|----------|
| | Model | Expt. | Model | Expt. |
| | Ψ | Ψ | Δ | Δ |
| 400 | 32.74 | 31.94 | 61.00 | 61.90 |
| 410 | 33.08 | 32.25 | 61.96 | 62.66 |
| 420 | 33.37 | 32.60 | 62.88 | 63.56 |
| 430 | 33.65 | 32.96 | 63.90 | 64.68 |
| 440 | 33.89 | 33.23 | 64.80 | 65.58 |
| 450 | 34.15 | 33.51 | 65.76 | 66.66 |
| 460 | 34.36 | 33.75 | 66.61 | 67.48 |
| 470 | 34.53 | 33.98 | 67.36 | 68.24 |
| 480 | 34.72 | 34.27 | 68.12 | 68.72 |
| 490 | 34.90 | 34.54 | 68.74 | 69.48 |
| 500 | 35.05 | 34.75 | 69.21 | 69.72 |

Table 6.4 contd.

α -phase

| Wt% Au | x | y | Lum. % | Sat. % |
|--------|--------|--------|--------|--------|
| 10 | 0.3148 | 0.3217 | 90.2 | 2.8 |
| 20 | 0.3185 | 0.3283 | 89.1 | 5.5 |
| 30 | 0.3233 | 0.3359 | 90.5 | 8.9 |
| 39 | 0.3294 | 0.3421 | 86.4 | 12.2 |

 β -phase

| Wt% Au | x | y | Lum. % | Sat. % |
|--------|--------|--------|--------|--------|
| 10 | 0.3587 | 0.3399 | 69.9 | 19.4 |
| 20 | 0.3544 | 0.3374 | 71.2 | 17.6 |
| 30 | 0.3533 | 0.3366 | 70.7 | 17.1 |
| 39 | 0.3541 | 0.3383 | 70.4 | 17.8 |

Table 6.5 Colour co-ordinates of the terminal solid solutions calculated from the two-phase model in the CIE 1931 Lxy scheme under illuminant 'C'.

CHAPTER SEVEN

FURTHER WORK

The two-phase model which has been developed shows the manner in which a nulling ellipsometer averages the optical properties of a two-phase surface. The discussion was limited to incoherent illumination since the ellipsometer used was designed for use with this type of illumination; the model, however, is not subject to this limitation and can be developed for coherent illumination.

The derivation for coherent illumination is analogous to the incoherent case with the exception of adding weighted Jones matrices in place of Mueller matrices. Thus defining the substrate phases α and β to have their properties described by a Jones matrix of the form

$$T_k = \begin{pmatrix} r_{sk} & 0 \\ 0 & r_{pk} \end{pmatrix}$$

where r_{sk} and r_{pk} are the complex amplitude reflection coefficients in the p-s directions of the k^{th} phase.

We obtain the matrix equation which describes the reflected wave amplitude as

$$\begin{aligned} E_\alpha + E_\beta \\ = (1 - Q)^{\frac{1}{2}} T_\alpha E_I + Q^{\frac{1}{2}} T_\beta E_I \end{aligned}$$

note:- the surface area proportions and thus intensity proportions are $(1 - Q)$ and Q , the amplitude proportions are thus $(1 - Q)^{\frac{1}{2}}$ and $Q^{\frac{1}{2}}$.

Equating this to a single-phase substrate gives

$$T_s E_I = \{ (1 - Q)^{\frac{1}{2}} T_\alpha + Q^{\frac{1}{2}} T_\beta \} E_I$$

$$T_s = (1 - Q)^{\frac{1}{2}} T_\alpha + Q^{\frac{1}{2}} T_\beta$$

two matrices are equal when corresponding elements are equal thus

$$r_s = (1 - Q)^{\frac{1}{2}} r_{s\alpha} + Q^{\frac{1}{2}} r_{s\beta}$$

$$r_p = (1 - Q)^{\frac{1}{2}} r_{p\alpha} + Q^{\frac{1}{2}} r_{p\beta}$$

and for m-phases

$$r_s = \sum_{i=1}^m Q_i^{\frac{1}{2}} r_{si}$$

$$r_p = \sum_{i=1}^m Q_i^{\frac{1}{2}} r_{pi}$$

the effective single-phase parameter ρ is then

$$\rho = \frac{r_p}{r_s} = \tan \Psi \exp i\Delta$$

The variation of Ψ and Δ as a function of volume fraction Q is shown in figure 7.1, the variation predicted by incoherent illumination is also shown for comparison.

The dependence of Ψ and Δ upon volume fraction is seen to be markedly different between coherent and incoherent illumination, in particular at small volume fractions of either α or β phases.

Consider an alloy in which the α -phase matrix contains a small volume fraction of β -phase, the theory predicts that simply by changing from coherent to incoherent illumination will cause the Ψ and Δ values to change by

several tenths of a degree. This change is well within the resolution of an ellipsometer. In principle the ellipsometer is capable of resolving Ψ and Δ to 0.003 degrees, this implies that a 0.01% β -phase precipitate is observable. In practice, however, the resolution will not be achieved as changing from a broadband filtered source to a laser will cause a small change in alignment and dispersion in the substrate will degrade the accuracy with which the null is located.

The change in the coherency of the illumination appears to provide a technique for examining small changes in phase composition near to phase boundaries, with the ability to detect small volume fractions of a precipitate. The method would require the use of two sources, one coherent, e.g. laser, and the other incoherent, e.g. filtered broadband source, which are interchangeable without causing the optics to be re-aligned. The effect observed is a small incremental change in Ψ and Δ which relaxes the constraint of constructing an ellipsometer with a high absolute accuracy.

It is proposed that this effect be examined using an ellipsometer and a sample within a vacuum chamber where the sample's characteristics may be set by an annealing process which is well defined and reversible, such as annealing at a temperature which passes through a phase-boundary.

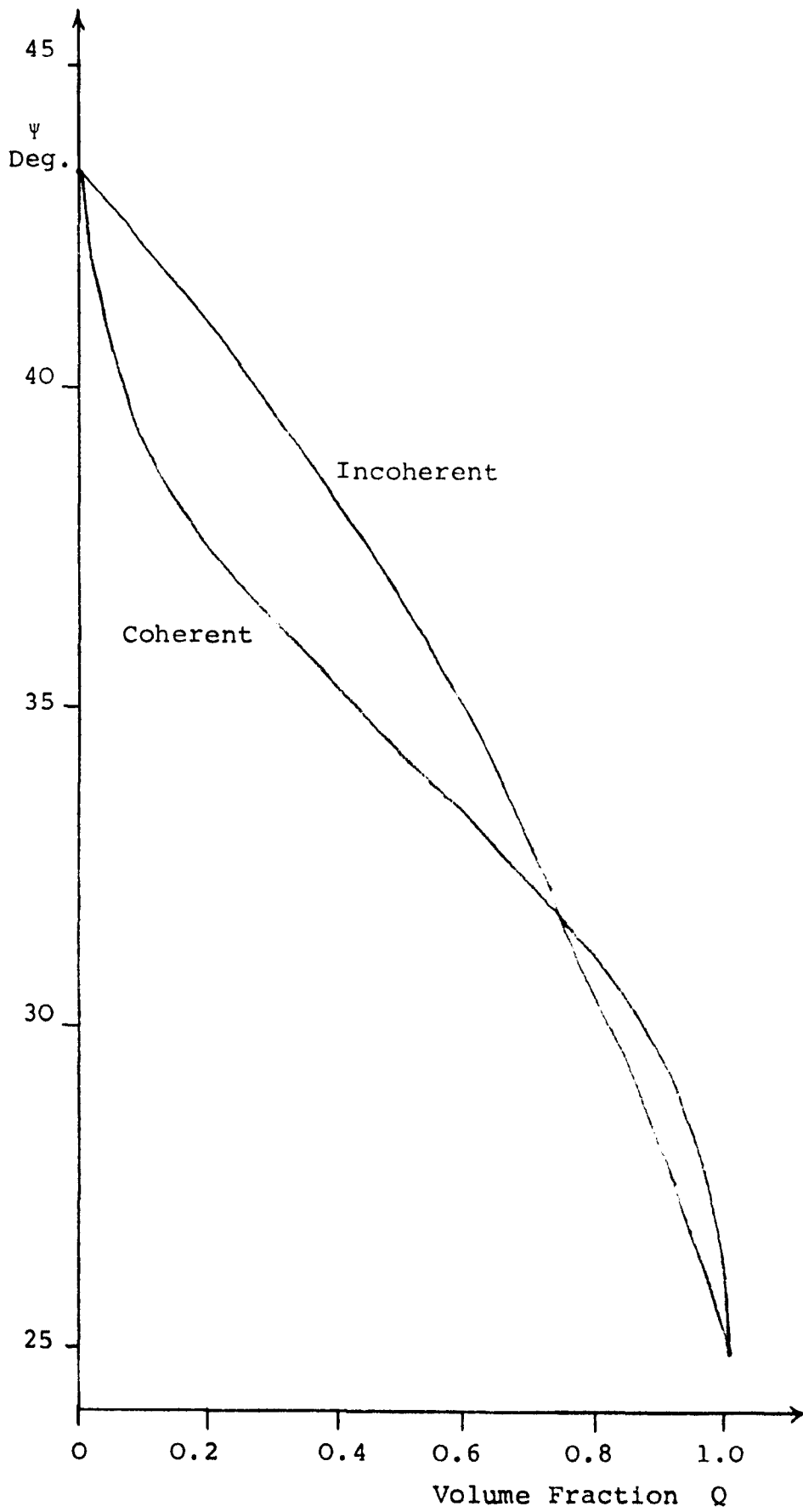


Figure 7.1 Dependence of ψ upon volume fraction
for coherent and incoherent illumination
184

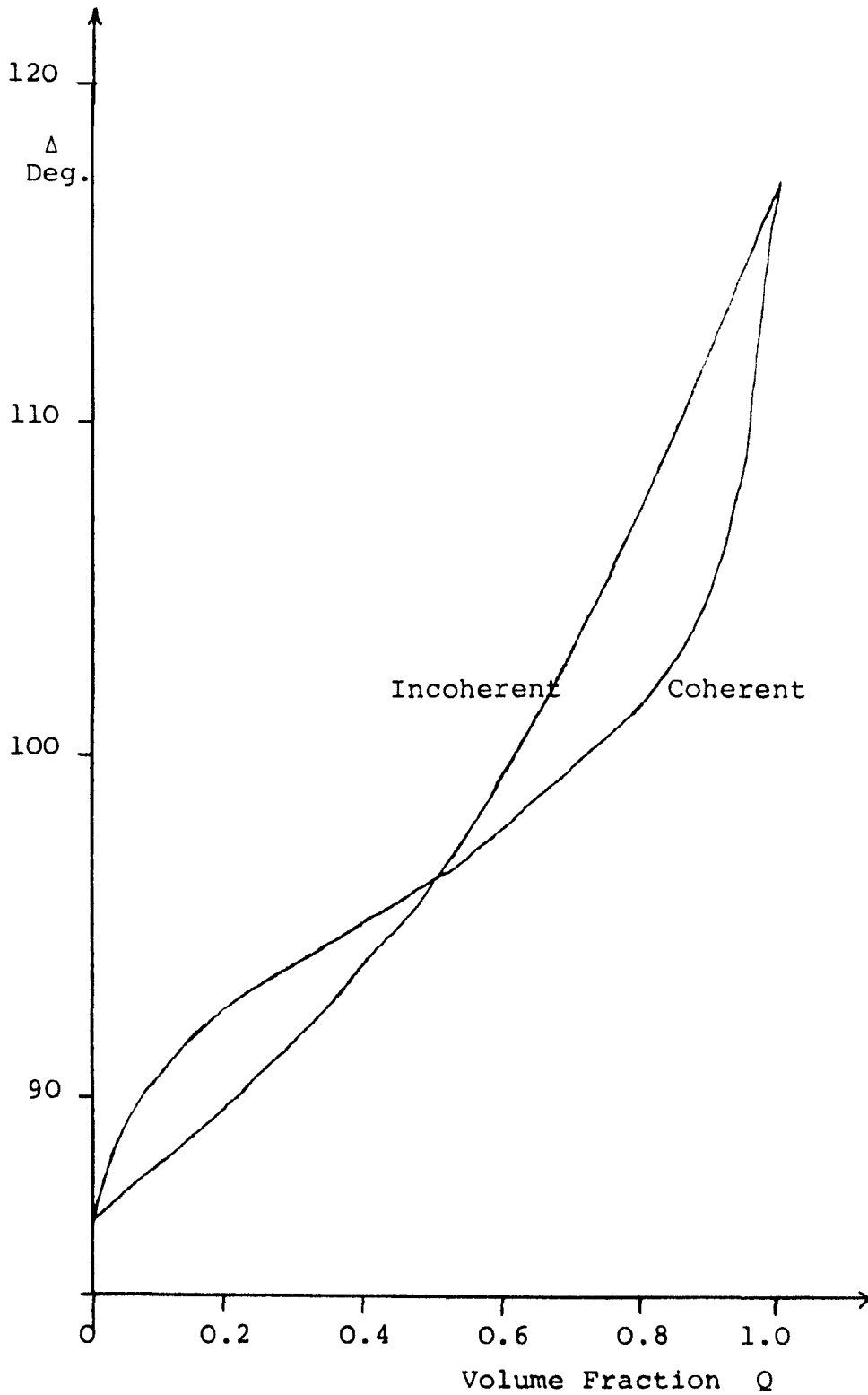


Figure 7.1 (contd) Dependence of Δ upon volume fraction for coherent and incoherent illumination.

References

- Aspnes D.E., Private Communication
- Azzam R.M.A. and Bashara N.M., J.Opt. Soc. Am.
61, 600, 1971 (a)
- Azzam R.M.A. and Bashara N.M., J. Opt. Soc. Am.
61, 773, 1971 (b)
- Azzam R.M.A. and Bashara N.M., J. Opt. Soc. Am.
61, 1118, 1971 (c)
- Azzam R.M.A. and Bashara N.M., J. Opt. Soc. Am.
61, 1236, 1971 (d)
- Azzam R.M.A. and Bashara N.M., J. Opt. Soc. Am.
61, 1380, 1971 (e)
- Azzam R.M.A. and Bashara N.M., J. Opt. Soc. Am.
62, 700, 1972
- Azzam R.M.A. and Bashara N.M., Ellipometry and
Polarised Light, North Holland Publishing
Company, 1977
- Bennett H.E. and Koehler W.F., J.Opt. Soc. Am.
50, 1, 1960
- Bouma P.J., Physical Aspects of Colour, MacMillan
and Co. Ltd. 1971
- Clapham P.B., Downs M.J. and King R.J., Applied
Optics 8, 1965, 1969
- Clarke K.M. Phd Thesis CNA A 1980
- El-Hosseiny F., J. Opt. Soc. Am. 65, 1279, 1975

Erlbach E. and Beaglehole D., Proc. Conf. on Electronic
Density of States Gaithersberg Ma. 1969(a)
Erlbach E. and Beaglehole D., Bull. Am. Phys. Soc. II
14, 322, 1969 (b)
Fukatani H., J. Phys. Soc. Japan 30, 399, 1971
German R.M., Guzowski M.M. and Wright D.C., Gold
Bulletin 1981
Gerrard A. and Burch J.M., Introduction to Matrix
Methods in Optics, John Wiley and Sons, London,
1975
Groenewald T., Quail R.W. and Krugel E., Research
Report No. 3/77, Worshipful Company of Goldsmiths
Guild J., Trans. Opt. Soc. (London), 27, 106, 1925-6
Holmes D.A., J. Opt. Soc. Am., 54, 1115, 1964
Holmes D.A., J. Opt. Soc. Am., 57, 466, 1967
Hollstein T., Kreibig U. and Leis F., Phys. Stat. Sol.
(b), 82, 545, 1977 (a)
Hollstein T., Kreibig U. and Leis F., Phys. Stat. Sol.
(b), 83, K49, 1977 (b)
Hunter W.R., Eaton D.H. and Soh C.T., Surface Sci.
20, 355.1970
Hunter W.R., J. Opt. Soc. Am., 63, 951, 1973
Jerrard H.G., J. Opt. Soc. Am., 42, 159, 1952
Jones R.C., J. Opt. Soc. Am., 31, 448, 1941 (a)
Jones R.C., J. Opt. Soc. Am., 31, 500, 1941 (b)
Jones R.C., J. Opt. Soc. Am., 32, 486, 1942
Kaye and Laby, Physical and Chemical Constants,
Longmans (1960)

Klein M.V., Optics, John Wiley and Sons Inc. 1970
 Kothiyal M.P., Applied Optics, 14, 2935, 1975
 Kothiyal M.P., J. Opt. Soc. Am., 65 352, 1975
 Kothiyal M.P., Applied Optics, 16, 1521, 1977
 Kothiyal M.P., Applied Optics, 17, 3350, 1978
 Kothiyal M.P., Applied Optics, 18, 1019, 1979
 Kuchni R.G., J. Opt. Soc. Am., 66, 497, 1976
 Leuser J., Metall, 3, 1949
 Lovibond J.W., J. Soc. Dyers Colourists, 3, 186, 1887
 M^CAdam D.L., J. Opt. Am., 32, 247, 1942
 M^CCrackin F.L., Passaglia E., Stromberg R.R. and
 Steinberg H.L., J. Res. Natl. Bur. Std.,
67A, 363, 1963
 M^CNichol E.F., Sci. Am., 211, 48, 1964
 M^CNichol E.F., Vision Research, 4, 119, 1964
 Mueller H., J. Opt. Soc. Am., 38, 661, 1948
 Muller R.H., Surface Sci., 16, 14, 1969
 Norton S.T. and M^CMullon J.G., Met. Trans.,
1, 46, 1949
 Oxley A.E., Phil. Mag., 21, 517, 1911
 Parkes R.E., Sumner R.E. and Appels J.T., J. Opt. Eng.
16, 332, 1977
 Poincaré H., Théorie Mathématique de la Lumière,
 Gauthiers-Villars Paris, 1892, Vol. II Ch. 12
 Rivory J., Opt. Comm., 1, 53, 1969
 Rivory J., Phys. Rev. B, 15, 3119, 1977

- Roberts E.F.I., Final Report on ' Optical Properties
of Metals and Alloys ', Worshipful Company of
Goldsmiths, London, 1978
- Roberts E.F.I., Clarke K.M. and Hunt R., Mats. Sci. &
Eng., 42, 71, 1980
- Roberts E.F.I. and Hunt R., Optica Acta, 29, 1683, 1982
- Ruston W.A.H., Farke, 4, 218, 1955
- Starenko I.P. and Lifshits V.A., Sbornk. Trudou. Vses
Nauchno-issled Proekt-konstrukt Inst. Yuvelir
Prom., 5, 1974
- Stiles W.S., Phys. Soc. Year Book, 1955
- Stokes G.G., Trans. Camb. Phil. Soc., 9, 339, 1852
- Winterbottom A.B., Royal Norwegian Sci. Soc. Rept.
No. 1, (F.Bruns, Trondheim, 1955)
- Wald G., Nat. Phys. Lab. Symp. No. 8 (1957)
- Wise E.M., Gold-recovery, properties and applications,
(D Van Nostrand Inc) pp.262 (1964)
- Wooten F., Optical Properties of Solids, Academic Press
1972
- Wright W.D., Trans. Opt. Soc., 29, 225, 1927-8
- Wright W.D., Proc. Phys. Soc. (London), 53, 93, 1941
- Wyszecki G. and Stiles W.S., Colour Science,
John Wiley and Sons, 1967

Appendix A

Listing of the Fortran IV program which calculates the volume fractions of a two-phase alloy from Ψ and Δ values of the alloy and its' terminal solid solutions.

```

TYPE RHTPHS.F4
C*****
C
C      CALCULATES THE BETA-PHASE PROPORTION ( Q ) OF AN ALLOY
C      FROM EXPERIMENTAL DATA OF THE ALLOY AND TERMINAL
C      SOLID-SOLUTIONS. ALL ANGLES IN DEGREES.
C*****
      EXTERNAL MONIT
      DOUBLE PRECISION FILEN1,FILEN2,FILEN3
      COMMON W(4)
      COMMON/MODEL/PA,DA,PB,DB,PSI,DELTA,PE,DE,Q
      REAL X(1),E(1)
      TYPE 100
100    FORMAT(1H , 'ENTER THE ALPHA,BETA AND ALLOY FILENAMES ')
      ACCEPT 110,FILEN1,FILEN2,FILEN3
110    FORMAT(3A10)
      OPEN(UNIT=1,DEVICE='DSK',FILE=FILEN1,ACCESS='SEQIN')
      OPEN(UNIT=2,DEVICE='DSK',FILE=FILEN2,ACCESS='SEQIN')
      OPEN(UNIT=3,DEVICE='DSK',FILE=FILEN3,ACCESS='SEQIN')
      E(1)=1E-6
      X(1)=1.0
      NX=1
      ESCALE=1E4
      KPRINT=0
      ICON=2
      MAXIT=50
      IFAIL=0
      READ(1,130) A1,A2,NP
      READ(2,130) A1
      READ(3,130) A1
130    FORMAT(1H ,/,3G)
      ERS=0.0
      QS=0.0
      SQ=0.0
      DO 140 I1=1,NP
      READ(1,150) WAV,ANAA,POLA
      READ(2,150) WAV,ANAB,POLB
      READ(3,150) WAV,ANAE,POLE
150    FORMAT(3F)
      PA=45.0-ANAA
      DA=2.0*POLA
      PB=45.0-ANAB
      DB=2.0*POLB

```

```

PE=45.0-ANAE
DE=2.0*POLE
CALL VAO4A(X,E,NX,F,ESCALE,KPRINT,ICON,MAXIT-MONIT,IFALL)
CALL CALCFX(NX,X,ERROR)
ERS=ERS+ERROR
QS=QS+Q
SQ=SQ+Q*Q
140 CONTINUE
ERMEAN=ERS/NP
QMEAN=QS/NP
QSIGMA=SQRT(SQ/NP-QM*QM)
TYPE 160,QMEAN,QSIGMA,ERMEAN
160 C FORMAT(1H,'VOLUME FRACTION OF BETA-PHASE = ',F7.4,3X
, 'SIGMA = ',F7.4,/' R.M.S. ERROR = ',F7.4,3X,'(DEG)')
STOP
END
SUBROUTINE CALCFX(NX,X,ERROR)
COMPLEX NAA
DIMENSION X(NX)
COMMON/MODEL/ PA,DA,PB,DB,PSI,DELTA,Q
NAA=CMPLX(1.0,0.0)
Q=X(1)*X(1)/(1.0+X(1)*X(1))
CALL INCOHERENT(PA,DA,PB,DB,Q,PSI,DELTA)
ERROR=SQRT((PSI-PE)**2+(DELTA-DE)**2)/2.0
RETURN
END
SUBROUTINE MONIT(NX,X,ERROR,ITERC)
REAL X(NX)
COMMON/MODEL/PA,DA,PB,DB,PSI,DELTA,PE,DE,Q
CALL CALCFX(NX,X,ERROR)
TYPE 100,Q,ERROR
100 C FORMAT(1H,'VOLUME FRACTION OF BETA-PHASE = ',F7.4,/'
, 'RMS ERROR = ',F7.4,3X,'(DEG.)')
RETURN
END

```

```

C*****
C
C      INCOHERENT ADDITION OF TWO STOKES-VECTORS FOR A TWO-PHASE
C      ALLOY. THE VOLUME FRACTION OF THE BETA-PHASE IS Q.
C      ALL ANGLES IN DEGREES.
C
C*****
C      SUBROUTINE INCOHERENT(PA,DA,PB,DB,Q,PSI,DELTA)
C      COMPLEX RS,RP,RSA,RPA,RSB,RPB,NAA,NS
C      REAL MRSA,MRPA,MRSB,MRPB,MRSPA,MRSPB
C      PHI=75.0
C      NAA=CMPLX(1.0,0.0)
C      QA=1.0-Q
C      PI=1.0
C      PA=PA*PI
C      DA=DA*PI
C      PB=PB*PI
C      DB=DB*PI
C      CALL RHSUBS(NAA,NS,PA,DA,PHI)
C      CALL RHREFL(NAA,NS,PHI,RSA,RPA)
C      CALL RHSUBS(NAA,NS,PB,DB,PHI)
C      CALL RHREFL(NAA,NS,PHI,RSB,RPB)
C      MRSPA=CABS(RSA)*CABS(RPA)
C      MRSA=CABS(RSA)
C      MRSPB=CABS(RSB)*CABS(RPB)
C      MRSB=CABS(RSB)
C      MRPB=CABS(RPB)
C      MRPA=CABS(RPA)
C      PSI=ATAN(SQRT((QA*MRPA*MRPA+Q*MRPB*MRPB)/(QA*MRSA*MRSA+
C Q*MRSB*MRSB)))*57.295779
C      DELTA=ATAN2((QA*MRSPA*SIND(DA)+Q*MRSPB*SIND(DB))
C , (QA*MRSPA*COSD(DA)+Q*MRSPB*COSD(DB)))*57.295779
C      IF(DELTA.LT.0.0) DELTA=DELTA+180.0
C      RETURN
C      END

```

```

C *****
C
C     COMPLEX REFRACTIVE INDICES OF A SURFACE, FROM R.I. AND
C     ANGLE OF INCIDENCE. ALL ANGLES IN DEGREES.
C
C *****
C     SUBROUTINE RHREFL(NAA,NS,PHI,RS,RP)
C     COMPLEX NAA,NS,RS,RP,A1,A2,A3,A4,CCOST,SINTT
C     SINTT=NAA*SIND(PHI)/NS
C     CCOST=CSQRT(1.0-SINTT*SINTT)
C     A1=NAA*COSED(PHI)
C     A2=NS*CCOST
C     RS=(A1-A2)/(A1+A2)
C     A3=NS*COSED(PHI)
C     A4=NAA*CCOST
C     RP=(A3-A4)/(A3+A4)
C     RETURN
C     END

C *****
C
C     RHSUBSATE N,K FROM PSI,DELTA,PHI AND AMBIENT R.I.
C     ALL ANGLES IN DEGREES.
C
C *****
C     SUBROUTINE RHSUBS(NAA,NS,PSI,DELTA,PHI)
C     COMPLEX NAA,NS,RO
C     TANPSI=SIND(PSI)/COSED(PSI)
C     TANPHI=SIND(PHI)/COSED(PHI)
C     RO=CMPLX((TANPSI*COSED(DELTA)),TANPSI*SIND(DELTA))
C     NS=NAA*TANPHI*CSQRT(1.0-4.0*RO*SIND(PHI)*SIND(PHI)/(RO+1.0)**2)
C     RETURN
C     END

```

Note: the subroutine VAO4A is a modified error minimisation routine described by Clarke(1980).

Appendix B

Listing of the Fortran IV program which calculates the Ψ and Δ of the terminal solid solutions from Q_i , Ψ_i and Δ_i of three duplex-phase alloys.

```

C*****
C      CALCULATION OF THE PSI-DELTA PAIRS FOR THE TERMINAL
C      SOLID-SOLUTIONS FROM THREE TWO-PHASE EXPTS. OF KNOWN
C      VOLUME FRACTION ( Q ) OF BETA-PHASE.
C      ALL ANGLES IN DEGREES.
C*****
      EXTERNAL MONIT
      COMMON W(28)
      COMMON/MODEL/P1,D1,P2,D2,P3,D3,PA,DA,PB,DB,Q1,Q2,Q3
      DIMENSION E(4),X(4)
      DOUBLE PRECISION FILEN1,FILEN2,FILEN3
      TYPE 100
100    FORMAT (1H , 'ENTER THE FIRST TWO-PHASE FILENAME AND VOLUME
      C FRACTION')
      ACCEPT 101,FILEN1,Q1
101    FORMAT(A10,G)
      TYPE 120
120    FORMAT(1H 'ENTER THE SECOND TWO-PHASE FILENAME AND
      C VOLUME FRACTION')
      ACCEPT 101,FILEN2,Q2
      TYPE 121
121    FORMAT(1H , 'ENTER THE THIRD TWO-PHASE FILENAME AND
      C VOLUME FRACTION')
      ACCEPT 101,FILEN3,Q3
      OPEN(UNIT=1,DEVICE='DSK',FILE=FILEN1,ACCESS='SEQIN')
      OPEN(UNIT=2,DEVICE='DSK',FILE=FILEN2,ACCESS='SEQIN')
      OPEN(UNIT=5,DEVICE='DSK',FILE=FILEN3,ACCESS='SEQIN')
      OPEN(UNIT=3,DEVICE='DSK',FILE='ALPHAT',ACCESS='SEQOUT')
      OPEN(UNIT=4,DEVICE='DSK',FILE='BETAT',ACCESS='SEQOUT')
      READ (1,130) A1,A2,NP
      READ (2,130) A1,A2,NP
      READ(5,130) A1,A2,NP
130    FORMAT(/3G)
      WRITE (3,125) A1,A2,NP
      N=4
      ESCALE=1000
      KPRINT=0
      ICON=2
      MAXIT=50
      IFAIL=0
      X(1)=0.5
      X(2)=0.7
      X(3)=0.5
      X(4)=0.7

```

```

DO 150 I1=1,4
E(I1)=0.0001
150 CONTINUE
125 FORMAT(1H ,'"ALPHA-PHASE TERMINAL SOLUTION"',/,2(F6.3,3X),I4)
WRITE (4,140) A1,A2,NP
140 FORMAT (1H ,'"BETA-PHASE TERMINAL SOLUTION"',/,2(F6.3,3X),I4)
TYPE 145
145 FORMAT(1H , 'WAVELENGTH ',3X, 'R.M.S. ERROR',3X, 'MEAN PSI ERROR',
C 3X, 'MEAN DELTA ERROR')
DO 160 I2=1,NP
READ(1,170) WAVE,ANA1,POL1
READ(2,170) WAVE,ANA2,POL2
READ(5,170) WAVE,ANA3,POL3
170 FORMAT(3G)
P1=45.0-ANA1
D1=2.0*POL1
P2=45.0-ANA2
D2=2.0*POL2
P3=45.0-ANA3
D3=2.0*POL3
CALL VAO4A(X,E,N,F,ESCALE,KPRINT,ICON,MAXIT,MONIT,IFAIL)
CALL CALCFX(N,X,ERROR)
CALL INCOHERENT(PA,DA,PB,DB,Q1,PSI1,DELTA1)
CALL INCOHERENT(PA,DA,PB,DB,Q2,PSI2,DELTA2)
CALL INCOHERENT(PA,DA,PB,DB,Q3,PSI3,DELTA3)
ERPSI=(P1-PSI1+P2-PSI2+P3-PSI3)/3.0
ERDELTA=(D1-DELTA1+D2-DELTA2+D3-DELTA3)/3.0
ANAA=45.0-PA
POLA=DA/2.0
ANAB=45.0-PB
POLB=DB/2.0
WRITE(3,180) WAVE,ANAA,POLA
WRITE(4,180) WAVE,ANAB,POLB
TYPE 190,WAVE,ERROR,ERPSI,ERDELTA
190 FORMAT(1H ,2X,F8.4,6X,F8.4,5X,F8.4,11X,F8.4)
180 FORMAT(1H ,2(F8.4,3X),F8.4)
160 CONTINUE
STOP
END

```

```

SUBROUTINE CALCFX(N,X,ERROR)
DIMENSION X(N)
COMMON/MODEL/ P1,D1,P2,D2,P3,D3,PA,DA,PB,DB,Q1,Q2,Q3
PA=(X(1)**2/(1.0+X(1)**2))*90.0
DA=(X(2)**2/(1.0+X(2)**2))*180.0
PB=(X(3)**2/(1.0+X(3)**2))*90.0
DB=(X(4)**2/(1.0+X(4)**2))*180.0
CALL INCOHERENT(PA,DA,PB,DB,Q1,PSI1,DELTA1)
CALL INCOHERENT(PA,DA,PB,DB,Q2,PSI2,DELTA2)
CALL INCOHERENT(PA,DA,PB,DB,Q3,PSI3,DELTA3)
WQ1=1.0
WQ2=1.0
WQ3=1.0
IF(WQ1.LT.0.5) WQ1=1.0-WQ1
IF(WQ2.LT.0.5) WQ2=1.0-WQ2
IF(WQ3.LT.0.5) WQ3=1.0-WQ3
ERROR=((P1-PSI1)**2+(D1-DELTA1)**2)*WQ1+((D3-DELTA3)**2
C +(P2-PSI2)**2)*WQ2+((D2-DELTA2)**2+(P3-PSI3)**2)*WQ3
ERROR=SQRT(ERROR)/6.0
RETURN
END
SUBROUTINE MONIT(N,X,ERROR,ITERC)
DIMENSION X(N)
COMMON/MODEL/ P1,D1,P2,D2,P3,D3,PA,DA,PB,DB,Q1,Q2,Q3
CALL CALCFX(N,X,ERROR)
TYPE 100,PA,DA,PB,DB,ERROR
100 FORMAT(1H ,5(F8.4,3X))
RETURN
END

```

Note: the subroutines INCOHERENT, RHREFL, RHSUBS and VAO4A are the same as those in appendix A.

Addendum

In treating potential sources of ellipsometric error with a unified analysis, Azzam and Bashara (1971a) derive a set of coupling co-efficients which relate component imperfections and azimuth errors into the surface parameter ρ . There is a typographic error in their table 1, (table 2.4 in this work), in the coupling co-efficient γ'_C . The correct expression is, Azzam and Bashara (1977)

$$\gamma'_C = \frac{\tan A \sec^2 C (1 - \rho_C \sec^2 P^* - \rho_C^2 \tan^2 P^*)}{(1 - \rho_C \tan C \tan P^*)^2}$$

Ellipsometry of polyphase substrates

E. F. I. ROBERTS and R. HUNT†

Department of Metallurgy and Materials, Sir John Cass School of Science and Technology, City of London Polytechnic, Whitechapel High Street, London E1, England

(Received 2 July 1981; revision received 2 June 1982)

Abstract. The ellipsometry of polyphase surfaces is examined and a model for the interpretation of two-phase surfaces proposed. The model is tested using the AgCu-CuAg binary system where the volume fractions of the two-phases were determined using the model and compared to the volume fractions calculated from the phase diagram. The volume fractions of the α phases examined were 26.2, 58.3 and 67.6 per cent. The model successfully determined these volume fractions to within 1 per cent.

1. Introduction

Classical ellipsometric studies have been devoted, for the greater part, to the determination of the thickness and refractive index of thin films on isotropic homogeneous substrates. However, the roots of ellipsometry are inextricably entwined with the optical properties of condensed phases and, in particular, with the electronic structure of conductors and non-conductors. Drude [1] developed his optical model for film-covered surfaces when frustrated by the tenacious and obstinate surface layers that developed on metallic surfaces during studies in pursuance of data for his free-electron model. Furthermore, contemporary ellipsometric studies rely heavily, if not totally, on an established and trustworthy value for the optical constants of the reflecting substrate. Such studies have generally been made on either 'pure' metals or alloys exhibiting complete solid solubility and, even in cases where this has obviously not been so, research workers have conveniently ignored the presence of a second (or further) phase. To some extent this omission is excusable since there has been a widespread acceptance of ellipsometric sampling as an averaging technique. Certainly when a specimen of considerable area is studied by a quasi-monochromatic beam, local second phase inhomogeneity and anisotropic variation in the substrate (< 10 per cent) have been assumed to have a much smaller effect than, say, film overgrowths. Attention has been paid to film inhomogeneity (in the form of refractive index gradients) and surface topography, but the inhomogeneities encountered in practical metallurgical alloy substrates have not received the thought they deserve, especially in view of the almost axiomatic assumptions of the original optical modelling and their obvious inapplicability to real situations.

Winterbottom [2] was a firm advocate of single crystal experimentation and, while reviewing optical anisotropy, reported corrosion results on either isotropic

† Based at Sira Institute Ltd, South Hill, Chislehurst, Kent BR7 5EH, England.

single crystals or fine-grained polycrystalline materials. This latter methodology was also promoted by Hayfield [3] who, in corrosion studies of anisotropic metals, ensured that their fine grain size endowed them with 'pseudo-isotropic' optical properties. These workers, however, did not have access to spectral scanning ellipsometry which, because of its potential diagnostic value, was bound to be introduced to film characterization studies. Additionally, the use of the optical dielectric function $\bar{\epsilon}(\lambda)$, or complex refractive index $\bar{n}(\lambda)$, to determine absolute reflectance values and/or colour characteristics of alloys and reflecting ore minerals, have provided an impetus to ascertain the influence of polyphase substrates on the ellipsometric parameters Δ and ψ . Last, it must be enjoined that in experiments conducted on duplex alloys an automatic nulling ellipsometer gave optical nulls as well defined and as consistently as single phase alloys and, practically, endorsed the practices mentioned above in the discussion of corrosion experiments [4].

2. Theory: the model

The model presented here is for a duplex substrate composed of two phases, α and β , in volume fractions Q_α and Q_β respectively. The surfaces are considered to be perfectly flat and specularly reflecting, and the exposed surface area fractions to equal the volume fractions. When polarized light, of known ellipticity, is incident on each phase, two wavefronts of differing ellipticity, are produced by reflection (figure 1). The reflected beams then combine to form an 'average' of the two polarization states.

Assuming that the incident light is incoherent, then the reflected beam will be described by a Stokes vector equal to the weighted sum of the Stokes vectors of the reflections from each phase [5]:

$$S_R = Q_\alpha S_\alpha + Q_\beta S_\beta, \quad (1)$$

where S_R is the reflected beam Stokes vector, and S_α and S_β are the respective normalized Stokes vectors of the reflected beams from the α and β phases. The two Stokes vectors S_α and S_β are represented in the Mueller matrix formulation by the

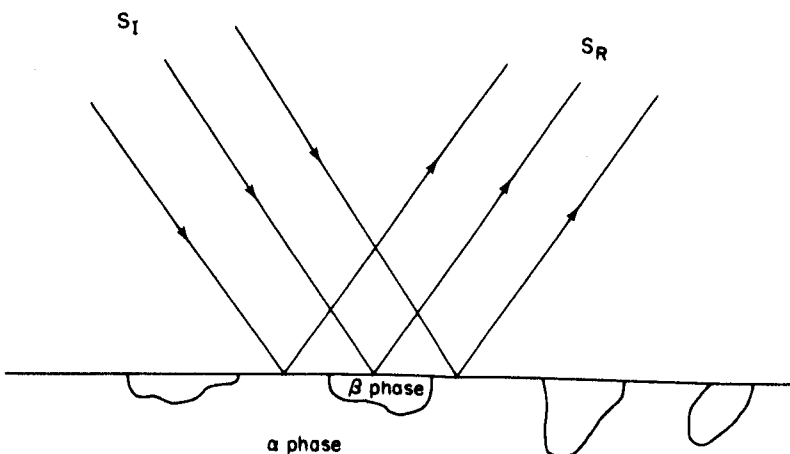


Figure 1. Reflection of the incident beam from a two-phase substrate.

product of the incident-beam Stokes vector, S_1 , and the Mueller matrix of each phase, M_α and M_β , respectively. Thus

$$S_\alpha = M_\alpha S_1, \tag{2}$$

$$S_\beta = M_\beta S_1. \tag{3}$$

Substituting equations (2) and (3) in equation (1) gives

$$S_R = (Q_\alpha M_\alpha + Q_\beta M_\beta) S_1. \tag{4}$$

The factor $Q_\alpha M_\alpha + Q_\beta M_\beta$ may now be equated with the pseudo-single-phase surface characterized by the matrix M_S :

$$M_S = Q_\alpha M_\alpha + Q_\beta M_\beta. \tag{5}$$

The matrices M_α and M_β can be derived for a surface represented by the Jones matrix [6]

$$\begin{vmatrix} 1 & 0 \\ 0 & \rho \end{vmatrix},$$

where $\rho = \tan(\psi) \exp(i\Delta)$, and the Mueller matrix for the surface is

$$M_g = \frac{1}{2} \begin{vmatrix} (1 + \rho_g \rho_g^*) & (1 - \rho_g \rho_g^*) & 0 & 0 \\ (1 - \rho_g \rho_g^*) & (1 + \rho_g \rho_g^*) & 0 & 0 \\ 0 & 0 & (\rho_g + \rho_g^*) & i(\rho_g - \rho_g^*) \\ 0 & 0 & i(\rho_g - \rho_g^*) & (\rho_g + \rho_g^*) \end{vmatrix}, \tag{6}$$

where $g = \alpha, \beta$ or S .

The factor $Q_\alpha M_\alpha + Q_\beta M_\beta$ may now be evaluated and equated to M_S , thus giving the equations

$$(1 + \rho_S \rho_S^*) = Q_\alpha (1 + \rho_\alpha \rho_\alpha^*) + Q_\beta (1 + \rho_\beta \rho_\beta^*), \tag{7}$$

$$(1 - \rho_S \rho_S^*) = Q_\alpha (1 - \rho_\alpha \rho_\alpha^*) + Q_\beta (1 - \rho_\beta \rho_\beta^*), \tag{8}$$

$$(\rho_S + \rho_S^*) = Q_\alpha (\rho_\alpha + \rho_\alpha^*) + Q_\beta (\rho_\beta + \rho_\beta^*), \tag{9}$$

$$(\rho_S - \rho_S^*) = Q_\alpha (\rho_\alpha - \rho_\alpha^*) + Q_\beta (\rho_\beta - \rho_\beta^*). \tag{10}$$

Note that equations (7) and (8) are equivalent (i.e. equation (7) = -equation (8)). Substituting $\rho_g = \tan(\psi_g) \exp(i\Delta_g)$ into equations (7), (9) and (10), we obtain directly from equation (7)

$$\tan^2(\psi_S) = Q_\alpha \tan^2(\psi_\alpha) + Q_\beta \tan^2(\psi_\beta) \tag{11}$$

since $Q_\alpha + Q_\beta = 1$, and from equations (9) and (10)

$$\tan(\psi_S) \cos(\Delta_S) = Q_\alpha \tan(\psi_\alpha) \cos(\Delta_\alpha) + Q_\beta \tan(\psi_\beta) \cos(\Delta_\beta), \tag{12}$$

$$\tan(\psi_S) \sin(\Delta_S) = Q_\alpha \tan(\psi_\alpha) \sin(\Delta_\alpha) + Q_\beta \tan(\psi_\beta) \sin(\Delta_\beta). \tag{13}$$

Eliminating $\tan(\psi_S)$ gives

$$\tan(\Delta_S) = \frac{Q_\alpha \tan(\psi_\alpha) \sin(\Delta_\alpha) + Q_\beta \tan(\psi_\beta) \sin(\Delta_\beta)}{Q_\alpha \tan(\psi_\alpha) \cos(\Delta_\alpha) + Q_\beta \tan(\psi_\beta) \cos(\Delta_\beta)}. \tag{14}$$

Equations (11) and (14) describe the averaging of ψ and Δ in a two-phase surface. The general forms for a surface containing n phases are:

$$\tan^2(\psi_S) = \sum_{p=1}^n Q_p \tan^2(\psi_p) \quad (15)$$

$$\tan(\Delta_S) = \frac{\sum_{p=1}^n Q_p \tan(\psi_p) \sin(\Delta_p)}{\sum_{p=1}^n Q_p \tan(\psi_p) \cos(\Delta_p)}, \quad (16)$$

noting that

$$\sum_{p=1}^n Q_p = 1.$$

Using the above equations, a set of effective ψ and Δ values for a hypothetical two-phase mixture was calculated as a function of volume fraction. The results, for α and β phases with the ψ and Δ values given in table 1 are shown in figure 2. The theory has

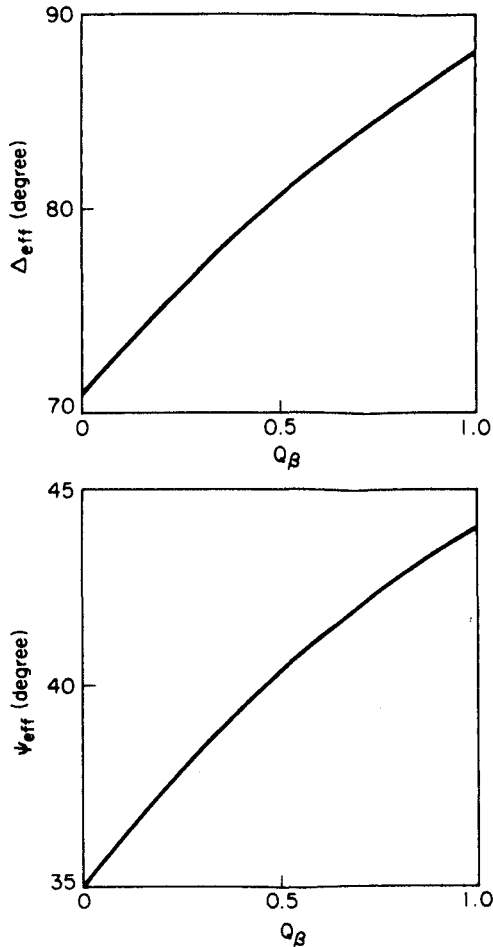


Figure 2. Variation of ψ and Δ as a function of volume fraction Q_β predicted by the model.

Table 1. Values of ψ and Δ (in degrees) used in calculating results plotted in figure 2.

| Phase | α | β |
|----------|----------|---------|
| ψ | 35.0 | 44.0 |
| Δ | 71.0 | 88.0 |

been tested on the Ag-Cu binary alloy system which exhibits almost complete solid-solid immiscibility. The copper- and silver-rich terminal solid solutions were each prepared for an equilibrium temperature of 873 K [7, 8]. Three duplex alloys from the system, as well as the terminal solid solutions, were examined ellipsometrically over the wavelength range 400–500 nm at 10 nm intervals. This wavelength range avoids the main absorption edges of silver and copper, but displays a large difference in optical characteristics between the two phases [9]. The model was tested by determining the volume phase proportions of the three duplex alloys from experimental measurements of ψ and Δ for the alloys and the terminal solid solutions. The method employed was to calculate the ψ and Δ of a duplex alloy from terminal solid solution data using an initial estimate of phase proportions and equations (15) and (16). An error function was then defined as

$$(\psi_{\text{exp}} - \psi_{\text{calc}})^2 + (\Delta_{\text{exp}} - \Delta_{\text{calc}})^2,$$

where ψ_{exp} and Δ_{exp} are experimental values, and ψ_{calc} and Δ_{calc} are values calculated from the model. The calculation was then repeated iteratively, varying the phase proportions until the error function was minimized. Noting that only one volume fraction need be adjusted independently in a duplex phase alloy, the volume fractions can be written as $1 - Q_\beta$ for the α phase and Q_β for the β phase. The summation index p in equations (15) and (16) extends over the two terminal solid solutions. This calculation was performed at each of the 11 wavelengths and the mean and root variance of the 11 values of Q_β formed. These results are given in table 2, together with the volume fractions determined from the equilibrium phase diagram.

It can be seen that in two out of the three cases the phase proportions derived ellipsometrically agree to within one root variance with those derived from the equilibrium phase diagram. However, in one case— $Q_\beta = 0.521$ —the difference is significant. It is possible that the error function defined above does not exhibit a single minimum and that the Q_β values are located in a local minimum which is not the deepest. However, the initial estimates of Q_β were varied from 0.2 to 0.8 and each gave results consistent to three significant figures in Q_β . It may be possible that the

Table 2. The volume fraction of α phase present in a series of duplex silver-copper alloys determined from the ellipsometric reflectance spectra and from the equilibrium phase diagram for Ag-Cu.

| Alloy composition, wt% actual (nominal) | Volume fraction of α phase | |
|--|-----------------------------------|-------------------|
| | Phase diagram | Ellipsometry |
| 30.1(30)Ag-69.9(70)Cu | 0.262 | 0.251 \pm 0.021 |
| 60.8(60)Ag-39.2(40)Cu | 0.583 | 0.521 \pm 0.014 |
| 69.2(70)Ag-30.8(30)Cu | 0.676 | 0.673 \pm 0.027 |

sample does have a phase proportion different from that expected by its preparation, and further work is required to confirm this.

Before concluding this brief communication it is worth drawing attention to several aspects of the work that may prove valuable to other workers. First, it should be pointed out that while the sample has been considered to be illuminated with incoherent illumination, a similar development, using complete or partial coherency, has shown that differences in optical characterization, e.g. Δ , ψ or R_n , (the reflectance at normal incidence), can be exaggerated and can open the way to differential coherency ellipsometry that appears to be extremely sensitive to surface phase structure; this work will be the subject of a future publication. Second, since an 'ideal' polyphase substrate may be compared to a 'real' polyphase substrate, any anomalous behaviour exhibited by the latter will appear in a difference spectrum. Thus, in figure 3 the difference spectrum ($\Delta R_n, \lambda$) shows two peaks at the positions of the observed absorption edges. This may be due to poor fitting but, since the silver-rich phases are known to exhibit surface plasmon effects, it is quite possible that these two features are due to such surface plasmons arising from the effective 'roughening' of an otherwise homogeneous silver-rich phase by the incursion of the copper-rich phase, or even differential polishing. However, since the silver surface plasmons usually enhance the reflectivity, further experimental work is required to substantiate this hypothesis and any other plausible explanation, e.g. grain-boundary absorption [10]. Finally, it is hoped that this work will lead to an optical method, with its attendant simplifications of apparatus design, to determine phase boundaries by *in situ* examination of the optical characteristics of alloys, and to enhance the quantitative aspects of metallography [11]. A study of single and duplex alloys from the Au-Ag-Cu system has been reported [4], but details of the phase boundary comparisons have yet to be published.

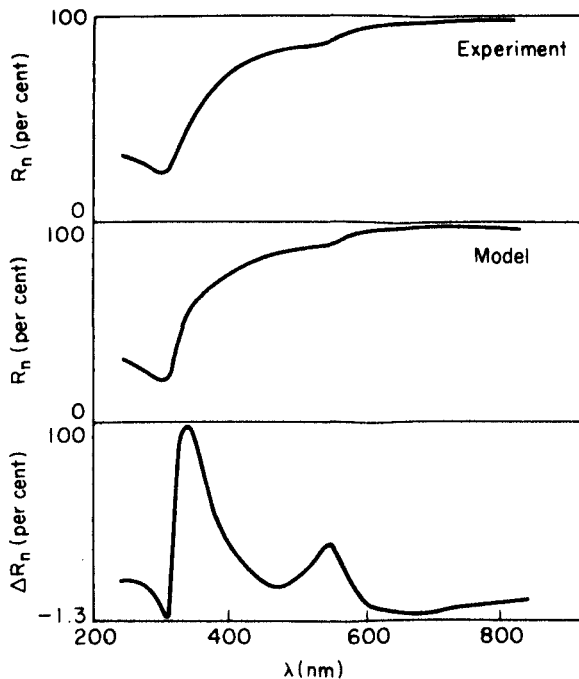


Figure 3. Reflectance and difference curves of an experimental and modelled alloy of volume fraction 0.324.

On examine l'ellipsométrie de surfaces polyphases et un modèle d'interprétation des surfaces biphasées est proposé. Le modèle est vérifié en utilisant des systèmes AgCu-CuAg où les fractions volumiques des deux phases ont été déterminées d'après le modèle et comparées aux fractions volumiques calculées à partir du diagramme de phase. Les fractions volumiques des phases examinées étaient 2,2, 58,3 et 67,6 pour cent. Le modèle a déterminé convenablement ces fractions volumiques à 1 pour cent près.

Die Ellipsometrie mehrphasiger Oberflächen wird untersucht und es wird ein Modell zur Interpretation zweiphasiger Oberflächen vorgeschlagen. Dieses Modell wird an einem binären AgCu-CuAg-System getestet, wobei die Volumenanteile der zwei Phasen anhand des Modells bestimmt wurden und mit dem aus dem Phasendiagramm bestimmten Volumenanteilen verglichen wurden. Die Volumenanteile der untersuchten α -Phasen betragen 2,2, 58,3 und 67,6 Prozent. Mit diesem Modell wurden die Volumenanteile innerhalb von 1 Prozent genau bestimmt.

References

- [1] DRUDE, P., 1889, *Wiedeman Annaln Phys.*, **36**, 884, 886.
- [2] WINTERBOTTOM, A. B., 1955, *Optical Studies of Metal Surfaces*. Kgl. Norske Videnskab. Selskabs, Skrifter No. 1 (Trondheim).
- [3] HAYFIELD, P. C. S., 1963, *Ellipsometry in the Measurement of Surfaces and Thin Films*, N.B.S. Misc. Publ. No. 256 (Washington: National Bureau of Standards), p. 157.
- [4] ROBERTS, E. F. I., CLARKE, K. MC., and HUNT, R., 1980, *Mater. Sci. Engng*, **42**, 71.
- [5] KLEIN, M. V., 1970, *Optics* (New York: John Wiley).
- [6] GERRARD, A., and BIRCH, J. M., 1975, *Introduction to Matrix Methods in Optics* (London: John Wiley).
- [7] ROBERTS, E. F. I., and CLARKE, K. MC., 1979, *Gold Bull.*, **12**, 9.
- [8] CLARKE, K. MC., 1980, Ph.D. Thesis, City of London Polytechnic.
- [9] RIVORY, J., 1977, *Phys. Rev. Sect B*, **15**, 3119.
- [10] HUNDERI, O., 1973, *Phys. Rev. B*, **7**, 3419.
- [11] GERMAN, R. M., GUZOWSKI, M. M., and WRIGHT, D. C., 1980, *J. Metals*, **32**, 20.

Reprinted from

Materials Science and Engineering

ELSEVIER SEQUOIA S.A., LAUSANNE

Optical Properties of Alloys*

E. F. I. ROBERTS, K. MC. CLARKE and R. HUNT

Department of Metallurgy and Materials, City of London Polytechnic, Whitechapel, London E1 (Gt. Britain)

SUMMARY

Results are reported of studies using an automatic nulling spectroellipsometer on binary and ternary alloys of single- and two-phase composition. The significance of these results is discussed in relation to the electronic structure and appearance of such alloys.

1. INTRODUCTION

Historically the optical properties of metals have been central to studies of the electronic structure [1 - 3]. The term "metallic lustre" is common recognition of the particular properties of opacity and high reflectance which have made possible the application and development of reflection optical microscopy. Considerable effort has been expended among mineralogists in classifying and measuring the optical characteristics of opaque minerals and not a little success can be reported for the optical discrimination of minerals by reflective photometry [4 - 6]. More recently colour characterization, standardization and quality control have featured in several metallurgical industries, e.g. the gold jewellery industry for aesthetic surface coatings [7 - 10]. Ellipsometric studies of thin film growth kinetics during the corrosion of metallic substrates can almost without exception be considered to involve composition alterations of the substrate [11]. This is particularly so in more practical studies of alloys where de-alloying and surface enrichment have been commonly observed. Consequently the systematic application of ellipsometry to the corrosion

of alloys demands an understanding of the optical characteristics of alloy substrates. The conventional ellipsometric models rely upon a perfectly plane homogeneous isotropic substrate [12, 13] and metallurgists will recognize the limitations of such ideal assumptions. The present programme was aimed at measuring the effects of alloying on ellipsometric measurements when both complete solid solutions and limited-range solid solutions occurred. Furthermore, the optical constants n and k of the alloys were related to their colour characteristics and a comparison was made with reflectance measurements.

2. EXPERIMENTAL STUDIES

Extensive optical studies of the Group Ib metals copper, silver and gold have contributed to the electron theory of metals [14 - 17]. The ternary system Au-Ag-Cu was chosen for study partly because of the theoretical framework and partly because gold jewellery alloys are based upon this system. The Au-Ag-Cu system also includes two series of solid solutions (Ag-Au and Cu-Au) and a eutectic (Ag-Cu) which extend into the ternary system. Additionally, the Cu-Au binary system possesses a series of order-disorder reactions and these also appear in the ternary system [18]. The nobility of the alloys promotes relative inertness from atmospheric attack and, apart from the copper-rich alloys, corrosion problems do not intrude.

All alloys were prepared from fine gold, fine silver and spec. pure copper. Samples were made at 10 wt.% intervals throughout the ternary diagram. Alloys were induction melted in carbon crucibles under a reducing atmosphere and bottom-cast into a polished steel dish containing oil. The cast bead was

*Presented at the International Chalmers Symposium on Surface Problems in Materials Science and Technology, Göteborg, Sweden, June 11 - 13, 1979.

worked into a plaquette by cold working and annealing. The final specimen was water quenched from a 16 h anneal at 600 °C. After mounting, the specimens were carefully polished metallographically down to a 0.25 μm diamond paste. No organic solvents were used after the final rinsing with distilled water. Within minutes of polishing the specimens were mounted on an automatic self-nulling high precision spectroellipsometer and measurements of the relative phase shift Δ and the relative amplitude change $\tan \psi$ were made at wavelength intervals of 5 nm from 250 to 800 nm [19]. The data collected were then processed on a DEC10 computer system to generate dispersions of the complex refractive index $\hat{n}(\lambda) = n(\lambda) - ik(\lambda)$, the complex dielectric function $\hat{\epsilon}(\lambda) = \epsilon_1(\lambda) + i\epsilon_2(\lambda)$ and the normal reflectance $R_n(\lambda)$. It was also possible to determine standard CIE colour coordinates for each of the alloys (CIE 1970) and to analyse the dispersion curves by multiple differentiation, normalization, difference calculations etc. Some of these results will be demonstrated in the discussion.

3. RESULTS

3.1. Solid solutions

Both the gold-based binary systems Au–Ag and Au–Cu form solid solutions (although in the latter case ordering may occur at temperatures below the final annealing temperature). Microscope and X-ray examinations of these alloys indicated that they were all single phase. The ternary diagram isothermal section for 600 °C displays an extensive two-phase region based upon the limited solid solubility regions formed in the Cu–Ag binary and its eutectic. Ternary alloys that are gold rich or contain relatively small quantities of the third component are also solid solutions. Figures 1 and 2 show the reflectance curves determined for the binary solid solution alloys Au–Ag and Au–Cu, and Fig. 3 shows similar curves for a gold-rich series of ternary alloys exhibiting only solid solutions.

3.2. Duplex alloys

The two-phase alloys are based upon the binary Cu–Ag limited-miscibility eutectic system. Two-phase ternary alloys occupy an

extensive range in the isothermal section studied here and the tie-lines for this range have been determined to lie almost parallel to the Ag–Cu composition line. Figure 4 shows the variation of reflectance for Ag–Cu and Figs. 5 and 6 show similar curves for ternary alloys with constant gold contents of 30 and 50 wt.%.

An analytical examination of the quantities computed from ϵ_1 and ϵ_2 is presented in the discussion.

4. DISCUSSION

4.1. Optical properties of solids

The reflectance of a metal at a given wavelength λ is determined by its refractive index $\hat{n}(\lambda)$ and by the surface topography. The relation is simple for an ideal plane film-free surface. Furthermore, the refractive index is equal to $\{\hat{\epsilon}(\lambda)\}^{1/2}$ where $\hat{\epsilon}(\lambda)$ is the dielectric function [1]. The refractive index and dielectric functions are in general complex quantities since they describe the attenuation and phase change of light incident upon the metal. The dielectric function can be understood in terms of the polarization of the metal by an electromagnetic wave. For metals at optical frequencies only polarization of the electrons is significant. A causal chain exists between fundamental electronic properties and the visual appearance of a metal. Optical measurements are made at some point in the chain such that fundamental information (e.g. the electronic structure) or gross visual properties may be usefully collected and quantified. The complex dielectric function may be expressed in real and imaginary terms:

$$\hat{\epsilon}(\lambda) = \epsilon_1(\lambda) + i\epsilon_2(\lambda)$$

The dielectric function of a material wherein the electrons are classically bound to the atoms is described by a lorentzian function. Such electrons may undergo forced vibrations at a resonant frequency ω_0 ; this resonance corresponds to a peak in ϵ_2 . For conduction electrons the natural frequency is zero — this gives rise to special lorentzian absorption known as Drude absorption. For a lorentzian oscillator the reflectance rises at low energies (long wavelengths) as ϵ_2 begins to rise but remains large until ϵ_1 approaches zero. Therefore the highly reflecting region of

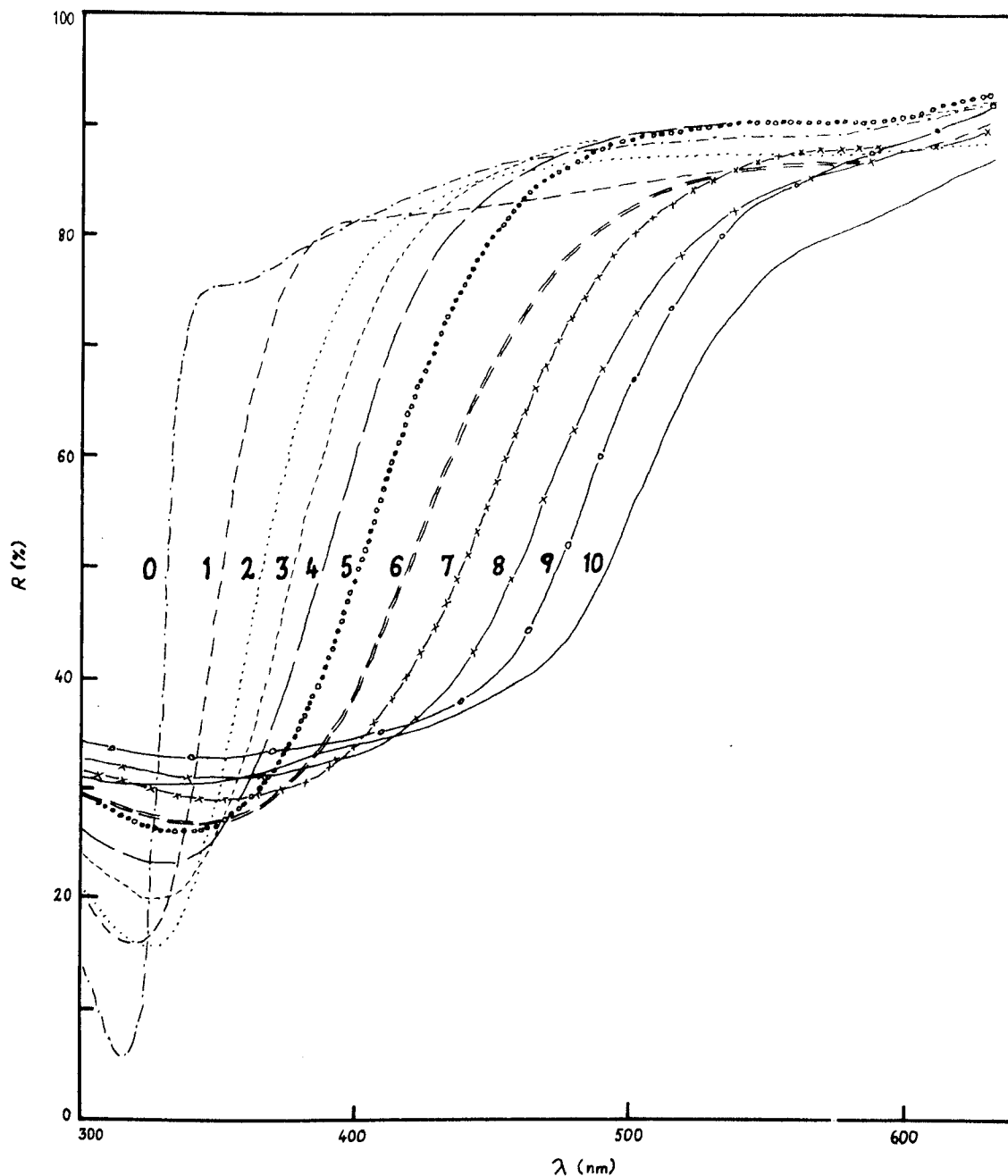


Fig. 1. Reflectance curves for Au-Ag single-phase binary alloys obtained by ellipsometry. The figures on the curves correspond to the nominal gold content (%) of the alloys.

a solid is on the high energy (short wavelength) side of the resonance frequency ω_0 . For metals with $\omega_0 = 0$ we have high reflectance at long wavelengths.

In addition to the Drude absorption that characterizes free-electron metals we have to consider interband transitions. If the range of such transition(s) is narrow the values of ϵ_2 , ϵ_1 and R will be similar to those of a single lorentzian oscillator. The additional absorp-

tion due to interband transitions reduces the reflectance. The high energy reflecting region may be completely suppressed by a succession of oscillators but structural features of the electronic bands will remain.

Metals are regarded as having free electrons. Partially filled bands or overlapping bands provide a continuum of unoccupied states adjacent to a continuum of occupied states which permits transitions at arbitrarily small

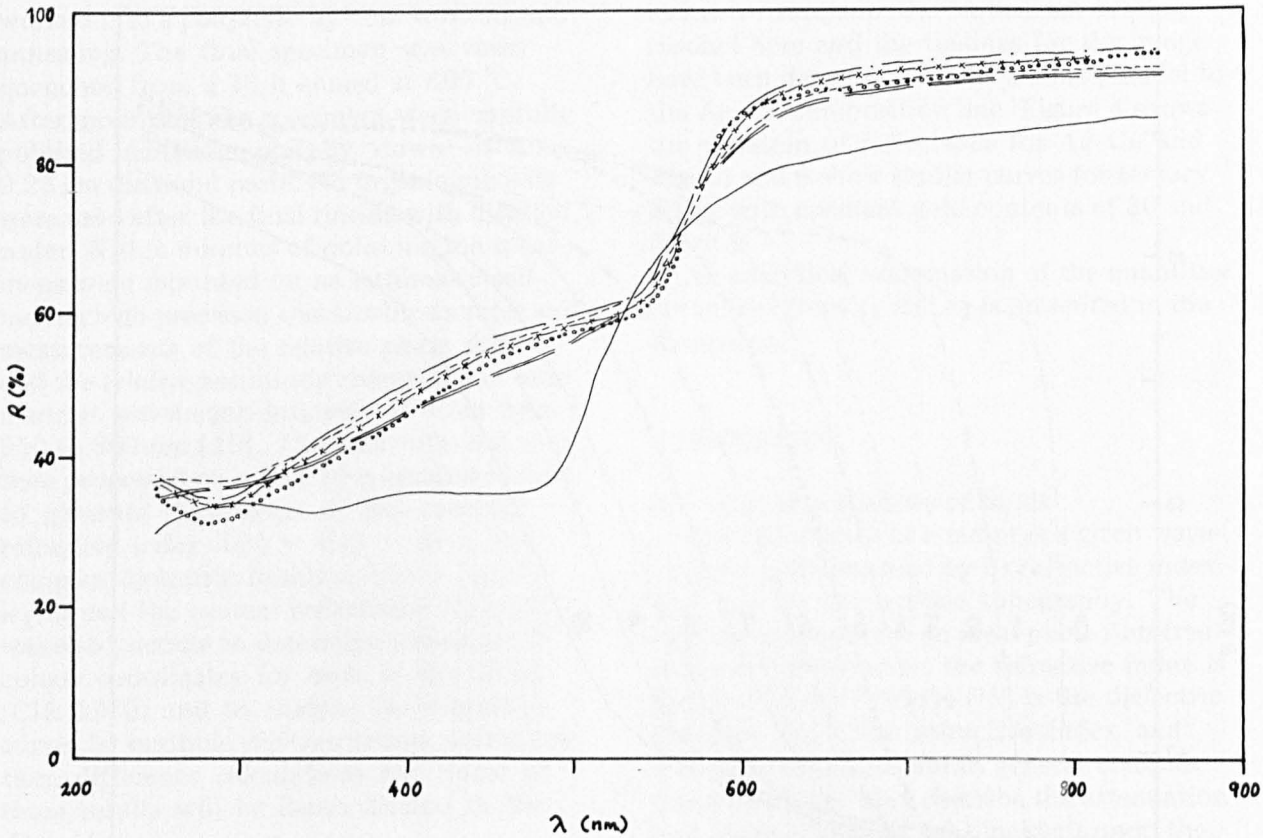


Fig. 2. Reflectance curves for Au-Cu single-phase binary alloys obtained by ellipsometry: —, 100Au; = =, 80Au-20Cu; ····, 60Au-40Cu; - · - ·, 40Au-60Cu; -x-, 20Au-80Cu; °°°°, 100Cu.

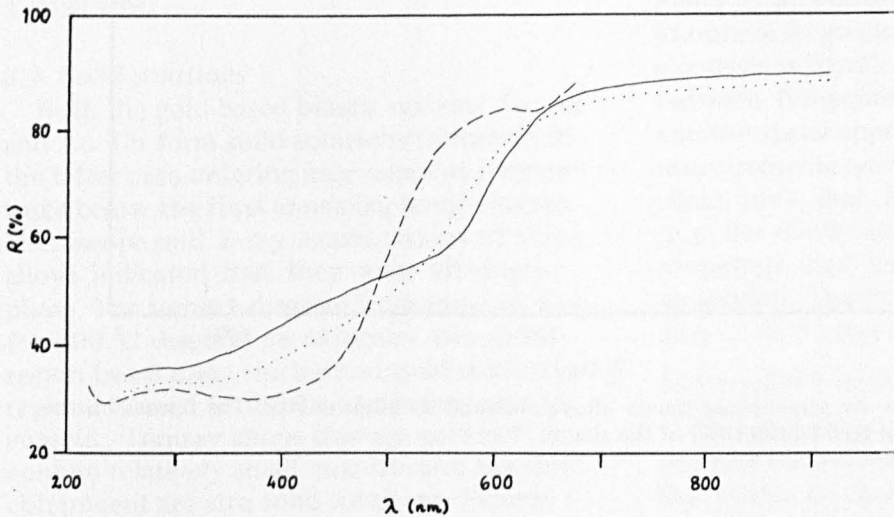


Fig. 3. Reflectance curves for 80Au- n Ag- m Cu single-phase ternary alloys obtained by ellipsometry: —, 80Au-20Cu; ····, 80Au-10Ag-10Cu; - - -, 80Au-20Ag.

photon energies. This explains the high reflectance at low energies. The onset of interband transitions causes the reflectance to fall. The intraband characteristics are determined primarily by the relaxation time τ , the density N of the conduction electrons and the effective mass m^* .

4.2. Effect of alloying

The reflectance curves for Au-Ag (Fig. 1) (calculated from ellipsometric data) show good correlation with curves determined spectrophotometrically for similar alloys by Wessel [20] and Fukutani and Sueoka [21]. There is also good agreement with the results

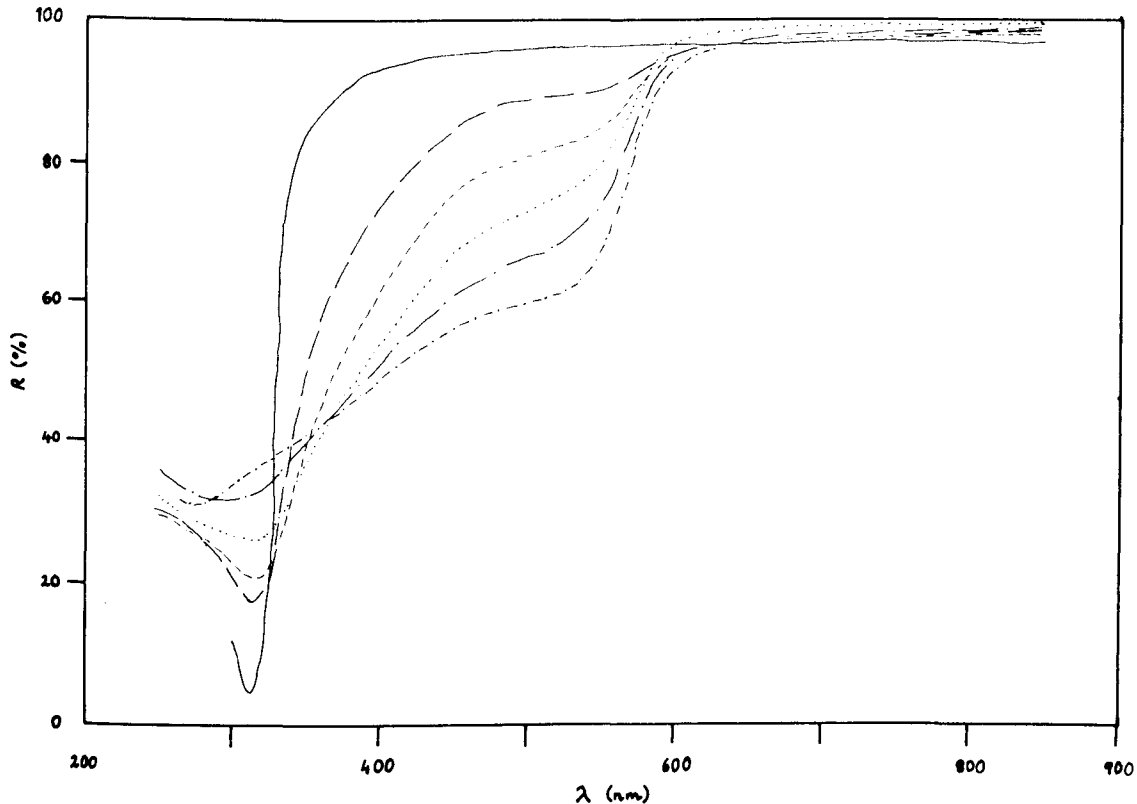


Fig. 4. Reflectance curves for Ag-Cu two-phase binary alloys obtained by ellipsometry: —, 100Ag; ---, 80Ag-20Cu; - - -, 60Ag-40Cu; ····, 40Ag-60Cu; - · - ·, 20Ag-80Cu; - - - ·, 100Cu.

obtained by Rivory [22] who made reflectance and transmittance measurements on thin vapour-deposited Au-Cu films. A number of workers, *e.g.* Friedel [23], have shown that dilute solid solutions of metals with similar electronic structures and weakly perturbed lattices form composite energy bands. Thus in some solid solutions alloying produces a smooth transformation of the energy bands and the dispersion curves of the optical constants or dielectric function will then also vary smoothly with composition throughout the solid solution range. The Au-Ag and Au-Cu disordered alloys obtained at 600 °C demonstrate this very well (Figs. 2 and 7).

Calculations of τ and m^* using these results do not reveal a marked dependence upon composition and any variations can be considered to arise as random elements, probably from surface preparation and the concomitantly induced damage. For the Au-Ag system (Fig. 7) the shift in the fundamental absorption edge is so large (1.5 eV) that no serious error arises from neglecting the intra-band contribution to $\epsilon_2(\omega)$ in the region of

the absorption edge. (This is not the case for the Au-Cu system.) No significant shift of the absorption peak at 3.8 eV occurs in the gold-rich alloys upon addition of silver. At this energy two different components of similar magnitude operate, namely the d band \rightarrow Fermi surface (FS) and the FS \rightarrow conduction band transitions. To identify the influence of these we must decompose the dielectric function into bound- and free-electron terms; it may be possible to determine the line shape and energy of the $d \rightarrow$ FS transition from thermomodulation optical experiments [24]. The present samples have smaller values of $\epsilon_2^b(\omega)$ than those of Rivory but evidently the conduction electron transition $L_2' \rightarrow L_1$ is weakened more than the d band transition. However, alloying silver with gold does not spread the conduction electron transition into the visible region and this obviates the necessity to include conduction band effects when discussing the visual appearance of Au-Ag alloys. The onset of interband transitions in both copper and gold is due to $d \rightarrow$ FS transitions over extended regions of the Brillouin zone. The variation of the onset

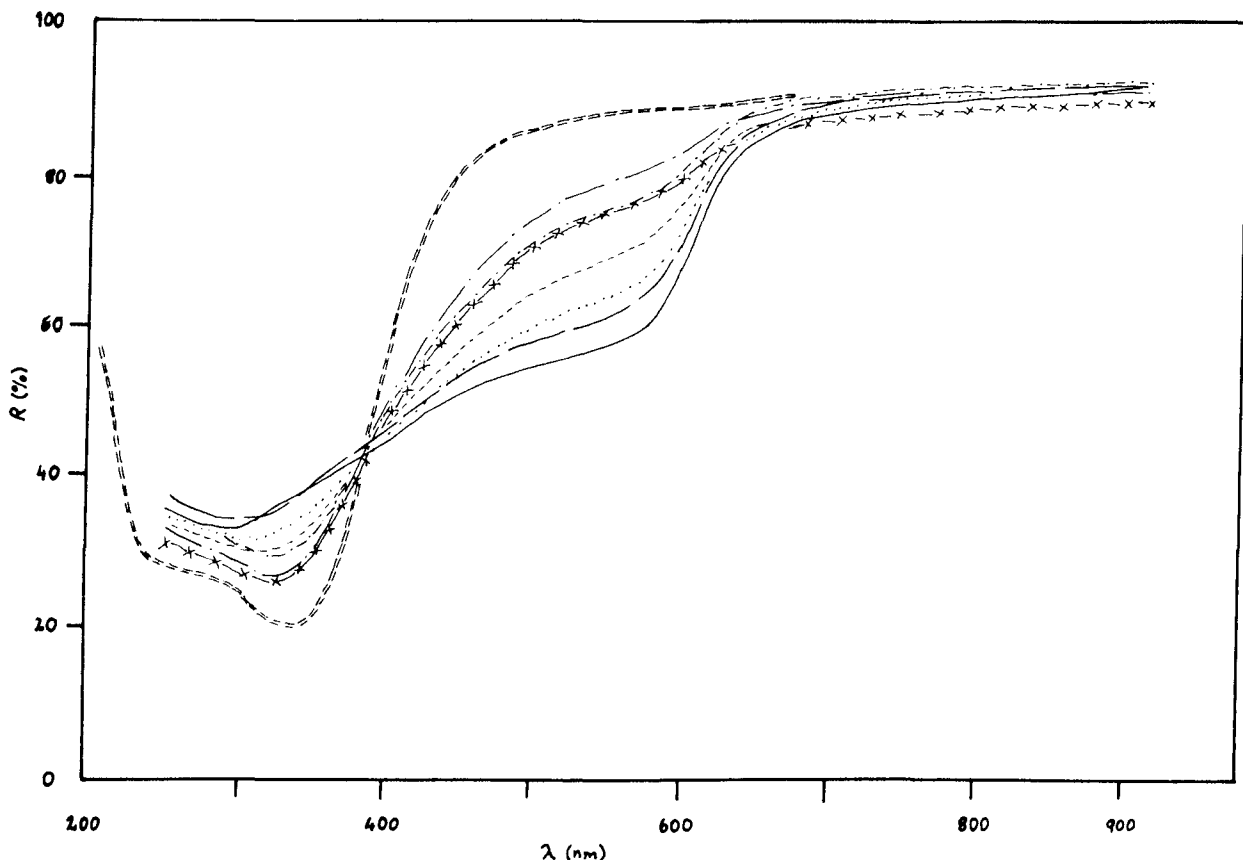


Fig. 5. Reflectance curves for l Au-30Ag- m Cu two-phase ternary alloys obtained by ellipsometry: —, 30Ag-70Cu; - - -, 10Au-30Ag-60Cu; ····, 20Au-30Ag-50Cu; - · - ·, 30Au-30Ag-40Cu; - · - · - ·, 40Au-30Ag-30Cu; - - - ·, 50Au-30Ag-20Cu; - x - x -, 60Au-30Ag-10Cu; = = =, 70Au-30Ag.

energy with composition has been determined for Au-Cu alloys (Fig. 8), no significant change being found for compositions containing up to 50 at.% Au. Beyond this composition the interband onset energy increases rapidly and monotonically to a final value of 2.5 eV for gold. This behaviour is similar to that of Au-Ag alloys but the deviation from linearity is much more marked. Piezo-reflectance measurements of the change of band gap with lattice spacing could be applied to Au-Cu alloys and corrections could be made to the above data leaving only variations due to the ionic potential of the alloying. The addition of copper to gold moves the peak in $\epsilon_2^b(\omega)$ near 3.8 eV to higher energies, and the lower maximum (or rather point of inflection) at 3.3 eV moves to lower energies upon addition of copper. The higher energy peak also moves more rapidly for copper-rich alloys. These results are in agreement with those of Rivory [22] but not with those of Beaglehole and Erlbach [25]. This rapid change with the copper-rich alloys is

consistent, however, with the observation of Beaglehole and Erlbach that the ionic potential effect on alloying gold and copper (which opposes the lattice effect in this system) is much weaker for copper-rich alloys than for gold-rich ones.

Several experiments were conducted on single-phase Ag-Cu terminal solid solutions. A silver-rich alloy (containing 6.6 at.% Cu) and a copper-rich alloy (1.25 at.% Ag) showed optical spectra remarkably similar to their respective solvents. The absorption edge was broadened slightly, however, by approximately 0.02 eV and apparently an impurity band centred at $\hbar\omega = 3$ eV occurred. Interestingly for small amounts of copper added to silver the changes were almost indistinguishable from roughness-induced surface plasmon absorption. The impurity band has been postulated as arising from virtual bound state absorption [22].

The heterogeneous alloys of the Ag-Cu binary eutectic system were also examined (Fig. 9). "Effective medium" calculations

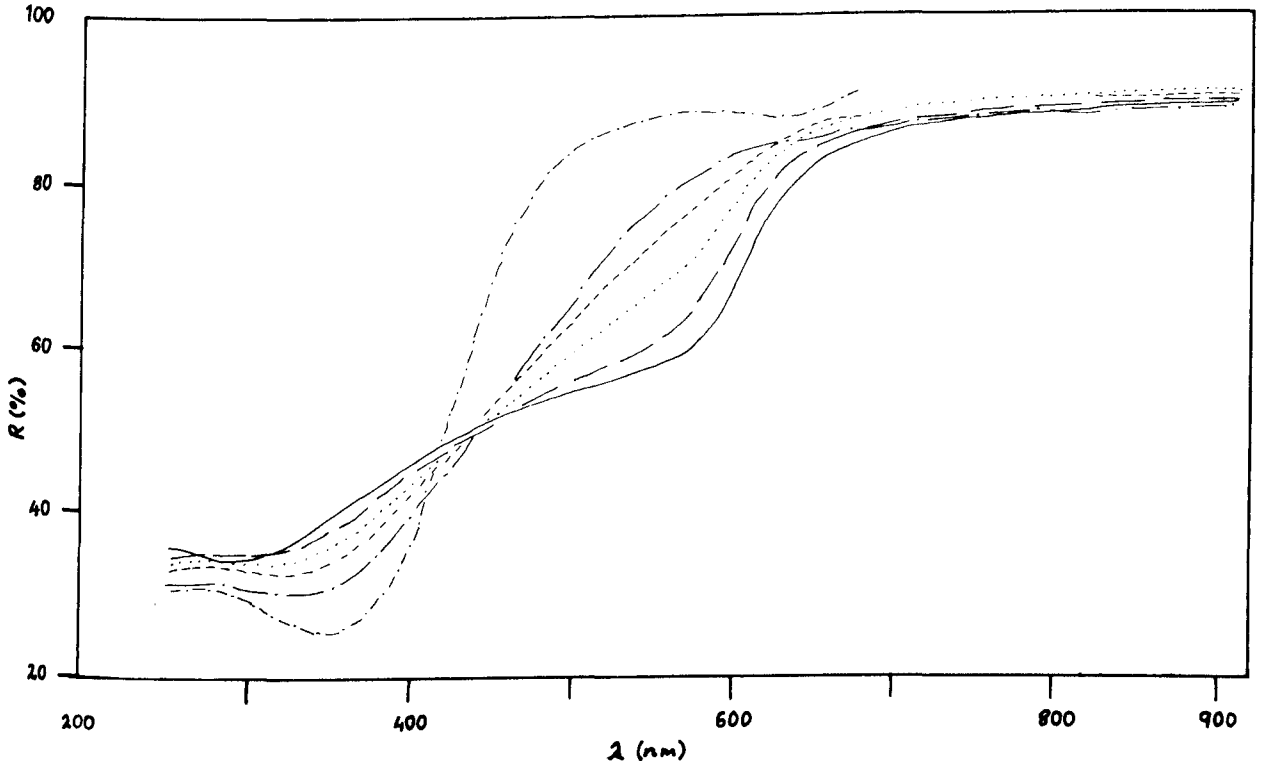


Fig. 6. Reflectance curves for 50Au- n Ag- m Cu two-phase ternary alloys obtained by ellipsometry: —, 50Au-50Cu; ---, 50Au-10Ag-40Cu; ····, 50Au-20Ag-30Cu; ----, 50Au-30Ag-20Cu; -·-·, 50Au-40Ag-10Cu; -·-·-·, 50Au-50Ag.

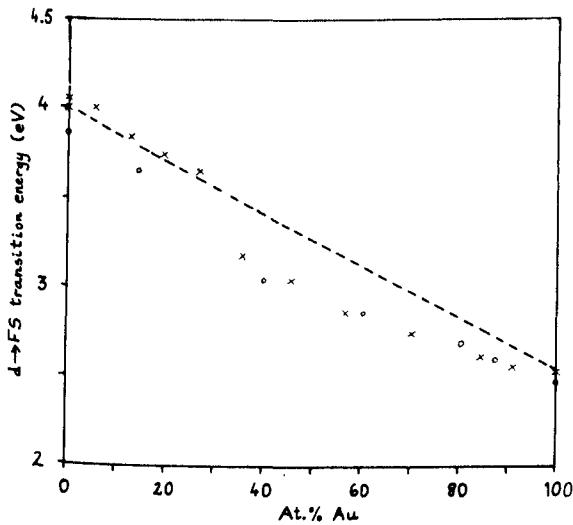


Fig. 7. The position of the low energy absorption edge for Au-Ag alloys: x, the energy for $d^2\epsilon_2/d\omega^2$ (this work); o, from ref. 22.

were used, neglecting the inhomogeneity of the material. The justification for this is presented below (the nulling ellipsometer established a clear null for these alloys no matter how the null was approached). The optical spectra for these alloys are qualitatively similar to the spectra of homogeneous alloys. The alloys show various amounts of

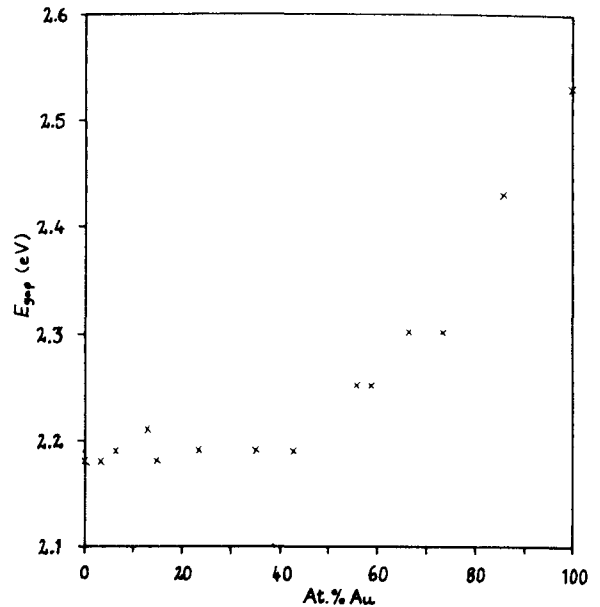


Fig. 8. The energy E_{gap} of the absorption edge in ϵ_2^b for Au-Cu alloys.

primary phase (α or β) and eutectic ($\alpha + \beta$). The optical constants of bulk α and β were determined from separate specimens; for any of the binary alloys the respective α and β phases have a constant composition and thus invariant optical constants. The optical

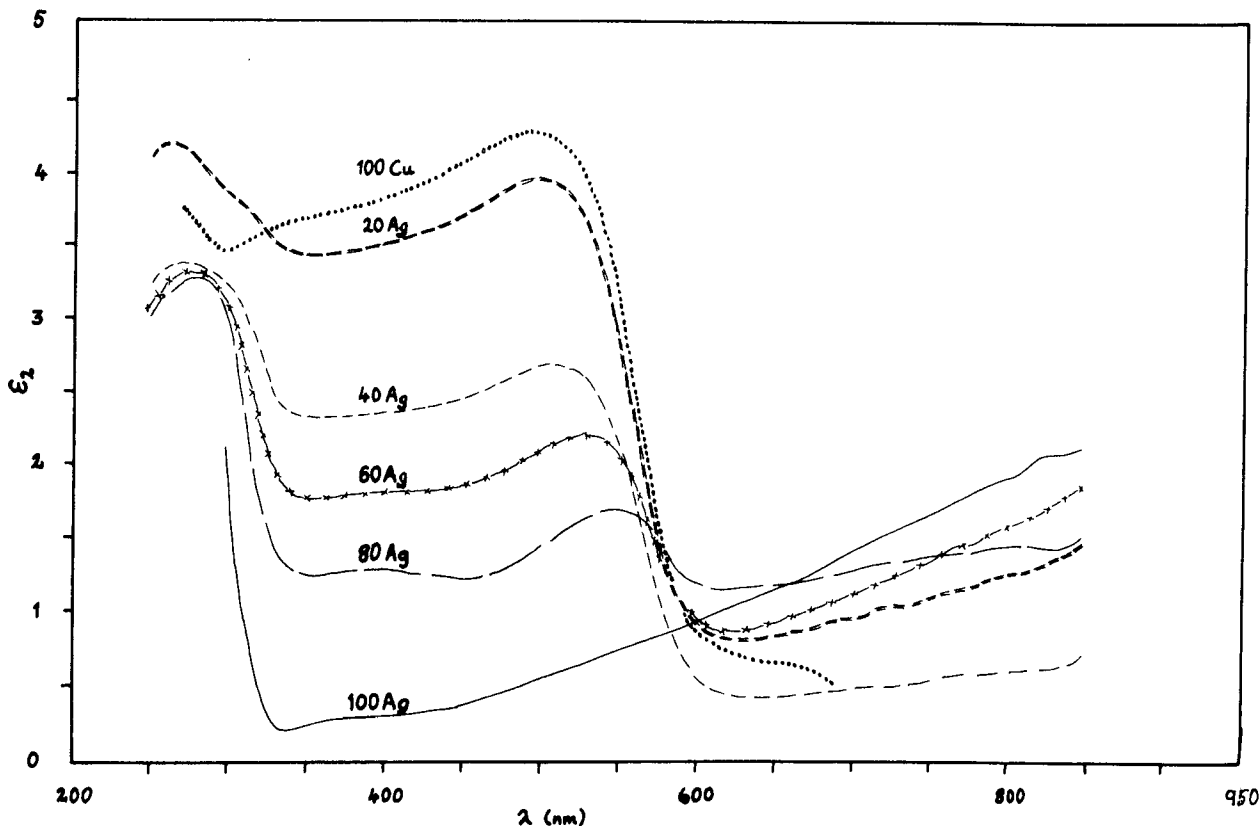


Fig. 9. The imaginary part ϵ_2 of the dielectric function for Ag-Cu alloys.

properties of the bulk alloy can thus be expected to be determined by the volume fractions and optical constants of each of the phases in the mixture. Since the α and β phases are almost pure silver and copper it is necessary to examine the influence of mixing on the spectral characteristics of these components. Firstly the sharp interband absorption of silver at 3.8 eV does not appear to be either shifted or broadened, although in the copper-rich alloys the detail tends to be obscured by the influence of the copper. While reflectivity for copper is high for energies greater than 1.9 eV the interband transition analogous to the 3.8 eV transition for silver occurs at 2.2 eV; upon mixing this copper edge appears to be neither shifted nor broadened. However, the plateau between 2.9 and 2.3 eV in copper rises steadily with the addition of silver until it completely disappears in the presence of pure silver. Furthermore, the slope between 2.9 and 3.8 eV increases steadily from pure copper to pure silver. Thus the two fundamental absorption edges in Ag-Cu do not move and only their relative strength alters with composition.

This suggests that apart from a slight terminal solubility the two components silver and copper retain their electronic and optical characteristics independently and that they will contribute to the final alloy behaviour in proportion to the volume fraction of the α and β phases.

The relative phase and amplitude changes occurring in incoherently reflected light at an inhomogeneous plane surface may be determined by comparing the sum of the two Stokes vectors arising from reflection at the two types of reflecting surfaces in the inhomogeneous alloy with the column vector of a single homogeneous phase surface. This appears to be legitimate since the nulling ellipsometer provides a well-defined unambiguous null as long as the sampling beam width is large compared with the dimension of the inhomogeneity. The resulting equations for the relative phase change Δ and the relative amplitude change $\tan \psi$ are

$$\Delta = \tan^{-1} \left\{ \frac{q |\rho_{s\alpha}| |\rho_{p\alpha}| \sin \Delta_\alpha + (1-q) |\rho_{s\beta}| |\rho_{p\beta}| \sin \Delta_\beta}{q |\rho_{s\alpha}| |\rho_{p\alpha}| \cos \Delta_\alpha + (1-q) |\rho_{s\beta}| |\rho_{p\beta}| \cos \Delta_\beta} \right\}$$

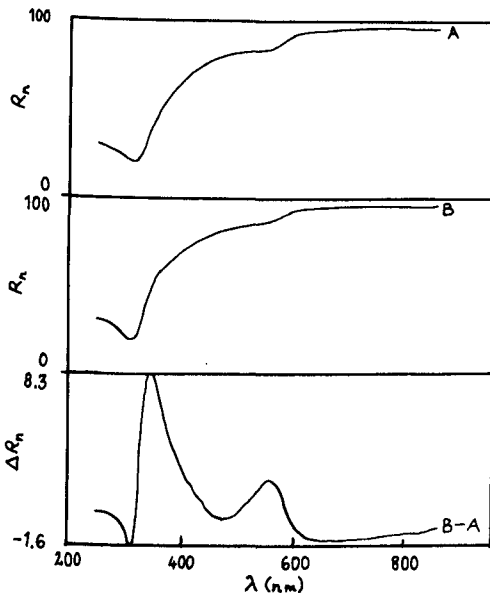


Fig. 10. Experimental (curve A, 70Ag-30Cu) and theoretical (curve B, volume fraction $q = 0.676$) reflectance curves for two-phase alloys with nominally the same volume fraction.

$$\tan \psi = \left\{ \frac{q |\rho_{p\alpha}|^2 + (1-q) |\rho_{p\beta}|^2}{q |\rho_{s\alpha}|^2 + (1-q) |\rho_{s\beta}|^2} \right\}^{1/2}$$

where ρ_s and ρ_p are the Fresnel reflection coefficients in the s and p directions, q is the volume fraction of α , $1 - q$ is the volume fraction of β , Δ is the relative phase change for phases α and β and the subscript indicates the phase.

Figure 10 shows a normal reflectance curve for a theoretical two-phase alloy with the same volume fractions of α (silver-rich terminal solid solution) and β (copper-rich terminal solid solution) as for the 70Ag-30Cu alloy used to obtain the experimental normal reflectance curve. If the optical spectra of two (or more) duplex alloys are available an inversion of the equations permits the determination of the optical properties of the terminal solid solutions. Furthermore this modelling explains special features of the colour identification of such duplex alloys when the identification is made from ellipsometrically derived normal reflectance and compared with normal spectrometry. It is easy to determine the CIE [26] chromaticity coordinates for each of the specimens using the normal reflectance determined by either spectrometry or spectroellipsometry. Colour theory predicts that the series of colours derived from a

mixture of two colours, e.g. white and red, will lie on a straight line in the chromaticity diagram. Such behaviour is *a priori* expected from the $\alpha + \beta$ alloy mixtures. However, the colour coordinates of such alloy mixtures determined ellipsometrically lie on a curve. Spectral reflectance (and hence the colour of metal alloys) will also vary with the angle of incidence of the probe beam. Care must therefore be exercised in comparing reflectance values, particularly those of polyphase alloys. The optical constants n and k and the dielectric functions do not suffer from this and therefore techniques to establish primarily these quantities are to be preferred for optical measurements of metals.

5. CONCLUSION

Spectroellipsometry has become accepted as a method of determining the optical characteristics of metals and alloys. Despite the extreme sensitivity of ellipsometry to surface films and surface preparation the application of environmental control, sample annealing and cleaning must promote the application of the technique to studies of reactive metals and alloys.

The optical behaviour of solid solutions is consistent with the model of extensive band mixing as the composition alters. The dielectric function in particular has a single band whose strength and peak alters progressively with composition. The behaviour of alloys which exhibit a solution limit and a separation into two (or more) phases differs in that the terminal phases retain their composition but alter their proportion (*i.e.* volume fraction). This effect is observed in the dispersion curves, particularly of the interband component of the dielectric function, as a separation of the constituent spectra which in turn vary in strength with volume fraction. The optical appearance and in particular the colour of the alloys can be determined objectively by computing the normal reflectivity R_n from the optical constants and calculating the CIE chromaticity coordinates. Variations in chromaticity coordinates correlate well with changes in alloying but care has to be taken in using the data for polyphase alloys. A model is introduced that permits the evalua-

tion of the optical characteristics of poly-phase alloys. The inversion of this model also permits the quantification of volume fractions of polyphase alloys or the determination of the chromaticity of constituent phases.

ACKNOWLEDGMENTS

The authors wish to thank Dr. L. L. Shreir for providing facilities within the Department of Metallurgy and Materials, the ILEA and The International Gold Corporation for funding the work reported here, and Mr. R. Cohen and Mrs. M. Evans who prepared the materials essential for the study.

REFERENCES

- 1 F. Wooten, *Optical Properties of Solids*, Academic Press, New York, 1972.
- 2 D. L. Greenaway and G. Harbeke, *Optical Properties and Band Structure of Semiconductors*, Pergamon, Oxford, 1968.
- 3 N. W. Ashcroft and N. D. Mermin, *Solid State Physics*, Holt, Rinehart and Winston, New York, 1976.
- 4 B. D. Cervell, C. Levy, N. F. M. Henry and T. N. Shadlun, *Bull. Mineral.*, 101 (1978) 234.
- 5 R. G. J. Strens and R. Freer, *Mineral. Mag.*, 42 (1978) 19.
- 6 R. G. Burns and D. J. Vaughan, *Am. Mineral.*, 55 (1970) 1576.
- 7 E. F. I. Roberts and K. Mc. Clarke, *Gold Bull.*, 12 (1979) 9.
- 8 G. E. Gardam, *Trans. Inst. Met. Finish.*, 41 (1964) 190.
- 9 G. E. Gardam, *Trans. Inst. Met. Finish.*, 44 (1966) 196.
- 10 R. S. Hunter, *The Measurement of Appearance*, Interscience, London, 1975.
- 11 D. Ross, *Ph.D. Thesis*, University of London, 1978.
- 12 P. Drude, *Ann. Phys. (Leipzig)*, 39 (1890) 514.
- 13 R. M. A. Azzam and N. M. Bashara, *Ellipsometry and Polarized Light*, North-Holland, Amsterdam, 1977.
- 14 L. G. Shultz, *Adv. Phys.*, 6 (1957) 102.
- 15 M. P. Givens, *Solid State Phys.*, 6 (1958) 343.
- 16 H. Ehrenreich and H. R. Philips, *Phys. Rev.*, 128 (1962) 1622.
- 17 P. O. Nilsson, *Solid State Phys.*, 29 (1974) 139.
- 18 W. S. Rapson and T. Groenewald, *Gold Usage*, Academic Press, New York, 1978.
- 19 E. F. I. Roberts and A. Meadows, *J. Phys. E*, 7 (1974) 379.
- 20 P. R. Wessel, *Phys. Rev.*, 132 (1963) 2062.
- 21 H. Fukutani and O. Sueoka, in F. Abelès (ed.), *Optical Properties and Electronic Structure of Metals and Alloys*, North-Holland, Amsterdam, 1965.
- 22 J. Rivory, *Phys. Rev., Sect. B*, 15 (1977) 3119.
- 23 J. Friedel, *Adv. Phys.*, 3 (1954) 446.
- 24 F. Antonangeli, E. Colarita, R. Rosei and S. E. Saluski, *Nuovo Cimento B*, 24 (1974) 121.
- 25 D. Beaglehole and E. Erlbach, *Phys. Rev., Sect. B*, 6 (1972) 1209.
- 26 *CIE International Lighting Vocabulary*, CIE, Paris, 3rd edn., 1970, p. 9.